University of Southampton

Surface Charge Measurement By The Pockels Effect

by

Yao Long SAM

A thesis submitted for the Degree of

Doctor of Philosophy

in

The Department of Electronics and Computer Science

Faculty of Engineering and Applied Science

October 2001

UNIVERSITY OF SOUTHAMPTON

ABSTRACT

FACULTY OF ENGINEERING AND APPLIED SCIENCE

DEPARTMENT OF ELECTRONICS AND COMPUTER SCIENCE

Doctor of Philosophy

SURFACE CHARGE MEASUREMENT BY THE POCKELS EFFECT

by Yao Long SAM

This thesis is concerned with the design and development of a surface charge measurement system using the Pockels effect. The measurement of surface charge is important in determining the electrical performance of high voltage insulation materials. The method proposed allows on-line measurement of charge and can generate two-dimensional images that represent the charge behaviour on the surface of the material under test.

The measurement system is optical and uses a Pockels crystal as the sensing element. The Pockels cell uses a wafer of Bismuth Silicon Oxide (BSO). Surface charge creates an electric field within the Pockels crystal and induces anisotropy. A laser light is used to detect any change in anisotropy. This approach allows non-destructive measurements since no direct electric signal or component interferes with the surface charge. Furthermore, the optical measurement system can dynamically observe and simultaneously quantify surface charge which is not possible using conventional methods. This allows the surface charge distribution under the influence of a time varying electric field to be studied. The system's accuracy and sensitivity have been improved through the use of an Optical Phase Modulator. The system uses a high speed CCD camera with a maximum frame rate of 1000 frames per second and Synchronisation Control Circuit to obtain a high temporal resolution. This has allowed the study of charge behaviour at mains power frequencies.

Surface charge distributions have been observed by applying both impulse and AC voltages to a needle electrode in direct contact with the BSO. AC surface discharge behaviour of polymeric materials bonded to the BSO has also been investigated. The effect of the surrounding environment has been experimentally examined by placing the cell inside a vacuum chamber. Surface charge measurements have been made at various atmospheric pressures. The effect of an electro-negative gas (Sulphur Hexafluoride) on the surface charge distribution has also been investigated.

Contents

List of Figures

List of Tables

List of Symbols and Abbreviations

Acknowledgements

1 Introduction 1

1.1 The Measurement of Surface Charge 1
1.2 Contents of This Thesis 6

2 The Theory of Measurement of Surface Discharge Using Pockels Effect 8

2.1 Introduction 8
2.2 Anisotropic Mediums 8
2.3 The Phase Retardation Induce by a Birefringent Crystal 13
2.4 The Pockels Effect 14
2.5 The propagation of the electromagnetic wave within a Pockels crystal 20
2.6 Electro-optic phase modulation 22
2.6.1 Transverse Mode 22
2.6.2 Longitudinal Mode 27

2.7 The Polarisation of Light 30
2.8 Jones Matrix 32
2.9 Fundamental Experiment 37

3 Using a Pockels Cell to Measure Surface Charge: Design Considerations 40

3.1 Introduction 40
3.2 Pockels Crystal as the Surface Charge Transducer 42
3.3 The Electro-optic Modulator 48
3.3.1Transverse Electro-optic Modulator 49
3.3.2 Longitudinal electro-optic Modulator 50
3.3.3 Modified Longitudinal electro-optic Modulator 50
3.3.4 High Frequency Modulation Considerations 51
3.4 Laser Source 52
3.5 Beam Expander 53
3.5.1 Keplerian Beam Expander 53
3.5.2 Galilean Beam Expander 54
3.6 Beam Splitter 55
3.7 Lens and Pinhole 56
3.8 CCD Camera 58
3.9 Synchronisation Control Circuit 60
3.10 Antireflection Coating 61
3.11 The Two Dimensional Measurement of Transmitted Light Intensity 61

4 AC Surface Discharge Measurement System Including a Waveplate 66

4.1 Introduction 66
4.2 Measurement Principle 67
4.3 An Equivalent System 69
4.4 The Measurement Procedure 71
4.5 Image Processing 73
4.6 Experimental Results 74

5 Surface Discharge Measurement System Including an Optical Phase Modulator (OPM) 80

5.1 Introduction 80
5.2 Improving the Spatial Resolution 81
5.3 The OPM and Its Measurement Principle 82
5.3.1 Determination of The Total Phase Retardation Distribution, $\Phi_{(x,y)}$ 83
5.3.2 Determination of the Equivalent Maximum Light Intensity Distribution, $I_{E(x,y)}$ 84
5.4 Image Averaging Technique 86
5.5 The Equivalent System 89
5.6 The Equivalent Maximum Light Intensity Distribution, $I_{E(x,y)}$ 89
5.6.1 Measurement Limits 90
5.7 Comparison the light signal between the OPM and 1/8 waveplate 91
5.8 The Measurement Procedure 92
5.8.1 Impulse Generator 92
5.8.2 Synchronisation Control 93
5.9 Validation of Measurement 94
5.10 Image Processing 95
5.11 Experimental Results 97
5.11.1 Positive Impulse Discharge 97
5.11.2 Negative Impulse Discharge 98
5.12 Conclusion 98

6 AC Surface Discharge Measurement 100

6.1 Introduction 100
6.2 The Measurement Procedure 100
6.3 Image Processing 102
6.4 Experimental Results 103
6.4.1 AC Surface Discharge First Half-cycle Positive 103
6.4.2 AC Surface Discharge First Half-cycle Negative 104
6.5 Discussion of Results 113
6.5.1 Electron Multiplication 113
6.5.2 The Surface Discharge Mechanism 118
6.5.3 Backdischarge 121

7 AC Surface Discharge Behaviour of Polymeric Materials and the Effect of Local Environmental Conditions 122

7.1 Introduction 122
7.2 The Experiment 123
7.2.1 Sample Preparation Using Compression 123
7.2.2 Sample Preparation Using Solvents 125
7.2.2.a PMMA 125
7.2.2.b LDPE 125
7.3 The Measurement Principle 126
7.4 Experimental Results 130
7.4.1 AC Surface Discharge Measurements of PMMA 130
7.4.2 AC Surface Discharge Measurements of LDPE 131
7.4.3 Discussion 135
7.5 AC Surface Discharge Under Different Environmental Conditions 137
7.5.1 Experimental Setup 137
7.5.2 Experimental Results 138
7.5.3 Discussion 142
7.6 Surface Discharge in the Electro-negative Gas SF_6 142
7.6.1 Experimental Setup 143
7.6.2 Experimental Results 144
7.6.3 Discussion 146

8 Conclusions and Further Work 147
8.1 Conclusions 147
8.2 Further Work 149

Appendices:

A: Developed Software for Optical System Including a Waveplate
B: Developed Software for Optical System Including an Optical Phase Modulator
C: Synchronisation Control Circuit
D: List of Publications

References:

List of Figures

1.1	Schematic of measurement of streamer tip using photo multiplier	3
1.2	(a) Experiment arrangement of electrostatic probe and (b) its equivalent circuit	3
2.1	Dielectric permittivity in the dielectric permittivity space (a) a sphere for an isotropic dielectric, (b) an ellipsoid for an anisotropic dielectric	10
2.2	Double refraction of incident light through an anisotropic medium	13
2.3	Phase retardation of a birefringent crystal	14
2.4	Rectangular lattice structure with a centre of symmetry	15
2.5	Rectangular lattice structure that lacks a centre of symmetry	18
2.6	The effect of the electro-optic tensor	22
2.7	A $LiNbO_3$ crystal as a transverse electro-optic modulator	23
2.8	A BSO crystal as a longitudinal electro-optic modulator	27
2.9	The states of polarisation of light as the phase difference between two orthogonal electric field components increases from 0 to 2π	30
2.10	Coordinate axes and the azimuth angle	32
2.11	Simple experiment arrangement to determine V_π	38
2.12	Transmittance of light intensity against phase retardation	39
3.1	Schematic diagram of the optical system for surface charge measurement	41

3.2	Facial orientation of Pockels crystal and incident direction of light beam	42
3.3	Incident light into a wedge y-cut crystal. (a) transmitted light experiences difference polarisation states. (b) transmittance light intensity when passed through an analyser set to 0° with respect to the light polarisation, (c) reverse strips of bright and dark pattern observed on screen when the analyser is set to 90°	45
3.4	BSO Pockels transducer (a) the surface charge induced electric field (b) the orientation of the crystal and the light polarisation	47
3.5	Longitudinal electrode-optic cells (a) with end electrode and small aperture, (b) with ring electrode and large aperture	50
3.6	Electro-optic crystal an resonant circuit	51
3.7	(a) Keplerian Beam Expander (b) Galilean Beam Expander	53
3.8	The role of the PBS (a) without surface charge deposited on the Pockels crystal (b) with surface charge deposited	55
3.9	Removing interference using a wedge cut crystal, lens and pinhole	57
3.10	Images obtained by the CCD camera (a) without using a pinhole and (b) with a pinhole (effective figures dimensions are 8mm by 8mm)	58
3.11	Block diagram of the CCD camera	59
3.12	Block diagram of the synchronisation control circuit	60
3.13	Experiment setup to illustrate the concept of the measurement light intensity due to Pockels effect	62
3.14	Non-uniform intensity distribution (with dimension of 8mm by 8mm) of light reflected at BSO crystal	63
3.15	Light intensity change due to phase retardation	64
3.16	Surface charge deposited on the Pockels cell by an applied field (effective figures dimensions are 8mm by 8mm)	64
4.1	Optical system with the used of 1/8 waveplate	67
4.2	Light intensity against the phase retardation with or without 1/8 waveplate	68
4.3	Equivalent model	70
4.4	Quantified light intensity with various input light power used	70

4.5	Matlab program flow chart to evaluate the surface charge density	71
4.6	Control signal for measuring surface charge with a 1/8 waveplate	72
4.7	(a) image, $I_{b(x,y)}$ recorded before the discharge and (b) image, $I_{Q(x,y)}$ recorded during the discharge lead to (c) surface charge density, $\Phi_{(x,y)}$ after image processing	73
4.8	Dynamic AC surface discharge (a) time dependence of surface charge distribution (b) surface charge density key (c) waveform of voltage and corresponding frame number (effective dimensions of these images are 4mm by 4mm)	76
4.9	Dynamic AC surface discharge (a) time dependence of surface charge distribution (b) surface charge density key (c) waveform of voltage and corresponding frame number (effective dimensions of these images are 4mm by 4mm)	77
4.10	Dynamic AC surface discharge (a) time dependence of surface charge distribution (b) surface charge density key (c) waveform of voltage and corresponding frame number (effective dimensions of these images are 4mm by 4mm)	78
4.11	Dynamic AC surface discharge (a) time dependence of surface charge distribution (b) surface charge density key (c) waveform of voltage and corresponding frame number (effective dimensions of these images are 4mm by 4mm)	79
5.1	Induced electric field within a BSO crystal	81
5.2	Optical system including an Optical Phase Modulator	82
5.3	Pulse modulation of optical phase	84
5.4	Removal of background noise using image average produce with (a) 1 (b) 30 (c) 100 and (d) 500 images	87
5.5	Equivalent Model	89
5.6	Improving the measurement sensitivity	90
5.7	Comparison of measured light intensity between 1/8 wave-plate and OPM	91
5.8	(a) Impulse generator and (b) waveform	92

5.9	Synchronisation control signal for measurement of surface charge due to a high voltage impulse	94
5.10	Image processing for the images	96
5.11	Surface discharge response to (a) positive 2kV, (b) negative 3.6kV and (c) surface charge density key (effective dimensions of both images are 8mm by 8mm)	99
6.1	Control signals for AC surface discharge measurements	101
6.2	The image sequence during an AC discharge	102
6.3	(a) Negative modulated image and (b) positive modulated image lead to (c) surface charge density distribution by image processing	103
6.4	Dynamic AC surface discharge (a) time dependence of surface charge distribution (b) surface charge density key (c) waveform of voltage and corresponding frame number (effective dimensions of these images are 8mm by 8mm)	105
6.5	Dynamic AC surface discharge (a) time dependence of surface charge distribution (b) surface charge density key (c) waveform of voltage and corresponding frame number (effective dimensions of these images are 8mm by 8mm)	106
6.6	Dynamic AC surface discharge (a) time dependence of surface charge distribution (b) surface charge density key (c) waveform of voltage and corresponding frame number (effective dimensions of these images are 8mm by 8mm)	107
6.7	Dynamic AC surface discharge (a) time dependence of surface charge distribution (b) surface charge density key (c) waveform of voltage and corresponding frame number (effective dimensions of these images are 8mm by 8mm)	108
6.8	Dynamic AC surface discharge (a) time dependence of surface charge distribution (b) surface charge density key (c) waveform of voltage and corresponding frame number (effective dimensions of these images are 8mm by 8mm)	109

6.9	Dynamic AC surface discharge (a) time dependence of surface charge distribution (b) surface charge density key (c) waveform of voltage and corresponding frame number (effective dimensions of these images are 8mm by 8mm)	110
6.10	Dynamic AC surface discharge (a) time dependence of surface charge distribution (b) surface charge density key (c) waveform of voltage and corresponding frame number (effective dimensions of these images are 8mm by 8mm)	111
6.11	Dynamic AC surface discharge (a) time dependence of surface charge distribution (b) surface charge density key (c) waveform of voltage and corresponding frame number (effective dimensions of these images are 8mm by 8mm)	112
6.12	Space charge formed by an avalanche mechanism	113
6.13	(a) electron ionisation of air molecule and (b) electron ionisation of material surface	114
6.14	(a) photon ionisation of a gas molecule and (b) photon ionisation process at the material surface	115
6.15	(a) electron detachment of ions by collision and (b) electron detachment by collision at the material surface	115
6.16	(a) photon detachment of ions and (b) photon detachment at material surface	116
6.17	(a) spontaneous electron detachment of ions and (b) spontaneous detachment at material surface	116
6.18	(a) electron detachment of a gas molecule and (b) electron detachment from a material surface	117
6.19	Different processes involved in the propagation of streamers and the deposition of surface charge	117
6.20	Propagation of avalanches to form streamer channel and deposition of surface charge under positive applied field	119
7.1	Experimental arrangement for surface discharge measurements of polymeric materials	123
7.2	Thin film compression	124

7.3	Attach thin polymer film onto the BSO crystal	124
7.4	Equivalent circuit for Pockels cell with a polymer film bonded to its backface	126
7.5	The field in (a) an air filled capacitor and (b) an air and dielectric filled capacitor	128
7.6	(a) Thermal agitation randomises polar molecules and a field aligns their dipoles, (b) Non-polar molecules have no permanent dipole moment and a field induces dipoles and orients them along the field	130
7.7	Surface charge distribution under AC response for PMMA with thickness 2μm bonded on BSO (effective dimensions of these images are 8mm by 8mm)	131
7.8	Surface charge distribution under AC response for PMMA with thickness 15μm bonded on BSO (effective dimensions of these images are 8mm by 8mm)	132
7.9	Surface charge distribution under AC response for PMMA with thickness 30μm bonded on BSO (effective dimensions of these images are 8mm by 8mm)	132
7.10	Surface charge distribution under AC response for PMMA with thickness 100μm bonded on BSO (effective dimensions of these images are 8mm by 8mm)	133
7.11	Surface charge distribution under AC response for LDPE with thickness 2μm bonded on BSO (effective dimensions of these images are 8mm by 8mm)	133
7.12	Surface charge distribution under AC response for LDPE with thickness 6μm bonded on BSO (effective dimensions of these images are 8mm by 8mm)	134
7.13	Surface charge distribution under AC response for LDPE with thickness 14μm bonded on BSO (effective dimensions of these images are 8mm by 8mm)	134
7.14	Surface charge distribution under AC response for LDPE with thickness 20μm bonded on BSO (effective dimensions of these images are 8mm by 8mm)	135

7.15	Electron detachment by photon ionisation form streamer branches	136
7.16	Vacuum Chamber add on for varying surface discharge environment condition	138
7.17	Surface charge distribution under AC response for chamber gas pressure at 101.3kPa (1atm) (effective dimensions of these images are 8mm by 8mm)	139
7.18	Figure 7.18 Surface charge distribution under AC response for chamber gas pressure at 20.7kPa (3psi) (effective dimensions of these images are 8mm by 8mm)	140
7.19	Surface charge distribution under AC response for chamber gas pressure at 41.4kPa (6psi) (effective dimensions of these images are 8mm by 8mm)	140
7.20	Surface charge distribution under AC response for chamber gas pressure at 82.7kPa (12psi) (effective dimensions of these images are 8mm by 8mm)	141
7.21	Surface charge distribution under AC response for chamber gas pressure at 137.9kPa (20psi) (effective dimensions of these images are 8mm by 8mm)	141
7.22	Paschen's curve for breakdown voltage varied with gas pressure	142
7.23	Surface charge distribution under AC response for 10% electro-negative gas SF_6 filled in the chamber at gas pressure 101.3kPa (1atm) (effective dimensions of these images are 8mm by 8mm)	145
7.24	Surface charge distribution under AC response for 10% electro-negative gas SF_6 filled in the chamber at gas pressure 68.9kPa (10psi) (effective dimensions of these images are 8mm by 8mm)	145
7.25	Surface charge distribution under AC response for 10% electro-negative gas SF_6 filled in the chamber at gas pressure 34.5kPa (5psi) (effective dimensions of these images are 8mm by 8mm)	146

List of Tables

3.1	Electric field component measured and crystal symmetry	42
3.2	Characteristic of some common electro-optics crystal	46
7.1	Electrical properties of some insulating materials	137
7.2	Relative electric strength of various electro-negative gases	143

List of Symbols and Abbreviations

Symbols

α	direction that the electric field and incident light can be applied
α	ionisation coefficient
α_s	surface ionisation coefficient
β	direction that the electric field and incident light can be applied
γ	direction that the electric field and incident light can be applied
η	attachment coefficient
ε_o	permittivity of free space
ε_r	dielectric constant
ε_r	dielectric constant for BSO
$\overline{\overline{\varepsilon}}_r$	dielectric tensor
ε_x	principle dielectric permittivity
ε_y	principle dielectric permittivity
ε_z	principle dielectric permittivity
Γ	mean absolute phase change
$\sigma_{z(x,y)}$	two-dimensional surface charge distribution
θ	azimuth angle
ω_o	natural frequency
ω	operating frequency of incident electromagnetic wave

$\omega_o^{/}$	displaced natural frequency
$\Delta\left(\omega_o^2\right)$	change of resonant frequency
χ	susceptibility
χ_1	linear susceptibility
χ_2	second order susceptibility
χ_3	third order susceptibility
χ_{ijk}	third susceptibility tensors
χ_{ijkl}	forth susceptibility tensors
ξ	modified co-ordinate
ϕ	angle between the polarisation of the linear polarised light and the principle axis parallel to α
Φ	phase retardation
$\Delta\Phi$	phase difference
$\Phi_{(x,y)}$	two-dimensional phase retardation
$\Phi_{(x,y)}$	two-dimensional total phase retardation
$\Phi_{q(x,y)}$	two-dimensional phase retardation due to surface charge distribution
Φ_M	modulated phase retardation
$\Phi_{nat(x,y)}$	natural birefrigence
λ	optical frequency of the incident light
A	effective area of the parallel electrode
A_x	component of the electric field vector along the x direction
A_y	component of the electric field vector along the y direction
B	particle B
C_β	capacitance of the electro-optic crystal
C_e	extraordinary component of the incident electric field vector
C_o	ordinary component of the incident electric field vector
C_{pg}	capacitance between the probe and the ground
C_{sp}	capacitance between the insulator surface and the probe
C_{sg}	capacitance between the area on the insulator surface

C_{sg1}	capacitance between the area on the insulator surface and grounded screen of the probe
C_{sg2}	capacitance between the grounded back-plate
C_p	capacitance of the polymer
C_o	capacitance of air filled parallel electrode
C_d	capacitance of dielectric filled parallel electrode
c	speed of light
D	electric displacement
d	crystal thickness
d	thickness of the BSO crystal
d	spacing between electrodes
E	electric field
$E(\omega)$	oscillatory electric field
E_o	magnitude of the applied dc field
$E_{z(x,y)}$	two-dimensional electric field distribution across the BSO
e	unit vector along the direction of the normal mode
e^-	electron
f_{in}	focal length of the input lens
f_{out}	focal length of the output lens
g	damping factor
I_0	transmittance of light at 0°
I_{90}	transmittance of light at 90°
I_{max}	maximum light intensity
$I_{(x,y)}$	two-dimensional distribution of transmitted light intensity due to the phase retardation
$I_{o(x,y)}$	maximum light intensity distribution of incident beam
$I_{b(x,y)}$	light intensity before the voltage is applied
$I_{q(x,y)}$	light intensity after the voltage is applied
$I_{offset(x,y)}$	constant offset component of the light intensity
$I_{M+(x,y)}$	positive modulated image

$I_{M-(x,y)}$	negative modulated image
$\Delta I_{D(x,y)}$	difference images
$I_{E(x,y)}$	equivalent maximum light intensity distribution
$I_{a(x,y)}$	initial light intensity distribution
$I_{+(x,y)}$	initial light intensity distribution during the positive modulated phase
$I_{-(x,y)}$	initial light intensity distribution during the negative modulated phase
$\Delta I_{(x,y)}$	difference images prior to discharge
$I_{n(x,y)}$	time varying noise
k	complex component of the dielectric constant
k_{ix}	restoring force constant to the x component
k_e	wave numbers of the extraordinary wave
k_o	wave number of the ordinary wave
m	electron mass
m	magnification of the beam
N	number of charged particle
n	refractive index
n_o	refractive index of ordinary axis
n_o	refractive index of the BSO
n_e	refractive index of extraordinary axis
n_x	refractive index of principle x axis
n_y	refractive index of principle y axis
n_z	refractive index of principle z axis
Δn	change of refractive index
n	number of the positive ions
n_o	initial number of the positive ions
$\mathbf{o}$	unit vector along the direction of the normal mode
P	induced polarisation
P_1	linear polarization
P_2	second order induced polarisation
P_3	third order induced polarisation

Q	charge
$\overline{\overline{r}}$	electro-optic tensor
r_{ij}	electro-optic coefficients
$R(\theta)$	rotation matrix
R_s	internal resistance of the modulation voltage source
r_{41}	electro-optic coefficient
$T(\Phi,\theta)$	Jones matrix for the transmittance of light
$T_{(x,y)}$	total transmittance
V_π	half-wave voltage
V_s	induced voltage on the probe by the charge
V_{out}	output voltage
v	velocity of electromagnetic wave
$+V_M$	positive modulating voltages
$-V_M$	negative modulating voltages
W_o	Jones matrix for the retardation plate
x	principle axis
x	electron displacement
$\dot{x}$	velocity of electron displacement
$\ddot{x}$	acceleration of electron displacement
$\mathbf{x}$	unit vector along the chosen direction in x
X	particle X
y	principle axis
$\mathbf{y}$	unit vector along the chosen direction in y
Y	Particle Y
z	principle axis

Abbreviations

A/D	Analogue to Digital
AC	Alternating Current
ADP	Ammonium Dihydrogen Phosphate
BSO	Bismuth Silicon Oxide
BGO	Bismuth Germanium Oxide
CCD	Charge Coupled Device
CCl_4	Tetra
CCl_2F_2	Freon
CdTe	Cadmium Telliride
fps	frames per second
GaAs	Gallium Arsenide
GIS	Gas Insulated Switchgear
HDPE	High Density Polyethylene
HV	High Voltage
KDP	Potassium Dihydrogen Phosphate
LDPE	Low Density Polyethylene
$LiNbO_3$	Lithium Niobate
N_2	Nitrogen
O_2	Oxygen
OPM	Optical Phase Modulator
PBS	Polarised Beam Splitter
PC	Personal Computer
pk-pk	Peak to peak
PM	Photo Multiplier
PMMA	Polymethylmethacrylate
SF_6	Sulphur Hexaflouride
SCSI	Small Computer System Interface
SSC	Synchronisation Control Circuit
TTL	Transistor Transistor Logic
XLPE	Cross Linked Polyethylene

Acknowledgements

Firstly, I would like to express my thanks to my Ph.D supervisor, Dr Paul Lewin, for his guidance during this research project. Over the last few years, his kindly assistance, advice and encouragement has not only driven me to complete my project but also helped in solving my personal problems. I appreciate the opportunities given to me by Prof Anthony Davies to conduct research in the High Voltage Lab. Also, thanks for his guidance and advice through out the project. I would like to take this opportunity to thank the National Grid Company, UK for their financial support. Thanks to Dr Simon Sutton of NGC for his supervision and discussion about the project. Furthermore, I would like to thank Dr Alun Vaughan who spent his valuable time helping me with the sample preparation. The advice and help given by Prof James Wilkinson and Dr Jonathan Luff from Optoelectronic Research Center, UK is unforgettable. I greatly appreciate their assistance in providing a clean room facility and workspace for me to carry on my project after the fire badly damaged the HV Lab. Thanks to Roland, Neil, Brian and Mark and other technicians for their support and time helping me to set up the experiment. Also thanks to Richard Howell for helping with the construction of electronic circuits. In addition, I would like to thank all of my colleagues in HV group for their help, advice and support when I encountered problems. Finally, the encouragement and support from my family will always be remembered.

To my dearest parents

Chapter 1

Introduction

1.1 The Measurement of Surface Charge

Surface discharge is regarded as a form of partial discharge which is produced by field concentration existing between a conductor and a solid dielectric. It is stochastic in nature, exhibiting significant statistical variability in pulse amplitude, waveform, time of occurrence, insulating material, particle contamination and dependence of surrounding environment [1,2]. Generally, surface discharges do not necessarily produce a uniform or symmetrical distribution of charge. Therefore two-dimensional measurement techniques have been developed to study the phenomena. Various approaches have been developed and used to record the surface charge distribution.

Initially a dust figure technique [3,4,5,6] was used to obtain the non-uniform surface charge pattern. This method provides a simple solution for visualising the two-dimensional surface charge distribution. The dust figure technique involves spraying a charged powder onto the surface of the material subject to the discharge. The charged powder used is a mixture of positive charged red-coloured lead oxide and negative charged yellow sulphur. The positive charged lead oxide will be attracted to the negative surface charge and the yellow sulphur to the positive surface charge on the

material. The resolution of the surface charge distribution obtained by this method depends on the size of the particle used and can be as small as a few microns. The disadvantage of this technique is that it requires a great deal of skill in order to obtain a clear figure, especially for insulating materials with low surface resistance e.g. glass. Furthermore, the figure obtained is difficult to preserve for any significant period of time. Also, lead oxide is poisonous and must not be inhaled during the experiment. Although the surface charge distribution is very easy to visualise by using a dust figure technique, the surface charge density cannot be quantified by this approach. The dust figure is technique classified as one of the Lichtenberg figure techniques to obtain surface charge distribution.

Another Lichtenberg figure technique is to use photographic methods [7,8,9]. During discharge and ionisation light is radiated and it can be recorded using photographic film. The radiated light during the discharge has a very short time duration of only a few microseconds. The film can be directly exposed to the surface discharge or light can be focussed onto the film using an optical lens.

Lichtenberg figures can also be obtained through the use of an image converter camera[10,11,12,13] consisting of a streak unit having a temporal resolution of up to 1ns. The streak unit enables the observation of the temporal growth of the discharge activity. The surface discharge mechanism can be visualised over a very short time scale, but measurement of surface charge density was originally impossible. However, a modern development [14] allows the charge density to be quantified using a streak camera.

The photo multiplier (PM) [15,16,17] was first used in the 1960's to detect the light emitted during a discharge and ionisation as shown in Figure 1.1. This approach gave a good observation of streamer development. The voltage was applied across a pair of parallel plate electrodes in order to obtain a uniform electric field. The streamer propagated across uniform field and the PM detected the streamer tip. This approach is useful for estimating the velocity of streamer growth by comparing the time difference between two PM signals and is still associated with other approaches e.g. the electrostatic probe [17]. The results show that the velocity of streamer growth is

around 10^5-10^6 ms^{-1}. However, this method is limited to one-dimensional measurements and the charge distribution and density cannot be determined.

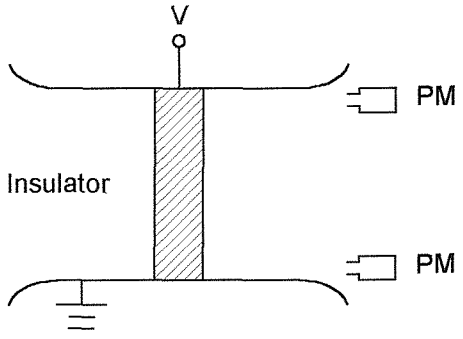

Figure 1.1 Schematic of measurement of streamer tip using photo multiplier

The development of the electrostatic scanning probe in the 1960's by Davies [18] has been widely used to obtain surface charge distributions on insulating materials [19,20] and also has the ability to quantify surface charge density. The arrangement of the probe is shown in Figure 1.2a and this can be represented by a capacitive equivalent circuit [21] as shown in Figure 1.2b where Q is the surface charge, C_{sg} is the capacitance between the area on the insulator surface and all earthed surface which comprises of the capacitance between the area on the insulator surface and grounded screen of the probe (C_{sg1}) and the capacitance between the grounded back-plate (C_{sg2}). V_s is the induced voltage on the probe by the charge Q. C_{sp} is the capacitance between the insulator surface and the probe and C_{pg} is the capacitance between the probe and the ground.

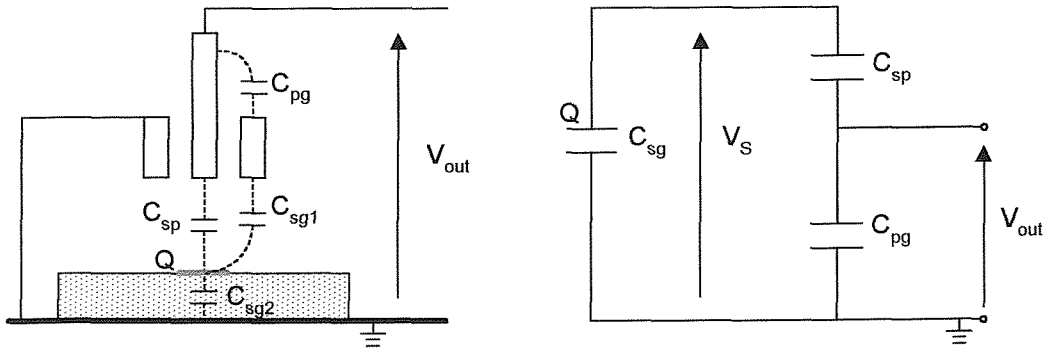

Figure 1.2 (a) Experiment arrangement of electrostatic probe and (b) its equivalent circuit

However, this technique has disadvantages that affect its performance. The thickness of the dielectric will cause measurement errors as the electric field becomes non-uniform as the thickness of the dielectric increases. Therefore, the capacitance model used for a thin sample must be modified if a thicker sample is under test [18,21]. The probe tip must be keep as small as possible for accurate measurement of surface charge. If the charging area is small, the measurement result will be influenced by the size of the probe tip. Furthermore, the gap between the probe and the dielectric surface must be kept to a minimum. Coexistence of positive and negative charge in close proximity can cause measurement error. The charge induced on the probe can be decreased by 15% due to any adjacent opposite charge [18]. The space charge built up in the bulk is another factor that effects measurement accuracy. The simple model cannot be applied for cases where bulk and surface charge exist in the same dielectric. Usually, the shape of the insulating material investigated using the electrostatic probe has a symmetry about its rotating axis e.g. disc or cone spacer and cylinder [19,20, 21,22]. Further development of the electrostatic probe has included the introduction of a λ function by Pederson [23,24,25] which considers the probe response due to the effect of adjacent charge and therefore improves the measurement accuracy achieving a better spatial resolution [21]. However, this method requires a large computer memory to perform the calculation for this model.

During the early of 1980's, the use of electro-optic sensors [26,27,28, 29,30,31,32,33] became popular for the measurement of electric fields. This method has several advantages [34] over conventional methods as it has less field distortion, no electronic circuit or power source and a wide frequency response (up to several Gigahertz). The optical measurement has no direct contact with the electric field hence avoiding electromagnetic interference error. This approach uses the electro-optic crystal as a transducer to transform an electric signal into an optical signal where the change of refractive index is proportional to the electric field. The electro-optic effect can be classified into either a linear effect or a quadratic effect. Generally, the linear electro-optic effect (Pockels effect) is used in the measurement of electric fields. Usually, the electric field measurement is arranged in the transverse configuration i.e. the field is perpendicular to the incident light so that the electrode of the crystal does not interfere with the optical signal. A photo diode is used to measure the change of the light

intensity. However, electric field measurement by the transverse configuration is limited to a one-dimensional measurement only i.e. the electric field across the crystal. The quadratic electro-optic effect (Kerr effect) [35,36,37,38,39,40,41,42] is used for the measurement of the space charge induced in liquid dielectrics due to an applied field. The use of a photo diode to detect the light intensity changes due to the Kerr effect is also limited to a one-dimensional measurement. If a Charge Coupled Device (CCD) camera is used the two-dimensional space charge distribution that exists within the liquid dielectric can be obtained [35,36,37].

Two-dimensional measurement of surface charge is now possible [43,44]. The linear electro-optic crystal is arranged in the longitudinal mode and a camera system is used to record the light intensity change due to surface charge on the Pockles crystal. More recently the optical measurement system has been significantly improved. The sensitivity of the system has been increased by using an Optical Phase Modulator (OPM) [45,46,47,48] instead of a wave-plate. Detection of the reflected light signal rather than the transmitted light signal acts to double the sensitivity of the Pockels crystal. Furthermore, the measurement of reflected light eliminates both the influence of the needle electrode attached to the back side of the crystal and the film optical characteristics. The availability at relatively low cost of high speed CCD cameras with frame rates of 1000 frames per second and a spatial resolution 256 by 240 pixels have also improved the measurement system. The high speed CCD camera increases the performance of the optical system providing better temporal resolution and enabling the observation of surface discharge under applied AC voltages. Improved computer processing speeds mean that large image data files can be rapidly analysed. Compared to the two-dimensional measurement of space charge using the Kerr effect [39,42], the optical measurement of surface charge requires fewer components and a less complicated image processing algorithm.

1.2 Contents of This Thesis

The thesis describes the development of an optical measurement system based on Pockels effect. In Chapter 2, the theory behind Pockels effect is detailed. The induced anisotropy of a Pockels crystal is used to alter the state of the polarisation of incident light. The Jones matrix analytical approach is discussed as it simplifies the mathematic model of light propagation through the Pockels crystal. Initial experimental results are presented that investigate the relationship between applied electric stress and the polarisation of incident light.

The design of the optical system is discussed in Chapter 3. The characteristic properties of various Pockels crystals including optical gain, facial orientation and operating wavelength are reviewed. The design of an Optical Phase Modulator that utilises Pockels effect is discussed. The choice of laser source, beam expander, beam splitter, optical lens and pinhole is described. The chapter also includes details about the use of a Charge Couple Device (CCD) camera to record two-dimensional images. The synchronisation of the measurement process using signals from the CCD camera is detailed. Some basic measurement results are also presented.

The use of a wave-plate to distinguish the charge polarity is discussed in Chapter 4. An equivalent model is described and the limitations of the measurement system are detailed. Image processing based on the measurement principle is reviewed and results from surface discharge experiments where the Pockels cell was subjected an 8kV peak to peak (pk-pk) AC applied voltage are presented.

Chapter 5 details the measurement principle of the optical system including an OPM which has increased sensitivity and accuracy when compared to the waveplate method. Natural birefringence is taken into consideration. Image averaging is used to remove spatial noise. The equivalent model of the measurement principle is introduced and the limitations of the system including consideration of non-uniform factors are detailed. The OPM measurement principle has been experimentally verified by examining surface charge due to positive and negative impulse voltages.

Results are presented of the measured surface charge distributions due to an impulse voltage.

Results from experiments investigating AC surface discharge distributions are presented in Chapter 6. AC 14kV peak to peak voltages have been applied across the Pockels cell. The chapter also includes discussion about the obtained results.

The measurement system has been used to investigate AC surface discharge phenomena on two different polymeric materials, Polymethylmethacrylate (PMMA) and Low Density Polyethylene (LDPE). Chapter 7 details sample preparation. The induced electric field within the BSO and the effect of an additional dielectric material are discussed. The optical system has been placed within a vacuum chamber to enable the measurement of AC surface discharge at various atmospheric pressures and results are presented. In addition, the surface discharge behaviour in the presence of the electro-negative gas Sulphur Hexaflouride (SF_6) is investigated and results are presented.

Conclusions and suggested further work are presented in Chapter 8. The Appendices include the information about the software developed to calculate the surface charge density from the light intensity image. Details about the Synchronisation Control Circuit are included together with its associated microcontroller program.

Chapter 2

The Theory of Measurement of Surface Discharge Using the Pockels Effect

2.1 Introduction

The optical measurement of surface charge density described in this thesis is based on the use of a crystal that exhibits linear electro-optic (Pockels) effect. The effect alters the phase of light due to the presence of an applied electric field across the crystal. Various crystals such as Lithium Niobate ($LiNbO_3$), Bismuth Silicon Oxide (BSO) and Quartz exhibit Pockels effect. In this chapter the theoretical model of the propagation of an electromagnetic wave through a linear electro-optic crystal is discussed.

2.2 Anisotropic Mediums

In isotropic mediums such as diamond and Natrium Chloride any incident light into the crystal will experience a dielectric permittivity that is independent of the wave propagation direction. As illustrated in Figure 2.1 the dielectric permittivity can be

represented by a sphere in the dielectric permittivity space and its dielectric properties remain constant for a light incident in any direction.

Light incident into an anisotropic medium will experience different dielectric permittivities depending on its direction. The dielectric permittivity space represents the three dielectric permittivities of the principal axes as shown in the Figure 2.1. This effect can be explained based on the electric displacement, D, its associated applied electric field, E and the induced polarisation, P that are parallel and defined as

$$\begin{aligned} D &= \varepsilon_o E + P \\ P &= \varepsilon_o \chi E \\ \varepsilon_r &= 1 + \chi \\ D &= \varepsilon_r E \end{aligned} \tag{2.1}$$

where ε_o, ε_r and χ are the permittivity of free space, the scalar dielectric constant and the scalar susceptibility respectively. In the general case, ε_r and χ are functions of frequency of the applied electric field. In an anisotropic medium which has a lack of cubic symmetry such as Sapphire, Calcite or Natrium Nitrate the electric displacement, D is not necessarily parallel the applied electric field, E [49,50,51,52]. Therefore, Equation. 2.1 must be modified into

$$D = \overline{\overline{\varepsilon}}_r E \tag{2.2}$$

where $\overline{\overline{\varepsilon}}_r$ is the dielectric tensor, which can be expressed in matrix form such that

$$\begin{pmatrix} D_x \\ D_y \\ D_z \end{pmatrix} = \varepsilon_o \begin{pmatrix} \varepsilon_{xx} & \varepsilon_{xy} & \varepsilon_{xz} \\ \varepsilon_{yx} & \varepsilon_{yy} & \varepsilon_{yz} \\ \varepsilon_{zx} & \varepsilon_{zy} & \varepsilon_{zz} \end{pmatrix} \begin{pmatrix} E_x \\ E_y \\ E_z \end{pmatrix} \tag{2.3}$$

By using an appropriate choice of crystal axes the dielectric tensor can be diagonalised so that

$$\begin{pmatrix} D_x \\ D_y \\ D_z \end{pmatrix} = \varepsilon_o \begin{pmatrix} \varepsilon_x & 0 & 0 \\ 0 & \varepsilon_y & 0 \\ 0 & 0 & \varepsilon_z \end{pmatrix} \begin{pmatrix} E_x \\ E_y \\ E_z \end{pmatrix} \tag{2.4}$$

such axes x, y and z are called the principal axes of the material and ε_x, ε_y and ε_z are called the principal dielectric permittivities. In the similar way the susceptibility tensor $\bar{\bar{\chi}}$ can be written in matrix form and the polarization, P is

$$P = \varepsilon_o \bar{\bar{\chi}} E \tag{2.5}$$

The three principal dielectric permittivities of the anisotropic material are no longer identical and its dielectric permittivity space will be represented by an ellipsoid as illustrated in Figure 2.1.

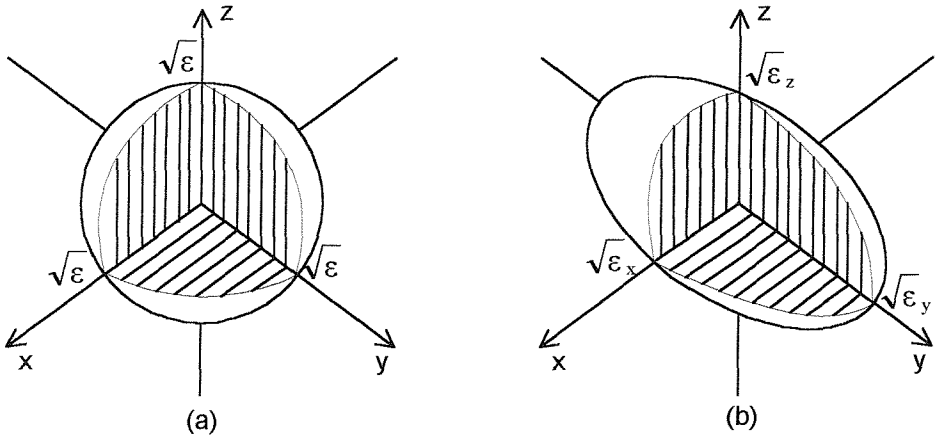

Figure 2.1 Dielectric permittivity in the dielectric permittivity space (a) a sphere for an isotropic dielectric, (b) an ellipsoid for an anisotropic dielectric

The dielectric permittivities space can be represented using the equation of an index ellipsoid, which is

$$\left(\frac{1}{\varepsilon_x}\right)x^2 + \left(\frac{1}{\varepsilon_y}\right)y^2 + \left(\frac{1}{\varepsilon_z}\right)z^2 = 1 \tag{2.6}$$

Crystals can be classified into three groups depending on the relationship between the principal permittivities. These classifications are isotropic, uniaxial and biaxial. Uniaxial and biaxial crystals are anisotropic media. Crystals with three equal principal dielectric permittivities, such that

$$\varepsilon_x = \varepsilon_y = \varepsilon_z \tag{2.7}$$

are called isotropic (Figure 2.1.a). If only two of the three principal dielectric permittivities are equal such that

$$\varepsilon_x = \varepsilon_y \neq \varepsilon_z \tag{2.8}$$

then the crystal is uniaxial. For a biaxial crystal, all three principal dielectric permittivities are different

$$\varepsilon_x \neq \varepsilon_y \neq \varepsilon_z \tag{2.9}$$

In the region of transparency for visible light, the crystal can also be characterised by the refractive indices of each axis. An isotropic crystal has one refractive index, i.e.

$$n = \sqrt{\varepsilon} \tag{2.10}$$

An uniaxial crystal has two principal refractive indices, i.e.

$$n_o = \sqrt{\varepsilon_x} = \sqrt{\varepsilon_y}, \qquad n_e = \sqrt{\varepsilon_z} \tag{2.11}$$

Whereas, a biaxial crystal has three principal refractive indices

$$n_x = \sqrt{\varepsilon_x}, \qquad n_y = \sqrt{\varepsilon_y}, \qquad n_z = \sqrt{\varepsilon_z} \tag{2.12}$$

The isotropic medium can be transformed into the anisotropic state subject to an external mechanical, electrical and magnetic force due to the reorientation of molecular dipoles within the crystal lattice. Thus the dielectric permittivities of the medium will change and the sphere in the dielectric permittivity space will alter into an ellipsoid.

Light incident into a transparent medium will cause the electrons of the medium to vibrate and a radiated electromagnetic wave will propagate through the medium. The velocity of the electromagnetic wave is dependent on the optical properties of the medium and is given by

$$v = \frac{c}{n} \tag{2.13}$$

where c is the speed of light in the free space. For an isotropic medium the velocity of light is independent of the direction of the incident light because the refractive index is constant in all directions. However the velocity of light propagating through an anisotropic medium depends on the directions of the incident light and is determined by the medium's indices of refraction. Consider a light beam incident into a uniaxial crystal propagating in the direction of the principal x axis as shown in Figure 2.2.

The two principal axes y and z will determine the velocity of light propagating through the medium. Since it is a uniaxial crystal the refractive index n_o and n_e are not the same and if n_o is less than n_e the y axis will be the fast axis and the z axis the slow axis. The light component in the fast axis propagates at a faster velocity than the light component in the slow axis resulting in the double refraction of the light. This double refraction is referred to as birefringence and depends on the light propagation direction. For certain incident directions the birefringence can be minimised or maximised. With reference to Figure 2.2, when the light travels in the direction of principal axis z no birefringence will be observed because $n_x = n_y = n_o$.

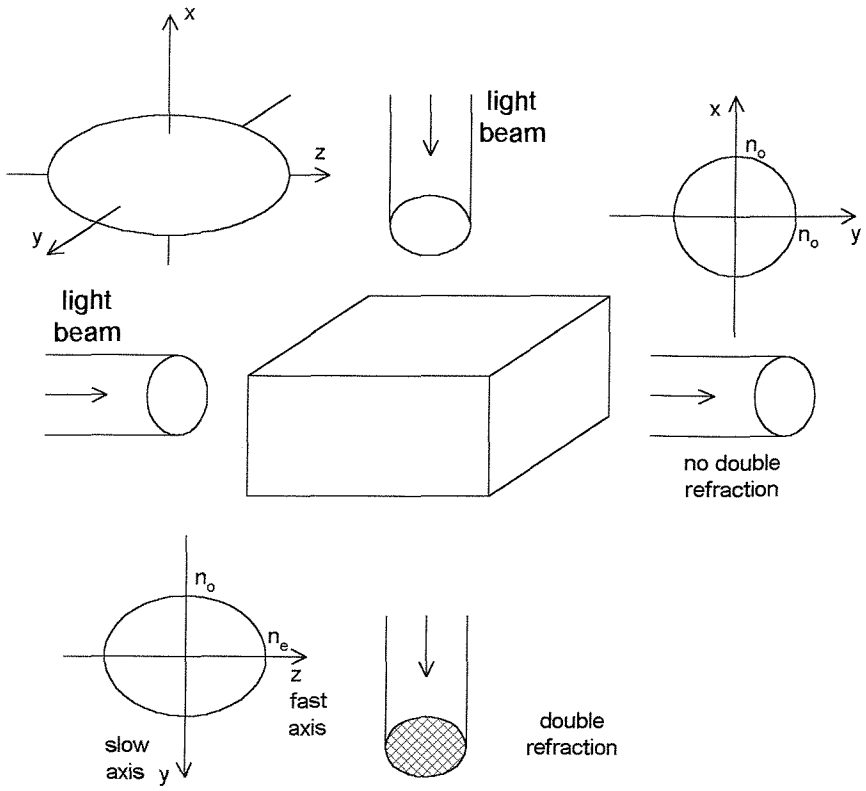

Figure 2.2 Double refraction of incident light through an anisotropic medium

2.3 The Phase Retardation Induced by a Birefringent Crystal

Consider linear polarised light incident along the principal axis z of a crystal that exhibits a birefringence with $n_y < n_x$ as shown in Figure 2.3. The linear polarised light can be divided into two identical electric field components one along the x-axis and the other along the y-axis. In this example, the x-axis is the slow axis and the y-axis is the fast axis. For linear polarised light propagating into the birefringent crystal the velocity of the electric field component of light along the axes is different and hence a phase retardation will be induced between the x and y electric field components of the incident light as shown in Figure 2.3.

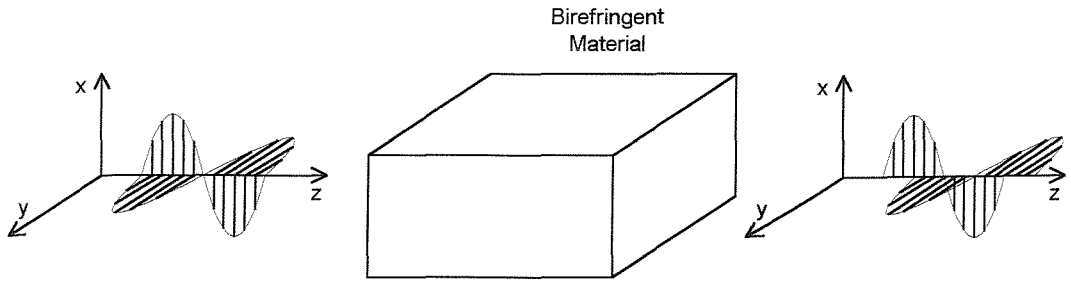

Figure 2.3 Phase retardation of a birefringent crystal

The phase retardation, Φ of the light transmitted through the birefringent crystal is proportional to the difference between the two principal refractive indices and the length of the crystal which is given by

$$\Phi = \frac{2\pi}{\lambda}(n_x - n_y)d \tag{2.14}$$

where λ is the wavelength of the incident light and d is the crystal thickness respectively.

2.4 The Pockels Effect

An isotropic crystal may alter into an anisotropic crystal due to the presence of an external force. The electro-optic effect where the crystal changes its isotropy due to an electric force is called Pockels or Kerr effect depending on whether the refractive indices change linearly or quadratically due to the applied electric field. The Faraday or magneto-optic effect is where the change of the refractive indices is caused by a magnetic field. Where a mechanical force causes a change of optical properties of the crystal it is the photoelastic effect. A Pockels crystal is the fundamental component of the optical surface charge measurement system. The surface charge deposited on the surface of the Pockels crystal creates an internal electric field that reorientates the crystal molecule dipoles and changes the crystal isotropy. Pockels effect is the interaction between two electric fields, one oscillating at the optical frequency and the other is a dc component.

For an incident electromagnetic wave at optical frequency the induced polarization is mainly contributed by the displacement of loosely outer valence electrons from their equilibrium positions. Consider the simple rectangular lattice structure [53] with a centre of symmetry i.e. isotropic crystal shown in Figure 2.4.

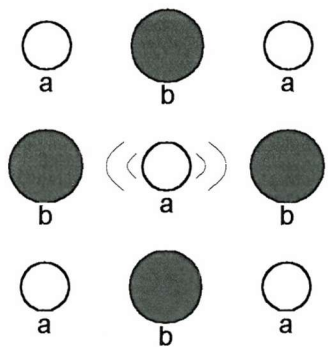

Figure 2.4 Rectangular lattice structure with a centre of symmetry

If the particle "a" is displaced towards particle "b" on the right side, the particle a will be pushed back to equilibrium by the repulsion of particle "b" on the right side and the attraction of particle "b" on the left side. The size and the direction of the restoring force on particle "a" can be described in terms of its potential energy as it moves in between particles "b" and therefore, the potential is symmetric about x at zero. The electron displacement, x in response to incident light can be modelled as a restoring force proportional to the displacement and a damping force proportional to the velocity, $\dot{x}$. Using the Lorentz model [53,54], the equation of motion of the electron in one-dimension is

$$\ddot{x} + g\dot{x} + \omega_o^2 x = -\frac{e}{m} E_x e^{j\omega t} \tag{2.15a}$$

and

$$\omega_o^2 = \frac{k_{ix}}{m} \tag{2.15b}$$

where g is damping factor, ω_o the natural frequency, m electron mass and k_{ix} restoring force constant to the x component. The solution for the displacement of a electron under the incident electromagnetic wave having angular frequency ω is

$$x = \frac{-e}{m} \frac{E_x}{\omega_o^2 - \omega^2 + j\omega g} \tag{2.16}$$

From $\varepsilon_r = 1 + \frac{P_x}{\varepsilon_o E_x}$ and $P_x = Nex$ gives

$$\varepsilon_r = 1 - \frac{Nex}{\varepsilon_o E_x} \tag{2.17}$$

where N is the number of charged particles. For an incident electromagnetic wave at the optical frequency the dielectric constant will be

$$\varepsilon_r = (n - jk)^2 = 1 + \frac{Ne^2}{m\varepsilon_o} \frac{1}{\omega_o^2 - \omega^2 + j\omega g} \tag{2.18}$$

where k is the complex component of the dielectric constant. Comparing real and imaginary parts gives

$$n^2 - k^2 - 1 = \frac{Ne^2}{m\varepsilon_o} \frac{\omega_o^2 - \omega^2}{\left(\omega_o^2 - \omega^2\right)^2 + \omega^2 g^2} \tag{2.19a}$$

$$2nk = \frac{Ne^2}{m\varepsilon_o} \frac{\omega g}{\left(\omega_o^2 - \omega^2\right)^2 + \omega^2 g^2} \tag{2.19b}$$

For wavelengths much longer than those in the absorption region, the imaginary part of the dielectric constant, ε_r becomes very small compared to the real part and the damping factor is negligible. Therefore, Equation 2.19a can be approximated as

$$n^2 - 1 = \frac{Ne^2}{m\varepsilon_o} \frac{1}{\left(\omega_o^2 - \omega^2\right)} \tag{2.20}$$

For an incident electromagnetic wave at optical frequency, the induced polarization is contributed by the outer valence electron of the lattice which is displaced by the

alternating applied field and a dipole moment exists. When the oscillation of electrons in the presence of the field are small, the induced polarization is proportional to the applied electric field as been shown in Equation 2.1. However, as the intensity of the applied electromagnetic wave increases the polarization is no longer proportional to the field. This behaviour is similar to the harmonic oscillation of a simple spring that becomes anharmonic as the amplitude of an external force becomes larger. Therefore, Equation 2.1 must be modified [55,56] in order to include anharmonic oscillation of electrons if higher electric fields are applied. Thus

$$P = \varepsilon_o\left(\chi_1 E + \chi_2 E^2 + \chi_3 E^3 + \cdots\right) \tag{2.21a}$$

$$P = P_1 + \left(P_2 + P_3 + \cdots\right) \tag{2.21b}$$

where χ_1 is the linear susceptibility and χ_2, χ_3 etc are the nonlinear susceptibility of the medium. P_1 is the linear polarization and P_2, P_3 etc are the nonlinear polarization. The linear polarisation is expressed as the susceptibility tensor where $P = \varepsilon_o \overline{\chi} E$.

Similarly, the nonlinear polarization P_2 and P_3 can be written as

$$P_i = \sum_{ij} \varepsilon_o \chi_{ijk} E_j E_k \tag{2.22a}$$

$$P_i = \sum_{ijk} \varepsilon_o \chi_{ijkl} E_j E_k E_l \tag{2.22b}$$

where χ_{ijk} and χ_{ijkl} are third and fourth rank tensors and E_i, E_j and E_k are the components of the applied electric field along the directions defined by i, j and k. The most important effects of the nonlinear polarization are the second order polarization and third order polarization. The second order polarization effects are second harmonic generation [57], optical rectification, parametric mixing, and the linear electro-optic (Pockels) effect. The third order polarization effects are third harmonic generation, two-photon absorption, the Raman effect and the quadratic electro-optic (Kerr) effect.

The polarization is dependent upon the higher order of the electric field and can be modelled using a restoring force that acts on the electron motion. Depending on the crystal symmetry, in a material having a centre of inversion, the non-linear susceptibility χ_2, χ_4, χ_6 etc are zero. Whereas for an material which lacks a centre of symmetry, the non-linear susceptibility χ_2, χ_3, χ_4 etc are non-zero Figure 2.5 shows the electron oscillation for an electromagnetic wave at the optical frequency incident into an anisotropic crystal which lacks of a centre of symmetry.

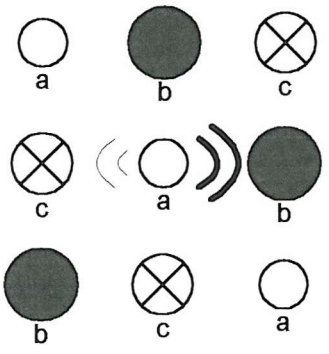

Figure 2.5 Rectangular lattice structure that lacks a centre of symmetry

The general Equation 2.15a of the oscillation of the electrons needs to be modified [55,56,58] by adding anharmonic terms to account for the effect of nonlinear polarization. Referring to the Equation 2.22a the nonlinear polarization will be affected by two applied electric fields therefore the equation describing the electron motion due to the effect of two applied fields having arbitrary frequency ω_1 and ω_2 is

$$\ddot{x}+ g \dot{x}+ \omega_o^2 x + q_2 x^2 = -\frac{e}{2m}\begin{pmatrix} E_1 \exp(i\omega_1 t) + E_1 \exp(-i\omega_1 t) + E_2 \exp(i\omega_2 t\ ) \\ + E_2 \exp(-i\omega_2 t\ ) \end{pmatrix} \quad (2.23)$$

For simplicity the higher order nonlinear terms x^3, x^4 etc are not included. If the nonlinear term q_2 is small then the solution of equation (2.23) can be approximated as

$$x = \frac{-e}{2m}\left(\frac{E_1 \exp(i\omega_1 t)}{\omega_o^2 - \omega_1^2 + i\omega_1 g} + \frac{E_2 \exp(i\omega_2 t)}{\omega_o^2 - \omega_2^2 + i\omega_2 g} + j(...) \right) \quad (2.24)$$

Analysis of Equation 2.24 reveals that it contains Fourier components whose frequencies are $\pm 2\omega_1$, $\pm 2\omega_2$, $\pm(\omega_1+\omega_2)$, $\pm(\omega_1-\omega_2)$ and zero rads^{-1}.

The equation (2.23) describes a general model for a second order nonlinear polarization and must be modified to include the dc electric field inherent with Pockels effect. This gives

$$\ddot{x}+g\dot{x}+\omega_o^2 x+q_2x^2=-\frac{e}{m}[E(\omega)+E_o] \tag{2.25}$$

where $E(\omega)$ represents the oscillatory electric field of the radiation at angular frequency ω and E_o is the magnitude of the applied dc field. In the absence of the anharmonic term the effect of the dc field is simply to produce a shift in the equilibrium position. Therefore, the oscillation of the electron can be modified in terms of the co-ordinate ξ, which is defined as

$$\xi = x+\frac{eE_o}{m\omega_o^2} \tag{2.26}$$

The equation of motion of the anharmonic oscillator can therefore be rewritten in terms of ξ to give

$$\ddot{\xi}+g\dot{\xi}+\left(\omega_o^2-\frac{2q_2eE_0}{\omega_o^2}\right)\xi+q_2\xi^2=-\frac{e}{m}E(\omega) \tag{2.27}$$

for simplicity the term proportional to $q_2E_o^2$ is negligible and can be ignored. The refractive index experienced by an incident field, $E(\omega)$ which is itself too small to produce nonlinear polarization and therefore the anharmonic term in equation (2.27) can also be disregarded. Thus the motion is as described by equation (2.15a) but with a resonant frequency which is displaced to ω_o', where

$$\omega_o^{/} = \left(\omega_o^2 - \frac{2q_2 eE_0}{m\omega_o^2} \right) \tag{2.28}$$

and the small change of the resonant frequency is

$$\Delta\left(\omega_o^2\right) = \omega_o^2 - \left(\omega_o^{/}\right)^2 = \frac{2q_2 eE_0}{m\omega_o^2} \tag{2.29}$$

The shift in resonant frequency caused by the applied field effects both n and k in Equation 2.19. In order to achieve adequate transmission through the medium, the wavelength of oscillation must be greater than that appropriate to the absorption edge and the condition $\omega_o^2 \rangle\rangle \omega g$ is applied. Hence, the refractive index only has real components and is given by Equation 2.20. From Equation 2.20, the small change of the refractive index due to the shift of the resonant frequency will be

$$\Delta n = \frac{\left(n^2 - 1\right)\Delta\left(\omega_o^2\right)}{2n\left(\omega_o^2 - \omega^2\right)}$$

$$\Rightarrow \Delta n = \frac{q_2 e\left(n^2 - 1\right)E_o}{m\omega_o^2 n\left(\omega_o^2 - \omega^2\right)} \tag{2.30}$$

the change of refractive index is therefore linearly proportional to the applied dc field.

2.5 The propagation of the electromagnetic wave within a Pockels crystal

The previous section has discussed the propagation of an electromagnetic wave through a medium that caused nonlinear polarization within the medium. Pockels effect is classified as a second order polarization due to two applied fields. When a dc electric field is present across the crystal, the ionic constituents move to new locations due to field strength. The charge on the ions and associated restoring force causes a change in the anisotropy. This effect exists only in crystals that do not possess inversion symmetry. These changes can be described in terms of the principal

refractive indices of the medium and the reorientation of the equation of index ellipsoid. Consider a crystal whose equation of the index ellipsoid is described using Cartesian coordinates [58,59] such that

$$\left(\frac{1}{n^2}\right)_1 x^2 + \left(\frac{1}{n^2}\right)_2 y^2 + \left(\frac{1}{n^2}\right)_3 z^2 + 2\left(\frac{1}{n^2}\right)_4 yz + 2\left(\frac{1}{n^2}\right)_5 xz + 2\left(\frac{1}{n^2}\right)_6 xy = 1 \qquad (2.31)$$

where the directions x, y and z are the principal dielectric axes. The cross terms yz, xz and xy exist in the equation for the ellipsoid in dielectric space (Figure 2.1) when it does not have symmetry about the x,y and z axes. For the linear electro-optic effect the change of refraction index $\Delta\left(\frac{1}{n^2}\right)$ is linearly proportional to the E_x, E_y and E_z components of the field. Since the change of the refractive index is dependent on the three components of the applied field then it can be described by the electro-optic tensor, $\overline{r}$ through the relationship,

$$\begin{pmatrix} \Delta(1/n^2)_1 \\ \Delta(1/n^2)_2 \\ \Delta(1/n^2)_3 \\ \Delta(1/n^2)_4 \\ \Delta(1/n^2)_5 \\ \Delta(1/n^2)_6 \end{pmatrix} = \begin{pmatrix} r_{11} & r_{12} & r_{13} \\ r_{21} & r_{22} & r_{23} \\ r_{31} & r_{32} & r_{33} \\ r_{41} & r_{42} & r_{43} \\ r_{51} & r_{52} & r_{53} \\ r_{61} & r_{62} & r_{63} \end{pmatrix} \begin{pmatrix} E_x \\ E_y \\ E_z \end{pmatrix} \qquad (2.32)$$

Typical magnitudes of the r_{ij} coefficients are of the order of 10^{-12} m/V. The non-zero elements r_{ij} depend on the symmetry of the crystal and are related to the symmetry of the piezoelectric tensor. The piezoelectric effect is an induced polarization within a medium produced by a stress existing across the medium. The piezoelectric effect can be thought as the reverse of Pockels effect in which the applied field causes a change of refractive index. Therefore, the matrix of electro-optic tensor, $\overline{r}$ is the transpose matrix of piezoelectric tensor. Hence the equation of the index ellipsoid must be modified to account for the change of the refractive index due to an electric field across the crystal, Thus Equation 2.31 can be rewritten as

$$\left[\frac{1}{n_1^2}+\Delta\left(\frac{1}{n^2}\right)_1\right]x^2+\left[\frac{1}{n_2^2}+\Delta\left(\frac{1}{n^2}\right)_2\right]y^2+\left[\frac{1}{n_3^2}+\Delta\left(\frac{1}{n^2}\right)_3\right]z^2$$
$$+2\left[\frac{1}{n_4^2}+\Delta\left(\frac{1}{n^2}\right)_4\right]yz+2\left[\frac{1}{n_5^2}+\Delta\left(\frac{1}{n^2}\right)_5\right]xz+2\left[\frac{1}{n_6^2}+\Delta\left(\frac{1}{n^2}\right)_6\right]xy=1 \quad (2.33)$$

The small change of the refractive indices in the presence of applied field across the crystal (Equation 2.32) results in new principal axes in the dielectric space. The upper three rows of electro-optic tensor, $\overline{\overline{r}}$, change the magnitude of the refractive index of the principal axes as the field is applied. The lower three rows the applied electric field has generated cross terms so x, y and z are no longer appropriate principal axes and the new principal axes are rotated. Consequently the principal axes have been changed in shape and rotated in space by the electric stress as shown in Figure 2.6.

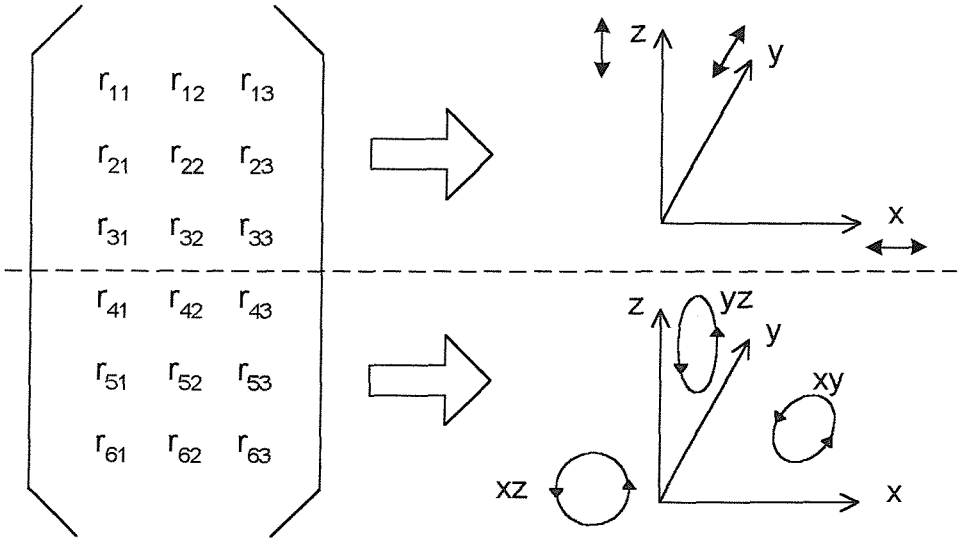

Figure 2.6 The effect of the electro-optic tensor

2.6 Electro-optic phase modulation

2.6.1 Transverse modulation

An applied electric field affects an electro-optic crystal by changing its indices of refraction and affecting its original principal axes. Consider the case of a Lithium Niobate crystal ($LiNbO_3$) where a dc field is applied transversely between electrodes

placed on its side faces, Figure 2.7. The field is parallel to the y-axis and the electromagnetic input wave propagates in the z direction.

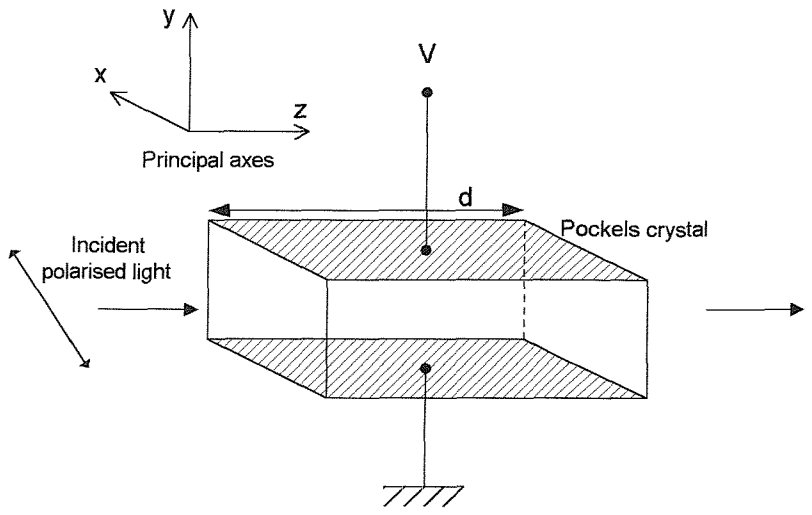

Figure 2.7 A $LiNbO_3$ crystal as a transverse electro-optic modulator

The crystal of $LiNbO_3$ is a crystal with symmetry 3m and its electro-optic tensor, $\overline{\overline{r}}$ has the following elements

$$\overline{\overline{r}} = \begin{pmatrix} 0 & -r_{22} & r_{13} \\ 0 & r_{22} & r_{13} \\ 0 & 0 & r_{33} \\ 0 & r_{51} & 0 \\ r_{51} & 0 & 0 \\ -r_{22} & 0 & 0 \end{pmatrix} \tag{2.34}$$

Combining Equation 2.32, 2.33 and 2.34 gives the equation of the index ellipsoid due to an electric field across the crystal which is

$$\left[\frac{1}{n_o^2} - r_{22}E_y + r_{13}E_z\right]x^2 + \left[\frac{1}{n_o^2} + r_{22}E_y + r_{13}E_z\right]y^2 + \left[\frac{1}{n_e^2} + r_{33}E_z\right]z^2 + 2r_{51}E_y yz + 2r_{51}E_x xz + 2(-r_{51})E_x xy = 1 \tag{2.35}$$

Since the applied field is in the y direction there are no field components in the x or z directions, therefore, the equation simplifies to

$$\left[\frac{1}{n_o^2}-r_{22}E_y\right]x^2+\left[\frac{1}{n_o^2}+r_{22}E_y\right]y^2+\frac{1}{n_e^2}z^2+2r_{51}E_y yz=1 \tag{2.36}$$

The cross term, yz is non-zero in the equation of index ellipsoid and rotates the principal axes y and z in the electro-optics equation of the index ellipsoid by the azimuth angle θ. It is necessary to determine the azimuth angle, θ which the principal axes y' and z' are related to the crystal axes

$$x = x' \tag{2.37a}$$

$$y = y'\cos\theta - z'\sin\theta \tag{2.37b}$$

$$z = y'\sin\theta + z'\cos\theta \tag{2.37c}$$

substituting for x, y and z gives

$$\begin{aligned}&\left[\frac{1}{n_o^2}-r_{22}E_y\right]x'^2+\left[\cos^2\theta\left(\frac{1}{n_o^2}+r_{22}E_y\right)+\frac{\sin^2\theta}{n_e^2}+2r_{51}E_y\sin\theta\cos\theta\right]y'^2\\&+\left[\sin^2\theta\left(\frac{1}{n_o^2}+r_{22}E_y\right)+\frac{\cos^2\theta}{n_e^2}-2r_{51}E_y\sin\theta\cos\theta\right]z'^2\\&+2\left[\sin\theta\cos\theta\left(\frac{1}{n_e^2}-\frac{1}{n_o^2}-r_{22}E_y\right)+r_{51}E_y\left(\cos^2\theta-\sin^2\theta\right)\right]y'z'=1\end{aligned} \tag{2.38}$$

In order to remove the cross term $y'z'$ the following condition must be satisfied

$$\left[\sin\theta\cos\theta\left(\frac{1}{n_e^2}-\frac{1}{n_o^2}-r_{22}E_y\right)+r_{51}E_y\left(\cos^2\theta-\sin^2\theta\right)\right]=0 \tag{2.39}$$

The azimuth angle θ is usually small since $r_{22}E_y$ is small compared to $\frac{1}{n_e^2}-\frac{1}{n_o^2}$.

Therefore,

$$\lim_{\theta\to 0} \quad \sin\theta=\theta,\ \cos\theta=1,\ \sin^2\theta=0 \tag{2.40}$$

Consequently,

$$\theta = \frac{-r_{51}E_y}{\frac{1}{n_e^2} - \frac{1}{n_o^2} - r_{22}E_y} \tag{2.41}$$

for small θ the cross term vanishes and the equation of index ellipsoid is

$$\left[\frac{1}{n_o^2} - r_{22}E_y\right]x'^2 + \left[\left(\frac{1}{n_o^2} + r_{22}E_y\right) + +2r_{51}E_y\theta\right]y'^2 + \left[\frac{1}{n_e^2} - 2r_{51}E_y\theta\right]z'^2 = 1 \tag{2.42}$$

terms containing θ can be assumed to be zero and the equation simplifies to

$$\left[\frac{1}{n_o^2} - r_{22}E_y\right]x'^2 + \left[\frac{1}{n_o^2} + r_{22}E_y\right]y'^2 + \left[\frac{1}{n_e^2}\right]z'^2 = 1 \tag{2.43}$$

Therefore, the new principal refractive indices are

$$\frac{1}{n_{x'}^2} = \frac{1}{n_o^2} - r_{22}E_y \tag{2.44a}$$

$$\frac{1}{n_{y'}^2} = \frac{1}{n_o^2} + r_{22}E_y \tag{2.44b}$$

$$\frac{1}{n_{z'}^2} = \frac{1}{n_e^2} \tag{2.44c}$$

the small change of refractive index, $\Delta n_{x'}$ due to the electric field in the new principal axis x' can be approximated as from

$$\frac{1}{n_{x'}^2} - \frac{1}{n_o^2} = -r_{22}E_y$$

$$\Rightarrow d\left(\frac{1}{n^2}\right) = -r_{22}E_y$$

$$\Rightarrow -2\frac{dn}{n^3} = -r_{22}E_y$$

$$\Rightarrow \Delta n_{x'} = \frac{n_o^3 r_{22} E_y}{2} \tag{2.45}$$

the change of the refractive index in axis x' due to the electric field is

$$n_{x'} = n_o + \Delta n_{x'}$$

$$n_{x'} = n_o + \frac{n_o^3 r_{22} E_y}{2} \tag{2.46}$$

Similarly the change of refractive index in the axis y' is

$$n_{y'} = n_o - \frac{n_o^3 r_{22} E_y}{2} \tag{2.47}$$

The index of refractive of principal axis z' remains unchanged due to an applied field in the y direction i.e.

$$n_{z'} = n_e \tag{2.48}$$

Therefore, the light propagating in the z direction through the LiNbO3 crystal can be resolved into two equal components in the x' and y' directions that have a phase difference or phase retardation over a travel distance, d through the crystal. The phase retardation will be

$$\Delta\Phi = \frac{2\pi}{\lambda}\left(n_{x'} - n_{y'}\right)d$$

$$\Delta\Phi = \frac{2\pi}{\lambda} n_o^3 r_{22} E_y d \tag{2.49}$$

2.6.2 Longitudinal Mode

It is possible to utilise Pockels effect when the applied field and the electromagnetic wave are both arranged along the same direction (Figure 2.8).

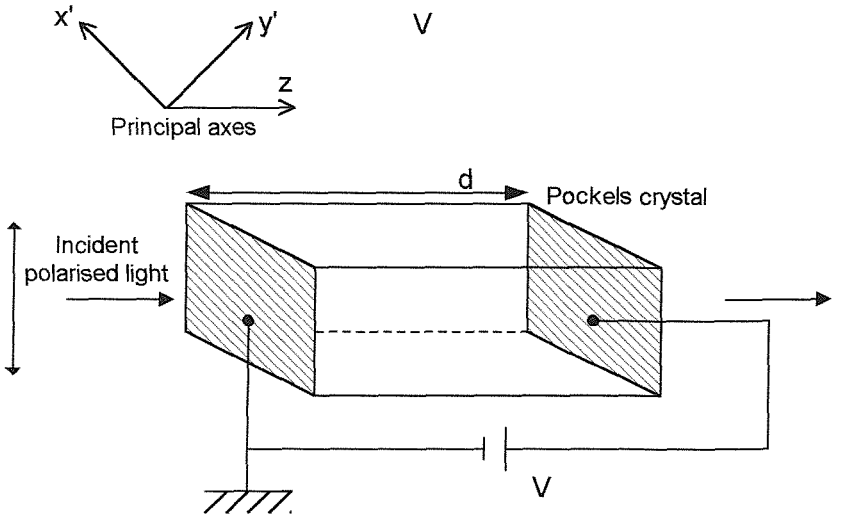

Figure 2.8 A BSO crystal as a longitudinal electro-optic modulator

This orientation arrangement is important in the development of surface charge measurements because by its nature the direction of electric field due to surface charge will be in the same direction as the light propagation. A Bismuth Silicon Oxide (BSO) crystal with crystallographic z-axis is used for this arrangement and it is isotropic without an applied field. BSO has symmetry 23 and its electro-optic tensor is

$$\overline{\overline{r}} = \begin{pmatrix} 0 & 0 & 0 \\ 0 & 0 & 0 \\ 0 & 0 & 0 \\ r_{41} & 0 & 0 \\ 0 & r_{41} & 0 \\ 0 & 0 & r_{41} \end{pmatrix} \tag{2.50}$$

The equation of the index ellipsoid of BSO under an electric field is

$$\left[\frac{1}{n_o^2}\right]x^2 + \left[\frac{1}{n_o^2}\right]y^2 + \left[\frac{1}{n_e^2}\right]z^2 + 2r_{41}E_x yz + 2r_{41}E_y xz + 2r_{41}E_z xy = 1 \tag{2.51}$$

For a field applied in the z direction, this equation reduces to

$$\left[\frac{1}{n_o^2}\right]x^2+\left[\frac{1}{n_o^2}\right]y^2+\left[\frac{1}{n_e^2}\right]z^2+2r_{41}E_z xy=1 \tag{2.52}$$

The equation of index ellipsoid of BSO is simpler than the Lithium Niobate ($LiNbO_3$) because the refractive indices of axes x and y are identical. The cross term in Equation 2.52 causes the principal axes x and y to rotate by an angle θ. Therefore, in order to remove the cross term component, the new axes x' and y' must be rotated by an angle $\theta=45°$. The z-axis remains unaltered for an applied field in z direction. The relationship between the x, y and x', y' axes is

$$x=x'\cos 45^o-y'\sin 45^o \tag{2.53a}$$

$$y=x'\sin 45^o+y'\cos 45^o \tag{2.53b}$$

Substituting Equation 2.53 into 2.52 gives

$$\left[\frac{1}{n_o^2}+r_{41}E_z\right]x'^2+\left[\frac{1}{n_o^2}-r_{41}E_z\right]y'^2+\left[\frac{1}{n_e^2}\right]z^2=1 \tag{2.54}$$

From the equation 2.54 the applied electric field causes the refractive indices of the new principal axes x' and y' to alter as

$$\frac{1}{n_{x'}^2}=\frac{1}{n_o^2}+r_{41}E_z \tag{2.55a}$$

$$\frac{1}{n_{y'}^2}=\frac{1}{n_o^2}-r_{41}E_z \tag{2.55b}$$

As $r_{63}E_z<<1$, the change in refractive index due to the applied field can be approximated by

$$n_{x'}=n_o-\frac{n_o^3 r_{41}E_z}{2} \tag{2.56a}$$

$$n_{y'} = n_o + \frac{n_o^3 r_{41} E_z}{2} \tag{2.56b}$$

Where the fast axis is x' and the slow axis is y' due to Pockels effect. The refractive indices of the principal axes x', y' and z' are no longer the same. The BSO crystal is transformed from the isotropic medium into the biaxial medium by the applied field. For polarised light travelling in the z direction with its polarisation set to an angle of 45° to the new principal axis x' and y', the linear polarised light can be resolved into two orthogonal equal components in the two principal axes x' and y'. The light component in the fast axis will travel at a faster speed than that in the slow axis under an applied field, E. The phase retardation of the light is given by

$$\Delta\Phi = \frac{2\pi}{\lambda} n_o^3 r_{41} E_z d \tag{2.57a}$$

$$\Delta\Phi = \frac{2\pi}{\lambda} n_o^3 r_{41} V_x \tag{2.57b}$$

where V_x is the applied voltage across the crystal. The phase retardation is independent of travel distance, d of the light. The crystal has become a wave plate with a phase retardation that is proportional to the applied field.

2.7 The Polarisation of Light

Polarised light is generally regarded as a linear polarisation. However, the state of polarised light can be linear, elliptical or circular [60]. The light is said to be linearly polarised when the orientation of the electric field is constant. If the electric field oscillates its magnitude and sign vary in time. The electric field or optical disturbance therefore resides in the plane of vibration. The combination of two orthogonal linearly polarised rays having equal frequency and magnitude with a phase difference $\pi/2$ will give circularly polarised light. This can be thought of as an electron oscillating circularly in the plane and the radiating electromagnetic wave propagates in the space. The circular polarisation light can be either right circular or left circular depending upon the oscillating direction of the electron. Elliptical polarisation is the case of light polarisation that is between linear and circular polarisation where the phase difference is less than $\pi/2$. Figure 2.9 shows different polarisation states as the phase retardation increases from 0 to 2π.

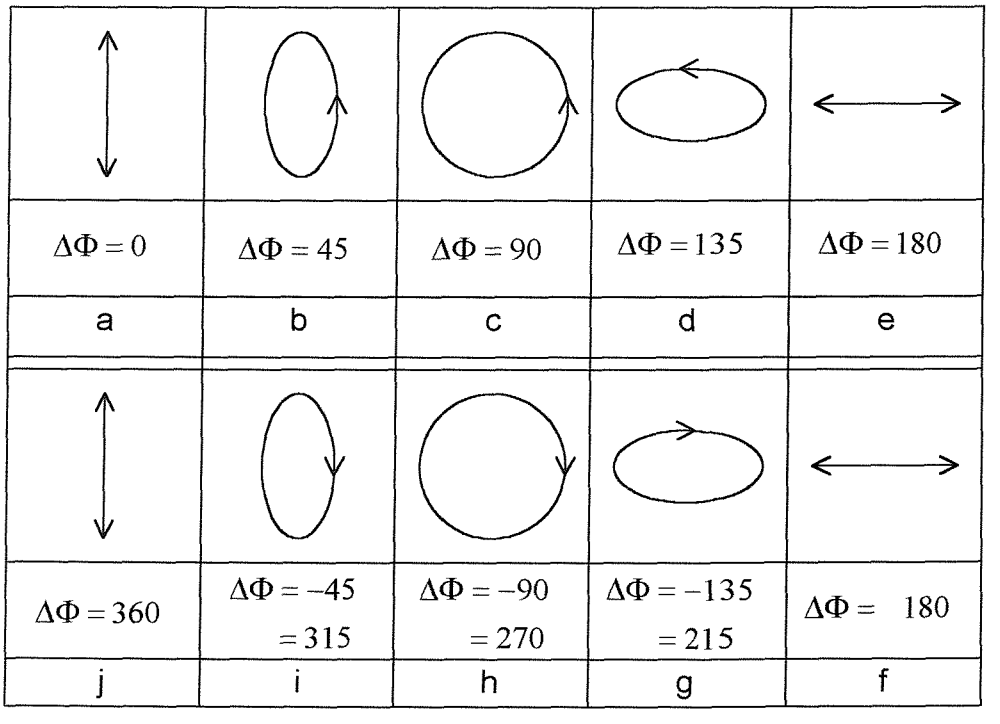

Figure 2.9 The states of polarisation of light as the phase difference between two orthogonal electric field components increases from 0 to 2π

As stated earlier in order to measure surface charge using BSO the linear polarised input wave is set at an angle of 45° to the principal axes x' and y'. Pockels effect causes the crystal to become a wave plate which retards the phase of light proportional to the applied electric field. As the applied voltage across the crystal increases from zero the output light wave makes a transition from linear polarisation to elliptical polarisation with the major axis aligned along the original polarisation direction (Figure 2.9b). Further increasing the applied voltage causes the crystal to become a quarter wave plate and the light changes from elliptical polarisation to circular polarisation, Figure 2.9c. As the applied field is increased further, the light changes state from circular polarisation to elliptical polarisation with the minor axis aligned along the original polarisation direction, Figure 2.9d. Increasing the electric field intensity causes the polarisation to become linear again but 90° rotated from its original polarisation direction (Figure 2.9e). At this point the crystal can be regarded as a half wave plate which transforms the linear polarised input wave into a linear polarised output wave where the polarisation direction has been rotated 90° from its original direction. If the applied field is further increased the phase retardation will change from π to 2π and the light polarisation return to its original state as shown in Figure 2.9f-2.9j.

The required applied voltage to make the BSO crystal behave as a half wave plate can be calculated. BSO has $r_{41}=5X10^{-12}$m/V, $n_o = 2.54$ and if the polarised light has an operating wavelength 632.8 nm, the required voltage, V_π to produce a phase difference of π rad is

$$V_\pi = \frac{\lambda}{2r_{41}n_0^3}$$
$$= 3861V \qquad (2.58)$$

2.8 Jones Matrix

The state of polarisation of light may be represented by a mathematical model, either using Stokes parameters or the Jones Matrix [61,62]. It is more convenient to express different states and orientation of the light polarisation by using the Jones Matrix which has fewer components and was invented in 1941 by the American physicist R. Clark Jones. The technique has the advantages of being applicable to coherent beams and at the same time being extremely concise. It is the most natural way to represent the beam in terms of the electric vector itself. In many applications, various devices can serve as optical elements that transmit light but modify the state of polarisation. Hence, by using the Jones Matrix the transformation of polarised light into another state by a optical device or the transmittance of light through a polariser can be easily determined. It is good practice to use the Jones matrix when analysing optical systems that consist of several wave plates or polarisers [63,64,65,66,67]. Consider Figure 2.10 [68], linear polarised light passing through a crystal with an azimuth angle, θ with respect to the fast axis of the crystal.

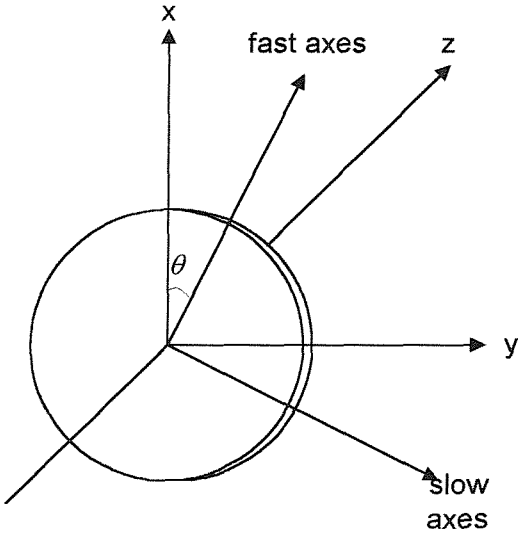

Figure 2.10 Coordinate axes and the azimuth angle

If the electric field components are written in column form, the Jones matrix is

$$E = \begin{pmatrix} A_x \\ A_y \end{pmatrix} \tag{2.59}$$

Where A_x and A_y are two complex numbers that represent the components of the electric field vector along the x and y directions. The x and y axes are the fixed chosen axes and in general are different from the principal axes of the crystal or the transmission axes of the polariser. To determine how light propagates in the crystal plate it is necessary to find the amplitudes of the normal modes. In normal mode of incidence and the light is totally transmitted, the amplitude of normal modes are obtained by a simple geometric projection which with reference to Figure 2.10 gives

$$C_e = \mathbf{e}\bullet\mathbf{x}A_x + \mathbf{e}\bullet\mathbf{y}A_y \qquad C_o = \mathbf{o}\bullet\mathbf{x}A_x + \mathbf{o}\bullet\mathbf{y}A_y \tag{2.60}$$

where **e** and **o** are the unit vectors along the direction of the normal modes usually the principal axes of the crystal or wave plate, **x** and **y** are the unit vectors along the chosen direction in x and y. C_e and C_o are the amplitudes of the normal modes along the principal axes e and o. Using the definition of the azimuth angles, θ in Figure 2.12, these two unit vectors are given as

$$\mathbf{e} = \mathbf{x}\cos\theta + \mathbf{y}\sin\theta, \qquad \mathbf{o} = -\mathbf{x}\sin\theta + \mathbf{y}\cos\theta \tag{2.61}$$

Using a matrix representation, Equation 2.60 can be rewritten as

$$\begin{pmatrix} C_e \\ C_o \end{pmatrix} = \begin{pmatrix} \mathbf{e}\bullet\mathbf{x} & \mathbf{e}\bullet\mathbf{y} \\ \mathbf{o}\bullet\mathbf{x} & \mathbf{o}\bullet\mathbf{y} \end{pmatrix} \begin{pmatrix} A_x \\ A_y \end{pmatrix} \tag{2.62}$$

From Equation 2.61 the Jones Matrix in Equation 2.62 under the coordinate transformation can be written as

$$\begin{pmatrix} C_e \\ C_o \end{pmatrix} = \begin{pmatrix} \cos\theta & \sin\theta \\ -\sin\theta & \cos\theta \end{pmatrix} \begin{pmatrix} A_x \\ A_y \end{pmatrix} = R(\theta) \begin{pmatrix} A_x \\ A_y \end{pmatrix} \tag{2.63}$$

where $R(\theta)$ represents the rotation matrix.

The component C_e is the extraordinary component of the incident electric field vector, whereas C_o is the ordinary component where both of these components have been

transformed from the original Jones Matrix in Equation 2.59 according to the azimuth angle transformation. For a wave plate having birefringence these two components C_e and C_o are the normal modes of the crystal and will propagate light with their own phase velocities. Because of the difference in phase velocity, one component travels faster than the other and a phase retardation is induced into the system. This retardation changes the polarisation state of the emerging beam.

If k_e and k_o are the wave numbers of the extraordinary and ordinary waves respectively, then the electric field of the emerging beam can be written as

$$\begin{pmatrix} C_e^{/} \\ C_o^{/} \end{pmatrix} = \begin{pmatrix} \exp(-jk_e d) & 0 \\ 0 & \exp(-jk_o d) \end{pmatrix} \begin{pmatrix} C_e \\ C_o \end{pmatrix} \tag{2.64}$$

where d is the thickness of the crystal plate.

Phase retardation is given by the difference of the exponents in equation 2.64 and is equal to

$$\Phi = (k_e - k_o)d = \frac{2\pi}{\lambda}(n_e - n_o)d \tag{2.65}$$

The phase retardation Φ is a measure of the relative change in phase, not the absolute change. The thickness, d of the crystal is much greater than λ. Consequently, the absolute change in phase caused by the plate may be substantially greater than the phase retardation. Let Γ be the mean absolute phase change

$$\Gamma = \frac{1}{2}(n_e + n_o)\frac{2\pi d}{\lambda} \tag{2.66}$$

Then Equation 2.64 can then be written in term of Φ and Γ as

$$\begin{pmatrix} C_e^{/} \\ C_o^{/} \end{pmatrix} = \exp(-j\Gamma) \begin{pmatrix} \exp(-j\Phi/2) & 0 \\ 0 & \exp(j\Phi/2) \end{pmatrix} \begin{pmatrix} C_e \\ C_o \end{pmatrix} \tag{2.67}$$

The reverse transformation of the Jones Matrix will require the conversion of the crystal eo coordinate system into the emerging xy coordinate system.

$$\begin{pmatrix} A_x' \\ A_y' \end{pmatrix} = \begin{pmatrix} \cos\theta & -\sin\theta \\ \sin\theta & \cos\theta \end{pmatrix} \begin{pmatrix} C_e' \\ C_o' \end{pmatrix} \tag{2.68}$$

By combining Equations 2.63, 2.67 and 2.68, the transformation due to the retardation plate is

$$\begin{pmatrix} A_x' \\ A_y' \end{pmatrix} = R(-\theta) W_o R(\theta) \begin{pmatrix} A_x \\ A_y \end{pmatrix} \tag{2.69}$$

where R(θ) is the rotation matrix and W_o is the Jones matrix for the retardation plate. These are given, respectively, by

$$R(\theta) = \begin{pmatrix} \cos\theta & \sin\theta \\ -\sin\theta & \cos\theta \end{pmatrix} \tag{2.70}$$

and

$$W_o = \exp(-j\Gamma) \begin{pmatrix} \exp(-j\Phi/2) & 0 \\ 0 & \exp(j\Phi/2) \end{pmatrix} \tag{2.71}$$

The phase factor exp(-jΓ) can be neglected provided interference effects are not important or observable. A retardation plate is characterised by its phase retardation Φ and its azimuth angle θ and is represented by the product of the three matrixes.

$$T(\Phi,\theta) = R(-\theta) W_o R(\theta)$$

$$= \begin{pmatrix} \cos\theta & -\sin\theta \\ \sin\theta & \cos\theta \end{pmatrix} \begin{pmatrix} \exp(-j\Phi/2) & 0 \\ 0 & \exp(j\Phi/2) \end{pmatrix} \begin{pmatrix} \cos\theta & \sin\theta \\ -\sin\theta & \cos\theta \end{pmatrix}$$

$$= \begin{bmatrix} \cos(\Phi/2) + j\cos 2\theta \sin(\Phi/2) & j\sin 2\theta \sin(\Phi/2) \\ j\sin 2\theta \sin(\Phi/2) & \cos(\Phi/2) - j\cos 2\theta \sin(\Phi/2) \end{bmatrix} \quad (2.72)$$

In the case where incident polarised light makes an angle θ with the fast axes of a birefringent crystal as shown in Fig. 2.10. The normalised Jones vector for the vertical linear polarised light having an electric field is

$$E_{linear} = \begin{bmatrix} 1 \\ 0 \end{bmatrix} \quad (2.73)$$

From Equation 2.72, the electro-optic crystal can be regarded as a phase retarder that alters the phase of the polarised light and will therefore have the normalised Jones vector

$$T(\Phi,\theta) = \begin{bmatrix} \cos(\Phi/2) + j\cos 2\theta \sin(\Phi/2) & j\sin 2\theta \sin(\Phi/2) \\ j\sin 2\theta \sin(\Phi/2) & \cos(\Phi/2) - j\cos 2\theta \sin(\Phi/2) \end{bmatrix} \quad (2.74)$$

The Jones vector for the electric field of light passing through the electro-optic crystal will be the product of Equation 2.72 and the Jones vector for the original electric field described in Equation 2.73. For the example of the linear polarised light incident to an electro-optic crystal with phase retardation, Φ and azimuth angle, θ then

$$E_{final} = T(\Phi,\theta).E_{linear}$$

$$E_{final} = \begin{bmatrix} \cos(\Phi/2) + j\cos 2\theta \sin(\Phi/2) & j\sin 2\theta \sin(\Phi/2) \\ j\sin 2\theta \sin(\Phi/2) & \cos(\Phi/2) - j\cos 2\theta \sin(\Phi/2) \end{bmatrix} \begin{bmatrix} 1 \\ 0 \end{bmatrix}$$

$$E_{final} = \begin{bmatrix} \cos(\Phi/2) + j\cos 2\theta \sin(\Phi/2) \\ j\sin 2\theta \sin(\Phi/2) \end{bmatrix} \quad (2.75)$$

If this light derived by the Jones vector in Equation 2.75 passes through an analyser which is set to an angle parallel to the original polarised light. The light transmittance will be [69]

$$I_0 = E_{final1} E^*_{final1} = \cos^2(\Phi/2) - \cos^2 2\theta \sin^2(\Phi/2) \quad (2.76)$$

If the analyser is set to be perpendicular to the original light then the light transmittance will be

$$I_{90} = E_{final2} E^*_{final2} = \sin^2 2\theta \sin^2(\Phi/2) \quad (2.77)$$

This approach simplifies the calculation of light intensity and it is easy to determine different polarisation states due to the presence of other optical devices. For example, if an extra quarter or half waveplate is inserted into the experiment. An extra matrix for the phase retarder can be included in the equation. Results can be easily obtained using a computer program.

According to Equations 2.76 and 2.77 to achieve maximum light transmittance the azimuth angle, θ must be set to be 45° i.e. the fast and slow axes are at 45° with respect to the polarisation of the incident light and the analyser must be set perpendicular with respect to the polarisation of the incident light then Equation 2.77 can be further reduced to

$$I_{90} = \sin^2(\Phi/2) \quad (2.78)$$

2.9 Fundamental Experiment

Theoretically an applied dc voltage of 3861V placed across a BSO crystal arranged in longitudinal mode will induce a phase retardation of π for a light source with 632.8nm wavelength. This has been verified by experiment as shown in Figure 2.11 using a z-cut BSO. The BSO crystal has a cross-sectional area of 25X25mm^2 and thickness of 1mm. The laser source used has a power output of 5mW with 1mm beam diameter. This laser source provided linearly polarised light with a wavelength of 632.8nm. The orientation of the linear polarised light was set to 45° with respect to the induced principal axes x' and y' of the crystal. The BSO sample was coated with thin gold film (~30nm) on both sides to act as electrodes. The thickness of the gold film was

minimised to allow light to be transmitted through the BSO. One side of the electrode was connected to earth while the other side was connected to a HV dc supply. The HV dc supply generated an electric stress across the crystal and the dc voltage was increased in 200V steps.

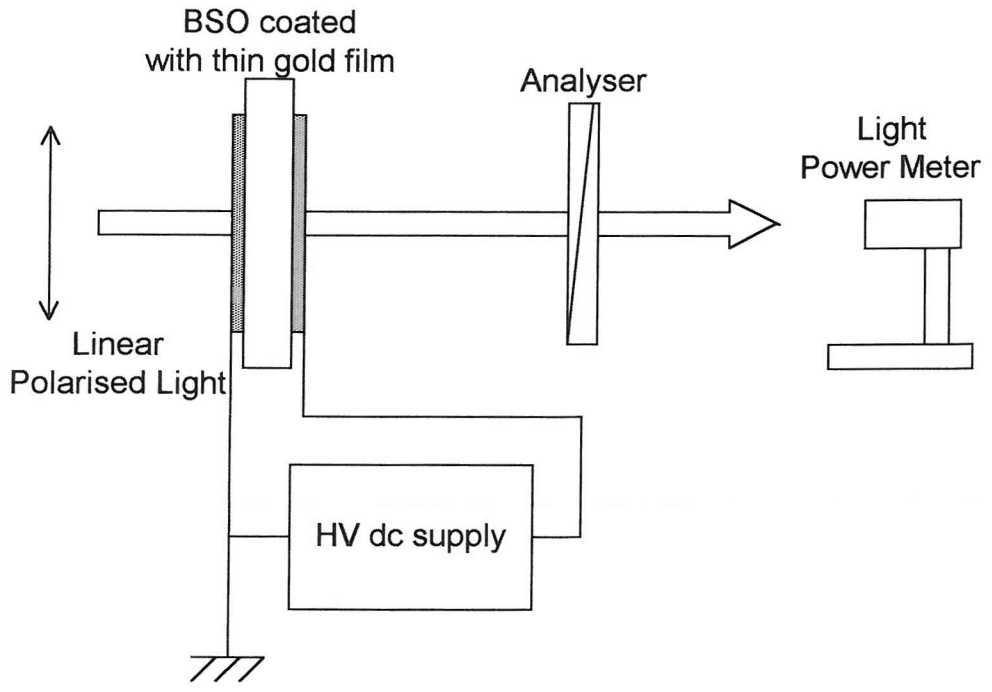

Figure 2.11 Simple experiment arrangement to determine V_π

An analyser was used to verify the change of light intensity due to Pockels effect. The analyser transmission axis was set to a angle of 90° to the linear polarised light and according to Equation 2.78 the transmittance of the light can therefore be expressed as

$$I = I_{\max} \sin^2\left(\frac{\Delta\Phi}{2}\right) \tag{2.79}$$

The power meter measured the transmittance of light travelling through the crystal which was altered in phase by Pockels effect and the change of the light intensity was recorded as the applied field increased. A typical result obtained for this experiment is shown in Figure 2.12. The theoretically obtained value of 3861V required to give a phase retardation of π means that ideally 7723V is required to change the light polarisation from 0 to 2π. Experimental results show that to obtain a change of phase

retardation of 2π the required applied voltage is approximately 7.7kV. This is in good agreement with the theoretical estimation and allows the useful range of the crystal to be determined. The useful range for the measurement of the electric field across the crystal is limited to the optical range of π after which the transmittance intensity waveform repeats for increasing applied voltage.

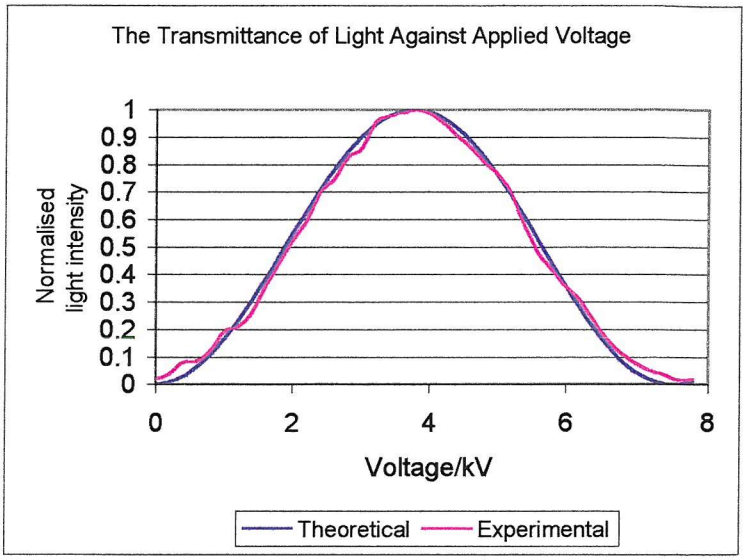

Figure 2.12 Transmittance of light intensity against phase retardation

Chapter 3

Using a Pockels Cell to Measure Surface Charge : Design Considerations

3.1 Introduction

Pockels crystals have been widely used for electric field measurement. Previous published research [26,27,28,29,30,31,32,33] has mainly been concerned with the measurement of an electric field that is present between two electrodes and therefore, the electric field profile is restricted to a single dimension. The measurement of surface charge density uses the same principle as electric field measurement because the surface charge on the Pockels crystal induces the electric field across it. The difference between surface charge measurement and traditional electric field measurement is that the measurement of surface charge density produces a two-dimensional profile. Moreover, as the Pockels crystal is arranged in the transverse configuration for the measurement of electric field, light propagating through the crystal does not interfere with the electrode. Usually, the incident light has a small diameter and the detection of light can be realised using a photo diode. However, to obtain a two-dimensional surface charge measurement it is necessary to use a large diameter beam (>10mm say). Therefore, optical surface charge measurement systems

[43,44] are more complex than optical electric field measurement systems. Along with the Pockels crystal the optical system requires the use of other optical and electronic components to detect the change of light intensity due to Pockels effect. A schematic diagram for the surface charge measurement system is shown in the Figure 3.1.

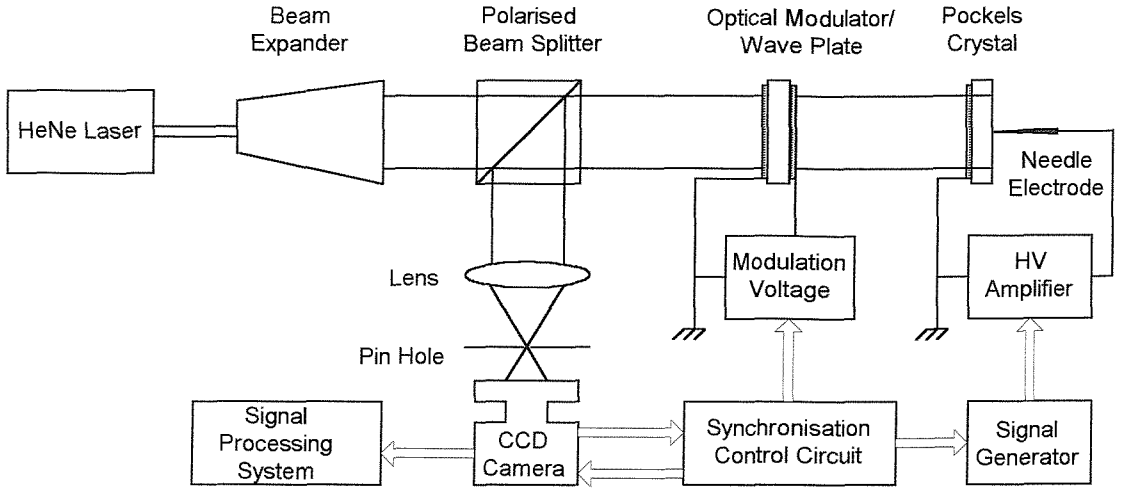

Figure 3.1 Schematic diagram of the optical system for surface charge measurement

The 17mW HeNe linear polarised laser source has wavelength 632.8nm with a beam diameter 1mm in diameter and is expanded by the beam expander to 30mm. The Polarised Beam Splitter serves as the polariser and analyser for the laser light transmitted through it. The wave plate or the optical modulator used in the system is required to distinguish charge polarity and improve the signal to noise ratio. A needle electrode is used to deposit surface discharge and it is connected to a HV supply. The plano-convex lens focuses the reflected beam into a small diameter and the light is monitored using a CCD camera array. The CCD camera records light intensity change due to surface charge existing on the Pockels crystal. The Synchronisation Control Circuit controls the timing of the measurement process i.e. camera starting frame, high voltage signal, etc. The image captured by the CCD camera during the discharge activities can be transferred to the computer for further analysis. Software written using the MATLAB programming environment has been developed to analyse the transferred data.

3.2 Pockels Crystal as the Surface Charge Transducer

The optical measurement of an electric field can be classified into two groups depending on the direction of the applied field and the incident light, these are the transverse and longitudinal modes of modulation. The crystal symmetry group also is important in determining the suitable direction of the applied field. An analysis of the relation of the applied field, incident light and the crystal symmetry has been made by Hidaka [34] which is shown in Table 3.1 and Figure 3.2.

Crystal Group Symmetry		3m	$\bar{4}$2m	32	23	$\bar{4}$3m
Material		$LiNbO_3$ $LiTaO_3$	ADP KDP	Quartz	$Bi_{12}SiO_{20}$ $Bi_{12}GeO_{20}$	ZnS, $Bi_4Ge_3O_{20}$
Transverse Mode of Modulation	Crystal Axis	(a)	(b)	(a)	(b)	(b)
	Output for $\phi = 0^o$	$r_{22}E_\alpha$	------	$r_{11}E_\beta$	$r_{41}E_\beta$	$r_{41}E_\beta$
	Output for $\phi = 45^o$	$r_{22}E_\beta$	$\sim(r_{63}E_\alpha)/2$	$r_{11}E_\alpha$	$(r_{41}E_\alpha)/2$	$(r_{41}E_\alpha)/2$
Longitudinal Mode of Modulation	Crystal Axis	------	(a)	(c)	(a)	(a)
	Output for $\phi = 0^o$	------	$r_{63}E_\gamma$	------	$r_{41}E_\gamma$	$r_{41}E_\gamma$
	Output for $\phi = 45^o$	------	------	$\sim r_{11}E_\gamma$	------	------

Table 3.1 Electric field component measured and crystal symmetry

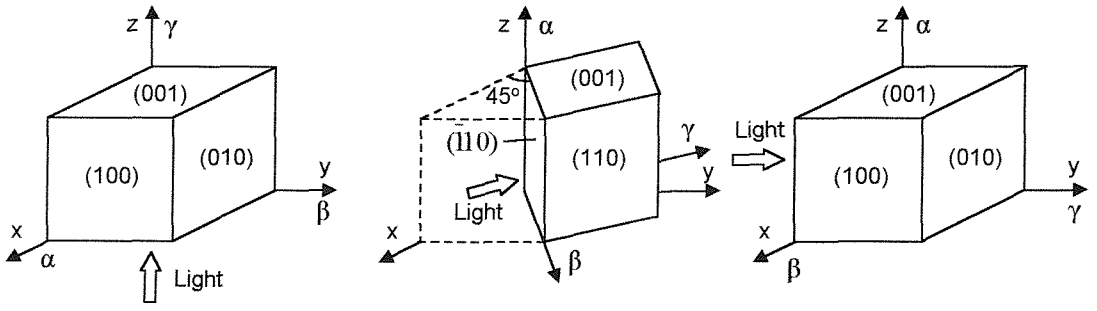

Figure 3.2 Facial orientation of Pockels crystal and incident direction of light beam

The direction x, y and z in the Figure 3.2 are the principal axes of the crystal. Whereas α, β and γ are the direction that the electric field and incident light can be applied. The

symbol ϕ is the angle between the polarisation of the linear polarised light and the principal axis parallel to α.

Among readily available nonlinear electro-optical crystals, Lithium Niobate ($LiNbO_3$) has been widely used in optoelectronics applications including parametric oscillation, holography, light modulators and acting as the substrate for integrated optics. $LiNbO_3$ can be modulated at very high speeds and modulations signals of up to tens of Giga-hertz have been reported [70,71,72,73] The crystal may find future application in the measurement of surface discharges that propagate very quickly. Initial development work used $LiNbO_3$ as the sensor device due to its availability and low cost. The characteristics and its suitability for this application need to be considered in detail.

The nonlinear electro-optical crystal of $LiNbO_3$ is an uniaxial crystal when there is no applied electric field across it i.e. $n_x = n_y = n_o$ and $n_z = n_e$. The crystal will transform from an uniaxial into a biaxial crystal if a field is applied across it. The crystal has symmetry of the 3m class with an elelctro-optic tensor as described by Equation 2.34. The $LiNbO_3$ crystallographic with its edge parallel to the principal x-axis is referred as x-cut (100), similarly a y-cut (010) and z-cut (001) crystal defined the axis that is parallel to the crystal edge. From Equation 2.35 which made one component of electric field E_x, E_y and E_z to be nonzero and the others to be zero, a y-cut $LiNbO_3$ is the only suitable orientation for this application because x-cut and z-cut would not exhibit birefringence when used in the longitudinal mode. Hence, the polarised light would not be phase retarded when it passed through either the x-cut and z-cut orientation. With y-cut $LiNbO_3$ the linear polarised light propagates in the direction of y-axis in the longitudinal configuration. The linear polarised light is set at an angle of 45° to the principal axes x and z which have the following electrically induced refractive indices

$$n_{x'} = n_o - \frac{n_o^3 r_{22} E_y}{2} \tag{3.1}$$

$$n_{z'} = n_e \tag{3.2}$$

and the phase retardation change is

$$\Delta\Phi = \frac{2\pi}{\lambda}(n_{z'} - n_{x'})d \tag{3.3}$$

$$\Delta\Phi = \frac{2\pi}{\lambda}(n_e - n_o)d + \frac{\pi}{\lambda}n_o^3 r_{22} E_y d \tag{3.4}$$

where $\frac{2\pi}{\lambda}(n_e - n_o)d$ is the natural birefringence of the crystal. The natural birefringence creates problems for surface charge measurement. The crystal thickness, d is much greater than the operating wavelength, λ so that the phase retardation can be any value within 0 to 2π. The natural birefringence can be eliminated by making the crystal thickness, d uniform by grinding and polishing its surface. Another possible solution is to add a compensating plate made from a naturally birefringent crystal that adds to the retardation of the $LiNbO_3$ to produce zero phase retardation across the system.

Although the non-zero phase retardation due the natural birefringence that exists on the $LiNbO_3$ crystal can be removed by inserting a compensating plate, the natural birefringence causes problems for a crystal having wedge cut dimensions. Initial development work involved the use of a Pockels cell with surface area 20mm by 20mm and average thickness of 1mm. The parallelism of the crystal was 6 minarc which mean that it had one end thicker than the other. The wedge cut dimension of $LiNbO_3$ was used to prevent multiple reflections of light causing interference effects to the surface charge image. Experiments have been conducted on a wedge y-cut $LiNbO_3$ as shown in Figure 3.3a. Due to the crystal dimensions the incident light will travel along different paths and therefore experience different states of polarisation. This effect can be observed using an analyser and strips of bright and dark patterns are observed (Figure 3.3b). Rotating the analyser by 90° causes the dark strips become bright and vice versa. Figure 3.3c shows the light intensity when the analyser is rotated by 90°.

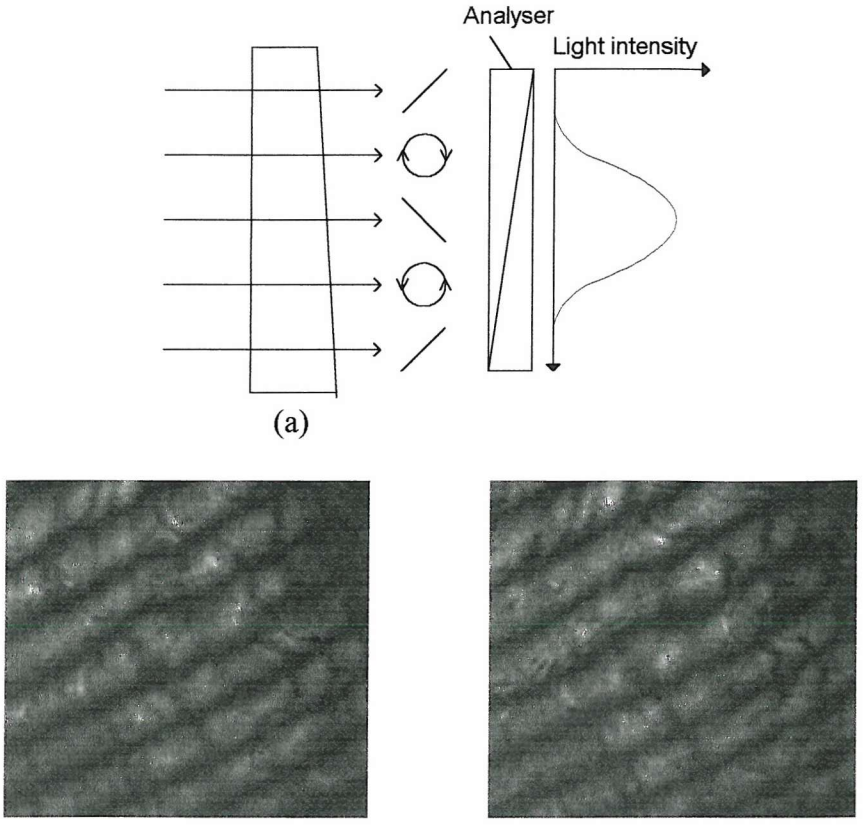

Figure 3.3 Incident light into a wedge y-cut crystal. (a) transmitted light experiences difference polarisation states. (b) transmittance light intensity when passed through an analyser set to 0° with respect to the light polarisation, (c) reverse strips of bright and dark pattern observed on screen when the analyser is set to 90°

The natural birefringence of the Pockels crystal is an unwanted effect, crystal symmetries which do not give natural birefringence are the classes $\bar{4}2m$, $\bar{4}3m$ and 23. Among these groups there are several commercial crystals such as Potassium Dihydrogen Phosphate (KDP), Ammonium Dihydrogen Phosphate (ADP), Gallium Arsenide (GaAs) Cadmium Telliride (CdTe) and Bismuth Silicon Oxide (BSO), However, GaAS and CdTe crystals that are only suitable for use with infrared light. Table 3.2 details some of the electro-optic crystals suitable for use in the longitudinal mode along with their electro-optic coefficients.

Material	Symmetry	Linear electro-optic coefficient, r	n_o/(pm/V)	$n_o^3 r$ /(pm/V)	Operating wavelength/ nm
Potassium Dihydrogen Phosphate (KDP)	$\bar{4}2m$	10.6	1.51	36.5	632.8
Deuterated Potassium Dihydrogen Phosphate (KD*P)	$\bar{4}2m$	26.4	1.51	90.89	632.8
Ammonium Dihydrogen Phosphate (ADP)	$\bar{4}2m$	8.5	1.52	29.9	632.8
Silver Thiogallate ($AgGaS_2$)	$\bar{4}2m$	3.0	2.553	49.91	632.8
Cadmium Telliride (CdTe)	$\bar{4}3m$	6.8	2.6	119.5	3900
Gallium Arsenide (GaAs)	$\bar{4}3m$	1.24	3.6	44.5	900
Bismuth Silicon Oxide (BSO)	23	5.0	2.54	81.9	632.8
Bismuth Germanium Oxide (BGO)	23	9.7	2.55	160.8	632.8

Table 3.2 Characteristic of some common electro-optics crystal

The higher the value of $n_o^3 r$ the greater the sensitivity of the surface charge density measurement. Ideally, the coefficient of $n_o^3 r$ must be large enough to ensure that the change of the phase retardation is measurable for a given applied stress. However, if the coefficient $n_o^3 r$ is too high then the maximum measurable applied stress will be too small. Results from published research on surface charge measurement using an electrostatic probe [19,74,75] have shown that charge densities in the region of tens of $pCmm^{-2}$ are present for applied stresses of tens of kilovolts. However, this measured surface charge density has a large spatial resolution when compared to results obtained by M. Sone, K. Toriyama and Y. Toriyama [76]. They have measured streamer channel widths with dimensions of 10-30μm. A constant charge confined in a smaller channel width will increase the effective surface charge density up to approximately $1nCmm^{-2}$ [21]. Of the crystals detailed in Table 3.2 BSO has been used for this experiment. For z-cut BSO having a thickness of 0.5mm the measurement

limitation is of the order of $1nCm^{-2}$ for the surface discharges due to an applied voltage of between 4 and 7kV.

The BSO used in the development of the experiment has a thin coating of Chrome to act as a transparent electrode and is arranged as shown in Figure 3.4.

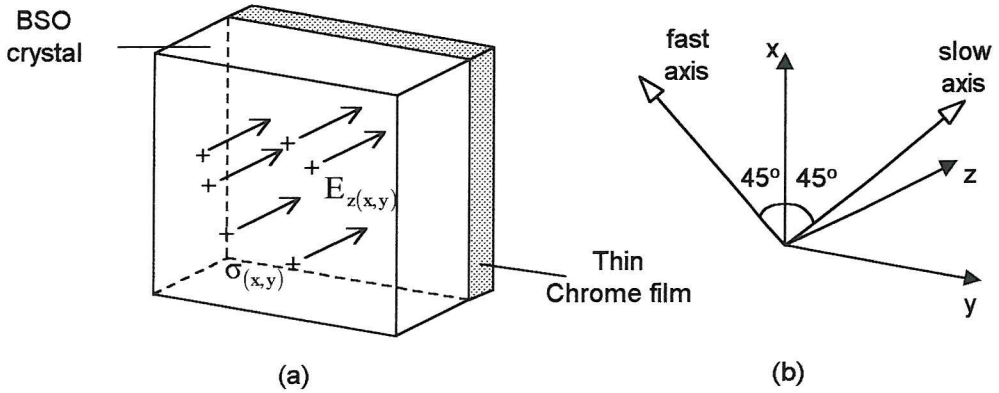

Figure 3.4 BSO Pockels transducer (a) the surface charge induced electric field (b) the orientation of the crystal and the light polarisation

The BSO crystal used in the experiment has an effective size of 20mm by 20mm with a thickness of either 500 or 160μm. The crystallographic of the crystal is z-cut (001), which means that the electric field and the direction of light propagation are parallel to the z-axis of the crystal as shown in Figure 3.4. One side of the BSO is coated with the thin Chrome transparent electrode. The transparent electrode allows light to be transmitted into the BSO crystal and is the ground electrode for the applied field. The principal axis, x and the incident light are at the angle $\Phi_p = 0^o$ in order that the transmitted light has maximum birefringence. Therefore, the induced fast and slow axis will be $\pm 45^o$ with respected to the incident light polarisation and the principal axis x. The electric field component of the incident light can be resolved into two equal components along the fast and slow axis. From Equation 2.57, the two-dimensional phase retardation, $\Phi_{(x,y)}$ of these two equal electric field components transmitted through the induced birefringence crystal at arbitrary position (x,y) is

$$\Phi_{(x,y)} = \frac{2\pi}{\lambda} n_o^3 r_{41} dE_{z(x,y)} \tag{3.5}$$

This expression does not contain natural birefringence, λ is the optical frequency of the incident light, n_o is the refractive index of the BSO, r_{41} is the electro-optic coefficient, d is the thickness of the BSO crystal and $E_{z(x,y)}$ is the two-dimensional electric field distribution across the BSO. The two-dimensional electric field induced by surface charge deposited at an arbitrary point (x,y) on the crystal has the following relationship

$$E_{z(x,y)} = \frac{\sigma_{(x,y)}}{\varepsilon_o \varepsilon_r} \tag{3.6}$$

where ε_o is the permittivity of free space and the ε_r is the relative permittivity. Hence, the phase retardation of the incident light transmitted is related to the surface charge on the BSO by

$$\Phi_{q(x,y)} = K\sigma_{z(x,y)} \tag{3.7}$$

$$\text{where constant } K = \frac{2\pi n_o^3 r_{41} d}{\lambda \varepsilon_o \varepsilon_r}$$

The above equations are valid if the electric field across the crystal is uniform and no space charge exists when the surface charge is deposited onto the BSO crystal.

3.3 The Electro-optic Modulator

An Electro-optic crystal has also been used as an optical modulator to alter the phase of light at a given instant. In general a modulator is a device which changes the irradiance, direction or polarisation state of the light passing through it. There are several general types of modulator such as mechanical choppers, passive modulators, electro-optic, magneto-optic and acousto-optic modulators. The first two types are

mainly used in laser Q-switching [77]. The remaining types alter the refractive index or other optical characteristics by the application of an external force that can be electrical, magnetic and mechanical. The electro-optic effect has already been discussed and an electro-optic modulator can be realised using a Pockels effect or a Kerr effect medium. For a modulator utilising Pockels effect the change of refractive index is proportional to the applied field whereas a modulator that uses the Kerr effect will change its refractive index proportional to the square of the applied field. Electro-optic modulators are widely used for controlling the phase intensity of a propagating beam. They are also used for a large number of applications such as Q-switching of a laser for generation of large optical pulses, optical beam deflection scanning, phase modulation and amplitude modulation [78].

The characteristics of the electro-optic modulator are important. The incident light into the modulator must be either linear or elliptical or circular polarised. The fast and slow axes of the modulator must be arranged at an angle of 45° with respect to the polarisation of the incident light in order to achieve a maximum output. Electro-optic modulators can sustain greater power inputs than optical fibres. Usually, a relatively high voltage of around 1kV is required in order to achieve a sufficient modulation effect. Commercially available modulators can work at frequencies up to a few Giga-hertz. There are two common cell configurations of electro-optic modulator, the transverse mode and longitudinal mode.

3.3.1 Transverse Electro-optic Modulator

The arrangement for transverse modulation has been discussed in Chapter 2. The transverse electro-optic modulator has an electric field applied normal to the direction of light propagation. The main advantage of transverse mode operation is that the electrodes do not interfere with the incident light. For a transverse mode modulator phase retardation is proportional to the applied field and the crystal length. Therefore, the length of the crystal can be increased to achieve a higher retardation for a given operational voltage. This implies that a lower applied field can be utilised in order to obtain a desired phase retardation [73]. However, for an input beam having a large diameter, the thickness of the crystal must also be increased. This results in a higher

applied voltage being required to give the same electric stress across a thinner crystal. To reduce the applied voltage the length of crystal could be increased to give a sufficient phase retardation but this modification results in a larger device.

3.3.2 Longitudinal electro-optic Modulator

In the longitudinal mode the electric field is parallel to the direction of propagation of the optical wave. Consequently it is a more complicated device than the transverse mode modulator. As the field is parallel to the direction of light propagation the light has to pass through the electrodes on the either side of the crystal and therefore, a transparent electrode is required. This can be achieved by depositing a transparent metal-oxide coating [79] (e.g. Tin Oxide, Indium Oxide or Cadmium Oxide) or a very thin metal coating (e.g. gold, chrome or aluminium) on the crystal surface with a thickness of tens of nanometers. The phase retardation is proportional to the applied voltage across the crystal and independent of the thickness of the crystal, d. This arrangement is more suitable for large input beam diameters than the transverse mode modulator.

3.3.3 Modified Longitudinal electro-optic Modulator

A modified longitudinal electro-optic modulator with a cylindrical crystal and ring or grid electrode as shown in Figure 3.5 has been developed to overcome the problem of transparent electrode deposition. The field is applied between the electrodes this configuration gives uniform transmission or polarisation across the effective aperture of the device. However, the physical dimensions of the device are limited and the construction far more complicated than the standard configuration of modulator.

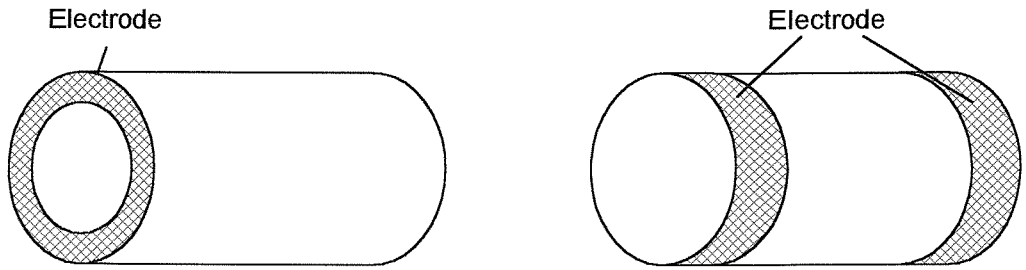

Figure 3.5 Longitudinal electrode-optic cells (a) with end electrode and small aperture, (b) with ring electrode and large aperture

3.3.4 High Frequency Modulation Considerations

In many applications the modulation signal is a very high frequency of a few gigahertz. The modulator must have a large bandwidth so that a wide frequency spectrum is available for any application. With reference to the circuit diagram shown in Figure 3.6 the electro-optic crystal is between two electrodes with a modulating field containing frequency, f_o applied to it.

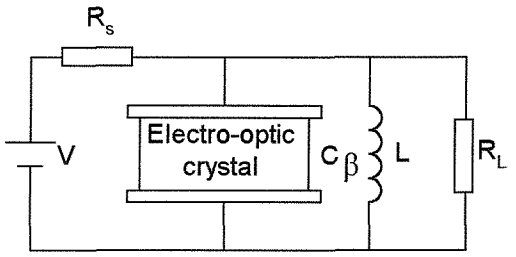

Figure 3.6 Electro-optic crystal an resonant circuit [78]

The capacitance of the modulator and finite transit time taken for the light to pass through it give rise to limitations in bandwidth and maximum modulation frequency. Let R_s be the internal resistance of the modulation voltage source and C_β the capacitance of the electro-optic crystal. If R_s is greater than the reactance of the crystal, most of the modulation voltage will be across R_s and only a small amount of potential will be applied to the crystal. For this research BSO was used as the electro-optic modulator with dimension of 20mm by 20mm and a thickness of 1mm. Therefore, the capacitance of the modulator is

$$C_\beta = \frac{\varepsilon_o \varepsilon_r A}{d}$$
$$= 198pF \qquad (3.9)$$

where ε_o is the permittivity of free space and ε_r is the dielectric constant for BSO (56). The modulator used in the surface charge optical measurement system is modulated with a square wave signal having a frequency of 1kHz. If only the

fundamental frequency of the applied modulated is considered then the reactance of the crystal is

$$X_c = \frac{1}{2\pi f_o C_\beta} \approx 800k\Omega \tag{3.10}$$

Therefore, the reactance of the modulator for an applied square signal at the frequency 1000Hz is very high. The internal resistance of the modulation source is of the order of 50Ω and therefore most of the modulation voltage is dropped across the modulator. Modulators working at higher frequencies have smaller reactance. Adding extra components in parallel to the modulator can solve potential problems. With reference to Figure 3.6 the inductor L is chosen so that at the modulation frequency the impedance of the circuit is purely resistive. The resistor R_L is large compared to R_S so that most of the modulation voltage is across the crystal.

3.4 Laser Source

The light source used in the optical system is a Helium Neon (HeNe) type laser. The HeNe laser offers several advantages such as reliability and low cost. It has coherence lengths of thousands of meters, high beam quality (TEM00), excellent pointing stability, low output noise and requires a simple electrical supply. The laser provides monochromatic light to the optical system with a wavelength of 632.8nm. The light is in the red region of the visible light spectrum. The laser source outputs a continuous wave of 17mW in power with beam diameter $1/e^2$ of 1mm. In the optical system the laser light is expanded into a larger diameter and transmitted through several optical components such as the polarised beam splitter (PBS), wave plate, lens and Pockels cell. Some of the optical power will be lost due to multiple internal and external reflection at the interfaces between air and the optical components. The light reflection is greatest at the interface between the gold electrode and the BSO crystal. Moreover, since the light signal detected by the CCD camera comes from reflection at the back face of the BSO only a small proportional of the laser light intensity is incident on the CCD camera. Consideration of light signal loss at the interfaces of the

optical system has been accounted for and the 17mW laser source is powerful enough so that light can still be detected by the CCD camera after multiple reflections.

3.5 Beam Expander

The HeNe laser source outputs a light beam with diameter 1mm. The surface discharge activities take place over a region of about 12mm diameter on the BSO. A beam expander is used to increase the input beam diameter of the light incident into the BSO. There are two types of beam expander configuration as shown in Figure 3.7 these are the Keplerian beam expander and the Galilean beam expander. The light intensity of the beam will be decreased by the expander after expansion.

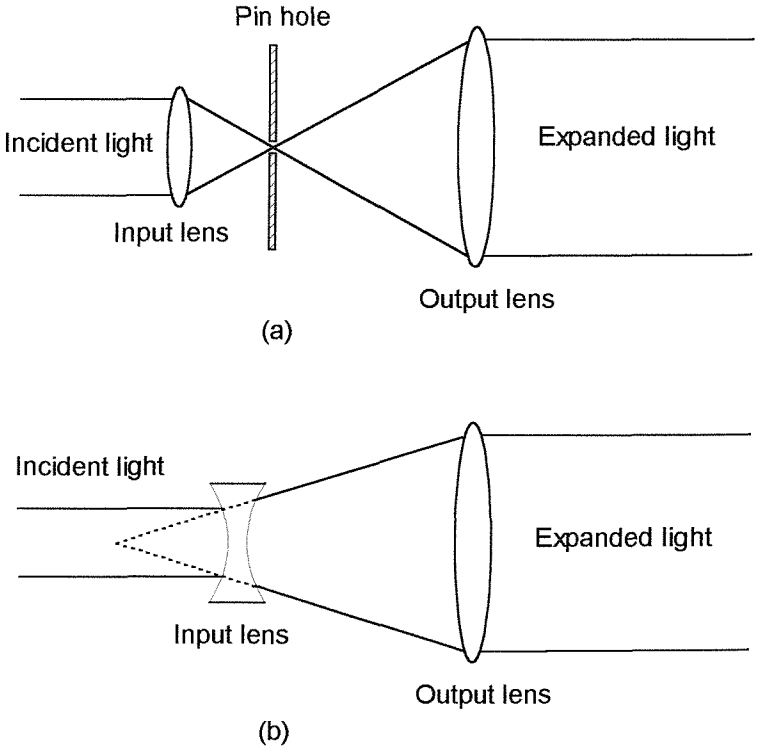

Figure 3.7 (a) Keplerian Beam Expander (b) Galilean Beam Expander

3.5.1 Keplerian Beam Expander

The Keplerian beam expander is composed of a pair of convex lenses separated by a distance $f_{in} + f_{out}$ as shown in Figure 3.7a where f_{in} and f_{out} are the focal length of the input and output lens respectively. The input ray is focussed at a distance of f_{in} and

a pinhole is used to prevent spherical aberration of the lens. The beam is defocussed at the pinhole and then is recollimated by the output lens to form a parallel beam with a larger diameter. The magnification of the beam is given by the ratio of output to input focal lengths which is

$$m = f_{out} / f_{in} \tag{3.11}$$

Due to the lenses configuration the Keplerian beam expander can only be safely used with a low power laser. The input beam is focused by the input lens of Keplerian beam expander to a small spot only a few tens of microns in diameter and the power density at the focus point can reach up to 10^{12} watt/cm^2. Such high power density will ionise the surrounding air, severely disrupt the beam characteristic and can also damage the optics.

3.5.2 Galilean Beam Expander

The Galilean Beam Expander can be thought of as the inverse of the Galilean telescope as shown in Figure 3.7b. This type of beam expander has one concave lens and one convex lens. The lenses are separated by the difference of the focal length $f_{out} - |f_{in}|$ and as in the Keplerian beam expander, the expansion ratio is the ratio of output to input focal lengths. For the use of high peak power lasers the Galilean configuration provides an alternative approach to beam expansion in which the beam never comes to a focal point, thus preventing ionisation in air and other catastrophic effects. An input concave lens is used in the system to diverge the input beam from a virtual point focus. A convex lens recollimates the diverging beam and therefore the beam never comes to a real focus in this configuration.

3.6 Beam Splitter

The vertical linear polarised light is retarded in phase after passing through the Pockels crystal when it has an electric field across it. In the optical system the Polarised Beam Splitter (PBS) serves as both the polariser and analyser. In general the function of the PBS is to separate the TM and TE components of an incident beam into two highly polarised output beams separated by 90°. For the laser which has expanded its beam diameter via the beam expander, its output light passes through the PBS and only the vertical polarised light component is transmitted and propagated to the Pockels crystal. If no surface charge exists on the Pockels crystal the light will be reflected and transmitted through the PSB back to the laser as there is no phase retardation change in the polarised light (Figure 3.8a).

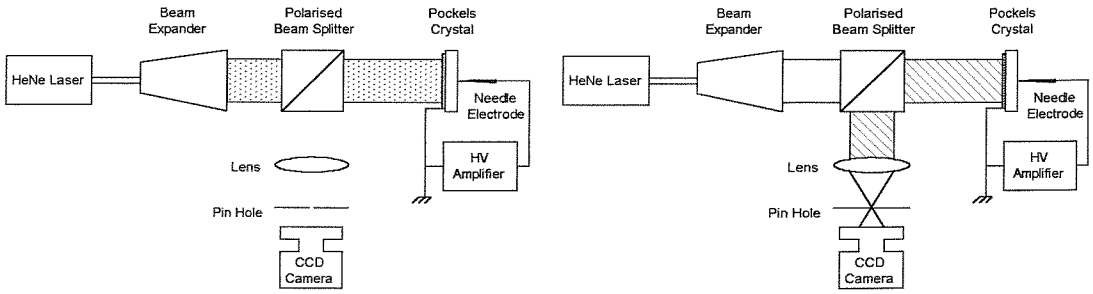

Figure 3.8 The role of the PBS (a) without surface charge deposited on the Pockels crystal (b) with surface charge deposited

Once surface charge has been deposited on the Pockels cell the internal field causes a change of the index of refraction and the polarised light changes its polarisation state. The light will reflect back from the BSO and will be split by the PBS as it contains other polarisation components (Figure 3.8.b). Therefore, the information about the surface charge is directed to the CCD camera.

3.7 Lens and Pinhole

A plano-convex lens is used in the optical system to focus the light beam into a small diameter. The CCD camera has an array of sensing elements which can be considered as individual photo diodes with an array size of 512 by 480 pixels within an area of 5mm by 4mm. However, at the maximum framing speed of 1000 frames per second (fps) the resolution of the image is reduced to 256 by 240 pixels. The length of an AC surface discharge streamer at 7kV is between 6mm to 9mm. Reflected light with a radius of 8mm is focussed into a diameter of 2mm by the lens. Different plano-convex lenses with various focal lengths have been used in the experiment in order to determine the most suitable. For a lens with shorter focal length the image focussed on the CCD sensing array will be smaller and hence less pixels are used to form the image. For a lens with longer focal length the image may have a larger dimension than the CCD sensing array. Experimental results show that the lens with a 150mm focal length used to focus image on the CCD camera utilises nearly all of the available CCD array.

The pinhole blocks light due to internal and external reflections caused by optical devices. If the BSO used in the optical system has both surfaces perfectly parallel, then the path of the light is first emitted into the BSO and transmitted through the crystal which will experience phase retardation due to the Pockels effect and finally out of the crystal. However, some of the light will not be transmitted from the BSO but will reflect back at the interface of the crystal. This causes interference and may influence the image causing it to be distorted. To overcome the problem of multiple internal reflections within the crystal, the crystal must be modified so that the surfaces of the BSO are no longer parallel (Figure 3.9). The parallelism angle between both surfaces is very small (approximately 6 minarc) so that the distance the light travels through the BSO can be considered constant.

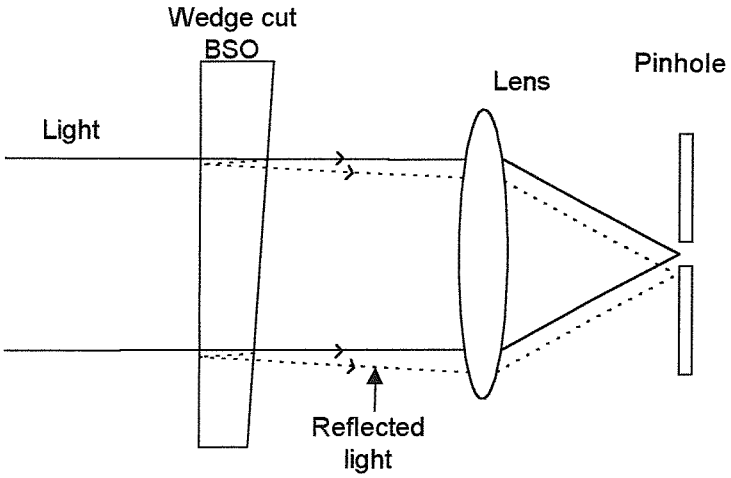

Figure 3.9 Removing interference using a wedge cut crystal, lens and pinhole

It can be seen from the Figure 3.9 that any transmitted light will be focussed by the lens and pass through the pinhole. However, light that has been reflected within the BSO crystal will be focussed by the lens at a different spot. The pinhole only allows transmitted light to pass through and any reflected light is effectively blocked. Therefore, the image formed on the CCD array will only consist of light that has experienced phase retardation due to Pockels effect. Figure 3.10a shows that the image recorded by the CCD camera without using a pinhole contains interference patterns, whereas in Figure 3.10b the use of a pinhole removes fringing from the image. Therefore, the pinhole can block unwanted light into the camera [45,46,47]. If the diameter of a pinhole is too large then too much light enter the camera whereas if its diameter is too small not enough light will enter the camera. The optimum diameter of the pinhole used in this experiment is 800μm.

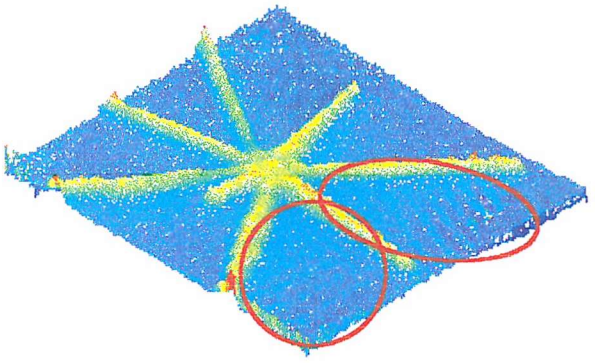

(a)

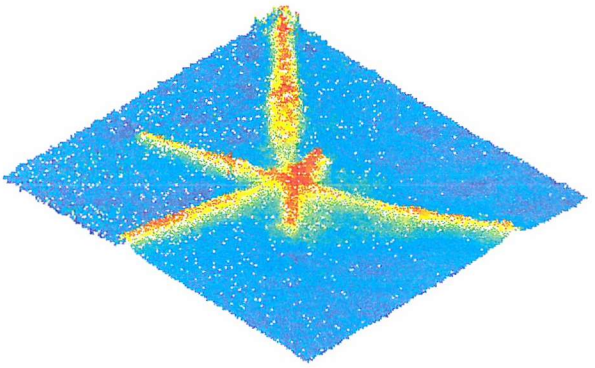

(b)

Figure 3.10 Images obtained by the CCD camera (a) without using a pinhole and (b) with a pinhole (effective figures dimensions are 8mm by 8mm)

3.8 CCD Camera

The camera used in the optical measurement system is a Charge Coupled Device (CCD) camera manufactured by Kodak Ltd. The camera can operate at a maximum speed of 1000 frames per second (fps) with a resolution of 256 by 240 pixels. Full resolution up to 512 by 480 pixels can be achieved at lower framing rates. The recording speed of 1000 fps is fast enough to measure the change of light intensity due to a 50Hz AC discharge and the resolution of 256 by 240 pixels gives a reasonable image quality. One thousand frames per second provides twenty light intensity profiles for each 50Hz AC cycle. The light intensity detected by the camera is quantified using an A/D converter into 256 levels, it therefore requires one byte of memory to represent each pixel. The camera includes a memory module that can store up to 1365 frames at full resolution. When operating at 1000 fps with a resolution of

256 by 240 pixels the memory can store 5460 frames which means that events can be continuously monitored for over 5 seconds. For measuring low levels of light intensity the exposure time can be increased in order to enhance the recorded light signal. However, this also increases the recorded background noise. It is advisable to keep the exposure time to a minimum in order to reduce background noise. The image monitor connected to the camera can be used to review the images stored in the camera memory before transfer to a PC for post-processing. The images stored in the memory can be downloaded to a PC via Small Computer System Interface (SCSI) interface port on the camera (Figure 3.11).

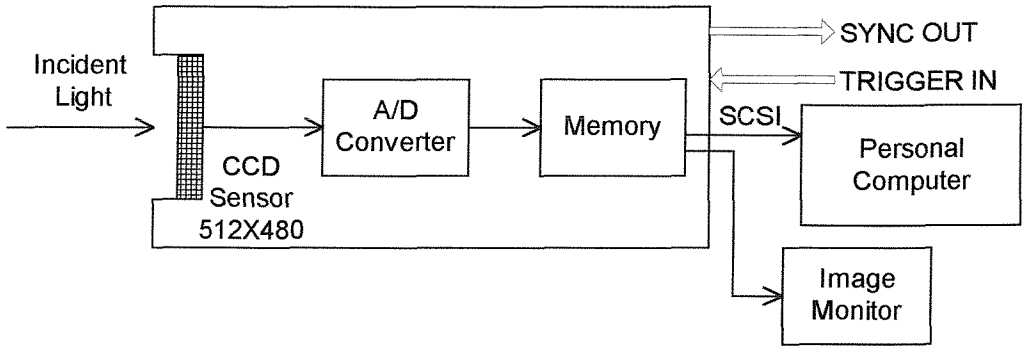

Figure 3.11 Block diagram of the CCD camera

The camera starts to capture images as soon as it is turned on, but images are only stored in the camera memory after it receives a start signal. The start signal can be triggered by a push button on the camera control panel or by a TTL 5V signal via the TRIGGER IN BNC connector. The camera outputs a TTL 5V pulse at BNC connector SYNC OUT when it records a new frame. Hence, there is a 1kHz pulse signal output from SYNC OUT when the camera captures image at 1000fps. This output signal is an independent source and cannot be synchronised with other events such as the instant when an AC discharge signal is applied to the needle electrode. Therefore, a control circuit was developed that used the output signal of the CCD camera as a master source in order to control other events within the measurement system.

3.9 Synchronisation Control Circuit

A Synchronisation Control Circuit has been developed based on the PIC16F84 microcontroller in order to use the output signal from the camera as a master source to activate other events in the measurement system. The PIC16F84 has a processing speed of 1MHz and is idea for controlling several events with a short time delay, such that the events can be assumed to be sychronised. Referring to Figure 3.13, the pulse waveform output from the SYNC OUT is via one bit of an input port to the microcontroller. The control signal acts to trigger the synchronisation control circuit so that the microcontroller will start to operate. The PIC16C84 microcontroller is programmed to detect the rising edge of the incoming signal. At the first detected rising edge the output of the microcontroller connected to the Optical Modulator Driver is set high and after the next rising edge is set low. The Optical Modulator Driver is therefore controlled by the signal from the microcontroller and generates $+V_M$ and $-V_M$ modulating voltages sequentially. The modulating voltage is modulated at half the frequency of the camera speed. The CCD camera will start to record the image in the camera memory after receiving a 5V TTL signal via TRIGGER IN from the synchronisation control circuit. The signal generator outputs a sinusoidal signal that is amplified by the HV amplifier to give AC HV up to 7kV. The number of cycles of AC signal are also controlled by the microcontroller. The details of the control sequence are discussed with the signal processing methods used for each experiment in Chapter 4, 5 and 6.

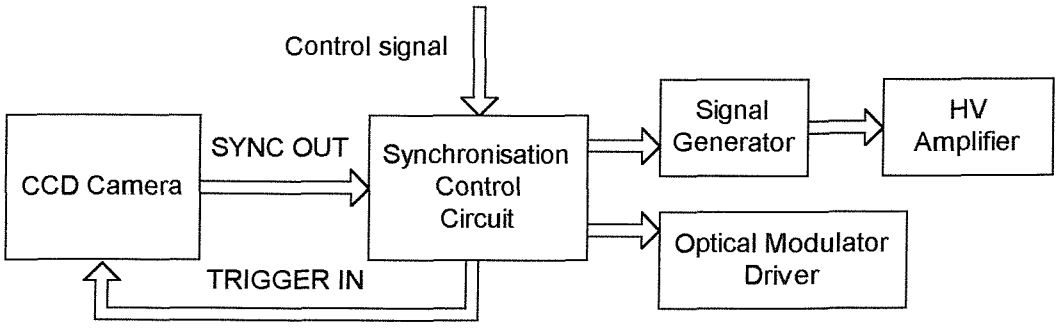

Figure 3.12 Block diagram of the synchronisation control circuit

3.10 Antireflection Coating

When light passes from one medium into another medium with a different refractive index, part of the light is reflected and part of the light transmitted. The intensity ratio of the reflected and transmitted components is determined by the refractive index of the two mediums and the incident angle. Generally, the reflected light represents a few percent of incident radiation. However, when using more than a few components, losses in transmitted light level can be accumulated rapidly. The corresponding losses in image contrast or modulation due to a weak reflected image superimposed on the desired image can be significant. Applications usually require that the reflected portion of incident light is ideally 0% for the PBS and 100% for the Pockels sensor. In a practical system the surface of optical elements can be coated with thin films of various materials such as Magnesium Fluoride to achieve a good performance. However, the reflection ratio depends on the optical properties, the operating wavelength and angle of incident light. By using multi layer coatings the reflection ratio can be optimised for several sets of conditions. To achieve better efficiency of the optical system a coating has been used on the PBS, plano-convex lens and quarter wave plate. This is the antireflection coating HEBBAR supplied Melles Griot Ltd. The HEBBAR coating gives excellent results as the reflection ratio approaches zero percent for the operating wavelength of 632.8nm.

3.11 The Two Dimensional Measurement of Transmitted Light Intensity

The main task of the optical arrangement is to determine the two-dimensional light intensity change. The change of the light intensity distribution is then used to evaluate the phase retardation distribution. Once the phase retardation distribution has been determined, the surface charge distribution across the BSO crystal can be easily calculated. The following experiment without the optical modulator or 1/8 wave-plate was undertaken to demonstrate that the measurement of transmitted light intensity was feasible.

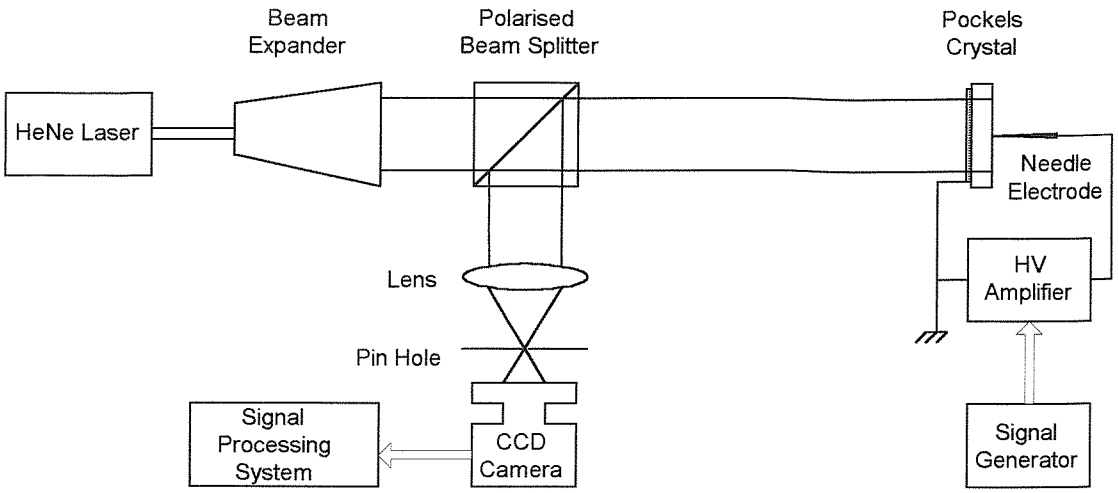

Figure 3.13 Experiment setup to illustrate the concept of the measurement light intensity due to Pockels effect

This circuit shown in Figure 3.13 only consists of the basic optical, electrical and electronic components required for the detection of light intensity. The two-dimensional distribution of transmitted light intensity due to the phase retardation caused by the Pockles effect is

$$I_{(x,y)} = T_{(x,y)} I_{o(x,y)} \sin^2\left(\frac{\Phi_{(x,y)}}{2}\right) \tag{3.12}$$

where $I_{o(x,y)}$, $T_{(x,y)}$ are the maximum light intensity distribution of incident beam and total transmittance at the position (x,y) respectively. Together with the phase retardation distribution, the maximum light intensity distribution is another non-uniform unknown factor in the measurement system and must be determined by using an extra optical component and image processing method. The electric field of the laser light used in the optical system has a non-uniform distribution, its electric field intensity decreases in all directions from the centre towards the edge of the beam as shown in Figure 3.14.

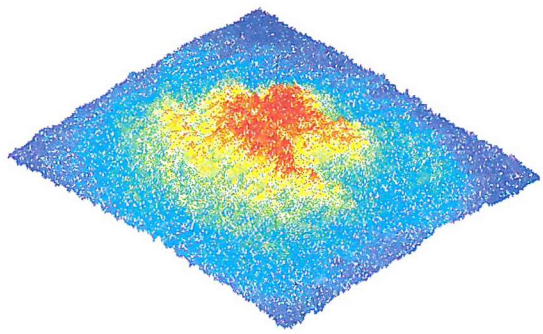

Figure 3.14 Non-uniform intensity distribution (with dimension of 8mm by 8mm) of light reflected at BSO crystal

The light intensity distribution, $I_{(x,y)}$ in the Equation 3.12 is the measured light transmitted from the BSO crystal. It has been shown [44,45,46] that the measurement of reflected light from the Pockels cell has certain advantages. The measurement of reflected light does not interfere with the needle, whereas the measurement of transmitted light would be complicated by the presence of the electrode. The test materials may have poor optical properties and act to scatter the transmitted light. The scattering effect by the test films can be reduced by measuring the reflected light from the interface between the crystal and the film. Furthermore, the reflected light travels twice the distance of transmitted light and hence the phase retardation of the light is doubled. This effect increases the sensitivity of the optical system for a given amount of surface charge on the crystal. Therefore, the transmittance of reflected light for a given surface charge at point (x,y) will be

$$I_{(x,y)} = T_{(x,y)} I_{o(x,y)} \sin^2\left(\Phi_{(x,y)}\right) \tag{3.13}$$

Since BSO has no natural birefringence and from Equation 3.13, a given magnitude of surface charge density will result in the same phase retardation change irregardless of charge polarity as shown in Figure 3.15.

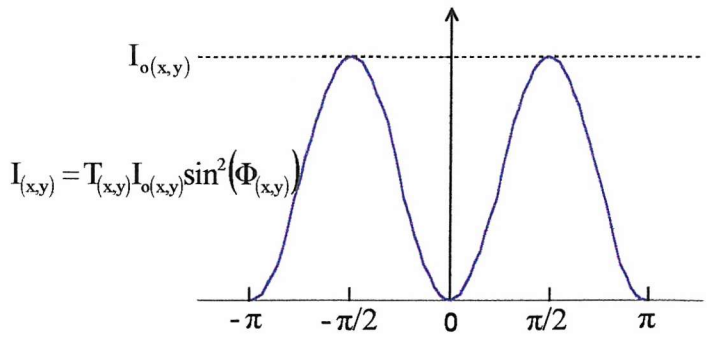

Figure 3.15 Light intensity change due to phase retardation

When the phase retardation is $\pm\pi/2$ then the light intensity reaches a maximum value I_o. $I_{o(x,y)}$ is non-uniform due to the Gaussian beam that is used and $T_{(x,y)}$ is the transmission and reflection ratio of the incident light. The light will be transmitted and reflected at the interfaces between the optical media in this case the interfaces are between the air, the BSO crystal, the chrome electrode and the test film. The chrome electrode is not uniformly deposited across the crystal surface and this will cause a non-uniform transmission and reflection ratio. Therefore, the term, $T_{(x,y)} I_{o(x,y)}$ represents the total non-uniform effect of using a Gaussian beam used and varying transmission and reflection ratio.

Deposition of surface charge onto the BSO surface has been demonstrated by applying AC high voltage of 7kV at the needle electrode. Charge was deposited onto the surface and the transmittance of light recorded by the CCD camera. Figure 3.16 shows a typical result.

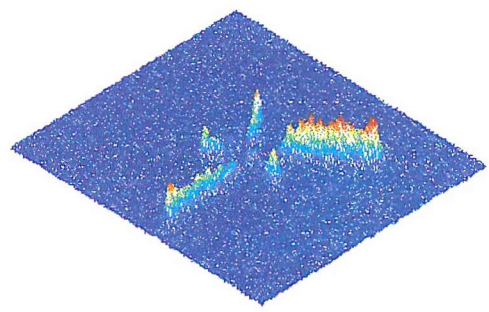

Figure 3.16 Surface charge deposited on the Pockels cell by an applied field (effective figures dimensions are 8mm by 8mm)

Positive and negative charge exists simultaneously on the BSO crystal (Figure 3.16). Research has demonstrated [4,5,6] that positive streamers move away from the needle electrode whereas negative charge accumulates around the electrode tip. Examination of the image recorded by the camera does not define charge polarity and if heterogeneous charge is deposited onto the cell only the charge magnitude can be readily estimated. Charge polarity discrimination is important and can be achieved through the use of additional optical components. With reference to Figure 3.16, it can be seen that some positive streamers appear to have a higher magnitude than others. This is due to the non-uniform light intensity distribution. The non-uniform light intensity distribution must be accounted for when determining the magnitude of the charge and this can be achieved using image processing techniques.

Chapter 4

AC Surface Discharge Measurement System Including a 1/8 Waveplate

4.1 Introduction

Previous research [26,27,28,29,30,31,32,33] on electric field measurement using Pockels effect has used a quarter waveplate to distinguish field polarity. A similar approach can be adopted for surface charge measurement. If a waveplate is inserted into the system it will introduce an additional phase retardation of the incident light. In order to distinguish the polarity of the surface charge deposited on the BSO crystal a 1/8 waveplate [80] was included within the optical system as shown in Figure 4.1.

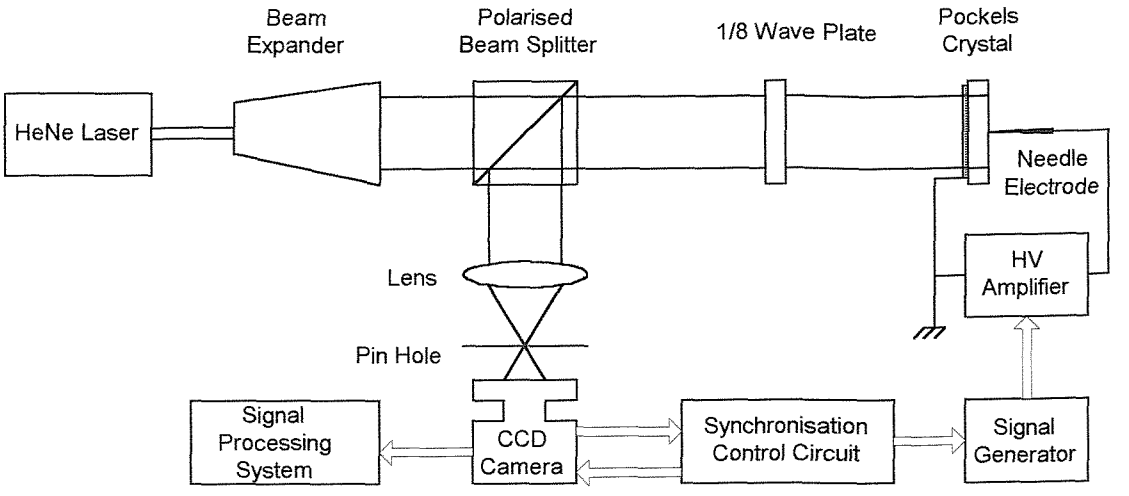

Figure 4.1 Optical system with the used of 1/8 waveplate

4.2 Measurement Principle

The 1/8 waveplate introduces an additional phase retardation of $\pi/4$ into Equation 3.13. Therefore, the phase retardation due to the surface charge, $\Phi_{(x,y)}$ will be optically biased by $\pi/4$ and the transmittance of the light will be modified to

$$I_{(x,y)} = T_{(x,y)} I_{o(x,y)} \sin^2\left(\frac{\pi}{4} + \Phi_{(x,y)}\right) \tag{4.1}$$

Equation 4.1 will be valid if the optical axis of the 1/8 waveplate is set to 45° with respect to the light polarisation which is ϕ_p=0°. The effect of introducing a 1/8 waveplate on the transmitted light intensity is shown in Figure 4.2. The 1/8 waveplate causes the initial light intensity before discharge to be biased from zero to half the maximum light intensity, $I_{o(x,y)}/2$. At a point where positive charge exists a positive retardation will cause an increase in light intensity. Whereas any negative charge on the BSO crystal surface will reduce the transmittance of light.

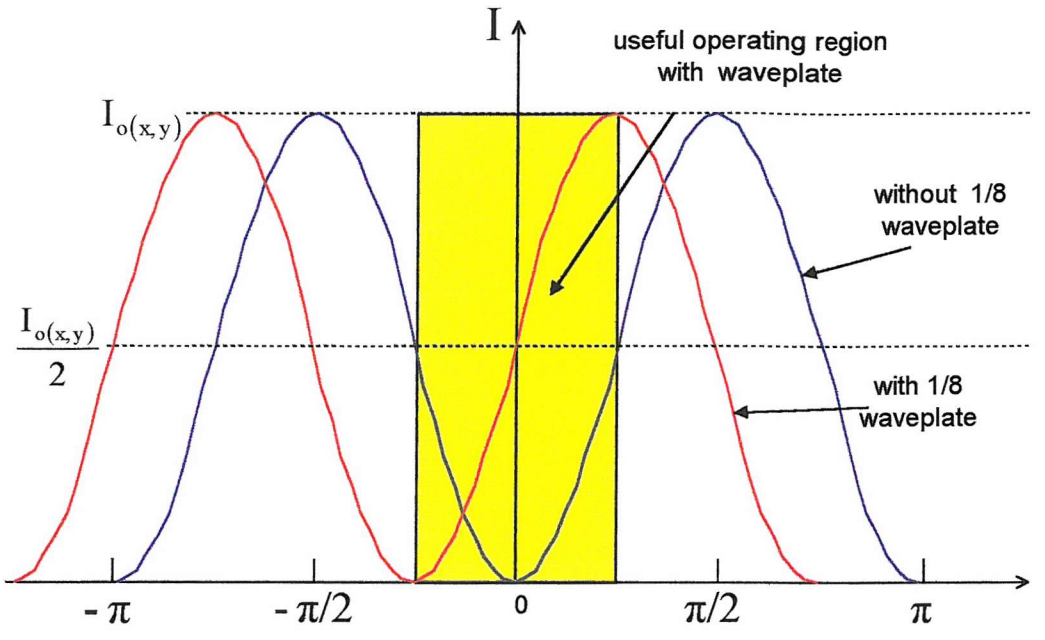

Figure 4.2 Light intensity against the phase retardation with or without 1/8 waveplate

Assuming that there is no surface charge present on the crystal prior to any discharge activity $\Phi = 0$, the measured light intensity, $I_{b(x,y)}$ before the voltage is applied will be

$$I_{b(x,y)} = T_{o(x,y)} I_{o(x,y)} \sin^2\left(\frac{\pi}{4}\right) = \frac{I_{o(x,y)}}{2} \tag{4.2}$$

Therefore, the initial light intensity recorded by the CCD camera prior to discharge is half of the maximum light intensity $I_{o(x,y)}$ and the maximum light intensity distribution across the BSO crystal can be determined using a 1/8 waveplate.

After charge is deposited on the BSO crystal through the application of a high voltage at the needle electrode, the phase retardation at point (x,y) may no longer be zero. The transmittance of light detected by the CCD camera due to the presence of surface charge is

$$I_{q(x,y)} = T_{o(x,y)} I_{o(x,y)} \sin^2\left(\frac{\pi}{4} + \Phi_{(x,y)}\right)$$

$$= I_{b(x,y)}\left(1 + \sin 2\Phi_{(x,y)}\right) \tag{4.3}$$

Therefore, the relationship between the phase retardation and the measured light intensity before and after the application of a high voltage across the crystal is

$$\Phi_{(x,y)} = \frac{1}{2}\sin^{-1}\left(\frac{I_{q(x,y)} - I_{b(x,y)}}{I_{b(x,y)}}\right) \tag{4.4}$$

If the phase retardation calculated by using Equation 4.4 is positive then positive surface charge is present. Negative surface charge will cause negative phase retardation. From the Figure 4.2, if too much charge is present then a phase retardation of greater than $\pm\pi/4$ will result, however the measured light intensity will be less than $I_{o(x,y)}$. Consequently, care must be taken to ensure that the surface charge deposited on the crystal must not cause an equivalent phase retardation of greater than $\pm\pi/4$. From Equation 3.7, for a 0.5mm thick BSO crystal with crystal orientation (001) the maximal surface charge density for an equivalent $\pm\pi/4$ in phase retardation is 1nCmm^{-2}.

4.3 An Equivalent Model

The optical phase retardation and the measured light intensity in the optical system can be represented using an equivalent model as shown in Figure 4.3. The model has been used to determine the required optical input power in order to maximise the performance of the system. Each pixel of the CCD camera array is represented by an 8 bit grey scale value. Using the waveplate ideally zero charge should return a value of 127, maximum light intensity a value of 255 and minimum light intensity a value of 0.

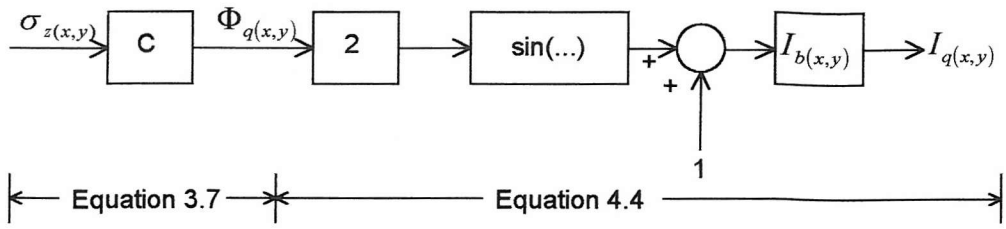

Figure 4.3 Equivalent model

Figure 4.4 shows the relationship between quantified light intensity at the camera and the power of the light source. If the light source is too bright then the CCD array becomes saturated for small values of phase retardation. Conversely, if the power of the light source is too small then maximum light intensity will not utilise the full grey scale range, this will result in a poorer signal to noise ratio. Practically when the light source is too bright it can be reduced using an attenuator.

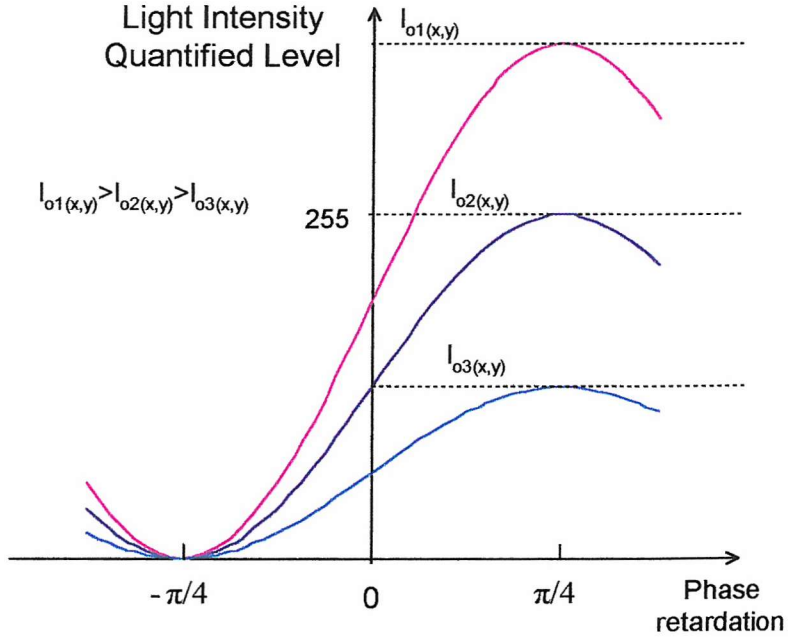

Figure 4.4 Quantified light intensity with various input light power used

From the model a program has been developed to evaluate the surface charge based on light intensity measurements. The flow chart of the program is shown in Figure 4.5.

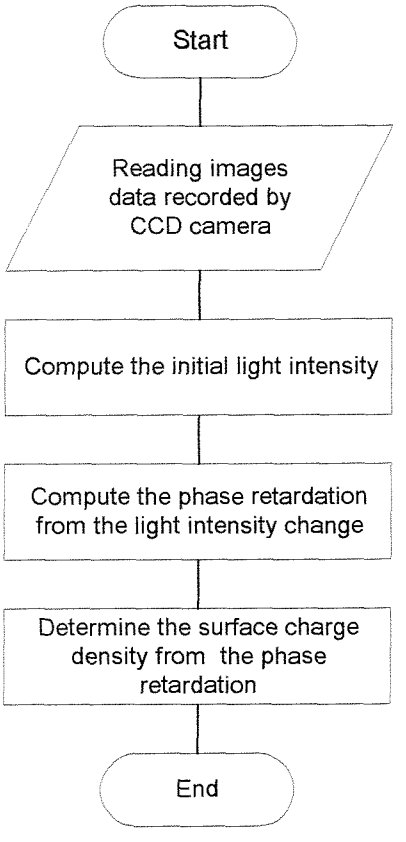

Figure 4.5 Matlab program flow chart to evaluate the surface charge density

4.4 The Measurement Procedure

An image processing program has been developed in order to determine surface charge from the light intensity images captured by the CCD camera. Data was obtained using the optical system and a BSO crystal with dimensions of 20mm by 20mm and thickness 0.5mm. The spatial resolution of the surface charge is related to the thickness of the crystal (500μm in this case). The needle electrode was just in contact with the crystal surface. Care was taken when aligning the needle electrode with the crystal. The needle could not touch the crystal surface because it would create local mechanical stress. Mechanical stress causes mechanically induced birefringence within the crystal and therefore causes measurement error of light intensity. The synchronisation control circuit based on the PIC16F84 microcontroller

was programmed to control the events associated with the measurement as shown in Figure 4.6.

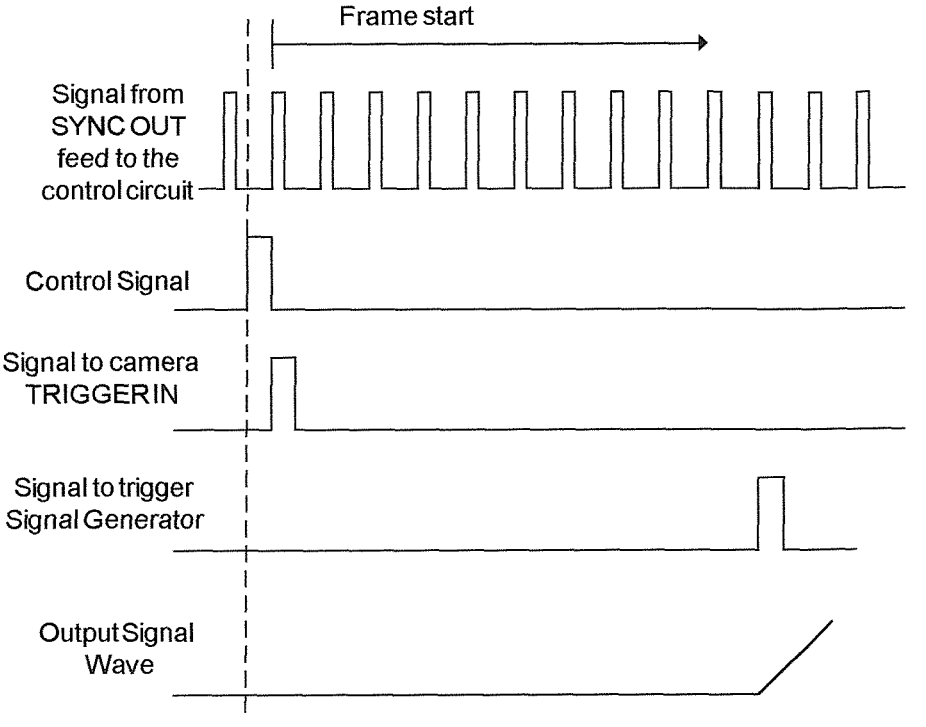

Figure 4.6 Control signal for measuring surface charge with a 1/8 waveplate

The camera signal is the master source in the optical system and outputs a pulse waveform of 1000Hz associated with the camera frame rate. Initially, the microcontroller receives the camera signal and then waits to be activated. After it is activated the microcontroller waits for a rising edge of an incoming pulse from the SYNC OUT of the camera. Once the first rising edge of the incoming pulse is detected the microcontroller will trigger the camera to start recording the light intensity. The initial frames are used to gather the information of the light intensity biased by a 1/8 waveplate and the maximum light intensity distribution for further image processing. After ten frames have been recorded by the CCD camera, the microcontroller triggers the signal generator. The signal generator produces a 50Hz sinusoidal wave into a power amplifier that provides an AC high voltage to the needle electrode. In this experiment the AC high voltage was ±4kV. The high voltage was applied to the crystal for two cycles (40ms). Therefore, 40 frames of light intensity change were recorded during the time that the voltage was applied to the needle electrode.

4.5 Image Processing

The frames recoded by the CCD camera were transferred into the computer memory for further analysis. The frames obtained before the surface discharge detail the light intensity biased by the waveplate as shown in Figure 4.7a. The light intensity distribution is non-uniform across the BSO sample. The frames obtained sequentially after the application of the surface discharge are compared individually with the frame in Figure 4.7a. For example, the frame captured after 15ms shown in Figure 4.7b is compared with the frames before discharge using Equation 4.4. The resultant data after image processing is the phase retardation distribution across the crystal (Figure 4.7c). The surface charge density distribution can then be determined from the phase retardation distribution using the Equation 3.7.

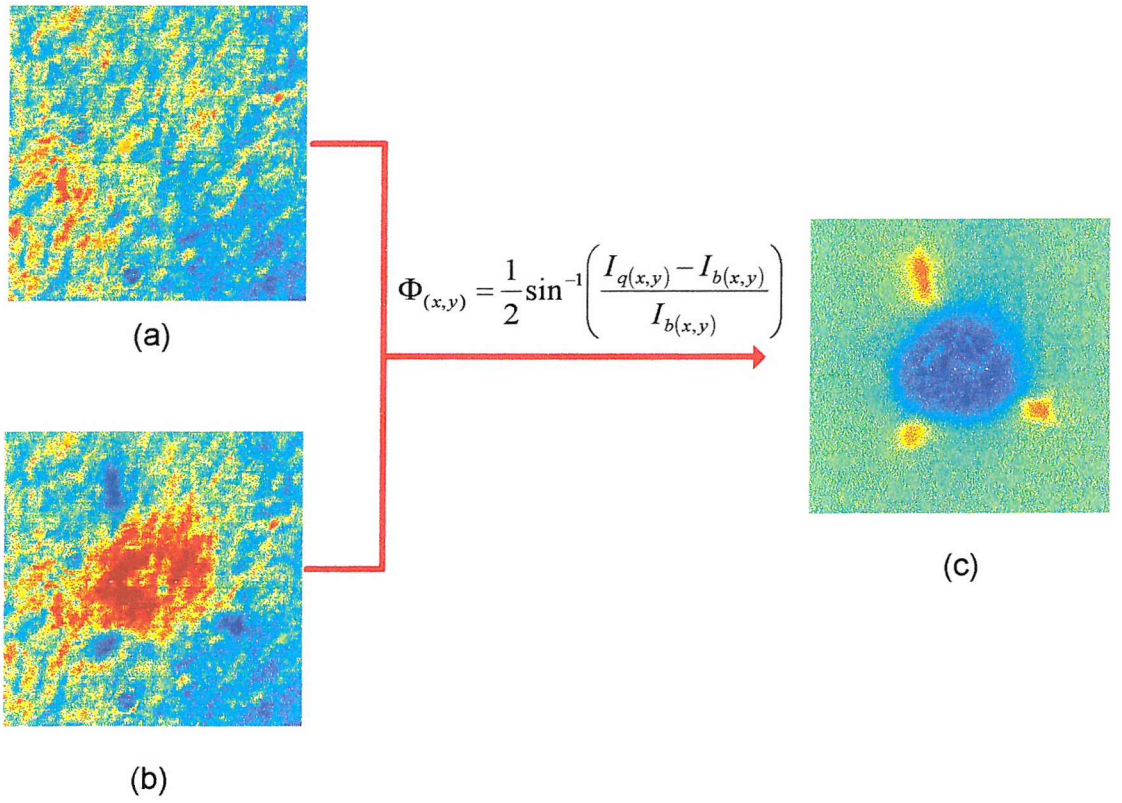

Figure 4.7 (a) image, $I_{b(x,y)}$ recorded before the discharge and (b) image, $I_{Q(x,y)}$ recorded during the discharge lead to (c) surface charge density, $\Phi_{(x,y)}$ after image processing

4.6 Experiment Results

An ac 50Hz ±4kV pk-pk applied voltage over two cycles was applied to a needle electrode mounted at the back of a BSO crystal. The location of the needle tip with respect to the crystal surface influences the measurement. If in direct contact with the backface of BSO there is an induced mechanical stress that causes distortion of the measurement. The needle electrode is mounted using an adjustable screw fitting. At the start of the experiment the needle is adjusted until it is within 100μm of the crystal surface. Figure 4.8 to 4.11 show typical surface discharge results obtained for two cycles of ac stress. The frame number corresponds to the time in milliseconds of the measurement. The surface charge is represented using a colour scale where dark blue represents $-0.6nCmm^{-2}$ and bright red $+0.6nCmm^{-2}$. Areas having no surface charge are represented as green in colour. The effective dimensions of the measurement results are 4mm by 4mm.

From Figure 4.8 it can be seen that initially, no measurable surface charge is observed until 1ms (Frame 1) after the ac voltage is initially applied. After 2ms there is positive charge deposited on the crystal surface (Frame 2) near to the needle tip. Although initially circular in shape, the deposited charge does not increase uniformly across the crystal surface, this is observable after Frame 3. As the applied voltage continues to increase more charge is deposited and positive streamers flow in a radial direction away from the needle tip. After 5ms the applied voltage is at its maximum and the positive streamers stop travelling away from the needle tip and are at their maximum length. For the time after 5ms the applied voltage falls, the positive streamers remain on the surface of the crystal and there is virtually no dynamic movement of the observed charge which is illustrated in Frames 6-9. When the voltage passes through zero the positive charge on the surface near the needle tip is neutralised. Frames 10-20 show the obtained measurements of surface charge during the first negative half cycle (Figure 4.9). As there is positive charge on the crystal as soon as the applied voltage is less than zero negative charge is deposited. This is known as negative backdischarge [3,4,5]. Approximately circular in shape the deposited negative charge is concentrated around the needle tip. As the negative applied voltage continues to increase the negative charge density continues to increase and expand radially which is shown in

Frames 11-15. The negative charge does not develop streamers as the positive surface discharge. With reference to Frame 15 when the applied voltage is –4kV the positive streamer tips have not been neutralised although the negative charge has expanded to its maximum density and radius. The negative surface charge has a smaller radius than the positive streamer that developed for a same magnitude of applied voltage but with opposite polarity. As with the first positive half cycle the negative surface charge pattern remains unaltered as the applied voltage increases towards zero volts as shown in Frame 16-19.

At the start of the second cycle positive streamers are again formed. Due to positive backdischarge some positive charge is observed around the zero crossing point in Frame 20. The presence of the negative charge distorts the propagation of the positive streamers and they only develop within the area charged negative shown in Frames 21-25 (Figure 4.10). When the applied voltage reaches its second peak at 25ms the deposited positive charge appears to have neutralised all of the negative charge. The original streamer tips from the first positive half cycle can still be clearly observed. As the voltage decreases toward zero there is no dynamic movement of surface charge (Frames 26-29). Around zero volts before the second negative cycle, negative charge is again observed in Frame 30 and it expands radially and increases in density as the negative applied voltage increases (Figure 4.11). Again only the tips of the positive streamers remain by the time that the applied voltage has reached –4kV (Frame 35). The positive streamer pattern that is observed during the second positive half cycle is very different to that observed during the first. This is due to the number of initially available free electrons around the needle electrode. During the first positive half cycle free electrons are present in the surrounding air generated by either cosmic rays or electron detachment from negative ions. During the positive half cycle these electrons are attracted to the anode and leaving low mobility positive ions within the region. The number of the positive streamers depends upon the applied voltage and the number of initially free electrons. In the case of second positive half cycle electrons have been liberated from the needle electrode during the previous negative half cycle. As the second applied positive voltage increases the positive streamers neutralise the electrons present around the needle tip.

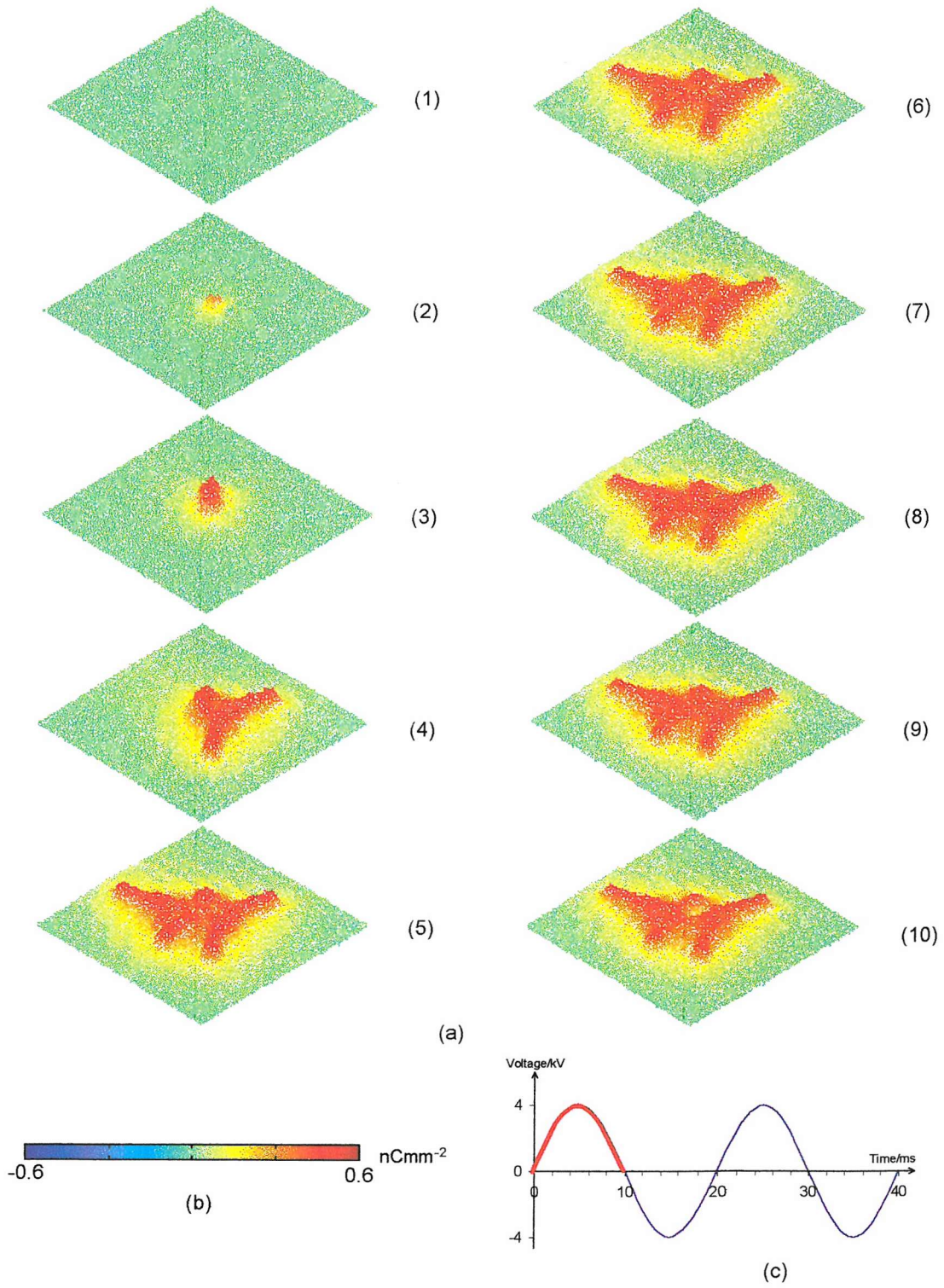

Figure 4.8 Dynamic AC surface discharge (a) time dependence of surface charge distribution (b) surface charge density key (c) waveform of voltage and corresponding frame number (effective dimensions of these images are 4mm by 4mm)

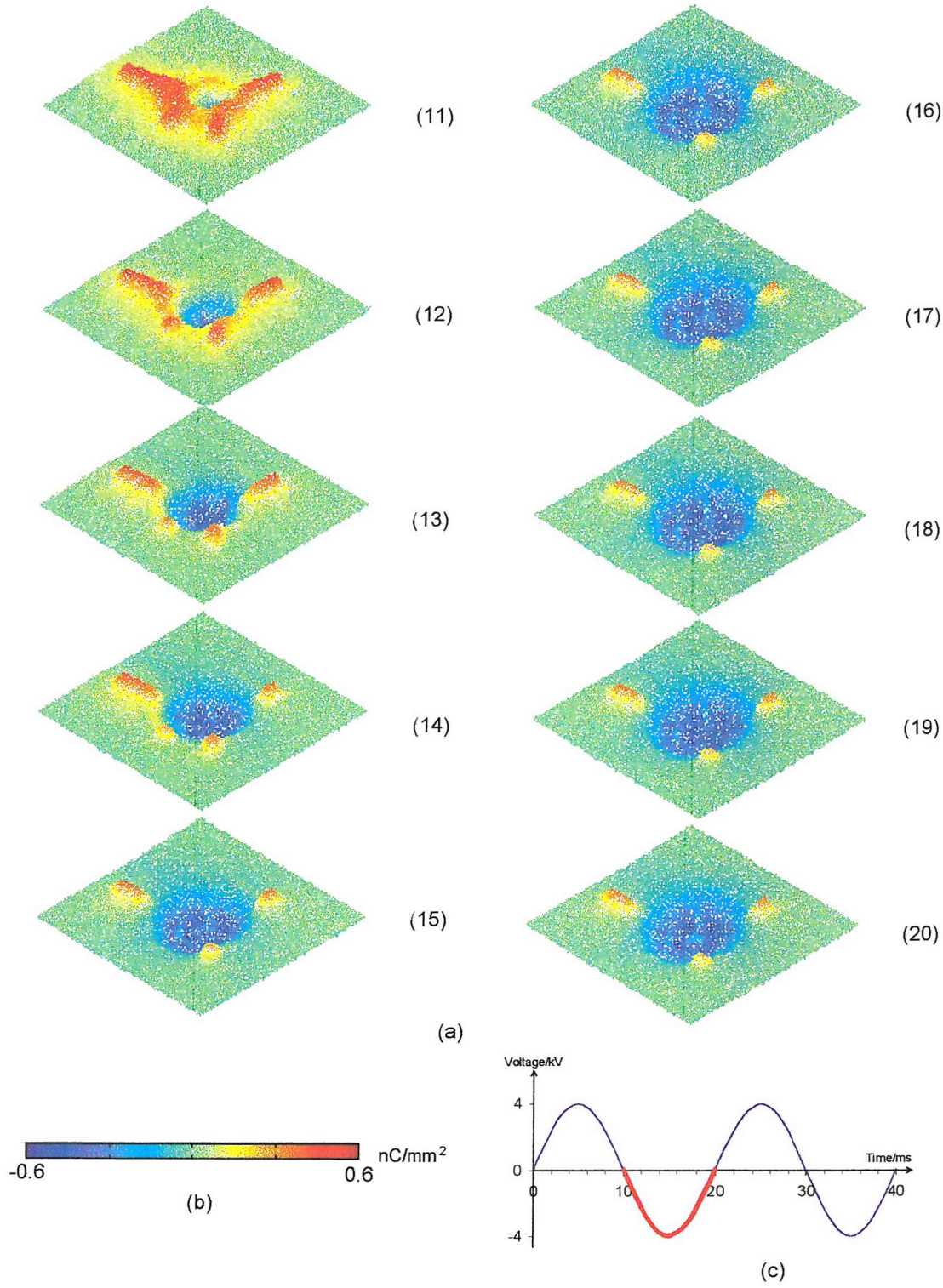

Figure 4.9 Dynamic AC surface discharge (a) time dependence of surface charge distribution (b) surface charge density key (c) waveform of voltage and corresponding frame number (effective dimensions of these images are 4mm by 4mm)

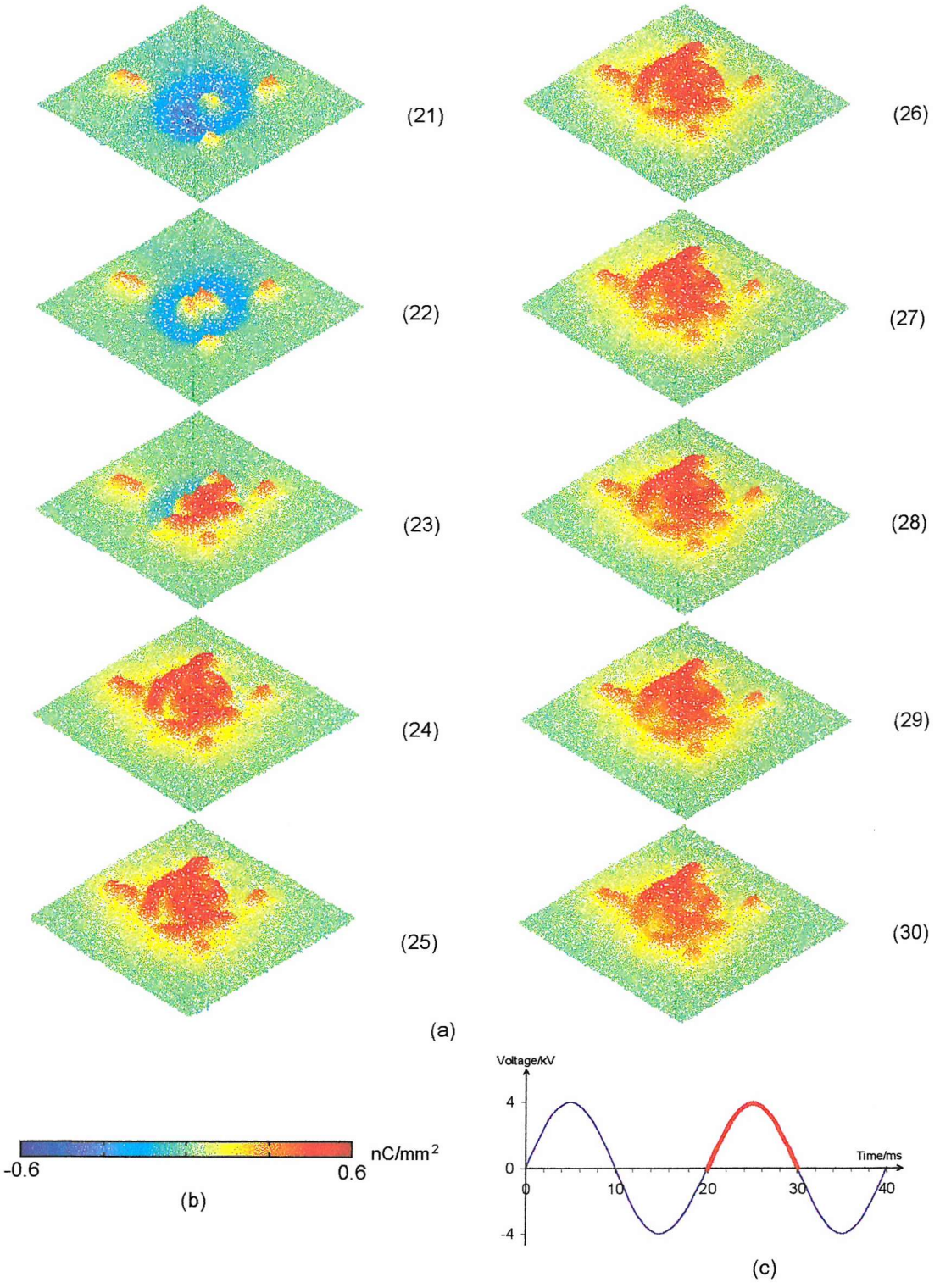

Figure 4.10 Dynamic AC surface discharge (a) time dependence of surface charge distribution (b) surface charge density key (c) waveform of voltage and corresponding frame number (effective dimensions of these images are 4mm by 4mm)

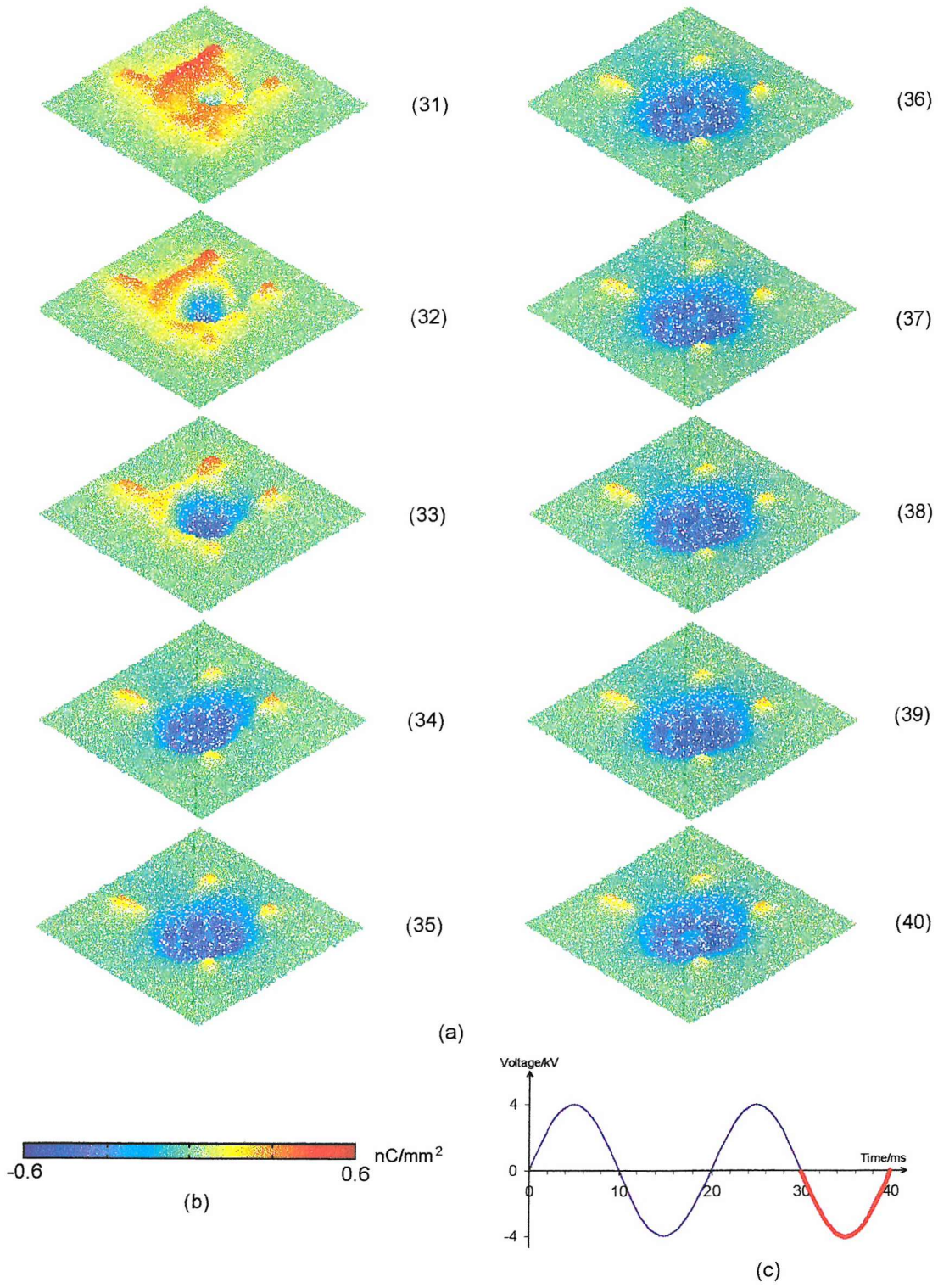

Figure 4.11 Dynamic AC surface discharge (a) time dependence of surface charge distribution (b) surface charge density key (c) waveform of voltage and corresponding frame number (effective dimensions of these images are 4mm by 4mm)

Chapter 5

Surface Discharge Measurement System Including an Optical Phase Modulator (OPM)

5.1 Introduction

As discussed in Chapter 4 there are two unknown factors in the practical measurement of light intensity namely the phase retardation distribution and the light intensity distribution. The optical system for the measurement of phase retardation distribution generated by a non-uniform surface charge distribution using an 1/8 waveplate provides a reasonable resolution of surface charge. However, this simple approach ignores several factors that limit overall practical performance. Optical noise can be generated by the light passing through air containing impurities or from being transmitted through optical components with imperfect interfaces. Time varying noise due to the non-stability of the laser light has also been neglected. The PBS introduces an offset to the light component due to the fact that it does not filter the light polarisation with 100% efficiency and a small constant offset is introduced into the measurement. Mechanical stress at the interface between optical devices and their

mountings can cause the photo elastic effect within the BSO crystal resulting in birefringence and distorting the measurement result.

5.2 Improving the Spatial Resolution

The performance of the optical system can be improved by increasing the spatial resolution of the surface charge measurement. The spatial resolution of the surface charge is approximately the same as the thickness of the BSO crystal used. The thickness of the BSO crystal is 500μm which is also the approximate spatial resolution around 0.5mm for surface charge measurement. To improve spatial resolution, a BSO crystal with an effective area of 20mm by 20mm having wedge cut dimensions and an average thickness of 160μm has been used as the sensing device. The BSO crystal is fragile and brittle therefore it must be supported by another substrate. BK7 glass with a thickness of 800μm was used to support the thin BSO crystal. The BSO crystal was bonded to the BK7 glass using an epoxy resin. The resin was about 20μm thick.

The electric field within the BSO crystal becomes non-uniform as the crystal thickness is increased (Figure 5.1). This results in lower resolution of the surface charge. Decreasing the thickness of the sample will ensure a uniform electric field across the sample for a given surface charge. With the use of a thinner crystal mounted on a glass substrate the spatial measurement of surface charge can be improved to approximately 160μm. However, the minimum thickness of the BSO is limited as it is very difficult to polish the wedge cut dimension crystal to thinner than 150μm. Furthermore, a thinner BSO crystal will produce a smaller phase retardation than a thicker one for the same surface charge,because the phase retardation is proportional to the thickness of the crystal (Equation 3.7).

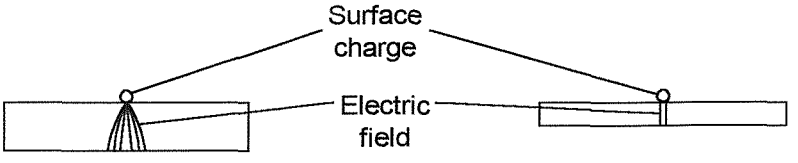

Figure 5.1 Induced electric field within a BSO crystal

Measurement results obtained using the 1/8 wave-plate show that a given surface charge on the BSO with 0.5mm thickness is equivalent to a phase retardation of $\pm\pi/6$. For a BSO with 160μm thickness and identical surface charge, the equivalent phase retardation is only $\pm\pi/18$. To overcome this reduction caused by the thinner Pockels crystal the 1/8 waveplate is replaced with an Optical Phase Modulator (OPM) [38,42] in order to determine charge polarity (Figure 5.2).

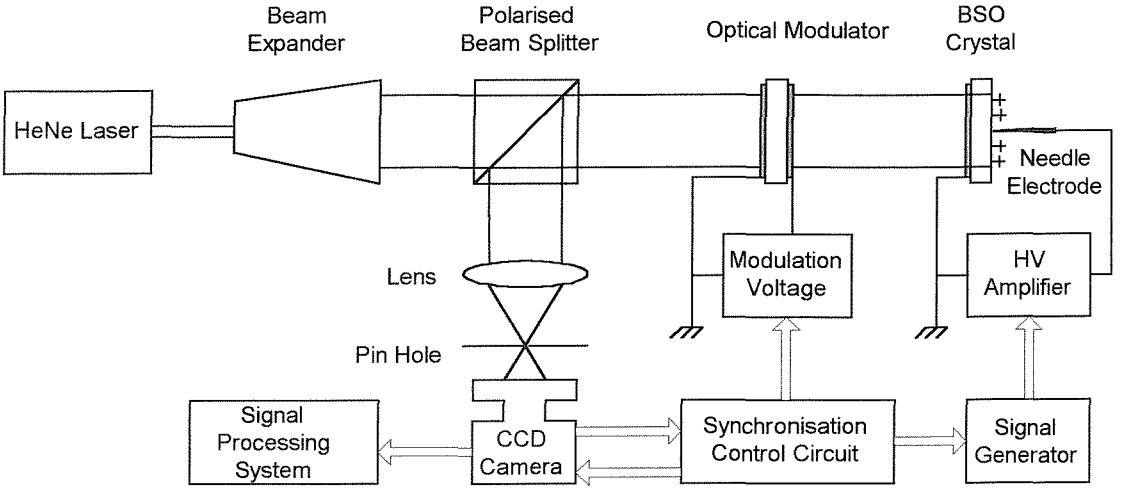

Figure 5.2 Optical system including an Optical Phase Modulator

5.3 The OPM and Its Image Processing [46,47,81]

The phase retardation consists of two components, the first is due to any surface charge that exists on the Pockels cell and the second one is due to natural birefringence of the optical devices. The natural birefringence is due to the photo elastic effect caused by mechanical stress between the optical device and its mounting. For simplicity, this small amount of natural birefringence was ignored in the analysis of the measurement system with the 1/8 wave plate. The total phase retardation distribution measured by the optical system including the natural birefringence distribution is

$$\Phi_{(x,y)} = \Phi_{q(x,y)} + \Phi_{nat(x,y)} \tag{5.1}$$

where $\Phi_{nat(x,y)}$ is the phase retardation cause by the residual mechanical stress which is generally small and non-dynamic. Hence the measured light intensity distribution by the optical system due to the phase retardation distribution is

$$I_{(x,y)} = T_{(x,y)} I_{o(x,y)} \sin^2\left(\Phi_{(x,y)}\right) + I_{offset(x,y)} \tag{5.2}$$

where $I_{offset(x,y)}$ is the constant offset component of the light intensity. The constant offset component is mainly due to the leakage of light when the light passes through the PBS.

5.3.1 The Determination of The Total Phase Retardation Distribution, $\Phi_{(x,y)}$

The OPM is constructed from another Pockels crystal. It is BSO crystal with surface area 25mm by 25mm and a thickness of 1mm. Placing a square wave voltage of $\pm V_M$ across it causes the light to be modulated in phase by $\pm\Phi_M$. The light intensity monitored by the CCD camera is altered by the phase modulation. There are two light intensity measurements, one for a positive phase modulation and the other when the phase modulation is negative i.e.

$$I_{M+(x,y)} = T_{(x,y)} I_{o(x,y)} \sin^2\left(\Phi_{(x,y)} + \Phi_M\right) + I_{offset(x,y)} \tag{5.3.a}$$

$$I_{M-(x,y)} = T_{(x,y)} I_{o(x,y)} \sin^2\left(\Phi_{(x,y)} - \Phi_M\right) + I_{offset(x,y)} \tag{5.3.b}$$

where Φ_M is the modulated phase produced by the modulating voltage. Since the OPM is arranged in a longitudinal mode the modulated optical phase is two-dimensional. The light intensity distribution, $I_{M+(x,y)}$ and $I_{M-(x,y)}$ are the images obtained during the positive and negative duration of the modulation pulse waveform (Figure 5.3).

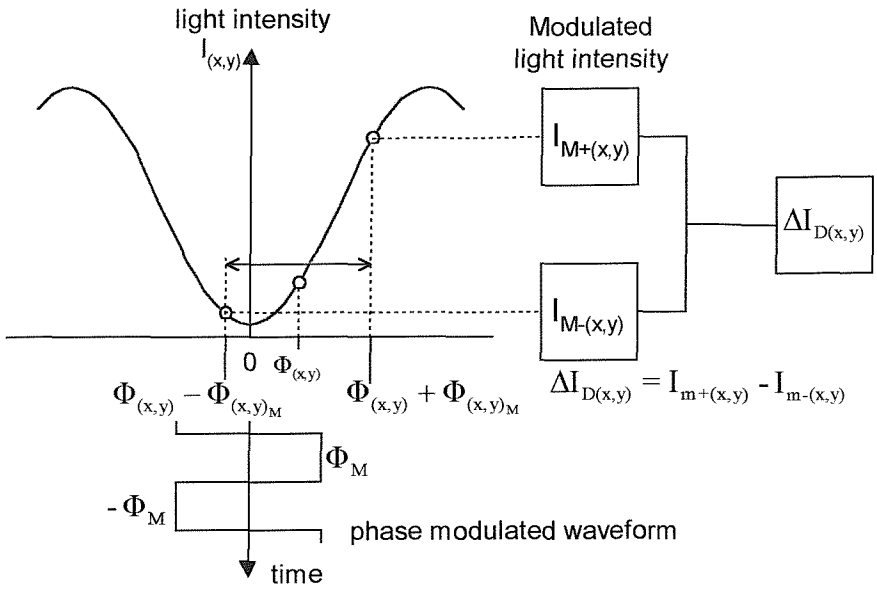

Figure 5.3 Pulse modulation of optical phase

With the introduction of the positive and negative modulated light intensity distribution into the optical system, the difference between two images, $\Delta I_{D(x,y)}$ is

$$\Delta I_{D(x,y)} = I_{M+(x,y)} - I_{M-(x,y)} = I_{E(x,y)} \sin\left(2\Phi_{(x,y)}\right) \tag{5.4}$$

where $I_{E(x,y)} = T_{(x,y)} I_{o(x,y)} \sin\left(2\Phi_M\right)$

where $I_{E(x,y)}$ is the equivalent maximum light intensity distribution. Using the method of images the constant offset component of the light intensity is eliminated. From Equation 5.4 the total phase retardation distribution can be determined i.e.

$$\Phi_{(x,y)} = \frac{1}{2} \sin^{-1}\left(\frac{\Delta I_{D(x,y)}}{I_{E(x,y)}}\right) \tag{5.5}$$

5.3.2 Determination of the Equivalent Maximum Light Intensity Distribution, $I_{E(x,y)}$

Using the OPM, the polarised light from the laser is altered in phase by the positive and negative modulating voltage placed across the OPM. The light reflected from the Pockels crystal is also shifted in phase by the OPM. The images captured by the CCD

camera can be used to determine the change in measured light intensity, $I_{D(x,y)}$, but the equivalent maximum light intensity distribution, $I_{E(x,y)}$, must be determined before any surface charge is present on the Pockels cell. The initial light intensity distribution prior to any discharge or modulating voltage applied to the OPM is caused by natural birefringence and the constant offset light component, such that

$$I_{a(x,y)} = I_{o(x,y)} \sin^2\left(\Phi_{nat(x,y)}\right) + I_{offset(x,y)} \tag{5.6}$$

Applying a modulating voltage to the OPM prior to any surface discharge activity produces a light intensity distribution that is due to the phase modulation of the OPM, natural birefringence and the constant offset light component. Thus the light intensity distribution during the positive and negative modulated phase will be

$$I_{+(x,y)} = I_{o(x,y)} \sin^2\left(\Phi_{nat(x,y)} + \Phi_M\right) + I_{offset(x,y)} \tag{5.7.a}$$

$$I_{-(x,y)} = I_{o(x,y)} \sin^2\left(\Phi_{nat(x,y)} - \Phi_M\right) + I_{offset(x,y)} \tag{5.7.b}$$

Using the method of images, the change in modulated light intensity distribution prior to surface discharge due to the OPM is

$$\Delta I_{(x,y)} = I_{+(x,y)} - I_{-(x,y)} = I_{E(x,y)} \sin\left(2\Phi_{nat(x,y)}\right) \tag{5.8}$$

From Equation 5.8 the natural birefringence can be determined

$$\Phi_{nat(x,y)} = \frac{1}{2} \sin^{-1}\left(\frac{\Delta I_{(x,y)}}{I_{E(x,y)}}\right) \tag{5.9}$$

The equivalent maximum light intensity distribution, $I_{E(x,y)}$ is an unknown factor in the determination of the natural birefringence distribution. However, it can be determined from using Equation 5.6 and 5.7, because

$$I_{+(x,y)} + I_{-(x,y)} - 2I_{a(x,y)} = \frac{I_{E(x,y)}(1-\cos 2\Phi_m)\cos(2\Phi_{nat(x,y)})}{\sin 2\Phi_m} \tag{5.10}$$

Squaring Equation 5.8 and substituting it into Equation 5.10 yield an equivalent maximum light intensity of

$$I_{E(x,y)} = \sqrt{\Delta I_{(x,y)}^{\,2} + \left[\frac{(I_{+(x,y)} + I_{-(x,y)} - 2I_{a(x,y)})\sin 2\Phi_m}{1-\cos 2\Phi_m}\right]^2} \tag{5.11}$$

Substituting this into Equation 5.5 and Equation 5.9 gives the total phase retardation distribution and the natural birefringence distribution. From Equation 5.1, Equation 5.5 and 5.9 the phase retardation distribution due to surface charge is the difference between the total phase retardation distribution and the effect due to natural birefringence, that is

$$\Phi_{q(x,y)} = \Phi_{(x,y)} - \Phi_{nat(x,y)} \tag{5.12}$$

Thus by using the OPM in the optical system the influence of the natural birefringence can be removed. Also, the constant offset light component is eliminated ensuring a higher accuracy in the measurement of surface charge density.

5.4 Image Averaging Technique

The measurement system combines laser optics with electronic imaging. Time-varying noise interferes with the light intensity measurement data. In the optical system, noise is caused by fluctuation of the laser power due to its non-stable power supply. The laser will also vary in intensity due to scattering effects from either the optical defects or from particles in the air. Electronic measurement systems also generate time-varying noise. An image averaging technique has been implemented in order to reduce noise levels and has been proved effective. Figure 5.4 shows the image averaging technique applied to the detected light intensity distribution from data obtained using the 1/8 wave plate. In this example, the CCD camera detects light intensity and records 500 frames, which is equivalent to 500ms. The resultant data are shown in Figure 5.4.

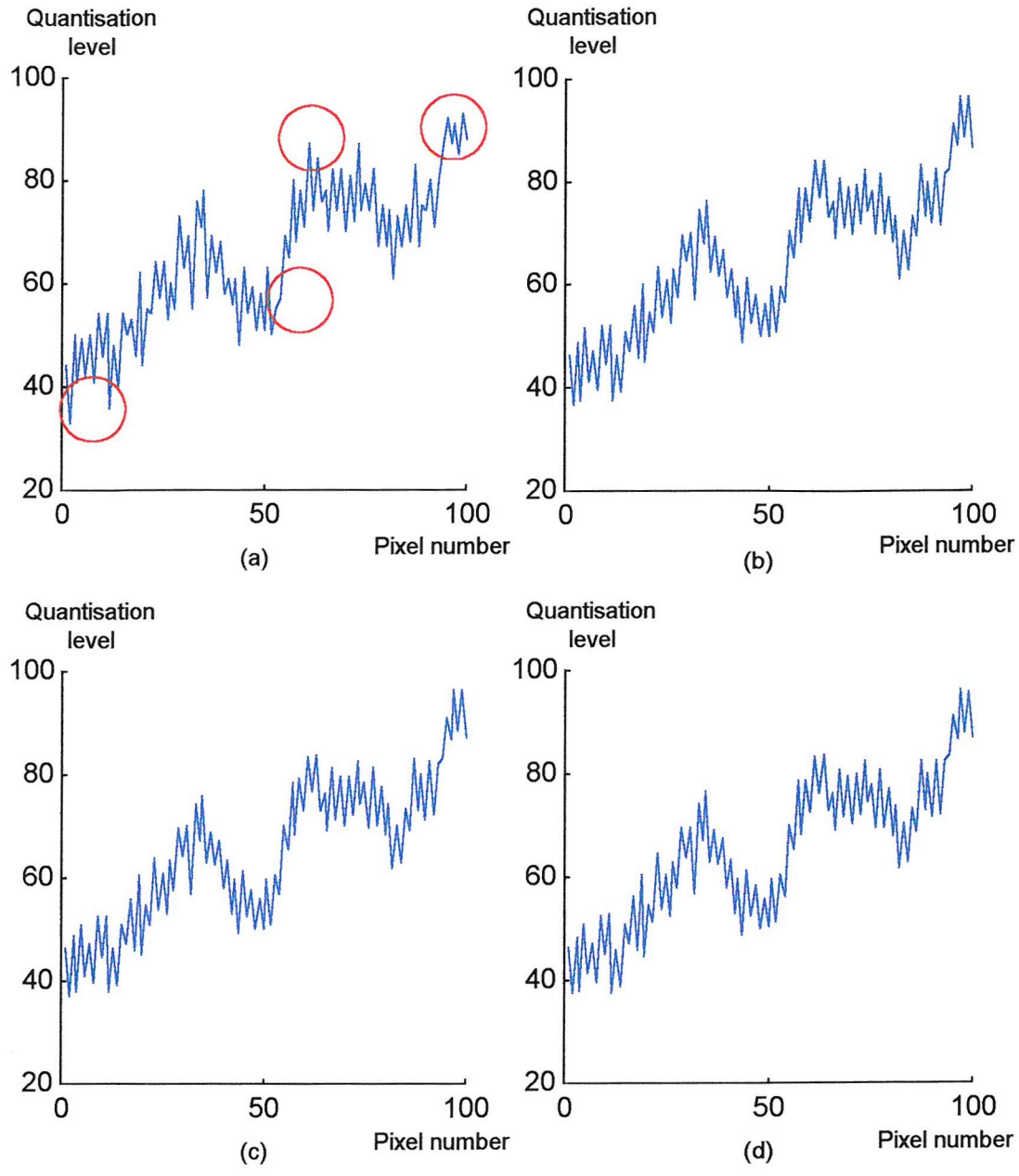

Figure 5.4 Removal of background noise using image average produce with (a) 1 (b) 30 (c) 100 and (d) 500 images

Figure 5.4a shows the data from a cross section of the light intensity distribution for a single image containing time-varying noise, that is

$$I_{(x,y)} = I_{o(x,y)} + I_{n(x,y)} \tag{5.13}$$

By averaging the captured images over a period of time a resultant image is derived such that

$$I_{lc(x,y)} = 1/N \sum_{i=1}^{N} \left(I_{o(x,y,i)} + I_{n(x,y,i)} \right) \tag{5.14}$$

where N is the total number of images used to generate the averaging image. As the value of N is increased the time-varying noise component is reduced and the resultant image, $I_{lc(x,y)}$ is approximately equal to $I_{o(x,y)}$. Figure 5.4b, c and d show the resultant average data from a cross section using this approach for 30, 100 and 500 frames respectively. Comparing Figure 5.4a to 5.4d reveals that the background noise is equivalent to 5 digitised levels. It can be seen that the filtered images are very similar and therefore only using 30 images is sufficient to reduce the noise to an acceptable level. Obviously, this technique is only useful for the measurement of a static phase retardation distribution. For static charge measurements this technique can be employed and if applied along with the method of images gives a difference of the modulated light intensity distribution of

$$\Delta I_{D(x,y)} = 2/N \sum_{i=1}^{N/2} I_{M+(x,y,2i-1)} - I_{M-(x,y2i)} \tag{5.15}$$

The corresponding light intensity distribution due to natural birefringence distribution and the constant offset component is therefore

$$I_{a(x,y)} = 1/N \sum_{i=1}^{N} I_{o(x,y)} \sin^2 \left(\Phi_{nat(x,y)} \right) + I_{offset(x,y)} \tag{5.16}$$

and the difference between the modulated light intensity due to the modulated phase is

$$\Delta I_{(x,y)} = 2/N \sum_{i=1}^{N/2} I_{+(x,y,2i-1)} - I_{-(x,y2i)} \tag{5.17}$$

5.5 The Equivalent System

The equivalent system model including the OPM is shown in Figure 5.5. With reference to the diagram the Pockels cell transforms the surface charge distribution an optical retardation distribution (Equation 3.7). The phase retardation includes the natural birefringence distribution and therefore the total phase retardation distribution is as described in Equation 5.1. The applied positive and negative modulating voltage on the OPM gives two modulated light intensity distributions. The total phase retardation distribution is related by a sinusoidal relationship to the difference modulated image, $\Delta I_{D(x,y)}$ as in Equation 5.4. The equivalent maximum light intensity distribution is used to determine both the phase retardation distribution and the natural birefringence distribution. With the detection of the difference image, $\Delta I_{D(x,y)}$ time-varying noise is introduced that can be minimised using the image average technique (Equation 5.15).

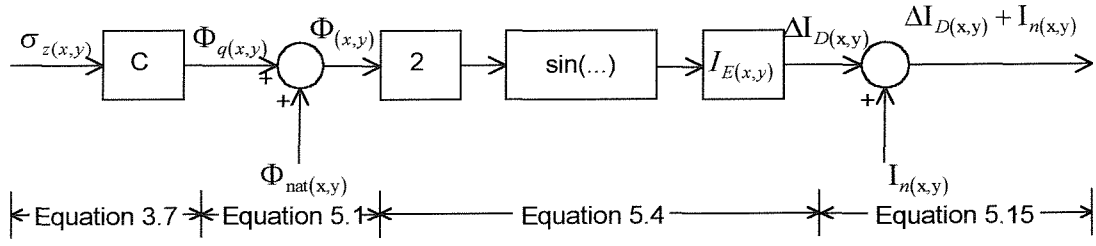

Figure 5.5 Equivalent Model

5.6 The Equivalent Maximum Light Intensity Distribution, $I_{E(x,y)}$

With reference to Equation 5.4 the signal level, $\Delta I_{D(x,y)}$ of the post processed measurement is proportional to the equivalent maximum light intensity distribution, $I_{E(x,y)}$. Hence, to improve measurement sensitivity, the magnitude of $I_{E(x,y)}$ must be maximised for a given surface charge on the Pockels cell. The signal, $I_{E(x,y)}$ can be increased in two ways either by increasing the maximum light intensity distribution

through increased laser optical power or by the increasing the modulated optical retardation, Φ_M by applying a higher modulating voltage across the OPM (Figure 5.6). The optimum modulated optical retardation for the system is e $\pm\pi/4$.

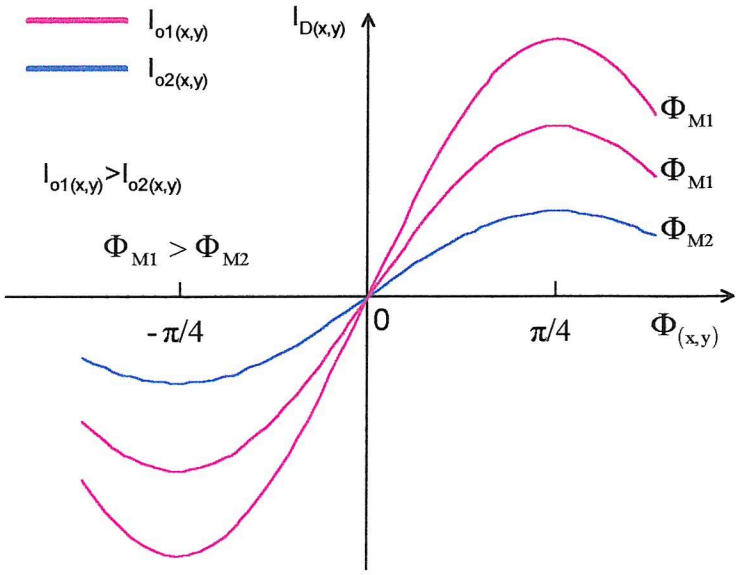

Figure 5.6 Improving the measurement sensitivity

It should be noted that the use of the OPM allows the magnitude and polarity of any surface charge to be determined simultaneously. Polarity is determined automatically through the use of the difference images. The negative values returned for a pixel indicate negative charge at that point because the modulation method has reduced light intensity for V_M and increased light intensity for $-V_M$.

5.6.1 Measurement Limits

Analysis of the equivalent system shows that the phase retardation is doubled and the maximum measurable surface charge is when $\sin 2\Phi = 1$, $\Phi = \pi/4$. If the surface charge density exceeds this limit, the light intensity will decrease for increasing values of charge density causing significant measurement errors. The thickness of the BSO crystal is 160μm and therefore the corresponding maximum surface charge density for a retardation of 45° is $3nCmm^{-2}$.

5.7 Comparison of Light Signal Between the OPM and 1/8 Waveplate

Previous published results [80] have shown that typical surface charges are of the order of $0.6nCmm^{-2}$. Therefore for a 160μm thick BSO cell the equivalent phase retardation will be approximately 10°. With reference to the analytical models, the light intensity change due to the phase retardation on the thin BSO cell would be very small if the 1/8 wave-plate were to be used (Figure 5.7).

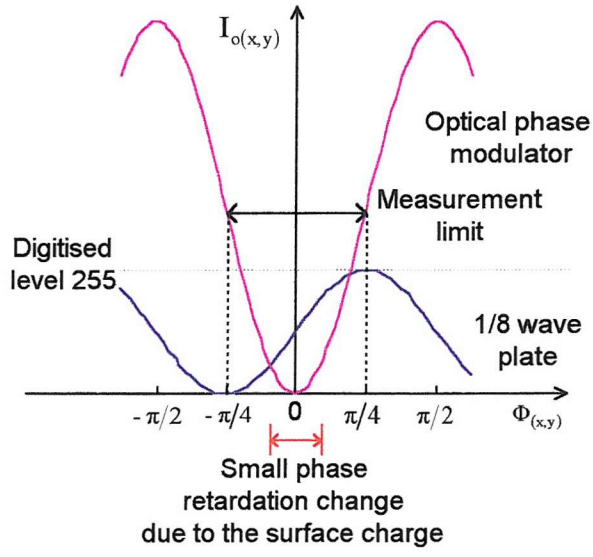

Figure 5.7 Comparison of measured light intensity between 1/8 wave-plate and OPM

The OPM performs better than the 1/8 wave-plate. With a low power laser the light intensity change due to the surface charge recorded by the CCD camera will be small and the full range of the CCD camera greyscale may not be utilised To increase the light intensity change due to the surface charge on the sample the optical power of the input laser can be increased. Care must be taken to ensure that the power of the input laser is not too high because this will cause the measurement to become saturated, limiting the maximum detectable charge. The change of the light intensity due to the surface charge plus the effect of the OPM must be kept below a grey scale value of 255 for a phase retardation of 45°. This also has the advantage of maximising the signal to noise ratio.

5.8 The Measurement Procedure

A series of measurements were undertaken to verify the proposed technique. The Pockels cell used had an effective area of 25mm by 25mm and was 160μm thick. The BSO crystal was glued to a BK7 glass substrate. A thin Chrome film approximately 5nm thick was coated onto the glass substrate to serve as a transparent electrode and grounded to ensure that there was a uniform electric field across the crystal due to any surface charge deposited on the BSO cell backface. A needle electrode was arranged to be 100μm above the surface of the BSO. The needle electrode was not allowed to exert any pressure on the BSO surface as it would then generate mechanical stress and distort the measurement results.

5.8.1 Impulse Generator

To employ the image averaging technique to the measurement data the surface charge deposited on the BSO crystal must remain static over the test period. By applying a high voltage impulse via the needle electrode surface charge will be rapidly deposited and remain on the backface of the cell. The surface charge completely decays over a period of two or three seconds if the front face of the cell is grounded. Averaging of thirty frames (corresponding to 30ms) just after the charge was deposited was used to produce the average image. A circuit was built as shown in Figure 5.8.a to generate a positive or negative high voltage impulse at the needle electrode.

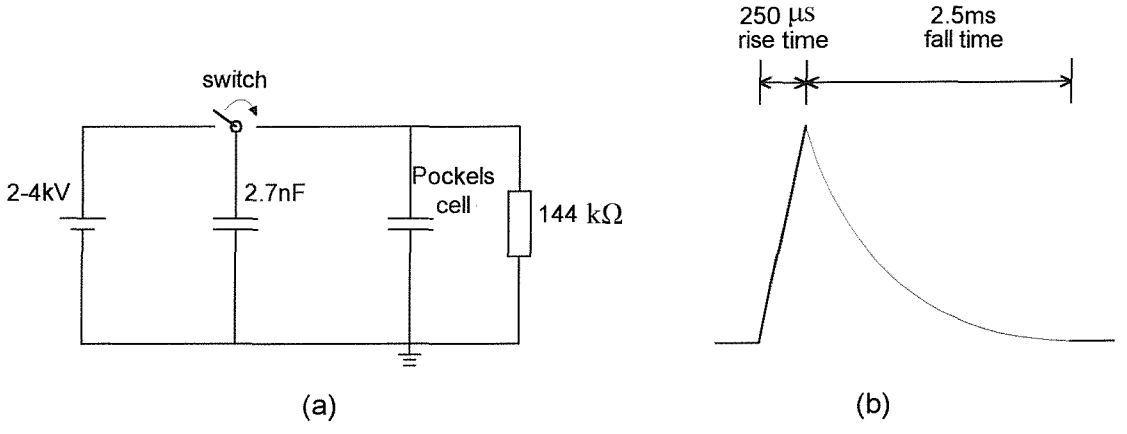

Figure 5.8 (a) Impulse generator and (b) waveform

A DC source was used to charge the 2.7nF capacitor. Once the capacitor was fully charged it was discharged via the needle electrode. The rise time of the discharge pulse is of the order of 250μs and the fall time can be controlled by suitable choice of a load resistor placed across the Pockels cell. In order to obtain a 2-4kV peak voltage with a fall time of 2.5ms a resistance of 144kΩ was required [82].

5.8.2 Synchronisation Control

The order of events is controlled by the Synchronisation Control Circuit (SCC) which is based on the micro-controller PIC16F84. The SCC receives signals from the CCD camera and controls the operation of the modulating voltage on the OPM, the camera shutter and the high voltage amplifier. With measurement of surface charge deposited by a high voltage impulse, synchronisation is not the main concern as the deposited charge is static over the measurement period. Initially, thirty images are recorded prior to the OPM modulating voltage being applied. These images are used to generate the average initial light intensity image, $I_{a(x,y)}$ due to the natural birefringence distribution and the constant offset light component using the image averaging technique. The modulating voltage is then applied across the OPM with a frequency of 500Hz and fifteen positive modulated images and fifteen negative modulated images are recorded to produce the difference image, $\Delta I_{(x,y)}$ (Figure 5.9). The difference image together with the initial light intensity image are used to calculate the natural birefringence distribution, $\Phi_{nat(x,y)}$ and equivalent maximum light intensity distribution, $\Delta I_{E(x,y)}$.

The microcontroller generates a 500Hz square wave to control the voltage applied to the OPM. This square wave is 90° out of phase with the synchronisation pulse from the camera. The OPM driver signal is generated immediately after the first SYNC OUT pulse following the control signal pulse (Figure 5.9b). The OPM voltage is first set positive and is amplified so that the OPM see a ±500V square wave. Delaying the start of the OPM square wave by 0.5ms after the synchronisation pulse from the camera ensures that the OPM has a maximum voltage across it. The camera exposure time is limited to ensure that the image is captured over the interval when the OPM voltage is constant. After several cycles of modulating voltage have been applied to

the OPM, the SCC sends a pulse to trigger the camera start in order to record images into the camera memory (Figure 5.9d). Fifteen positively and fifteen negatively modulated light intensity distribution images are recorded after which the SCC triggers the impulse generator (Figure 5.9e,f). The surface discharge due to the HV impulse voltage is deposited within 3-4ms. The images recorded during the development of the surface charge are not used to determine the phase retardation distribution. Only the images after the impulse voltage has returned to zero are used to calculate the surface charge density. Again, fifteen positively and fifteen negatively modulated images are recorded to produce the difference image, $\Delta I_{D(x,y)}$ using the image averaging technique. The surface charge recorded in these thirty images is assumed to be static over the recording period of 30ms.

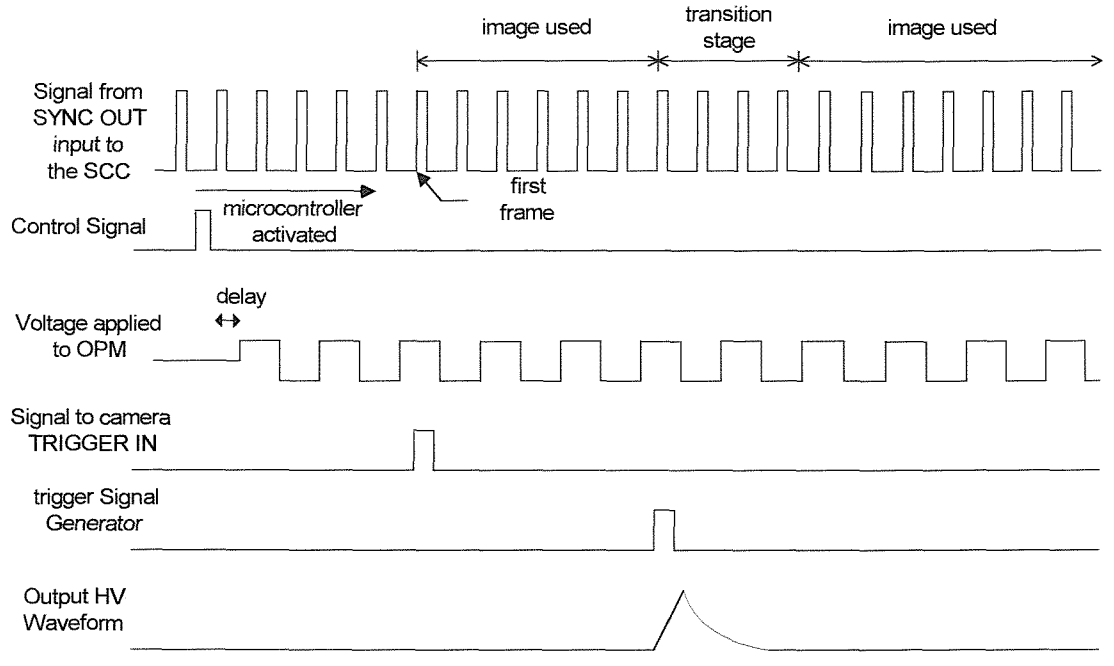

Figure 5.9 Synchronisation control signal for measurement of surface charge due to a high voltage impulse

5.9 Validation of Measurement

After captured images have been transferred from the CCD camera to the computer, image processing generates a two-dimensional surface charge profile. Due to the complexity of the array operation, pre-defined criteria are used to check the validation

of the measurement. Errors can be introduced either optically or by the CCD camera causing light noise levels. A measurement is valid if the following criteria are satisfied. From Equation 5.10

$$I_{+(x,y)} + I_{-(x,y)} - 2I_{a(x,y)} > 0 \tag{5.18}$$

and from Equation 5.4 and Equation 5.8

$$\Delta I_{E(x,y)} \geq \left|\Delta I_{D(x,y)}\right| \tag{5.19}$$

$$\Delta I_{E(x,y)} \geq \left|\Delta I_{(x,y)}\right| \tag{5.20}$$

5.10 Image Processing

The initial light intensity distribution due to the natural birefringence distribution and the constant offset light component along with the light intensity distributions for positively and negative optical retardation by the OPM are shown in Figure 5.10a, b and c respectively. Using Equation 5.8 and Equation 5.10 these three images produce the two images shown in Figure 5.10d and e. The image in the Figure 5.10d is produced using Equation 5.10 and is tested using Equation 5.18. If Equation 5.18 is not satisfied then a zero is returned and no further processing is carried out at this point. Using the images shown in Figure 5.10d and e and Equation 5.11 produce the image that is the equivalent maximum light intensity distribution $\Delta I_{E(x,y)}$ (Figure 5.10f). The natural birefringence distribution $\Phi_{nat(x,y)}$ can be calculated using the images in Figure 5.10e and f and Equation 5.9 (Figure 5.10g).

The light intensity distributions after the impulse discharge for positively and negatively optical retardation by the OPM are shown in Figure 5.10h and i respectively. These two images are used to generate the difference image, $\Delta I_{D(x,y)}$ as shown in Figure 5.10j. By using the equivalent maximum light intensity distribution (Figure 5.9f) the total phase retardation distribution can be determined and this must

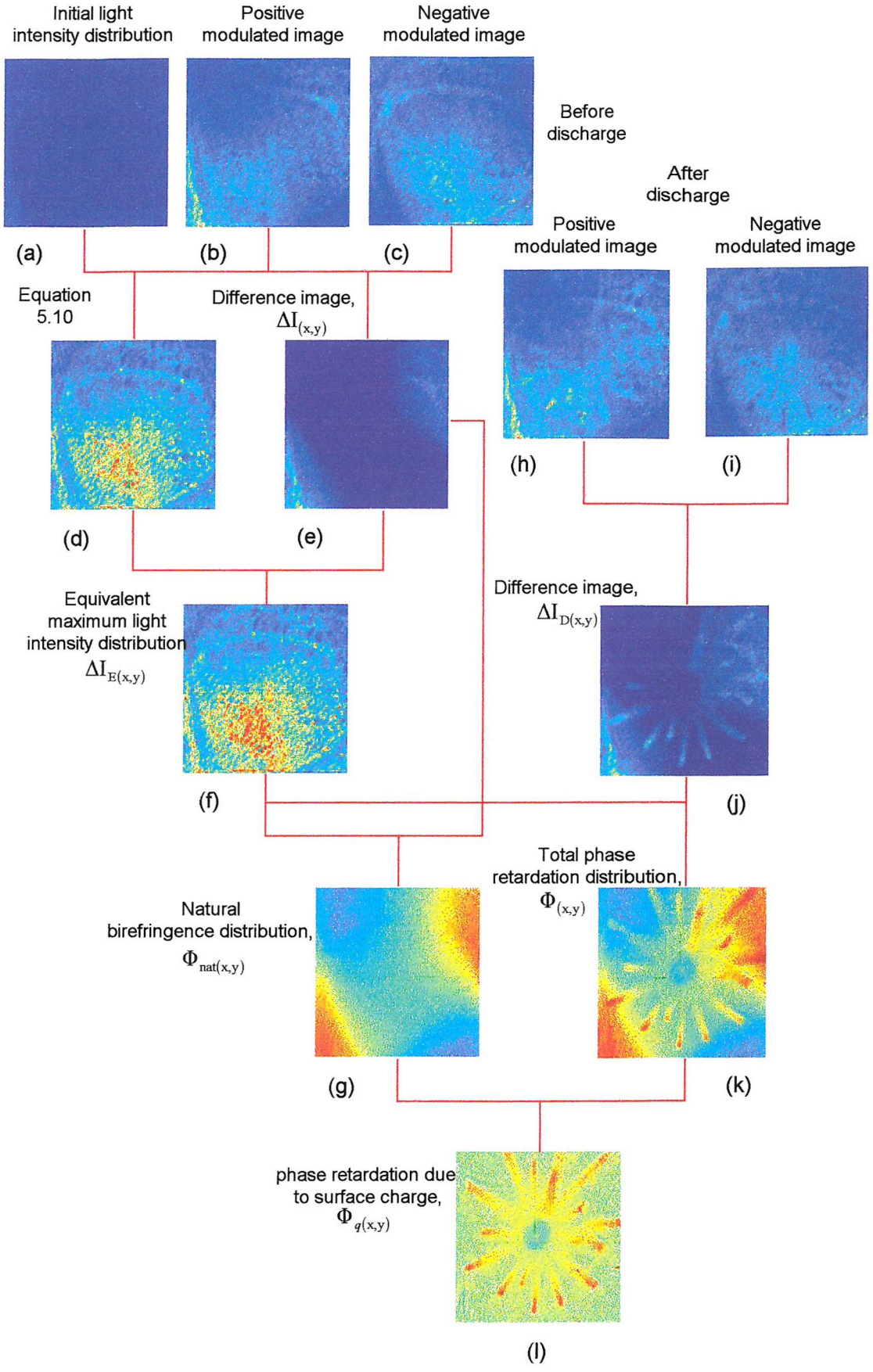

Figure 5.10 Image processing for a HV impulse discharge

satisfy Equation (5.19) (Figure 5.10k). The phase retardation distribution due to any surface charge can be calculated by subtracting the natural birefringence distribution from the total phase retardation distribution using Equation 5.12 (Figure 5.10l). It is then straightforward to convert this image into a image of surface charge using Equation 3.7

5.11 Experimental Results

Figure 5.11a and b shows the surface charge developed for positive and negative HV impulses applied to the needle electrode. The effective dimensions of the images shown are 8mm by 8mm. The peak value of the positive applied voltage was 2kV whereas the peak negative voltage was 3.5kV. Under normal atmospheric conditions and at room temperature, positive surface charge is propagated by streamers and negative surface charge expands radially under the applied field. For the same magnitude of applied field but with opposite polarity, the positive charge streamer has a longer radius than the radially distributed negative surface charge. Hence, for this experiment higher negative voltages were applied to maximise the negative discharge area.

5.11.1 Positive Impulse Discharge

A positive 2kV peak impulse voltage having rise time of 250μs and fall time of 2.5ms was applied to the needle electrode. Figure 5.11a shows the surface charge distribution obtained. The positive surface charge distribution is concentrated in streamers that move radially away from the needle electrode. The streamer channels have a uniform surface charge density distribution of 0.6 $nCmm^{-2}$ and a radius of approximately 6mm. Some negative surface charge is observed towards the centre of the crystal. The reason for this negative surface charge is due to the negative backdischarge as the applied field decreases towards zero potential. Negative backdischarge has also been observed during the measurement of AC surface discharges as the applied field decreases from the maximum to zero and it acts to neutralise the positive streamer channels near the needle tip.

5.11.2 Negative Impulse Discharge

A negative 3.5kV impulse voltage with a 250μs rise time and 2.5ms fall time was applied to the needle electrode in order to deposit negative surface charge (Figure 5.11b). The surface charge distribution due to a negative impulse voltage is very different to images obtained for positive impulse. The negative surface charge has higher density near the needle tip and reduces its magnitude symmetrically in all direction from this point. The positive surface charge observed in Figure 5.11b is due to positive backdischarge. The backdischarge occurs when the applied field approaches zero potential. Due to the negative surface charge near the needle tip the positive streamer channels do not propagate radially. The positive streamer channels are distorted and neutralise the negative charge near to the needle tip.

5.12 Conclusion

The implementation of an Optical Phase Modulator along with associated signal processing significantly improves the resolution and accuracy of the measurment system. Noise levels have also been reduced. A series of experiments have been undertaken to investigate static charge formed on the back surface of the BSO cell using positive and negative high voltage impulses. Obtained results have demonstrated that positive and negative charge behave very differently. Further results are presented in the next chapter.

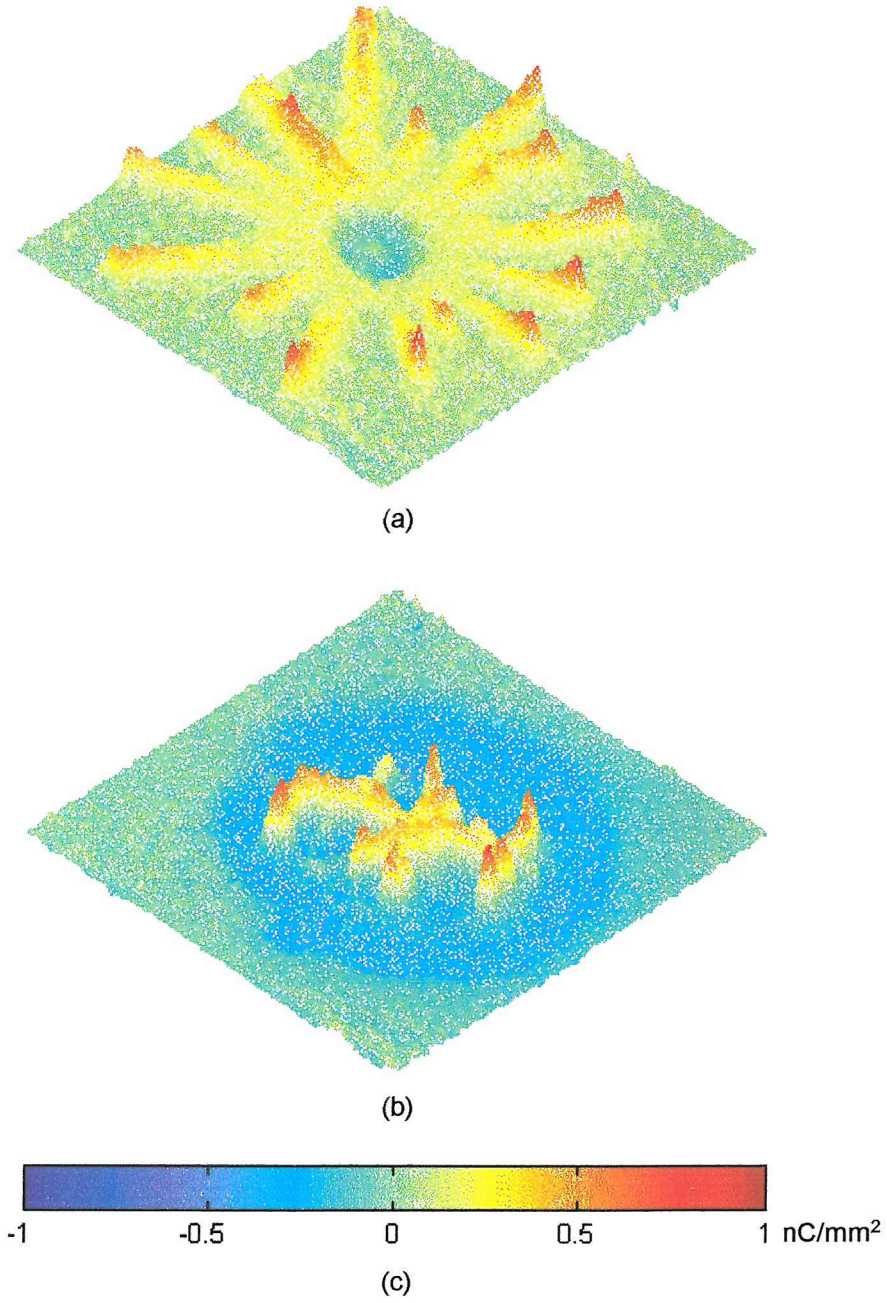

Figure 5.11 Surface discharge response to (a) positive 2kV, (b) negative 3.6kV and (c) surface charge density key (effective dimensions of both images are 8mm by 8mm)

Chapter 6

AC Surface Discharge Measurement

6.1 Introduction

There is considerable interest in AC surface discharge phenomena both in the selection of suitable insulation materials for high voltage equipment and in obtaining greater understanding of breakdown behaviour. This research has concentrated on developing a system that can measure dynamic surface charge at power frequencies. A similar approach to that used for static measurements is employed. However, image averaging to remove noise cannot be utilised in the measurement of AC surface discharge. Averaging can only be partially used to obtain the initial and the modulated light intensity distribution prior to the application of any AC voltage. The image obtained during the AC discharge cannot be averaged, as the surface charge distribution on the backface of the crystal is affected by the applied field.

6.2 The Measurement Procedure

The experimental arrangement is identical to that used for the impulse discharge measurements discussed in Chapter 5 except that the impulse generator is replaced by

a HV AC source. Surface charge can be deposited at a higher stress under AC conditions compared to impulse conditions without saturation of light intensity. An AC 50Hz ±7kV peak voltage of duration 40ms (two complete cycles) was applied to the needle electrode. The control signals of the SCC for the measurement are shown in Figure 6.1.

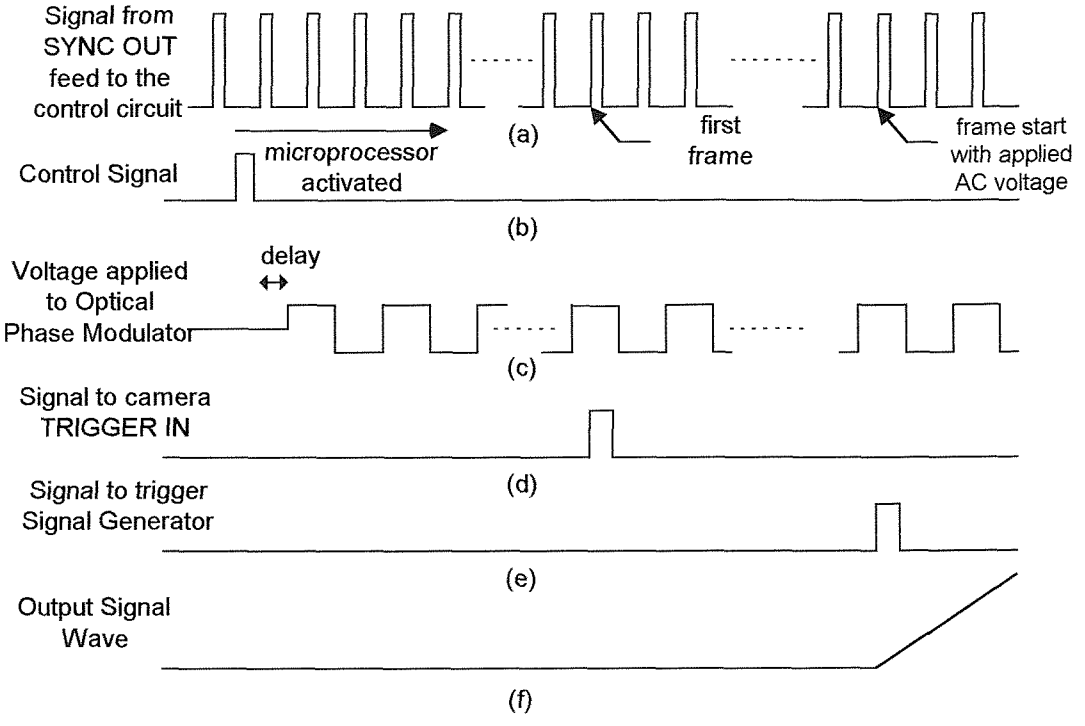

Figure 6.1 Control signals for AC surface discharge measurements

As shown in Figure 6.1 upon triggering the SCC, the camera records the positive and negative phase modulated light intensity distributions prior to applying the AC HV signal. After fifteen positive and fifteen negative phase modulated images have been recorded the SCC triggers the AC signal generator. The signal generator output is amplified by a high voltage amplifier to give ±7kV pk-pk. The period of the AC high voltage is controlled by the pulse width of the input signal to the signal generator. The light intensity distribution due to surface discharge, including alternating positive and negative is recorded over forty images at 1000fps corresponding to two cycles of applied AC voltage.

6.3 Image Processing

The image processing of the AC surface discharge measurement is similar to the impulse discharge measurement except the image averaging technique is only partially employed due to the dynamic development of the AC surface discharge. The initial light intensity distribution due to the natural birefringence distribution and constant offset light component measured under positive and negative phase modulation image are used to determine the natural birefringence distribution $\Phi_{nat(x,y)}$ and equivalent maximum light intensity distribution, $I_{E(x,y)}$. Surface charge is dynamic during the period that the AC voltage is applied and the difference of the modulated light intensity is obtained using the method of images as shown in Figure 6.2.

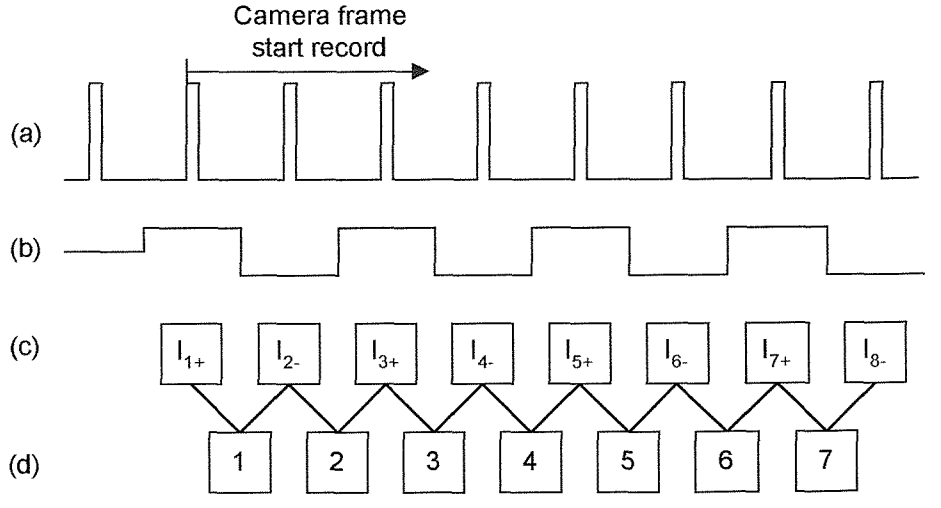

Figure 6.2 The image sequence during an AC discharge

The sequence of phase retardation change, $\Phi_{(x,y,i)}$ as the voltage is applied is obtained using the difference image which is [47]

$$\Phi_{(x,y,i)} = \frac{1}{2}\sin^{-1}\left[\frac{I_{M+(x,y,i)} - I_{M-(x,y,i+1)}}{I_{E(x,y,)}}\right] \qquad (6.1a)$$

for odd numbered images and

$$\Phi_{(x,y,i)} = \frac{1}{2}\sin^{-1}\left[\frac{I_{M+(x,y,i+1)} - I_{M-(x,y,i)}}{I_{E(x,y,)}}\right] \qquad (6.1b)$$

for even numbered images.

A sequence of the time varying surface charge distribution is then calculated by the subtraction of the non-uniform natural birefringence distribution from the total phase retardation distribution. The temporal resolution of the images is 1ms which is the same as the camera frame rate. This is a significant improvement over previous work [47,81] where the temporal resolution was half of the camera frame rate and it was not possible to make measurements at 50Hz.

An example of the resultant image produced from the difference modulated image with an area 8mm by 8mm is shown in Figure 6.3. Figure 6.3a shows the light intensity distribution biased by negative phase modulation and there are four streamer channels observed on the crystal whereas in Figure 6.3b the next image biased by positive phase modulation has eight streamer channels. The surface charge distribution is calculated using these two images (Figure 6.3c). The resultant image is the difference between the two modulated images and it is evident that the extra streamer channels have lower charge density than those observed in Figure 6.3a.

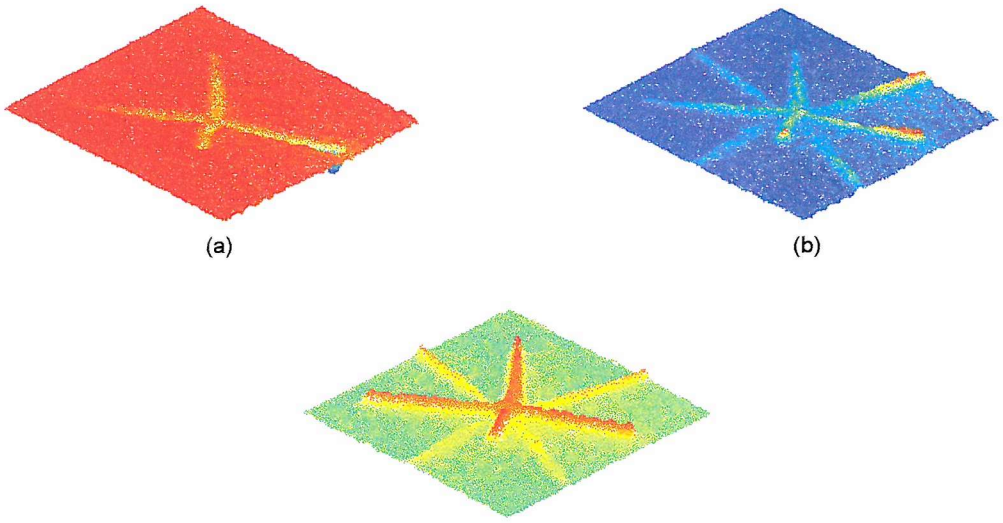

Figure 6.3 (a) Negative modulated image and (b) positive modulated image lead to (c) surface charge density distribution by image processing

6.4 Experimental Results

6.4.1 AC Surface Discharge First Half-cycle Positive

Figure 6.4-6.7 show the development of surface charge due to an AC 50Hz ±7kV pk-pk applied voltage over two cycles where the first half-cycle is positive

(Figure 6.4). The surface charge is first observed as a small spot 1ms after the onset of the applied AC stress. As the field increases from zero potential to its maximum, positive streamers travel radially from the needle electrode. The development of the streamer is within a few nanosecond [4,5,6,14] and it is not possible to observe streamer growth with a temporal resolution of 1ms. The number of streamer channels increases as the applied field increases to 7kV (Figure 6.4, 1-5ms). As the applied field decreases towards zero potential the surface charge appears static (Figure 6.4, 6-8ms). Before reaching zero potential negative backdischarge is observed and negative surface charge appears around the needle electrode (Figure 6.4, 9-10ms). As the negative applied field is increased the negative surface charge expands radially (Figure 6.5, 11-15ms) with a higher intensity at the centre and becomes static when the negative field reaches its peak value. The negative surface charge remains static (Figure 6.5, 16-18ms) as the negative applied stress decreases. Positive backdischarge is observed (Figure 6.5, 19-20ms) and positive streamer channels appear around the needle tip while the applied voltage is still negative. The positive streamer channels develop again in the second positive half cycle (Figure 6.6, 21-25ms), however, the streamer channels are no longer radially distributed due to the presence of negative surface charge. Negative charge is observed on the crystal surface during the second negative half cycle (Figure 6.7) and behaves similarly to the first negative half cycle.

6.4.2 AC Surface Discharge first half cycle negative

Figure 6.8-6.11 show the development of surface charge due to an AC 50Hz ±7kV pk-pk applied voltage over two cycles where the first half-cycle is negative. The negative surface charge is first observed after 1ms. As the applied field increases from the zero potential to its peak negative value, the negative charge expands radially having greatest charge density near needle tip (Figure 6.8, 1-5ms). Positive back discharge is observed as the voltage waveform near zero crossing point (Figure 6.8, 9-10ms). The positive streamer channels developed in the first positive half cycle (Figure 6.9, 11-15ms) are similar to those seen in the second positive half cycle of the previous experiment (Figure 6.6, 21-25ms). Figure 6.10 and Figure 6.11 detail the surface charge behaviour over the second cycle. The obtained results are similar to those obtained during the first cycle except that the outer positive streamer tips are not neutralised by the negative charge.

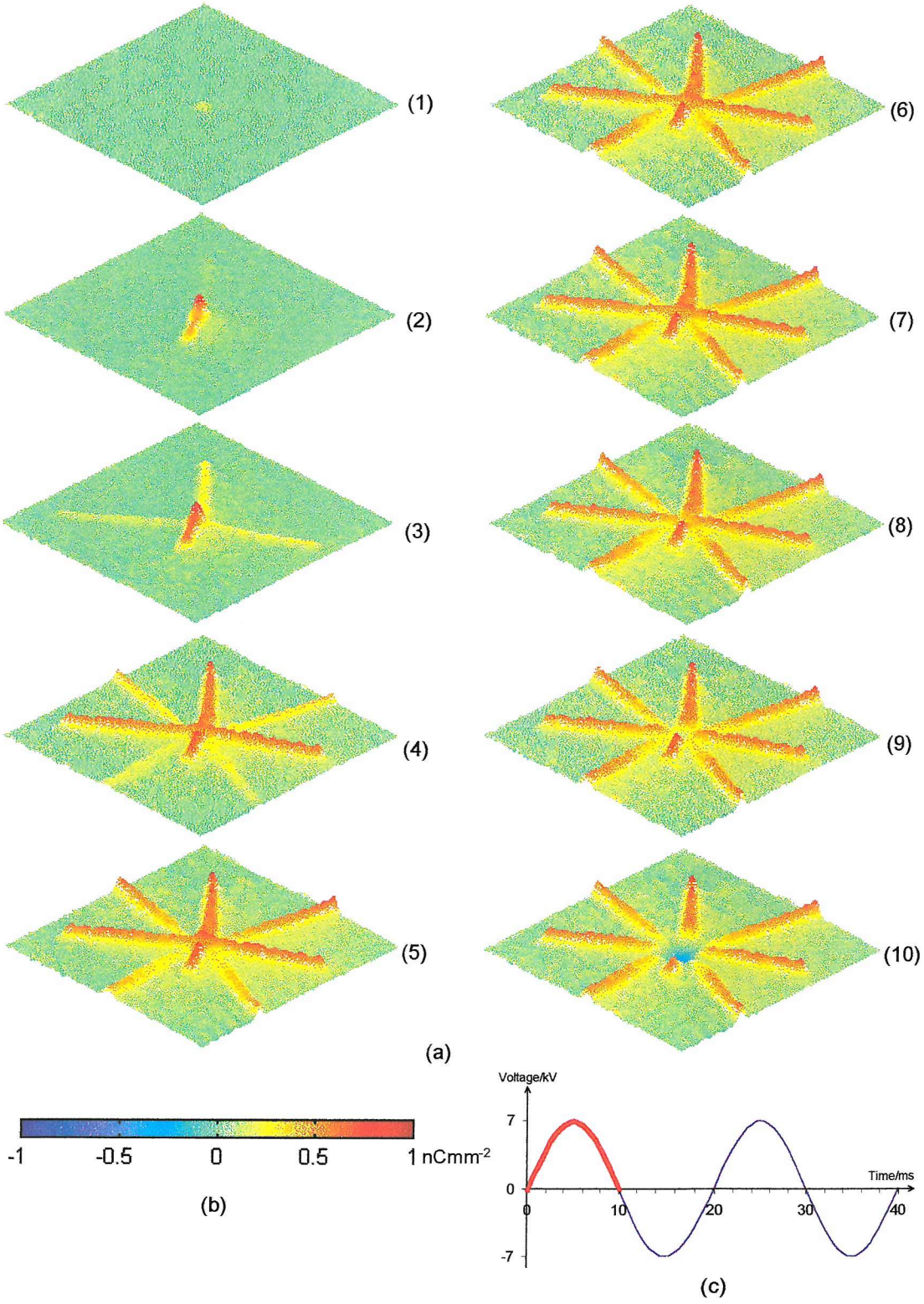

Figure 6.4 Dynamic AC surface discharge (a) time dependence of surface charge distribution (b) surface charge density key (c) waveform of voltage and corresponding frame number (effective dimensions of these images are 8mm by 8mm)

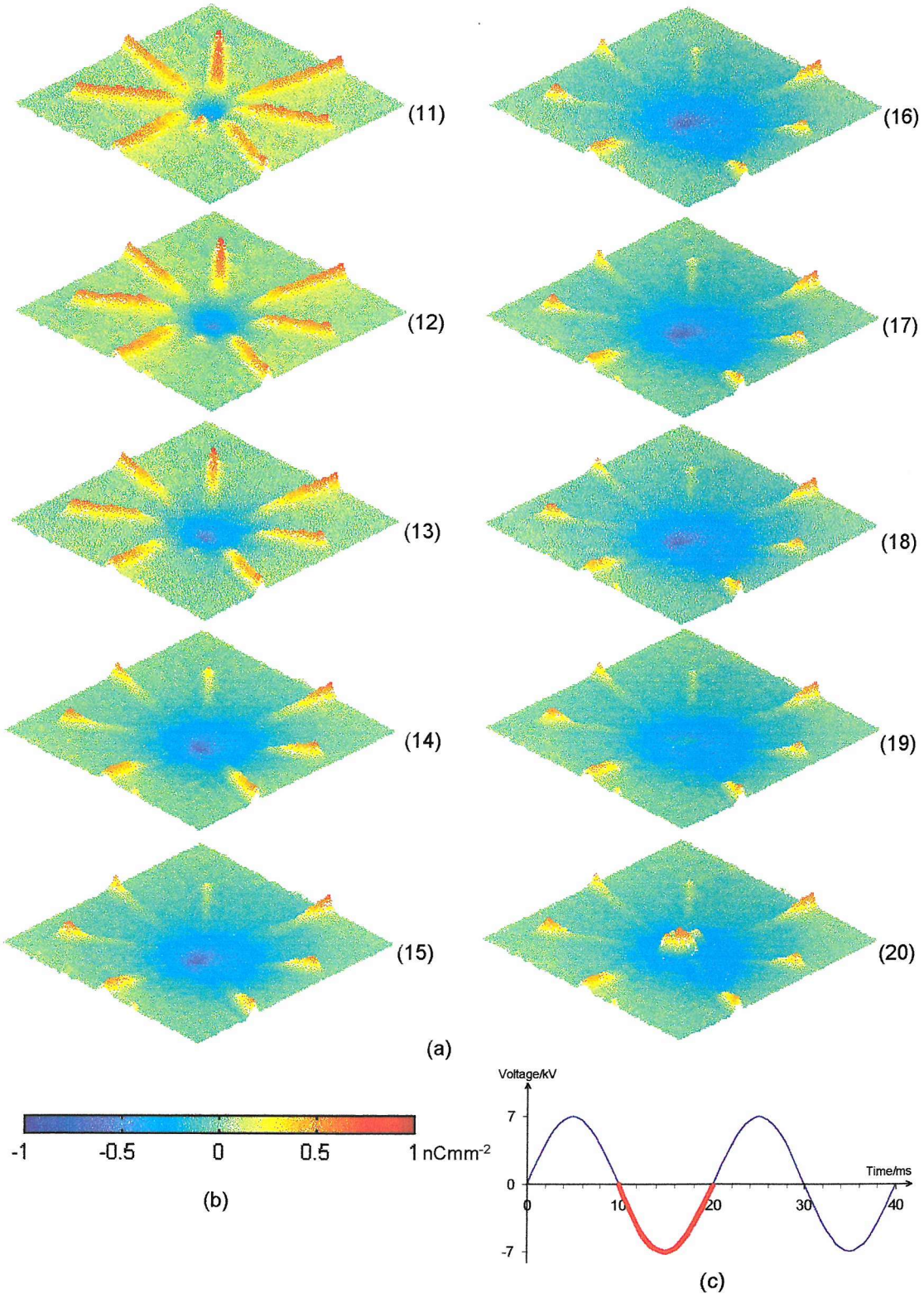

Figure 6.5 Dynamic AC surface discharge (a) time dependence of surface charge distribution (b) surface charge density key (c) waveform of voltage and corresponding frame number (effective dimensions of these images are 8mm by 8mm)

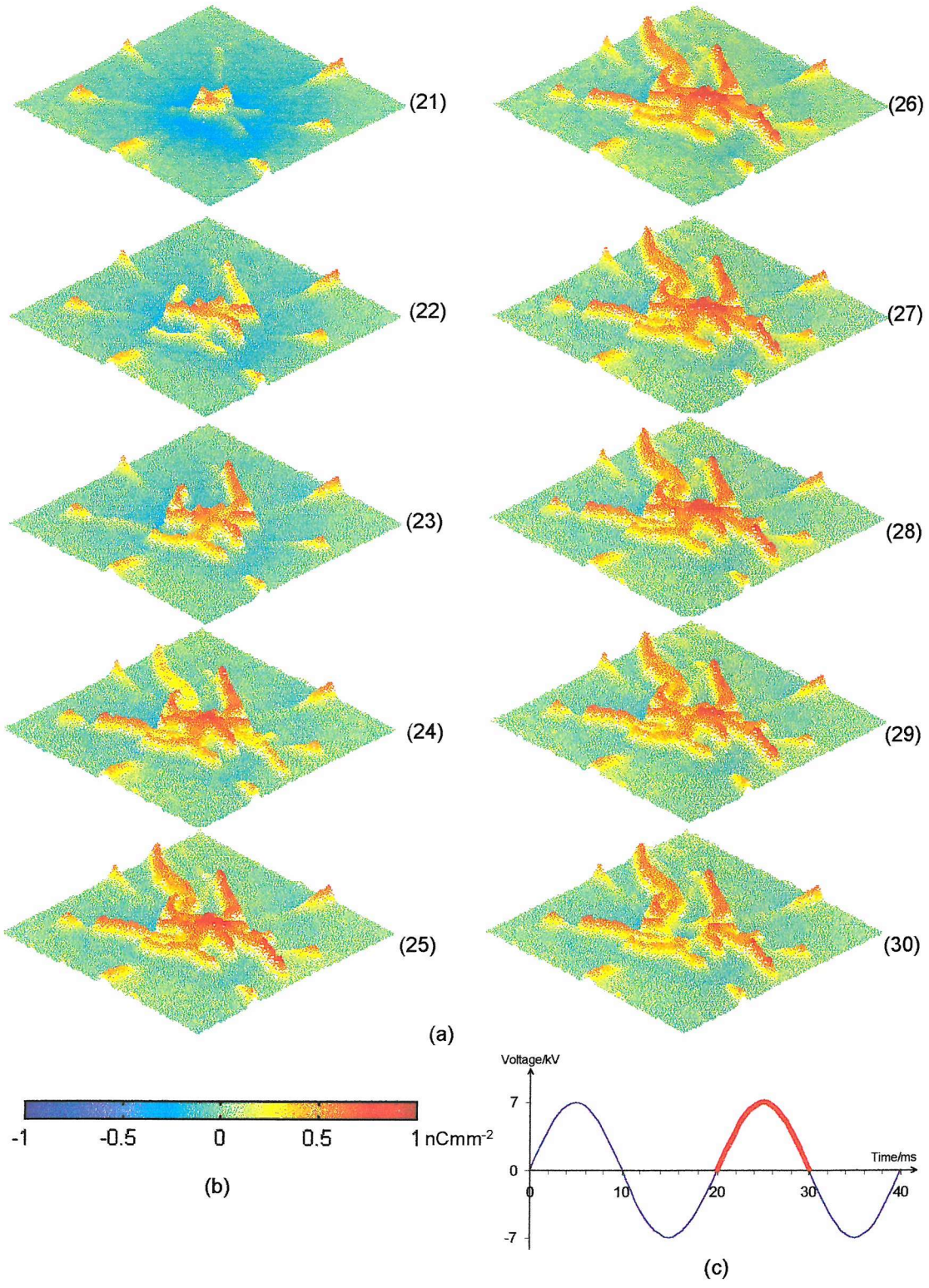

Figure 6.6 Dynamic AC surface discharge (a) time dependence of surface charge distribution (b) surface charge density key (c) waveform of voltage and corresponding frame number (effective dimensions of these images are 8mm by 8mm)

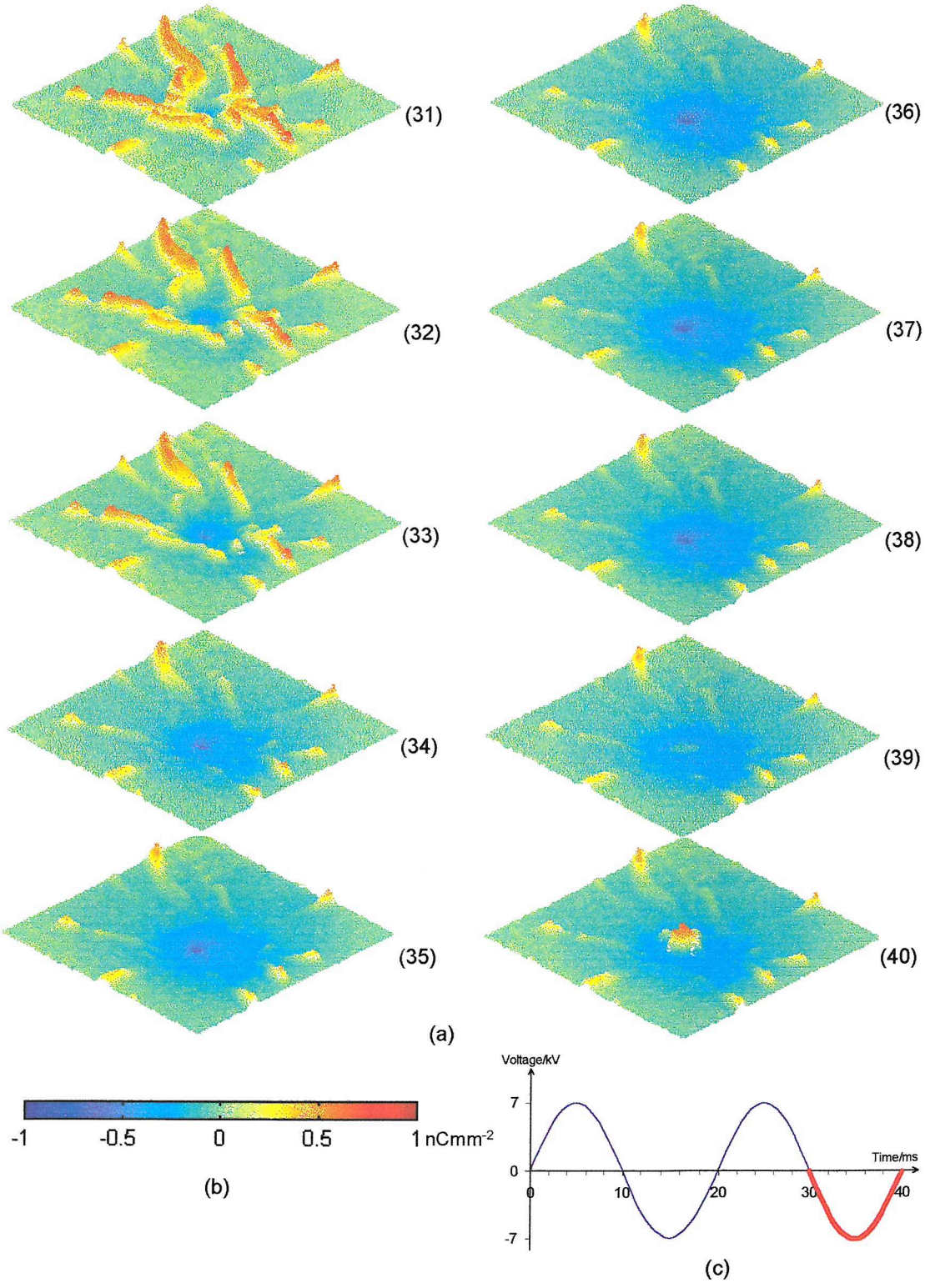

Figure 6.7 Dynamic AC surface discharge (a) time dependence of surface charge distribution (b) surface charge density key (c) waveform of voltage and corresponding frame number (effective dimensions of these images are 8mm by 8mm)

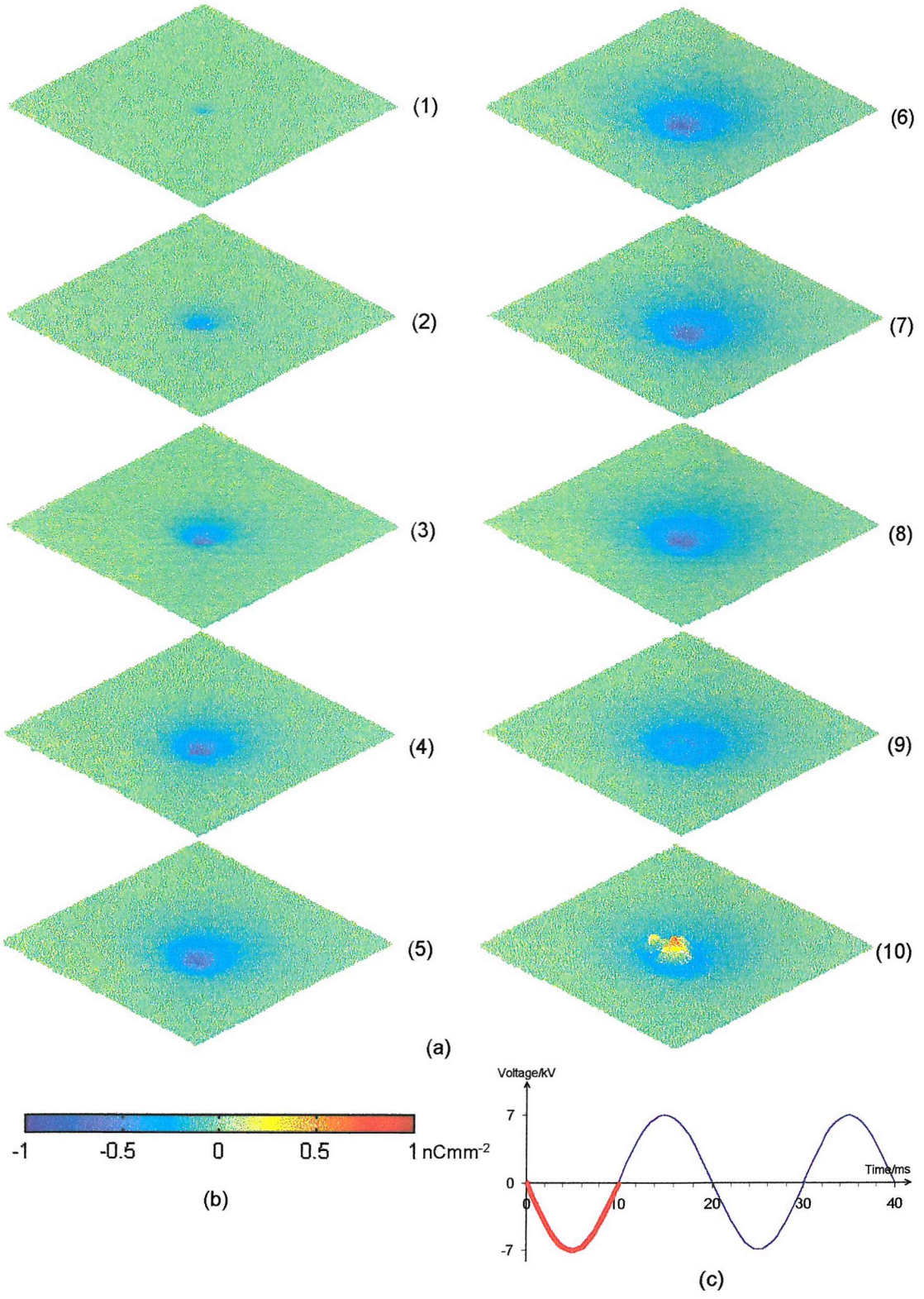

Figure 6.8 Dynamic AC surface discharge (a) time dependence of surface charge distribution (b) surface charge density key (c) waveform of voltage and corresponding frame number (effective dimensions of these images are 8mm by 8mm)

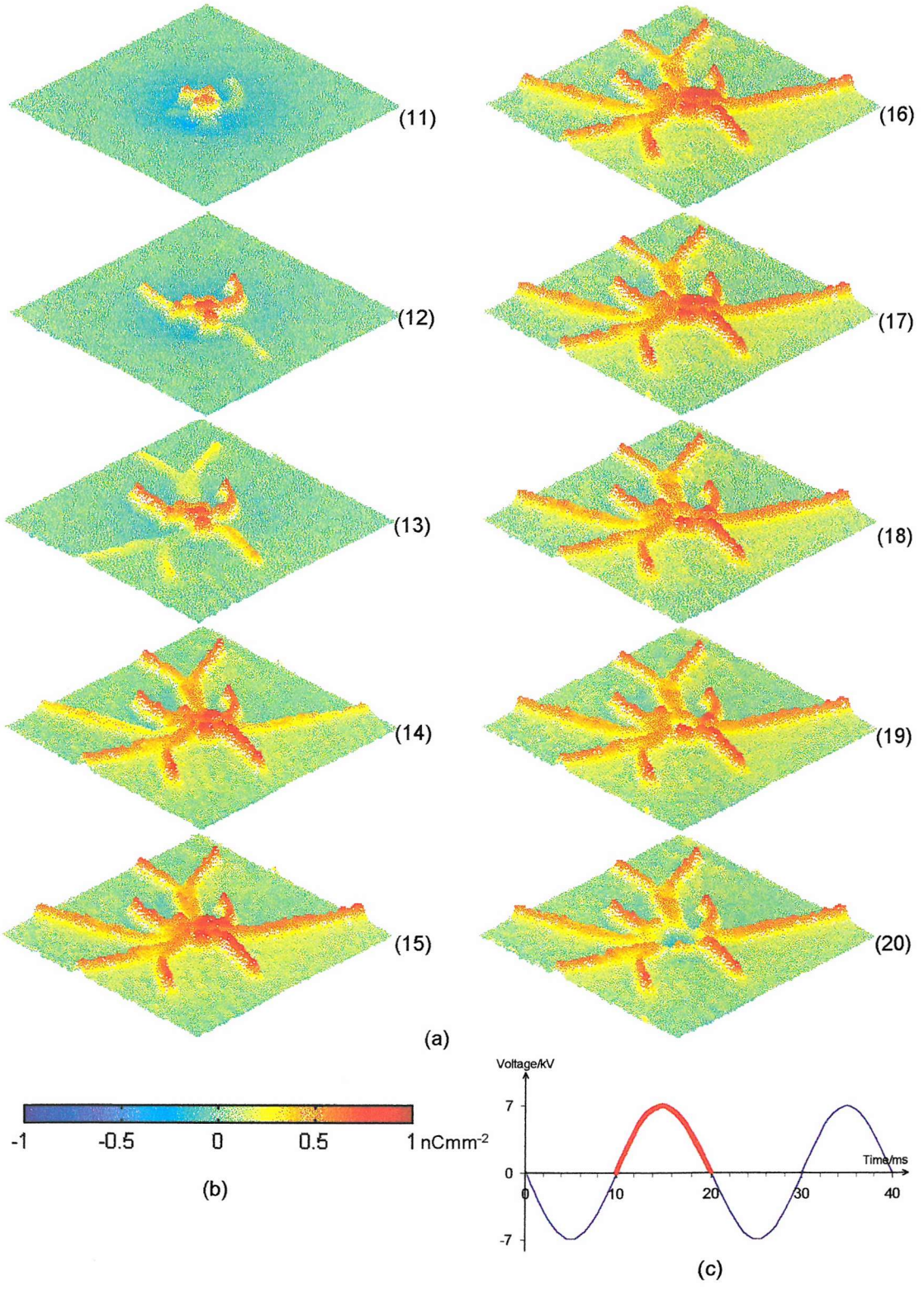

Figure 6.9 Dynamic AC surface discharge (a) time dependence of surface charge distribution (b) surface charge density key (c) waveform of voltage and corresponding frame number (effective dimensions of these images are 8mm by 8mm)

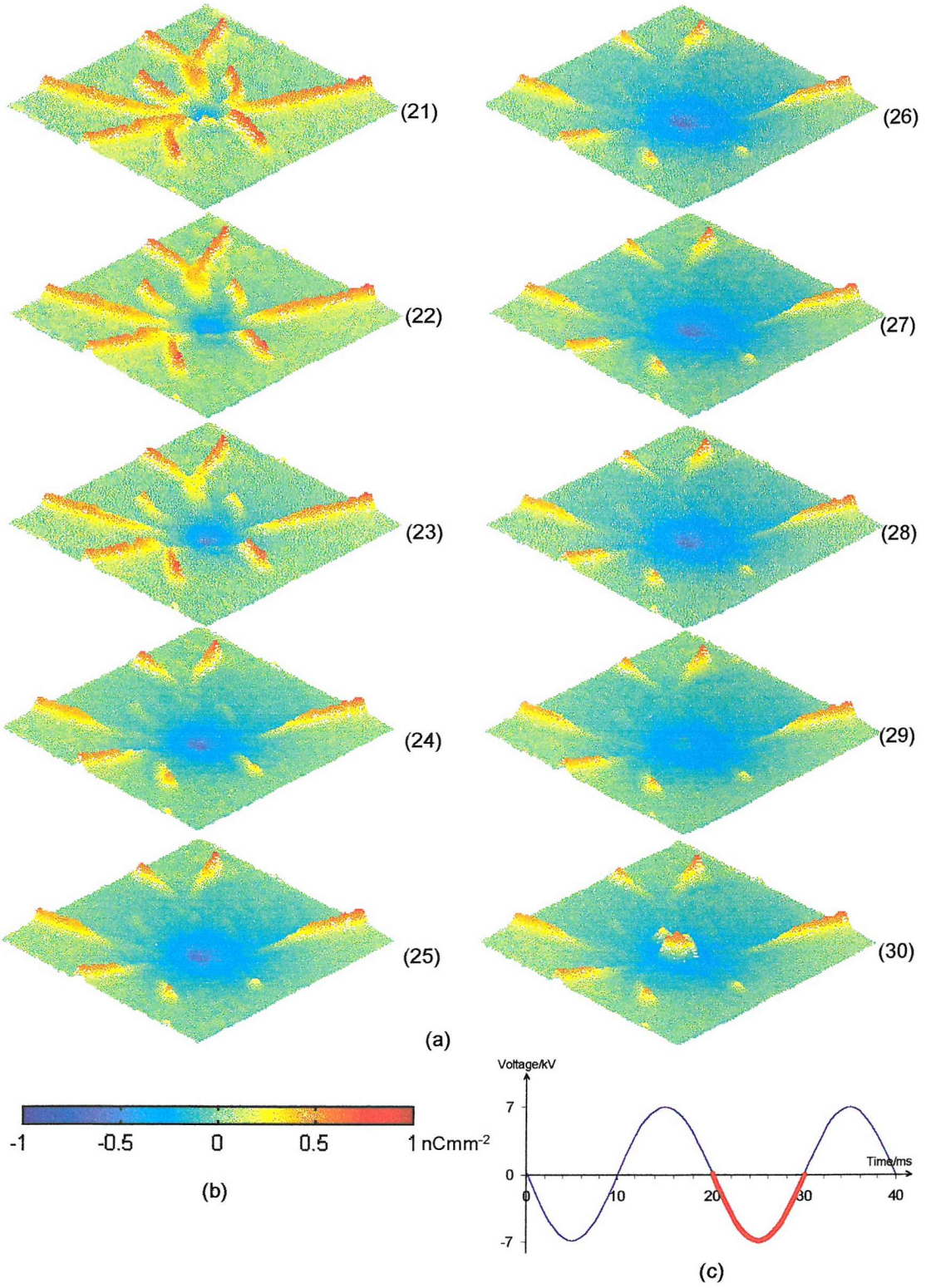

Figure 6.10 Dynamic AC surface discharge (a) time dependence of surface charge distribution (b) surface charge density key (c) waveform of voltage and corresponding frame number (effective dimensions of these images are 8mm by 8mm)

UNIVERSITY OF SURREY LIBRARY

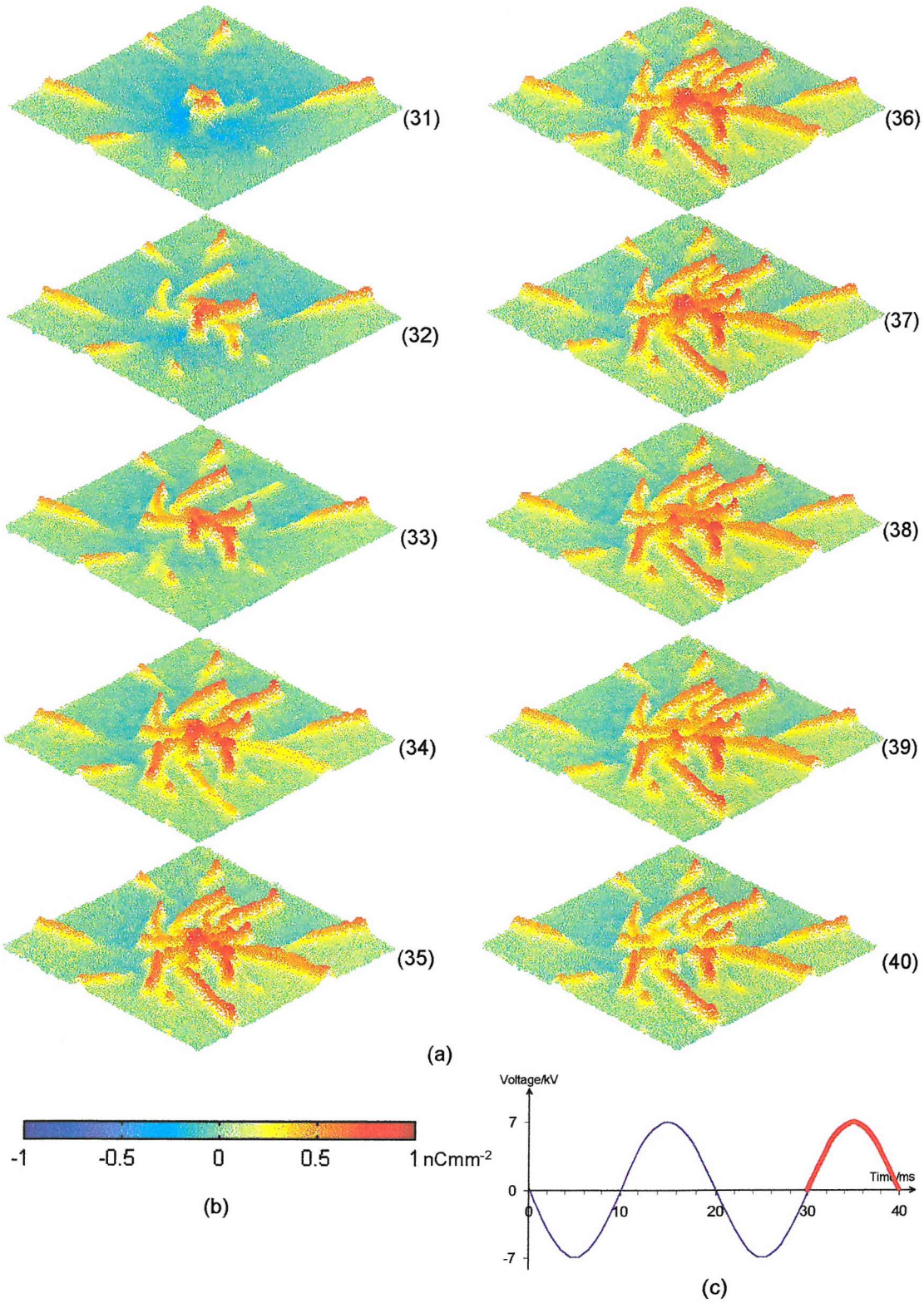

Figure 6.11 Dynamic AC surface discharge (a) time dependence of surface charge distribution (b) surface charge density key (c) waveform of voltage and corresponding frame number (effective dimensions of these images are 8mm by 8mm)

6.5 Discussion of Results

The obtained surface charge distributions are field dependent and the characteristic patterns observed are determined by the initial polarity of the applied voltage. Positive surface charge forms streamer-like channels that travel radially from the needle electrode whereas the negative surface charge appears to have a hemispherical shape with high charge concentration at its centre. The radius of negative surface charge expands as the negative field is increased. The different surface charge distributions for positive and negative fields are due to the mobility of positive ions and negative electrons.

6.5.1 Electron Multiplication

The streamer of a positive charge is a highly conducting, luminous, filamentary, fast propagating discharge. It is effectively a plasma channel that propagates by connecting individual avalanches. The space charge formed by an avalanche mechanism effects the local electric field as shown in Figure 6.12 where 0 represents the starting point.

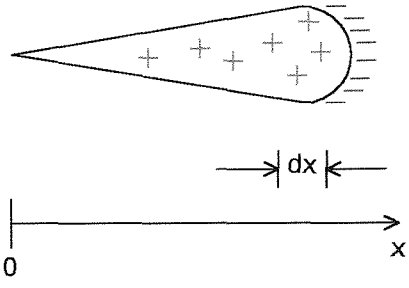

Figure 6.12 Space charge formed by an avalanche mechanism

The number of the ions between 0 and the distance x increases exponentially such that

$$n = n_o e^{(\alpha-\eta)x} \tag{6.3}$$

where n_o is the initial number of the positive ions, α is the ionisation coefficient and η is the attachment coefficient. For surface discharge the ionisation coefficient is the

sum of the surface ionisation coefficient and the ionisation coefficient for surrounding air. The surface attachment coefficient is defined in a similar way, it is the sum of the surface attachment coefficient and the attachment coefficient for surrounding air. Surface discharge is a complicated mechanism which may involve many other processes such as cosmic radiation, photon initiation, ion impact, photon ionisation and electric field modification [1,83].

There are two ionisation process involved in surface discharge, these are electron ionisation and photo ionisation [21]. If an electron acquires enough energy from the applied field and collides with a gas molecule, then the collision will liberate an electron from the neutral molecule, creating one free positive ion and two free electrons (Figure 6.13a). This is the basic process in the development of avalanches and is regarded in the discharge growth model as the ionisation coefficient of air, α_o. Alternatively, high energy electrons may collide with a surface molecule to create two free electrons and one fixed positive surface ion (Figure 6.13b). This process is determined by the surface ionisation coefficient, α_s.

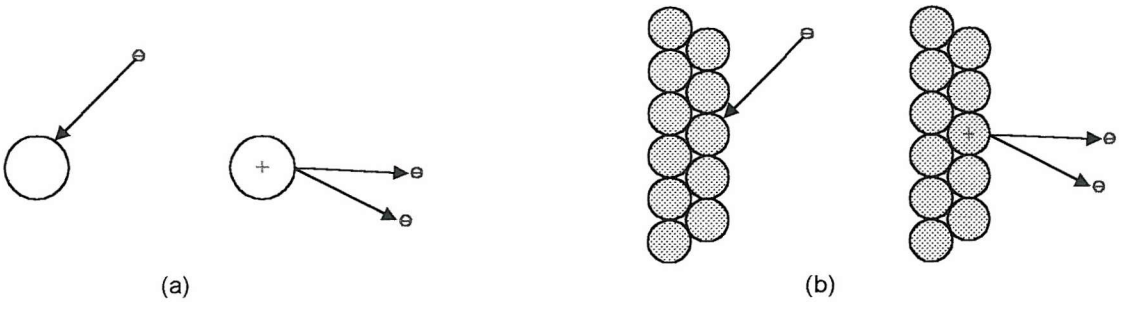

Figure 6.13 (a) electron ionisation of air molecule and (b) electron ionisation of material surface [21]

Ionisation of molecules can also be enhanced by photon ionisation. Excited molecules that have acquired energy from accelerated electrons may return to their ground state by releasing photons. The released photon may remove an electron from a neutral gas molecule and create a new free positive ion (Figure 6.14a). The photon could collide with a surface molecule creating a secondary electron and a fixed positive ion (Figure 6.14b).

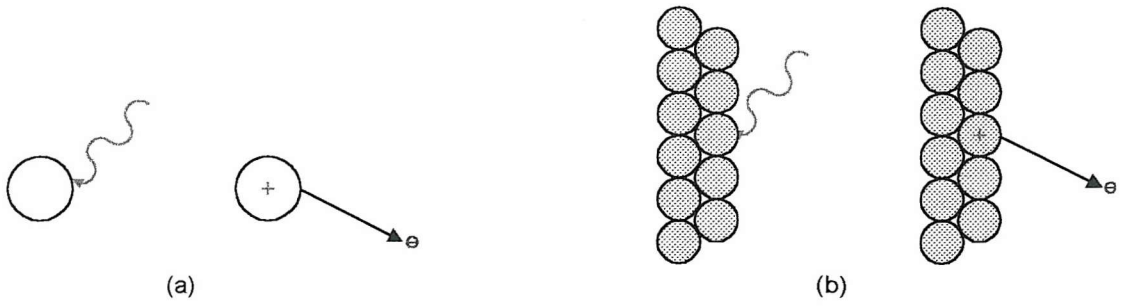

Figure 6.14 (a) photon ionisation of a gas molecule and (b) photon ionisation process at the material surface [21]

Free electrons can also be created by the detachment process, where a negative ion collides with an accelerated electron causing it to give up its electron resulting in a neutral gas molecule and two free electrons (Figure 6.15a). Similarly, if a high energy electron hits a negative surface ion it may cause an extra electron (Figure 6.15b).

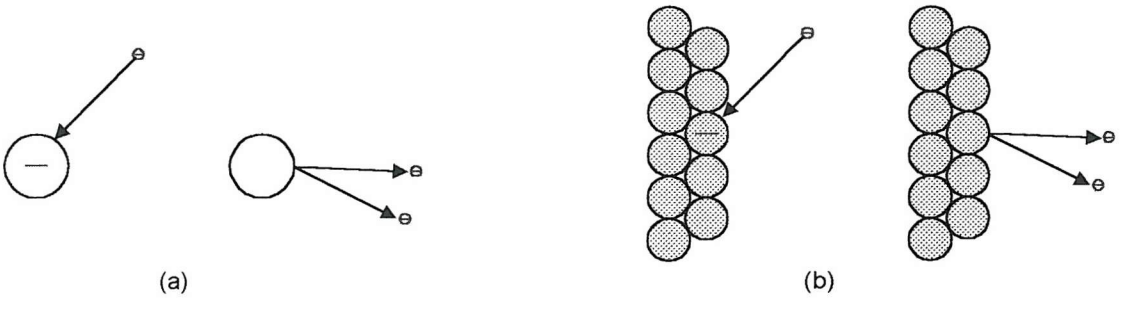

Figure 6.15 (a) electron detachment of ions by collision and (b) electron detachment by collision at the material surface [21]

Photon detachment also causes an extra electron to be liberated from a negative gas ion or a negative surface ion (Figure 6.16). Spontaneous detachment of free electrons from negative gas ions or surface ions is possible although it is rare (Figure 6.17). It is more common that the negative gas ion accelerated by the field collides with a neutral gas molecule that gives up an extra electron.

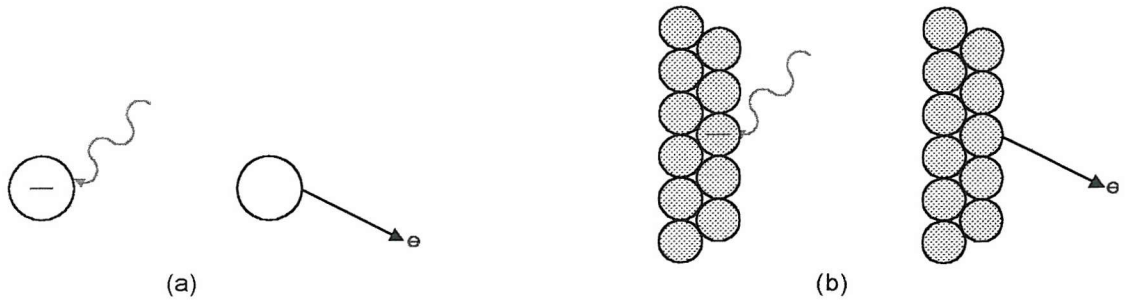

Figure 6.16 (a) photon detachment of ions and (b) photon detachment at the material surface [21]

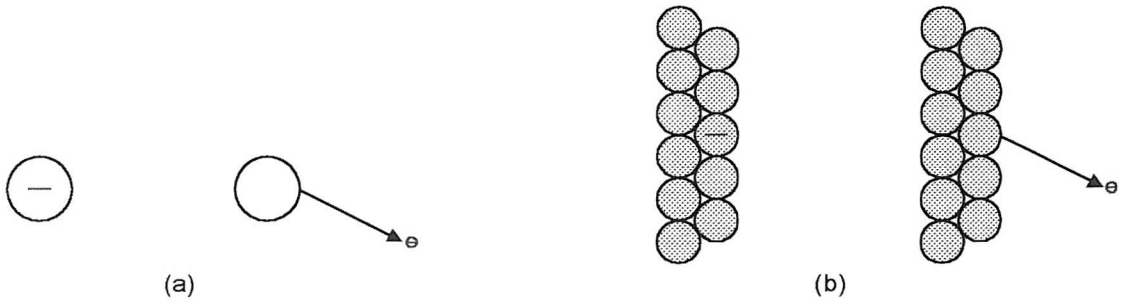

Figure 6.17 (a) spontaneous electron detachment of ions and (b) spontaneous detachment at the material surface [21]

The number of the free electrons involved in the discharge mechanism can be reduced by the attachment process and accounted for in Equation 6.3 by the attachment coefficient. The free electron can be attached to a neutral gas or surface molecule to become a free or fixed negative ion as shown in Figure 6.18. The possible degree of attachment is referred to as the electro-negativity of the gas or material. For example, gas insulated switchgear (GIS) systems are filled with the electro-negative gas SF_6 to increase the breakdown voltage. Normal air is slightly electro-negative due to oxygen combining with water vapour to form $O_2(H_2O)_n$. this complex form has increased the probability to pick up free electron to from O_2^- ions and $O_2^-(H_2O)_n$.

(a) (b)

Figure 6.18 (a) electron detachment of a gas molecule and (b) electron detachment from a material surface [21]

Electron capture can occur by either one of two mechanisms [84]. A molecule can capture a free electron to become an unstable ion, that then divides into two stable particles, a neutral particle and a negatively charge particle. The excess energy is the kinetic energy of two particles.

$$(XY)+e^{-}\rightarrow(XY)^{-}_{unstable}\rightarrow(X)+(Y)^{-} \tag{6.4}$$

Alternatively, three-body collision between two neutral molecules and an electron can produce a stable negative ion and a neutral molecule. Any excess energy is absorbed by the two particles.

$$(XY)+e^{-}+B\Leftrightarrow(XY)^{-}+B+energy \tag{6.5}$$

The overall process of the electron ionisation and attachment process is shown in the Figure 6.19

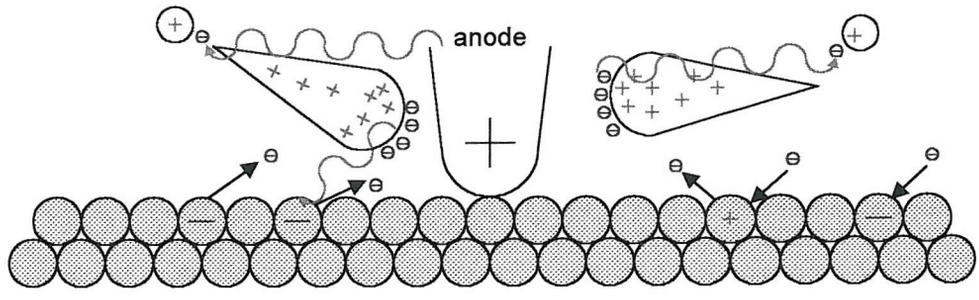

Figure 6.19 Different processes involved in the propagation of streamers and the deposition of surface charge

6.5.2 The Surface Discharge Mechanism

In the point-plane electrode arrangement, the field is the highest at the needle tip and decreases with radial distance. Initially, free electrons in air may have been generated by cosmic rays, detachment from a negative ion, field emission and photon initiation [83]. Under an applied positive field, the electron near the needle tip will be accelerated and move from the weak field region into the high field region. The high energy electron will collide with heavier molecules to give up other electrons and create positive ions by ionisation. These positive ions will have a low mobility of approximately 2.5cm^2/Vs whereas electron mobility is of the order of 10^2-10^3cm^2/Vs [5,6]. The positive ions remain stationary within the applied field for a short time. The repeated ionisation of molecules causes a multiplication of the number of positive ions. The number of ions increases exponentially over a distance x according to Equation 6.3.

$$n = n_o e^{(\alpha-\eta)x} \tag{6.3}$$

The initial electron will thus cause an avalanche which increases in magnitude as shown in Figure 6.12. The positive ions produced by the ionisation remain stationary and are concentrated in the avalanche tip. According to Equation 6.3, 75% of the charge is situated in 8% of the avalanche length. If the tip of the avalanche contains a sufficient number of ions (10^8) [1,83,85,86], a large space charge will affect the electric field in the needle electrode. When the avalanche reaches the needle electrode and all electrons are removed (Figure 6.20a) a positive space charge remains with 75% of it in its tip, the charge has a diameter of roughly 30μm [85,87]. Thus these ions enhance the local field at the tip of the streamer channel to sustain subsequent electro-impact ionisation that is responsible for streamer growth and propagation (Figure 6.20b). It is estimated that the mean electric field in the surface charge region left in the positive streamer channel reaches a value of 20-30kVmm^{-1} [14,87]. Corresponding to this strong field, the ionisation increases and more photons are released (Figure 6.20c). The number of photons created per unit length is larger than the number of the ions per unit length. Hence, a large number of photons have a high probability of colliding with a gas molecule and causing further ionisation. New

avalanches are started which move in the direction of the surface charge (Figure 6.20d). The tip of this new avalanche melts together with the original one so that the surface charge grows gradually to produce a faintly luminous streamer channel (Figure 6.20e). The streamer channels can form branches if a longer gap is involved. This is caused by the stochastic nature of the process. The region of high field strength at the streamer is also active at some positions. The photon emission may cause two electrons to start two avalanches that cause a branch from the streamer channel to be created.

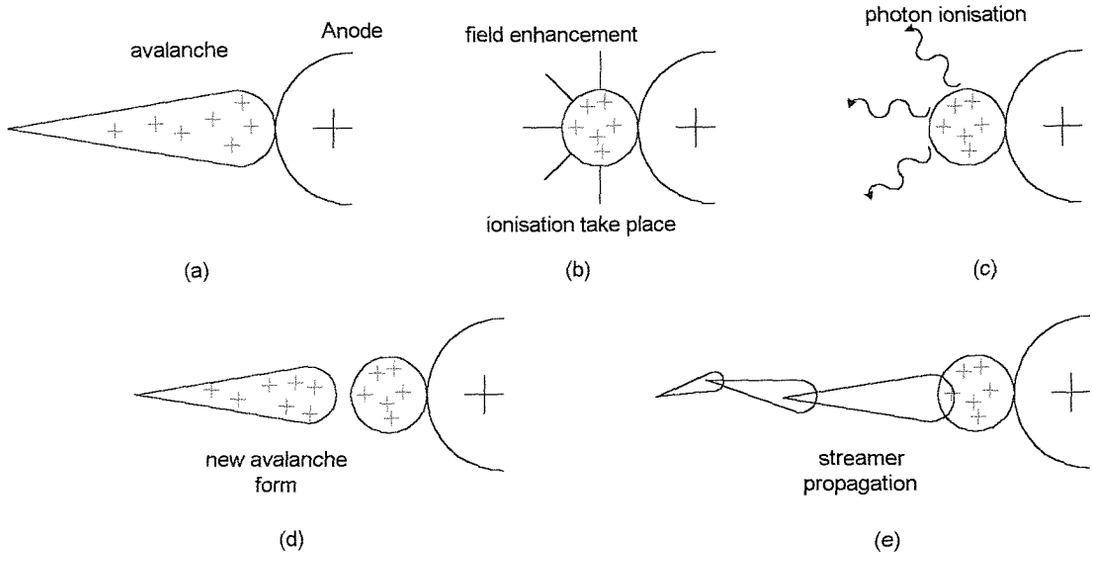

Figure 6.20 Propagation of avalanches to form streamer channel and deposition of surface charge under positive applied field

Surface charge distributions caused by a negative applied voltage are due to electrons being liberated from the needle electrode and travelling from the high field region towards the weak field region. The average velocity for positive streamer growth at an applied voltage of 20kV, pulse width 3ns and 760Torr gas pressure is 6.12 X 10^6 m/s. Whereas, for negative surface discharge created under identical experimental conditions but at opposite polarity, the typical velocity will be 2.58 X 10^6 m/s [6]. As observed, negative surface charge has a uniform distribution and the effect of field enhancement is not significant. Since there is different field enhancement effects due to either positive or negative surface charge distributions and due to photon ionisation in the positive surface discharge, the radius of the positive streamer channels are

greater than the radius of the negative surface charge distribution for the same strength of applied field. It is the evident that the negative surface charge distribution produced during the subsequent negative half cycle only neutralises the centre of the positive streamer channels. The tail of the streamer channels beyond the radial extent of negative charge remains unaffected.

When the electric field is initially applied over the positive half cycle, a positive streamer tip is initially formed (Figure 6.4, 1ms), the tip is due to the electric field generated around the needle electrode. As the field increases several streamer channels burst out from the needle electrode due to ionisation. At this point, the free electrons move from the weak field region towards the high field region and attach to the anode which in time achieves equilibrium and prevents further discharge. In order to make subsequent positive streamer channels the local field must be increased and the equilibrium disturbed. The new streamer channels are restricted to the region between existing channels due to the shielding effect of the internal field produced by them. Therefore, a spoke-like positive surface charge distribution is observed. In contrast for negative surface discharge the electrons are liberated uniformly, leaving positive ions around the cathode and the consequent equilibrium prevents further discharge. As the applied field is increased the equilibrium is disturbed and electrons are pushed away by the field thus increasing the radius of the area of negative charge.

When the electric field is initially applied over the negative half cycle, negative surface charge is deposited uniformly across the crystal. In the subsequent positive half cycle, the positive streamer channels develop differently compared to when the applied field starts over the positive half cycle. This is due to the presence of the negative surface charge surrounding the needle electrode, thus the positive streamer channels in the subsequent positive half cycle attempt to neutralise the surrounding negative surface charge. This creates complicated curved streamer channels around the needle electrode. For an applied ac surface discharge which last over several cycle, the residual positive streamer tails remain on the surface whereas the surface charge around the needle electrode is always distorted by the ac applied field.

6.5.3 Backdischarge

Backdischarge occurs as the applied voltage approaches zero volts but before the zero crossing point is reached. In the case of negative backdischarge, as the positive electric field is applied to the needle the electrons move from the weak field region to the high field region. These electrons accumulate around the needle tip and the electron density becomes high and achieves an equilibrium with the needle tip. As the applied stress starts to decrease, the equilibrium is no longer maintained and the opposite charge strength becomes higher than the applied field. The field gradient between the positive and negative charge is high enough to cause the return flow of electrons and hence neutralise the centre part of the streamers as observed in Figure 6.4 10ms, Figure 6.6 30ms and Figure 6.9 20ms. During the negative half cycle electrons are liberated from the needle tip and move uniformly from the high field region to the weak region leaving positive charge near the needle tip. As the applied negative field in the needle electrode starts to decrease equilibrium is not maintained. The electric field due to positive charge around the needle tip is now higher than the needle tip itself causing positive streamers to burst out and neutralise the electrons present (Figure 6.5 20ms, Figure 6.8 10ms and Figure 6.10 30ms).

Chapter 7

AC Surface Discharge Behaviour of Polymeric Materials and the Effect of Local Environmental Conditions

7.1 Introduction

Polymeric materials such as Low Density Polyethylene (LDPE) and Polymethylmethacrylate (PMMA) have properties that are ideal for use as electrical insulating materials within a wide range of commercial products. They have good mechanical properties and the advantages of high electrical breakdown strength, high electrical resistivity and low dielectric loss. In many practical applications involving the use of insulation, high electrical stresses can be generated at the edges of the interface between a conductor and the solid insulation by the existence of a non-uniform electric field. This may cause local sparking and or corona along the surface of the insulation. The presence of surface discharge activity is a significant problem for polymeric insulators [88]. Any discharge can cause a slow deterioration of the insulator surface in the long term through three mechanisms: firstly through slow erosion by ionic bombardment of ions in the sparks, secondly by chemical

degradation of the insulation material and thirdly from carbonisation of the material surface. Conducting deposits are formed on the surface and this will influence the electrical characteristics of the insulator. Therefore, the measurement system has been used [89] to observe surface charge behaviour of polymeric material.

7.2 The Experiment

Figure 7.1 shows the optical system for the measurement of surface charge density of polymeric films subjected to an applied ac electrical stress. The polymer material is bonded onto the BSO crystal and the needle electrode is just in contact with the polymer surface. The polymer materials investigated were Low Density Polyethylene (LDPE) and Polymethylmethacrylate (PMMA). The quality of the surface charge measurement is dependent on the light reflected from the backface of the crystal. It is therefore very important that any test material is in good contact with crystal surface.

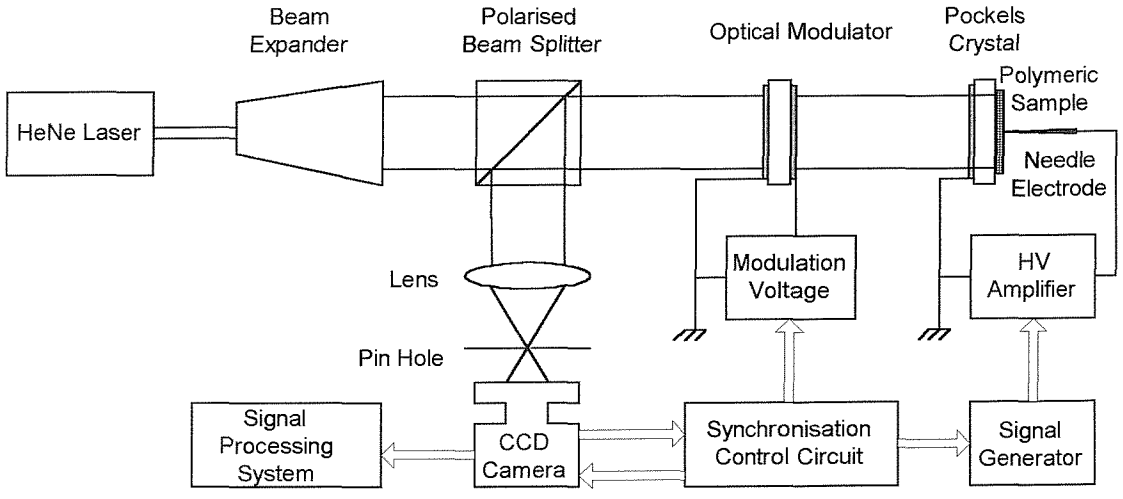

Figure 7.1 Experimental arrangement for surface discharge measurements of polymeric materials

7.2.1 Sample Preparation Using Compression

The polymer sample can be directly bonded onto the BSO crystal by either compression or using suitable solvent. For compression, the sample must be a thin

film. In order to prepare thin films, the raw material is sandwiched between melonex and steel plates as shown in Figure 7.2.

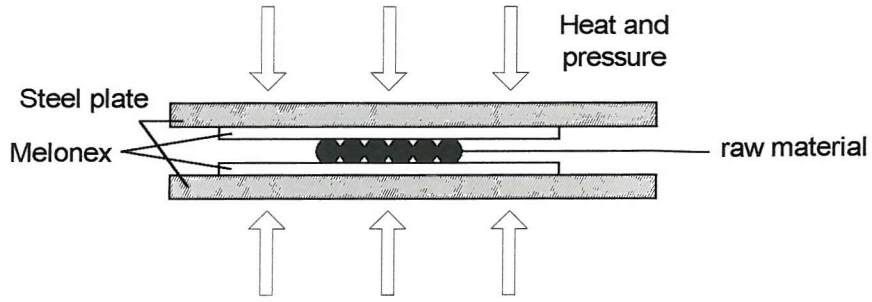

Figure 7.2 Thin film compression

The steel plates are heated above the melting point of the polymeric material. Once the material starts to melt, a compressive force is applied. The thickness of the thin film is determined by the pressure applied. For example, a pressure of 4bar on LDPE at a temperature of 130° will give a 50μm thick film. The desired pressure is held for a few minutes to allow the melted polymer to flow and the system is allowed to cool before the pressure is removed. The thin film is then cut into the desired shape and is attached to the BSO crystal as shown in Figure 7.3.

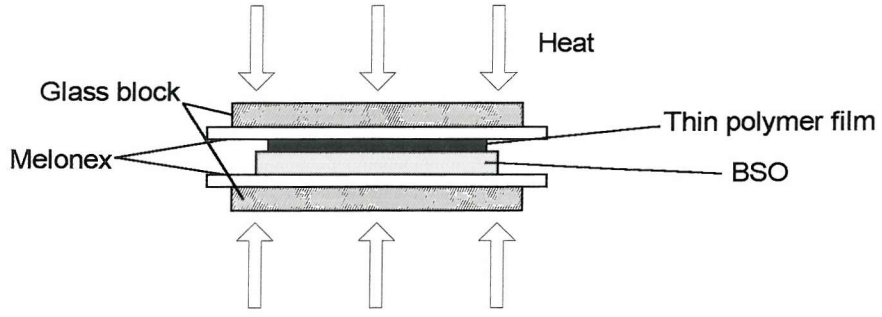

Figure 7.3 Attach thin polymer film onto the BSO crystal

This time the thin film is placed on the BSO crystal and then sandwiched between two melonex sheets that are on glass blocks. The whole assembly is placed in vacuum oven and baked at 10 degrees above the melting point of the polymer for 3-4 hours before being allowed to cool down to room temperature. This method has been successfully used to bond films thicker than 30μm to crystals that are 1mm thick,

however failure usually results in the crystal breaking. It is not a suitable approach for thinner crystals or for crystals bonded to a BK7 glass substrate. The thermal expansion rate of the BSO crystal and the BK7 glass substrate are different consequently mechanical stress exists between the BSO crystal and the glass which is permanent and distorts the measurement of birefringence.

7.2.2 Sample Preparation by Using Solvents

The use of solvents to dissolve polymeric materials allowing the application of very thin films to the backface of the Pockels cell has been investigated. The method of sample preparation is dependent on the polymer that is to be investigated.

7.2.2.a PMMA

Various thicknesses of PMMA have been deposited onto the BSO surface and tested. Initially, 1 gram of PMMA was dissolved in 20 ml acetone giving a 5% solution. The solution was heated so that the PMMA rapidly dissolved in the solvent. After the PMMA had completely dissolved, two or three drops of the solution were applied onto the BSO surface using a pipette. This was left to dry forming a layer of PMMA approximately 2-3 μm thick. In order to deposit various thicknesses of PMMA the concentration of PMMA solution was varied. Using this method PMMA films 80-100 μm thick could be deposited using 11% PMMA solutions. Experimentation revealed that for samples of PMMA 80-100 μm thick the quality of the optical measurement was limited as the results were very noisy. It is also worth noting that if the sample on the backface is too thick then space charge within the bulk of the test material may effect the validity of the measurement.

7.2.2.b LDPE

Experimentation has revealed that increasing PMMA concentration in acetone increases the thickness of the deposited layer onto the BSO. However, increasing the concentration of LDPE in xylene beyond 3-5% results in the deposited layer forming discrete agglomerations and a discontinuous surface. To overcome this problem

layers can be built up sequentially. 200 mg of LDPE was dissolved into 20 ml xylene in order to give a concentration of 1% LDPE in solution. Two or three drops of dissolved LDPE were placed on the BSO crystal surface and left for a few minutes in order to start to solidify. The layer formed was approximately 2 μm thick. The crystal was then examined using a microscope to ensure that the deposited film was continuous over the crystal surface. In order to increase the thickness of the deposited LDPE, the process was repeated using the 1% solution. The thickness of the sample was increased in 2-3 μm increments. AC surface discharge measurements were conducted for a range of thicknesses of LDPE up to 20 μm.

7.3 The Measurement Principle

In the optical system of the surface charge measurement the phase retardation of the Pockles crystal is linearly related by the Equation 3.7.

$$\Phi = K\sigma \tag{3.7}$$

If the Pockels cell is bonded to a thin polymer film, the electrical equivalent circuit is two capacitors connected in series where C_p is the capacitance of the polymer and C_β is the BSO crystal capacitance (Figure 7.4).

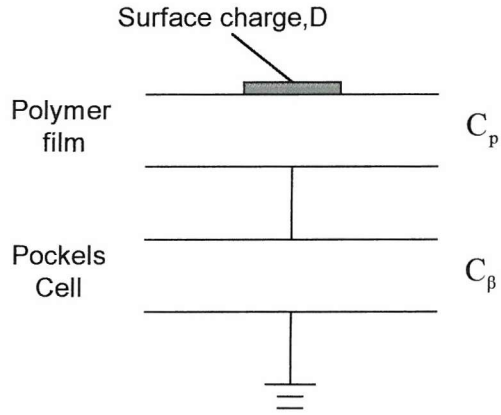

Figure 7.4 Equivalent circuit for Pockels cell with a polymer film bonded to its backface

The effect on the surface charge measurement of the polymer bonded to the Pockels cell has been investigated theoretically (Figure 7.5). In the simplest case a pair of parallel electrodes with a air gap having a permittivity of ε_o (Figure 7.5a) will have a capacitance, C_o of

$$C_o = \frac{\varepsilon_o A}{d} \tag{7.1}$$

where A is the effective area of the electrode and d is the spacing between electrodes. If a dielectric medium with dielectric constant ε_r is inserted between the parallel electrode the capacitance will be altered to

$$C_d = \varepsilon_r C_o \tag{7.2}$$

The increase in capacitance due to the dielectric medium is because of polarisation, P in the medium in which

$$C_d = \frac{Q}{V} = \frac{DA}{V} = \frac{(\varepsilon_o E + P)A}{V}$$

and since $V = Ed$ therefore,

$$C_d = \frac{\varepsilon_o A}{d} + \frac{PA}{Ed} \tag{7.3}$$

Thus Equation 7.3 shows that the presence of a dielectric material inside parallel electrodes increases the capacitance by a factor of ε_r with polarisation induced in the medium. If the parallel plate electrodes are only partially filled with a dielectric medium, it can be considered as two capacitors connected in series (Figure 7.5b). The concept of constant voltage and constant charge across the partially filled parallel plate electrodes has been investigated in order to understand the induced electric field and polarisation that may occur within the Pockels cell.

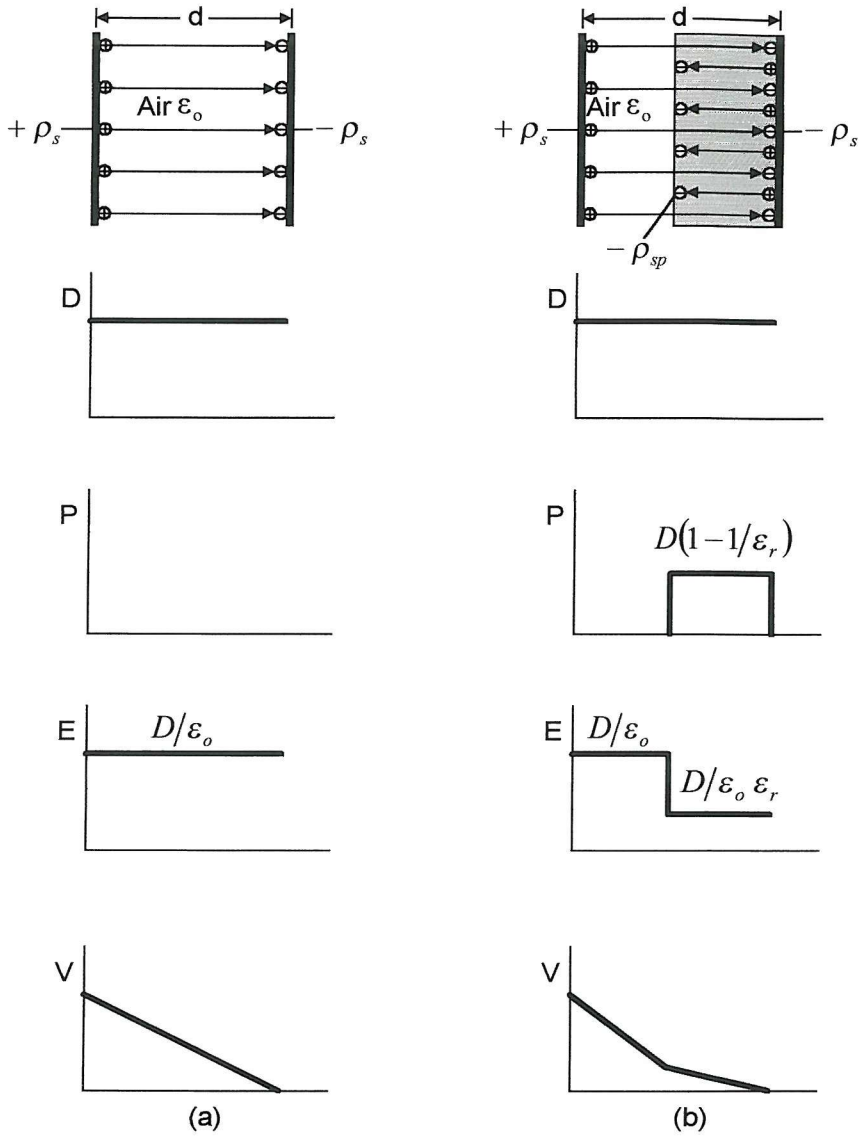

Figure 7.5 The field in (a) an air filled capacitor and (b) an air and dielectric filled capacitor [90]

If a dc source were to be connected across a parallel plate capacitor then voltage dropped across it would be the same magnitude whether it was air filled or partially filled with a dielectric medium. However, the capacitance of the partially filled arrangement is greater than the air filled arrangement. Therefore from the relationship, Q = CV there must be more charge induced within the partially filled system.

If a constant charge, Q is deposited onto the two parallel plate systems, then in the partially filled case the free charge on the parallel plates polarises the dielectric leading to a decrease in the electric field between the plates and in turn decreasing the

potential difference. The charge is identical in both systems due to the greater capacitance of the partially filled arrangement.

Therefore in the case where a constant surface charge, D is deposited on the Pockels cell without polymer bonded to it the electric field induced within the BSO is related with the surface charge as

$$E = \frac{D}{\varepsilon_o \varepsilon_r} \tag{7.4}$$

If the same amount of surface charge were to be deposited onto polymer film bonded to the Pockels cell then the electric field induced will be identical to the BSO crystal only case. The surface charge vector, D is constant (Figure 7.5b), there is a lower electric stress within the polymer if it has higher dielectric constant but the field within the BSO crystal is identical in both cases.

When positive surface charge is deposited on the polymer surface, the field of the surface charge will polarise the molecules. Thus an electric field induces the dipoles and orients them along the direction of an external electric field. Figure 7.6 shows the dielectric material polarised by an external field, E caused by deposited surface charge. Inside the material, the adjacent charge of the dipoles will annul each other, leaving only negative surface charge on the left hand side and positive surface charge on the right hand side. In theory, the induced positive surface charge on the right hand side is identical to the deposited surface charge. If second dielectric material is placed adjacent to the previous one then the same amount of surface charge will be induced on the side of the new material. Thus electric field across the Pockels crystal is unaffected by the presence of a polymer bonded to its backface.

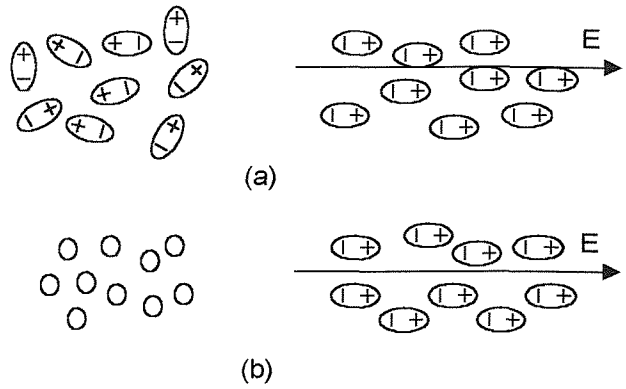

Figure 7.6 (a) Thermal agitation randomises polar molecules and a field aligns their dipoles, (b) Non-polar molecules have no permanent dipole moment and a field induces dipoles and orients them along the field

However, the thickness of the polymer will affect the induced surface charge on polymer. For very thin samples, the dipoles are aligned by the applied external field and the same amount of the charge is induced on the other side of the polymer. As the polymer thickness increases, misalignment of dipoles can occur. In addition, thermal motion tends to randomise dipole alignment. Hence, the surface charge induced on the other end of the polymer will suffer from attenuation and may not identical match the deposited charge. Furthermore, the electric stress within a sample can be assumed constant over small spacing. However, as the thickness of the sample increases, the electric field will decrease by the ratio 1:r where r is the radius from the point charge.

7.4 Experimental Results

7.4.1 AC Surface Discharge Measurements of PMMA

Figure 7.7-7.10 show the results obtained for different thicknesses of PMMA for an applied AC 50Hz voltage at ±7kV pk-pk for a single cycle. Even for very thin samples the discharge pattern is significantly different to that obtained for BSO crystal itself. There are far more branches in the streamers and the positive charge density is greater near the needle tip. Increasing the thickness of the PMMA causes a greater number of positive streamers to branch out from the needle tip. The discharge profile when the applied voltage is negative 7 kV is similar to results obtained for

BSO crystal only, in that the negative surface charge neutralises the positive streamer around the needle electrode but the positive charge at the streamer tips is still present.

7.4.2 AC Surface Discharge Measurements of LDPE

The surface charge for a range of thicknesses of LDPE bonded onto the backface of the BSO crystal for an applied AC 50Hz voltage of ±7kV pk-pk over a single cycle is shown in Figure 7.11-7.14. Unlike PMMA the streamers produce side branches that become interconnected resulting in a positive charge profile that resembles a spoked wheel [8]. With LDPE bonded onto the BSO accurate measurements are only possible if the sample thickness is less than 20 μm due to the poor optical quality of the LDPE. Light is scattered at the interface between the LDPE and the BSO and results in increasing the background noise level. The peak negative AC surface discharge measurement is similar to results obtained for BSO only and PMMA samples.

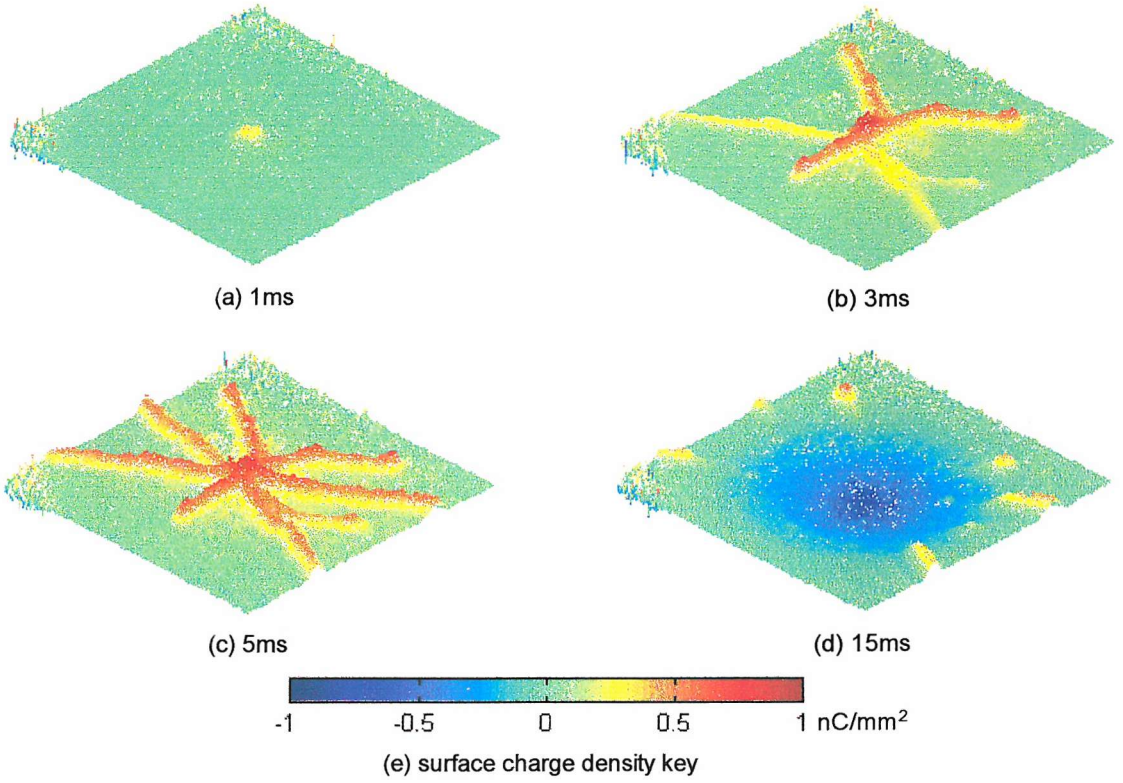

Figure 7.7 Surface charge distribution under AC response for PMMA with thickness 2μm bonded on BSO (effective dimensions of these images are 8mm by 8mm)

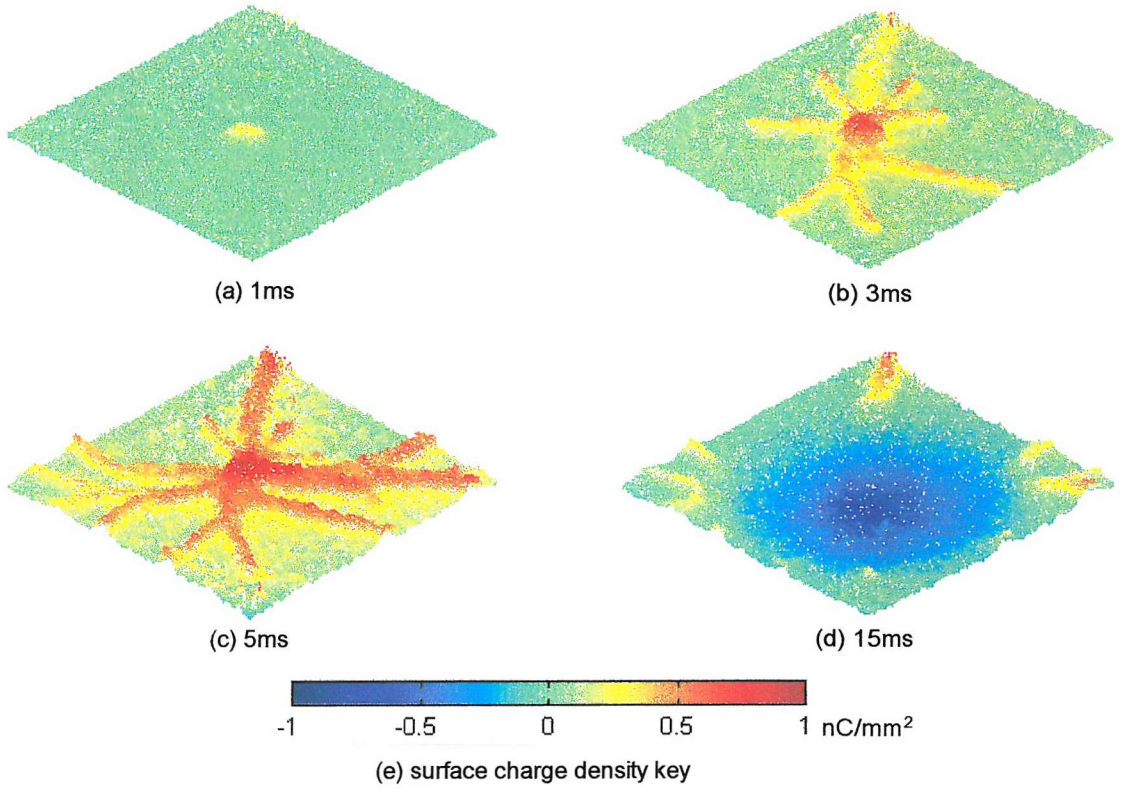

Figure 7.8 Surface charge distribution under AC response for PMMA with thickness 15μm bonded on BSO (effective dimensions of these images are 8mm by 8mm)

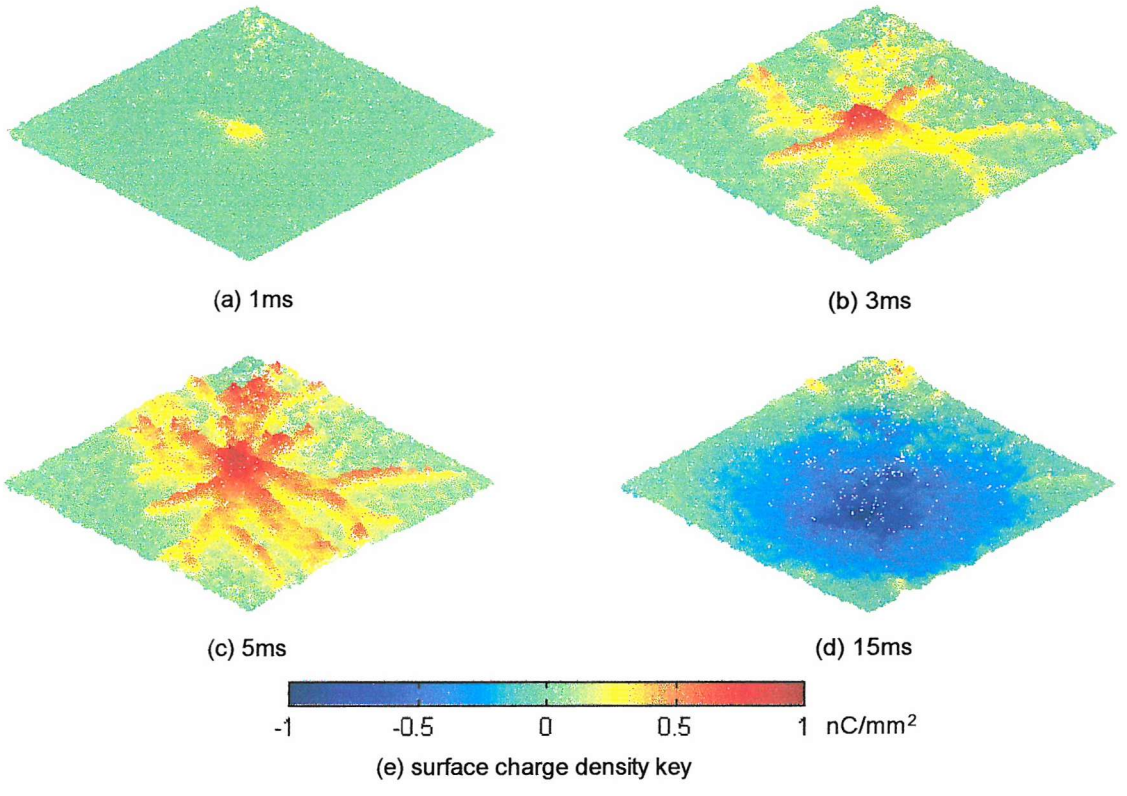

Figure 7.9 Surface charge distribution under AC response for PMMA with thickness 30μm bonded on BSO (effective dimensions of these images are 8mm by 8mm)

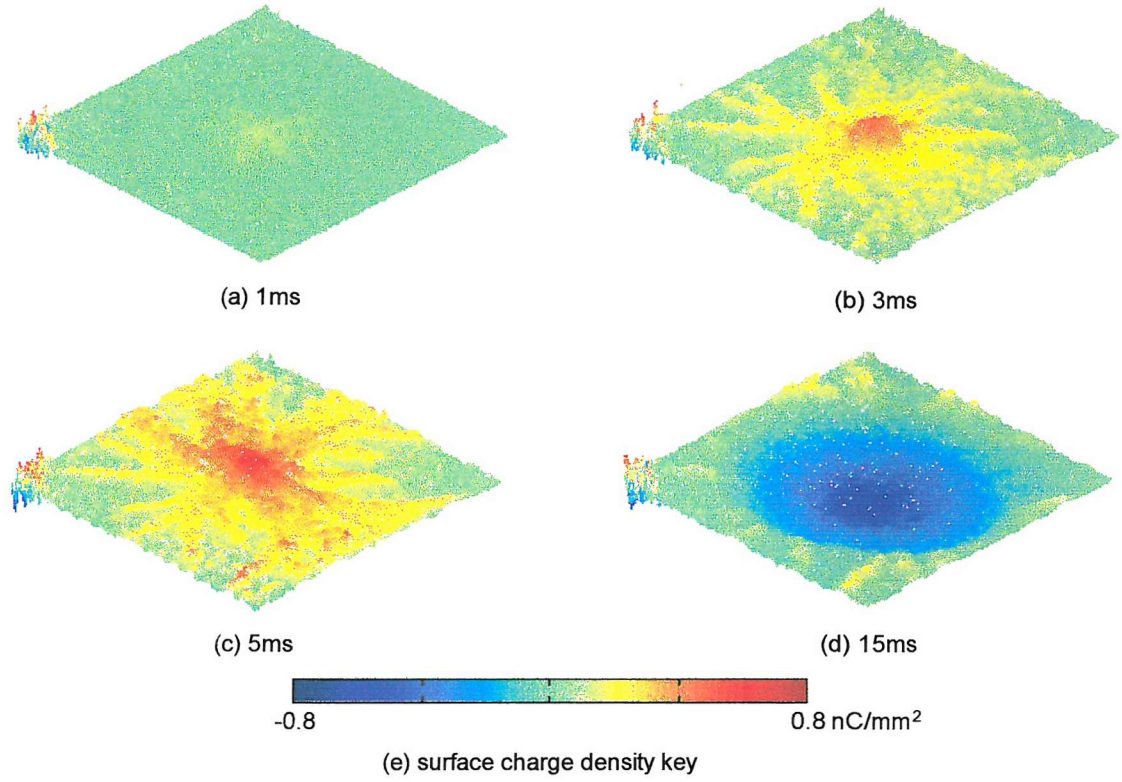

Figure 7.10 Surface charge distribution under AC response for PMMA with thickness 100μm bonded on BSO (effective dimensions of these images are 8mm by 8mm)

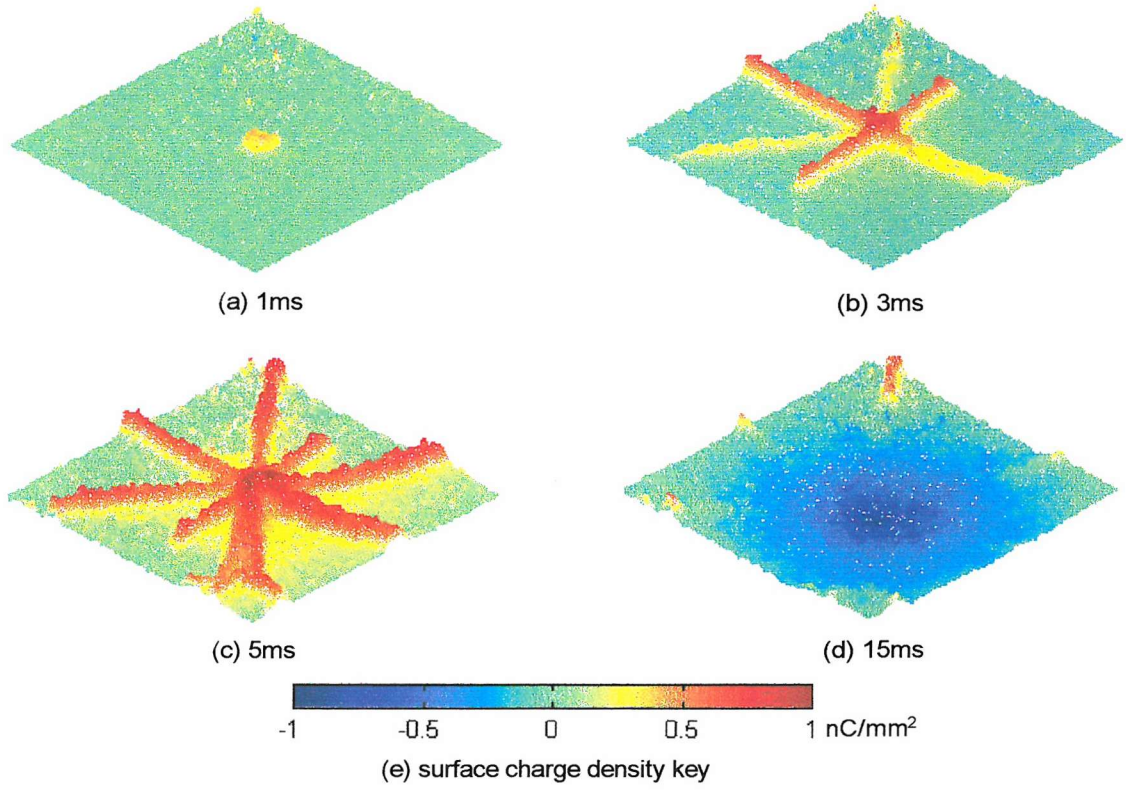

Figure 7.11 Surface charge distribution under AC response for LDPE with thickness 2μm bonded on BSO (effective dimensions of these images are 8mm by 8mm)

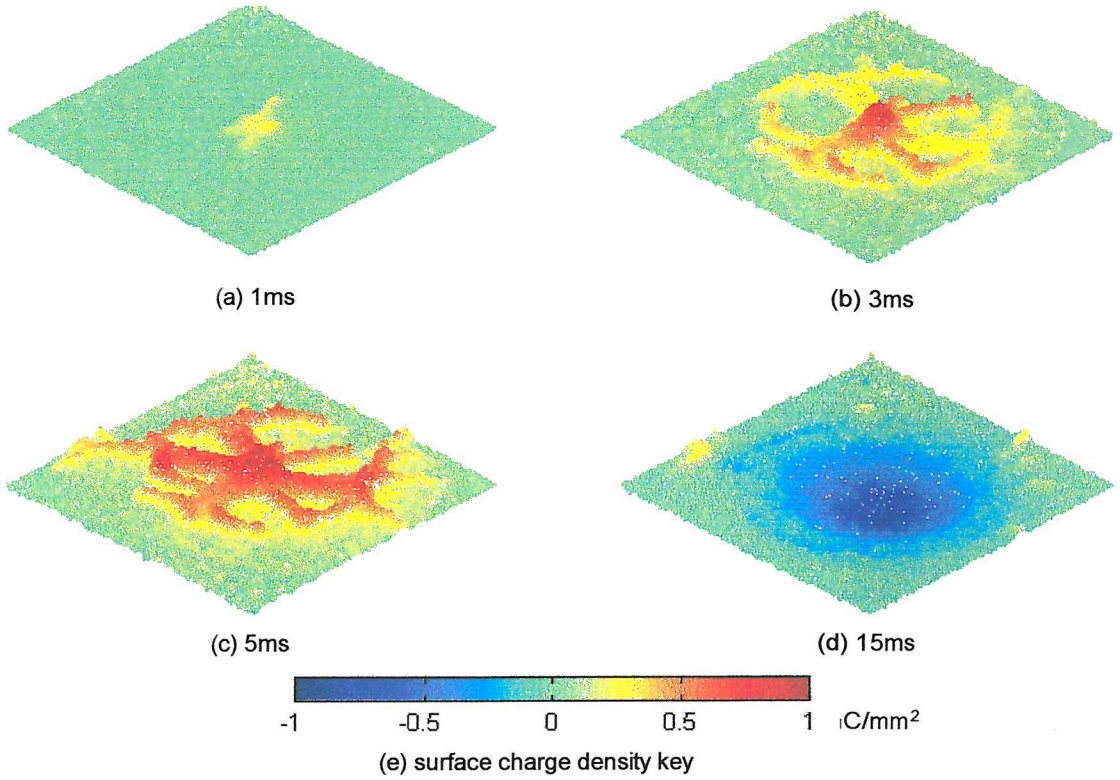

Figure 7.12 Surface charge distribution under AC response for LDPE with thickness 6μm bonded on BSO (effective dimensions of these images are 8mm by 8mm)

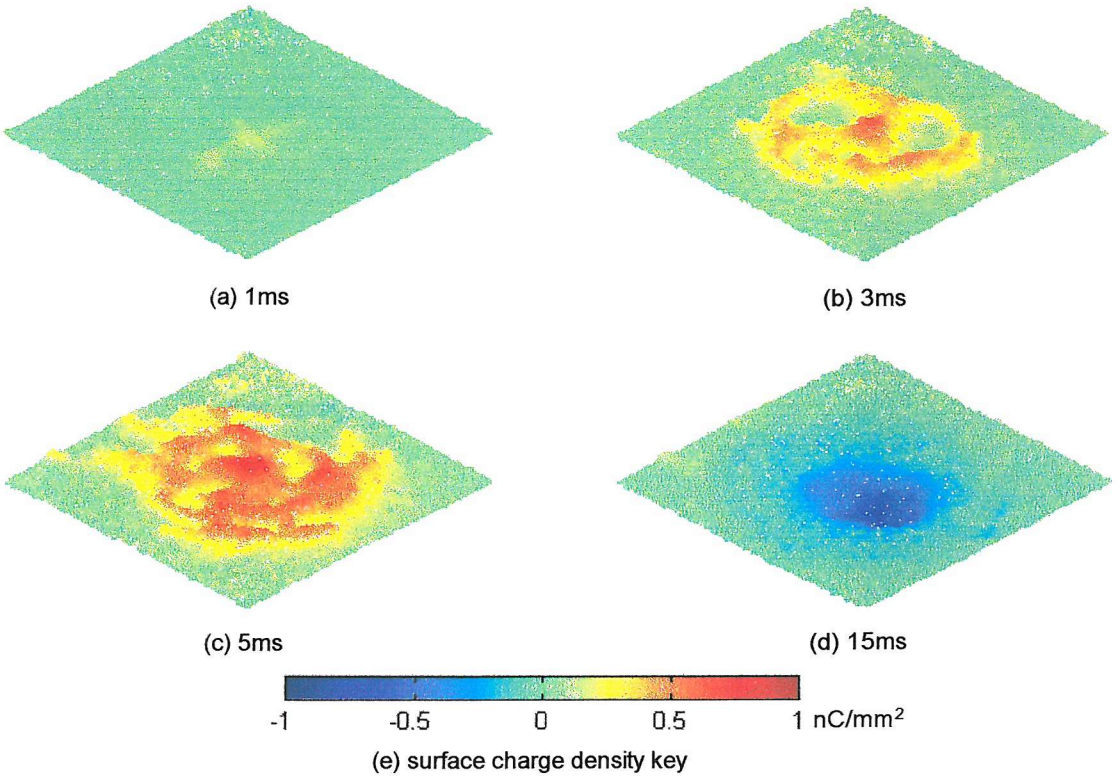

Figure 7.13 Surface charge distribution under AC response for LDPE with thickness 14μm bonded on BSO (effective dimensions of these images are 8mm by 8mm)

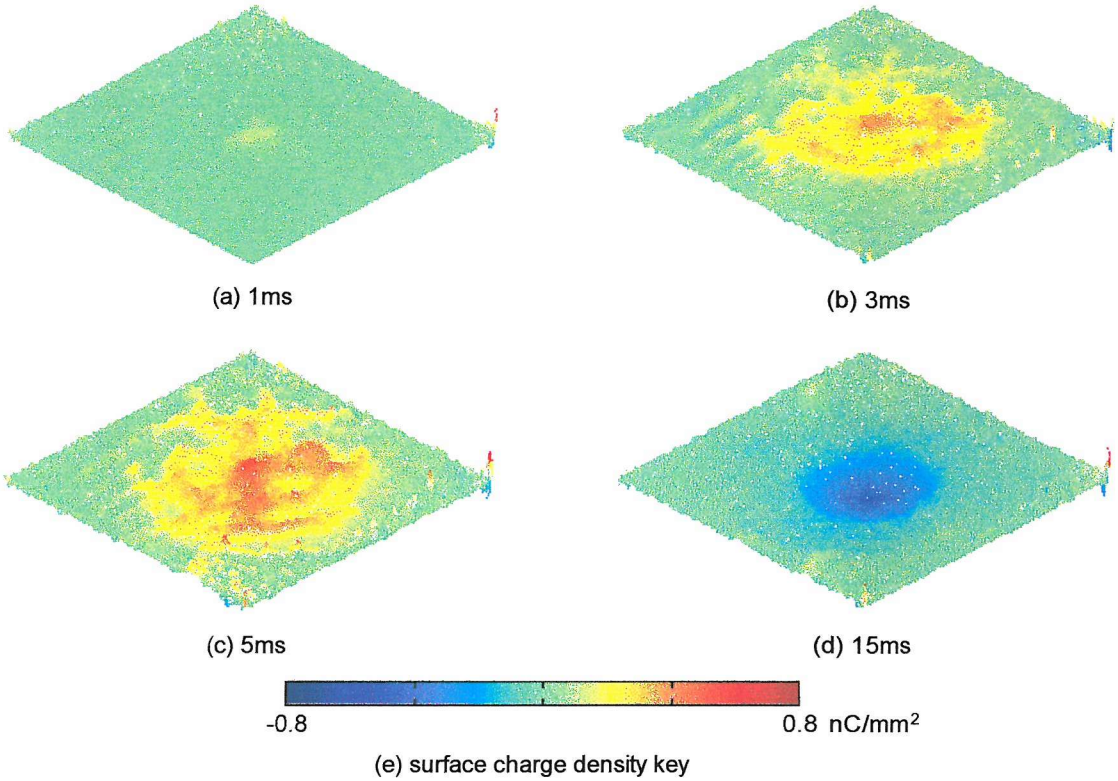

Figure 7.14 Surface charge distribution under AC response for LDPE with thickness 20μm bonded on BSO (effective dimensions of these images are 8mm by 8mm)

7.4.3 Discussion

The experimental results obtained for surface discharge on PMMA and LDPE are significantly different to results obtained for the BSO crystal only. The free electrons that exist around the needle electrode play an important role in the propagation of streamers and surface discharge. Under an applied positive field, electrons near the needle tip will be accelerated by the field and move from the weak field region into the high field region. The high energy electrons will collide with heavier molecules to give up another electron and by ionisation create positive ions which remain stationary for a short time. The repeated ionisation of molecules causes a multiplication of the number of electrons and positive ions which form avalanches. The subsequence avalanches join together and propagate as streamers. The photon ionisation process increases the probability of new electron creation which can cause the streamer channels to form branches. For the surface discharge of BSO, the multiplication of electrons is due to electron and photon ionisation of air molecules.

The electrons bonded on the BSO surface are hard to remove by collision and photon ionisation. Therefore, the streamer propagates in a straight line. Whereas for the surface discharge of PMMA and LDPE, the electrons bonded to the polymeric surface are easier to remove. The surface ionisation coefficient, α_s is important in determining the enhancement of electron multiplication which results in a secondary electron emission avalanche [91]. The photons created due to field enhancement increase in number (Figure 7.15) and there is an increased probability of collision with a gas or surface molecule. Photon ionisation is an important factor in streamer growth and influences the surface charge distribution [92,93]. The electrons due to ionisation are from air or surface molecules and several new avalanches can be formed at the streamer tips. The streamers channels will branch and will not propagate in a straight line.

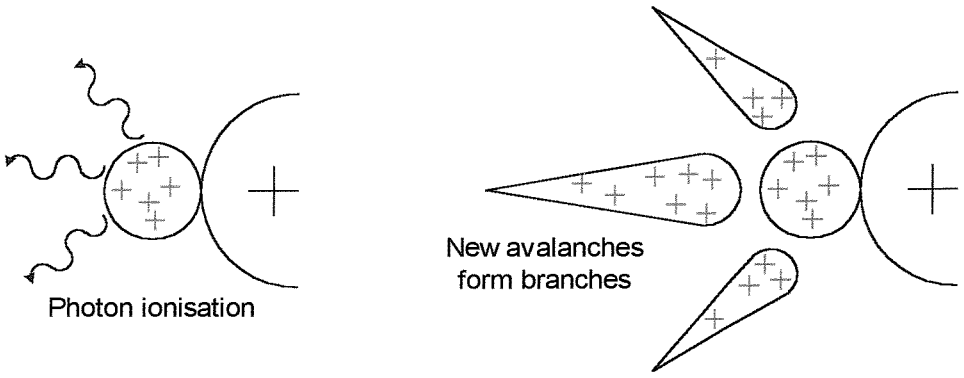

Figure 7.15 Electron detachment by photon ionisation form streamer branches

The surface discharge distribution on PMMA and LDPE shown in Figure 7.7-7.14 have different profiles. This may due to differences in surface characteristics and future work will try to establish if there is a correlation between surface charge distribution and material morphology. Table 7.1 show the characteristics of some insulating materials that are 1mm thick. However, it is likely that the most significant parameter in determining surface charge distribution is the local environment. This has been investigated experimentally.

Insulating Material	Relative permittivity	Surface resistance, Ω	Specific resistance, Ωcm
Bakelite	5.4	$6.3x10^{11}$	$1.7x10^{13}$
Glass	6.9	$2.3x10^{13}$	$2.6x10^{12}$
Epoxy	4.2	$4.9x10^{15}$	$6.9x10^{15}$
Telfon	1.9	$6.9x10^{15}$	$9.5x10^{16}$
Acryl	3.1	$8.6x10^{15}$	$6.8x10^{16}$
Rubber	2.5	$1.1x10^{16}$	$4.7x10^{16}$
Polyethylene	2.1	$1.1x10^{16}$	$6.8x10^{16}$

Table 7.1 Electrical properties of some insulating materials

7.5 AC Surface Discharge Under Different Environmental Conditions

The local environment is a significant factor affecting surface charge behaviour [86]. For example, gas insulated switchgear (GIS) systems use compressed gas to increase the minimum breakdown voltage. The use of compressed gas has several advantages, it has a low dielectric constant and hence low dielectric losses. Higher breakdown stress can be achieved by increasing the gas pressure. The electrodes are cooled by convection of the dense gas. However, there are some disadvantages with this approach. The system requires a pressure tight construction to prevent gas leakage. Extra insulators are required to support the system. Any dust or dirt within the system can have a very detrimental effect on the withstand voltage. Dust and dirt particles have field concentration at their edges. The dielectric constant of dust is high especially if it has absorbed water. These particles move towards high field regions under an applied field. They can adhere and form larger particles. The field emissions where dust and dirt have collected play an important role. Therefore, the gas must be clean, dust-free and extremely dry to prevent moisture absorption by any particulate. The electrode and solid insulator surfaces must also be dry.

7.5.1 Experimental Setup

In order to study the effect of gas pressure on surface discharge measurement, a vacuum chamber was added to the optical system as shown in Figure 7.16. The vacuum chamber has two valves, one connected to a vacuum pump and the other

connected to a compressor in order to control the gas pressure inside the chamber. The chamber contains a BK7 glass window which has excellent optical properties and allows light to be transmitted through it.

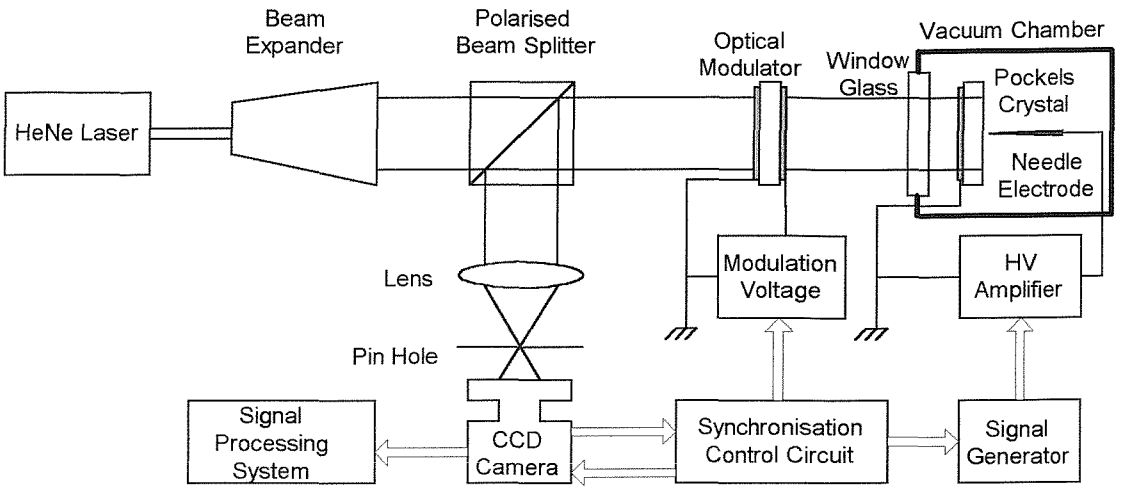

Figure 7.16 Vacuum Chamber add on for varying surface discharge environment condition

7.5.2 Experimental Results

The applied voltage used for these experiments was 50Hz, ±4kV peak. A lower applied voltage was used than in previous experiments since it was expected that more discharge activity would occur at lower pressure. If the applied voltage is too high, the obtained results may not clearly demonstrate the effect of different gas pressures. Gas pressures of 1 atm (101.3kPa), 20.7kPa (3psi), 41.4kPa (6psi), 82.7kPa (12psi) and 137.9kPa (20psi) were used. Each measurement was for a single cycle with positive half cycle first and for each pressure the surface charge distributions after 1ms, 3ms, 5ms and 15ms respectively are shown in Figure 7.17-7.21. After 1ms the discharge had just initiated, after 3ms the applied stress was increasing, at 5ms the applied stress was at the positive 4kV peak and by 15ms the applied stress was at the negative peak.

The ac surface discharge for a gas pressure of 1atm is shown in Figure 7.17. As the applied voltage starts from the positive half cycle, positive streamer channels develop radially from the needle electrode and negative surface charge appears around the needle tip during the subsequent negative half cycle. The surface charge distribution

at atmospheric pressure was used as the reference for comparing discharge at other gas pressures. Figure 7.18 shows the ac surface discharge for a gas pressure of 20.7kPa (3psi). Three streamer channels are observed forming in the positive half cycle. The positive streamer channels have a lower surface charge density compared to the measurement at 1atm, however, the width of the streamer channel is greater. The maximum travel radius of surface charge for both positive and negative applied stresses increase as the pressure is decreased. Figure 7.19 show the ac discharge at the gas pressure 41.4kPa (6psi). Positive streamer channels appear during the positive half cycle. One of the streamer channels is wider than the other two. The travel radius of the surface charge distribution is greater than at 1atm but less than the 20.7kPa case. Figure 7.20 shows the discharge at 82.7kPa (12psi) gas pressure. Again as the gas pressure is increased then the travel radius of the surface charge distribution is reduced. Figure 7.21 shows the discharge distribution for a gas pressure of 137.9kPa (20psi) the length of the streamer channels are shorter compared to the 1atm measurement.

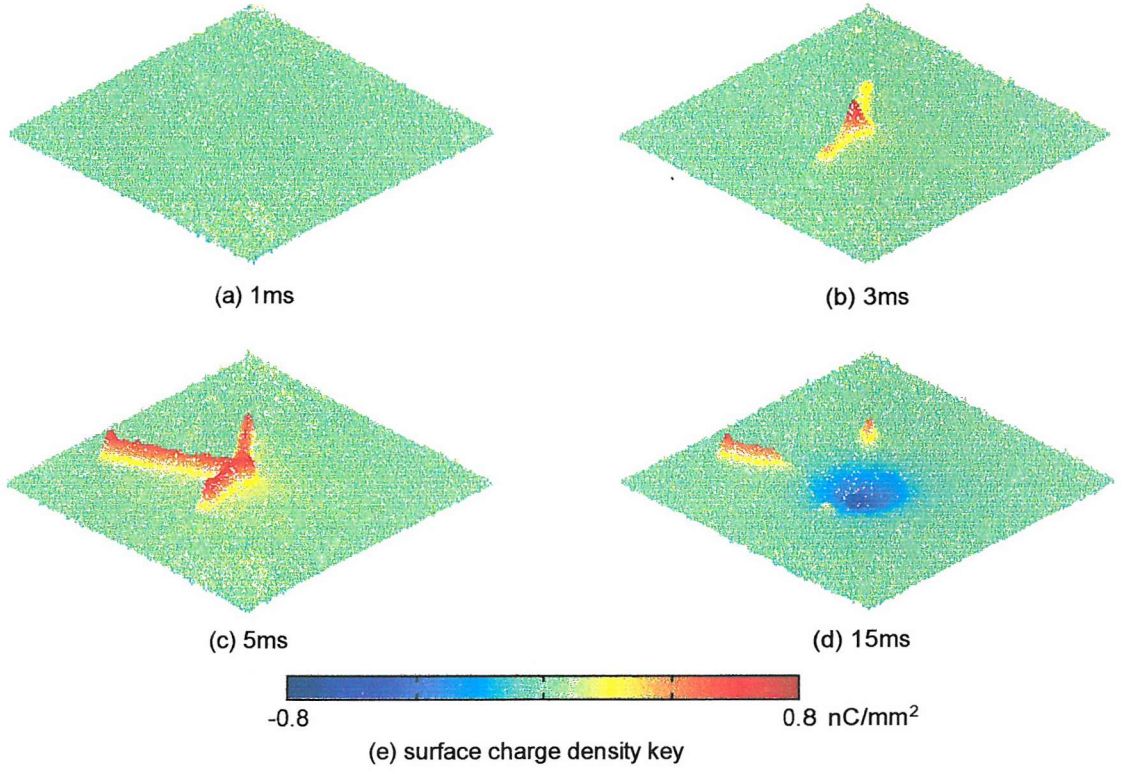

Figure 7.17 Surface charge distribution under AC response for chamber gas pressure at 101.3kPa (1atm) (effective dimensions of these images are 8mm by 8mm)

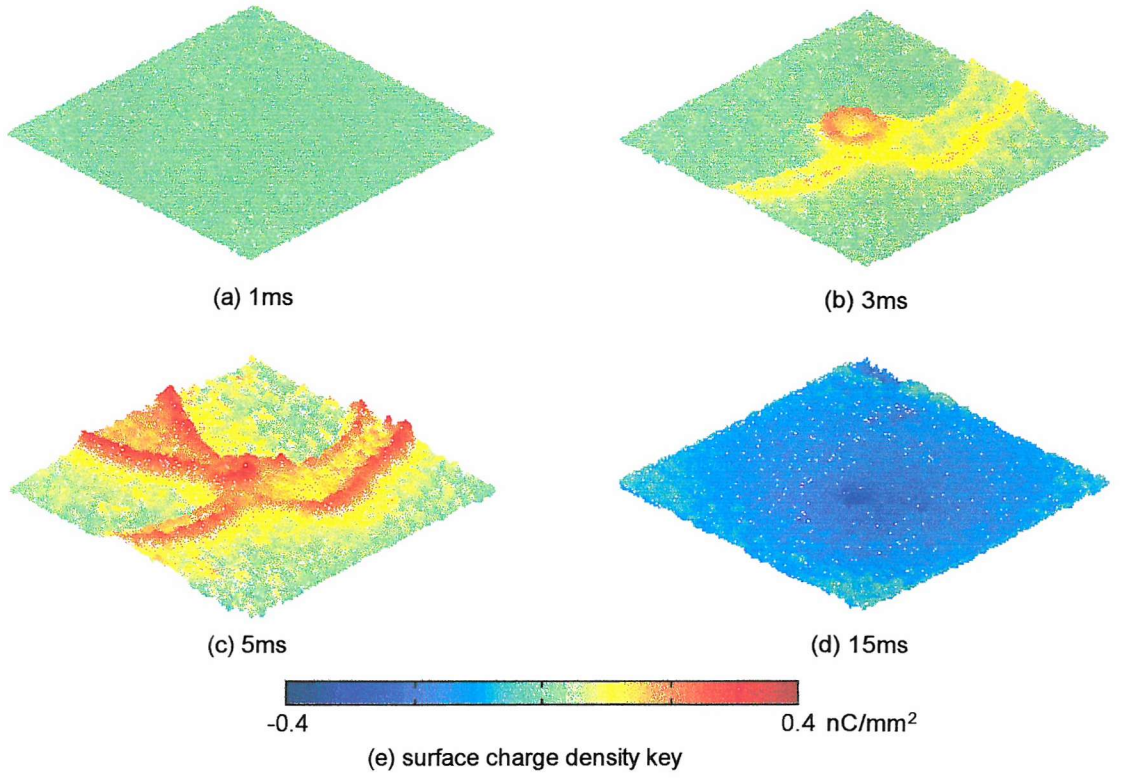

Figure 7.18 Surface charge distribution under AC response for chamber gas pressure at 20.7kPa (3psi) (effective dimensions of these images are 8mm by 8mm)

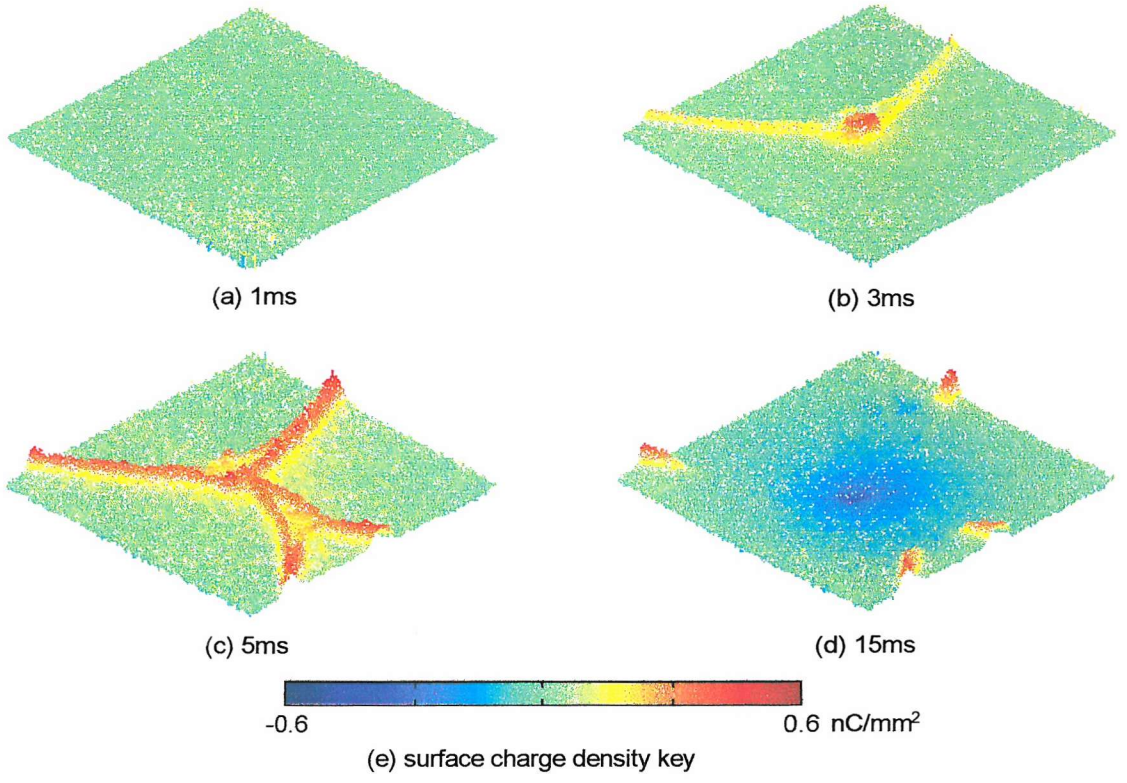

Figure 7.19 Surface charge distribution under AC response for chamber gas pressure at 41.4kPa (6psi) (effective dimensions of these images are 8mm by 8mm)

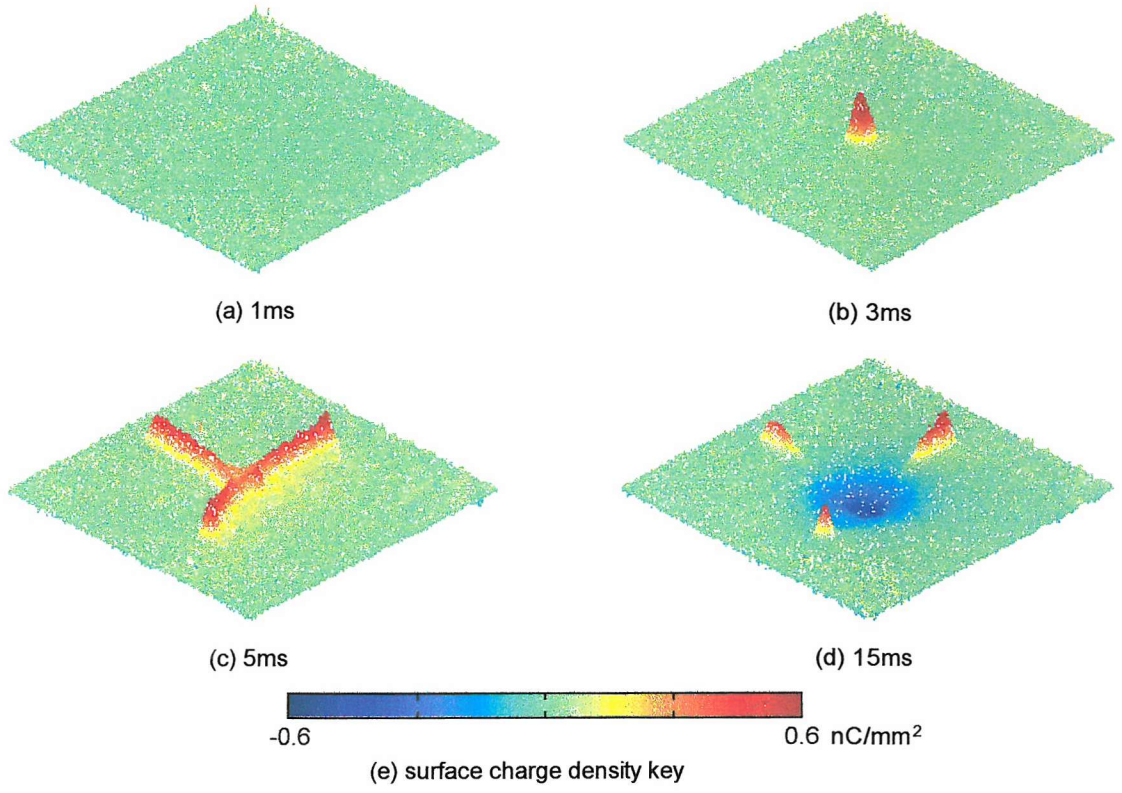

Figure 7.20 Surface charge distribution under AC response for chamber gas pressure at 82.7kPa (12psi) (effective dimensions of these images are 8mm by 8mm)

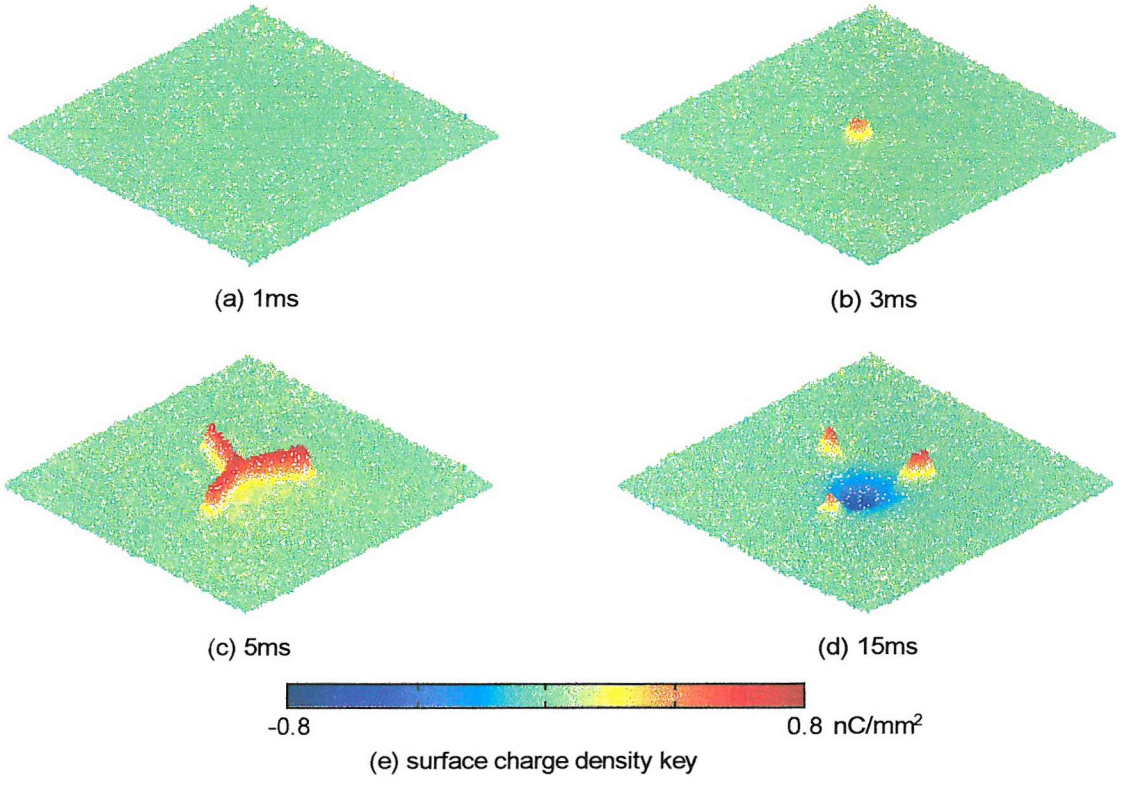

Figure 7.21 Surface charge distribution under AC response for chamber gas pressure at 137.9kPa (20psi) (effective dimensions of these images are 8mm by 8mm)

7.5.3 Discussion

In a parallel-plate electrode system, a breakdown voltage varies with pressure as described by the Paschen's curve (Figure 7.22). This curve shows the minimum required breakdown voltage for a discharge to occur. Paschen's curve is also applicable to other gases but the minimum point will be different [94]. On the right hand side of the minimum point as the gas pressure is reduced the free mean path between air molecules is increased. This increases the possibility that electrons will gain sufficient energy and velocity to cause ionisation. The obtained experiment results show that there is more discharge activity as the gas pressure is reduced from 137.9kPa to 20.7kPa. The minimum of the curve is located around 100Pa for a parallel-plate electrode at spacing of 10mm. Further reducing the gas pressure from the minimum increases the breakdown voltage. This is due to the decrease in the number of molecules available to collide with electrons. Hence higher applied electric stresses are required to initiate any discharge activity.

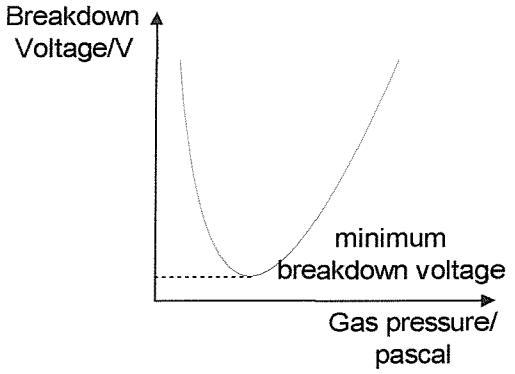

Figure 7.22 Paschen's curve for breakdown voltage varied with gas pressure

7.6 Surface Discharge in the Electro-negative Gas SF_6

Breakdown voltage can be increased by using an electro-negative gas. The electro-negative gas Sulphur Hexafluoride (SF_6) is commonly used in GIS systems. Like other electro-negative gases, SF6 has a higher breakdown voltage compared to normal air. In an electro-negative gas the electrons easily attach to gas molecules to form heavy negative ions which are relatively slower compared to the active high mobility

electrons that are responsible for ionisation. According to Equation 6.3 the multiplication of electrons over a distance of x metres is

$$n = n_o e^{(\alpha-\eta)x} \tag{6.3}$$

where n_o is the initial number of the positive ions, α is the ionisation coefficient and η is the attachment coefficient. Hence, decreasing the number of electrons through the attachment process acts to reduce the process of electron multiplication within the electro-negative gas. Initial free electrons play an important role in the multiplication of electrons and must be accelerated at high stress to form sufficient avalanches in order to obtain breakdown. Reducing their number increases the breakdown voltage of the insulating system. Table 7.2 shows breakdown voltages for several gases relative to normal air. Even a small quantity of these electro-negative gases can be added to air to effectively increase the breakdown voltage. The efficiency of the electro-negative gas can be further improved by increasing the gas pressure [86,95]. In a GIS system the operating pressure is usually 5atm. Higher pressures are avoided as there is a risk of condensation in cold weather conditions. For example, from Table 7.2 using SF_6, combined with a higher pressure at 5atm increases the breakdown voltage by a factor of 11.5

Nitrogen	N_2	1
Sulphur hexafluoride	SF_6	2.3
Freon	$CC1_2F_2$	2.4
Tetra	$CC1_4$	6.3
Oxygen	O_2	slightly electro-negative
Air	Contains O_2	slightly electro-negative

Table 7.2 Relative electric strength of various electro-negative gases

7.6.1 Experimental Setup

Surface charging of a GIS system under dc or impulse stress has been studied by several investigators [19,74,75,95,96,97,98]. The surface discharge behaviour due to

high electric stress existing at the interface between the solid dielectric and SF_6 can be simulated using the arrangement shown in Figure 7.16. The vacuum chamber is filled with the required quantity of SF_6 by using the vacuum pump to remove air from the chamber reducing pressure from 101.3kPa to 89.6kPa. The valve connected to the SF_6 tank was then opened so that the chamber pressure returns to 1atm. The chamber therefore contained 10% SF_6 and 90% air. An ac 50Hz voltage ±7kV pk-pk was applied to the needle electrode for one cycle. A higher electric field was used in this experiment since significantly less discharge activity was expected due to the presence of an electro-negative gas.

7.6.2 Experimental Results

Figure 7.23 shows the measured AC discharge for 1atm pressure of air containing 10% SF_6 when exposed to a single cycle of AC stress at the time intervals of 1ms, 3ms, 5ms and 15ms respectively. From 1ms to 5ms positive charge is deposited but only propagates a very short distance from the needle electrode. However the negative surface charge developed during in the subsequent negative half cycle is enhanced by the surrounding electro-negative gas. The maximum travel radius of the negative surface charge is greater than the discharge in normal air for the same amplitude of applied field and consequently any positive surface charge is completely neutralised by the deposited negative charge. Repeating the experiment but at a lower pressure by using the vacuum pump to reduce the pressure to 68.9kPa (10psi) yields the results shown in Figure 7.24. There are some positive streamer channels that propagate further than at 1atm due to a greater free mean path for the remaining gas molecules. Again, the negative surface discharge is enhanced by the SF_6 and neutralises all of the positive charge. Further reducing the pressure to 34.5kPa (5psi) gives the results shown in Figure 7.25, the positive streamer channels develop a wheel-like pattern at lower pressure. Negative surface charge again completely neutralises the positive streamer channels during the negative half cycle.

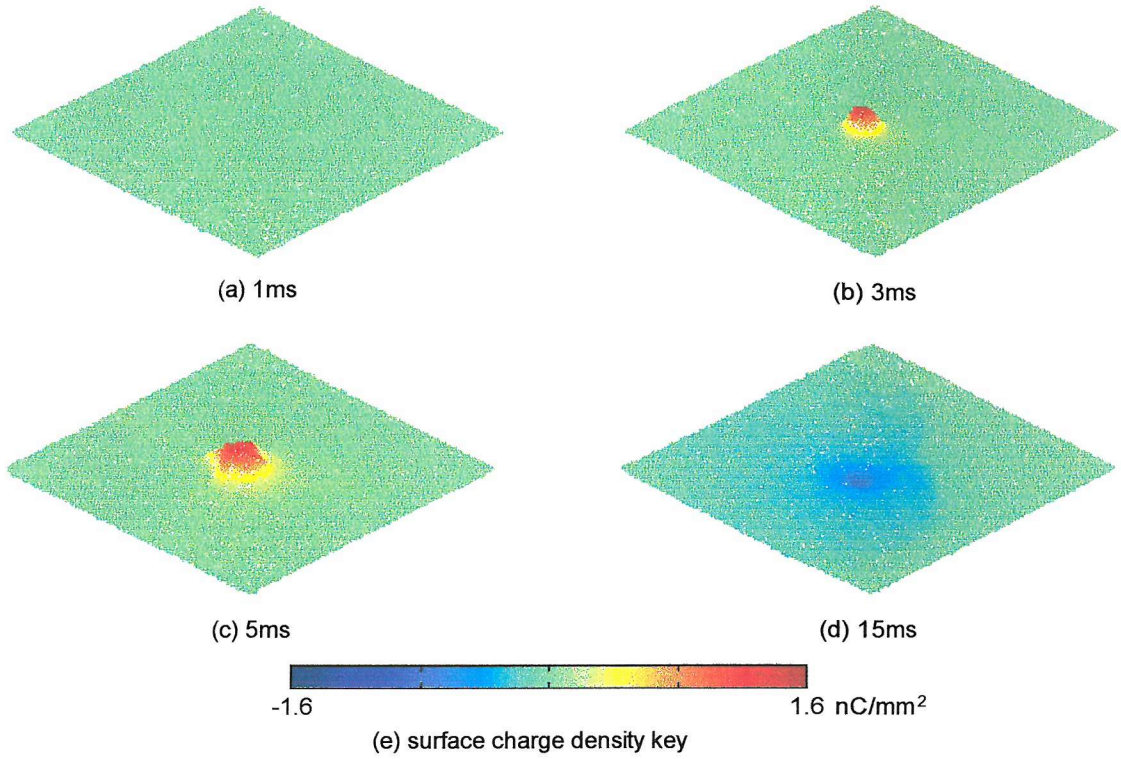

Figure 7.23 Surface charge distribution under AC response for 10% electro-negative gas SF_6 filled in the chamber at gas pressure 101.3kPa (1atm) (effective dimensions of these images are 8mm by 8mm)

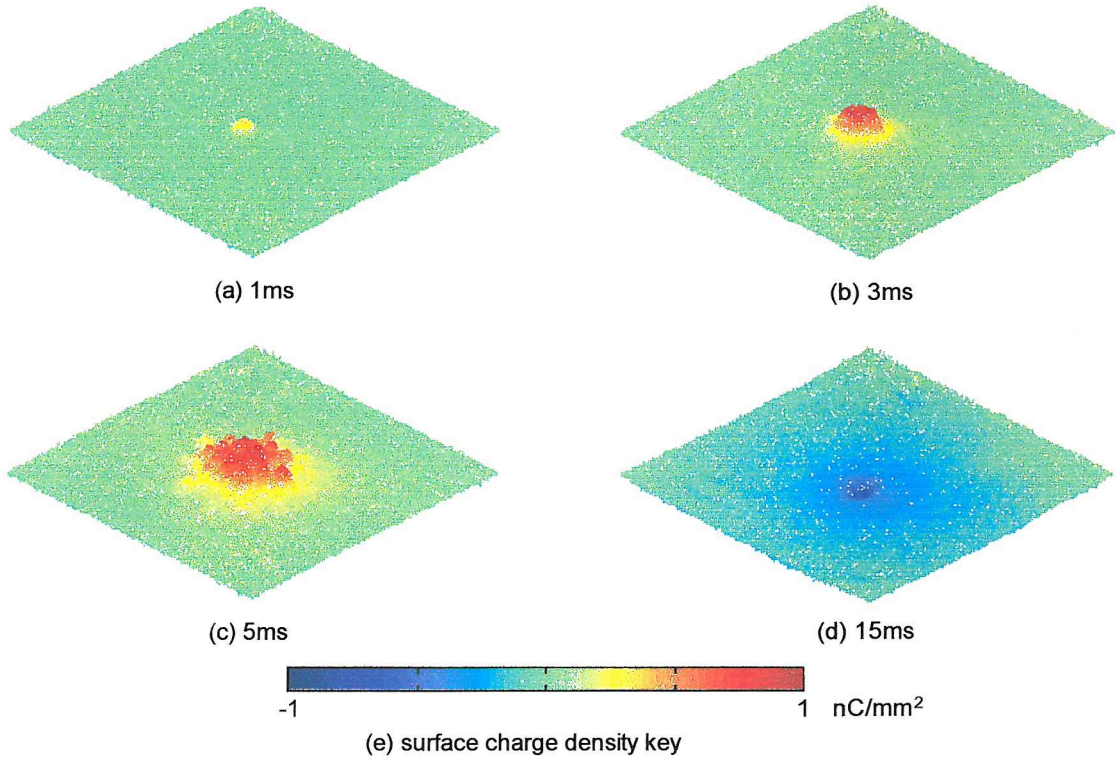

Figure 7.24 Surface charge distribution under AC response for 10% electro-negative gas SF_6 filled in the chamber at gas pressure 68.9kPa (10psi) (effective dimensions of these images are 8mm by 8mm)

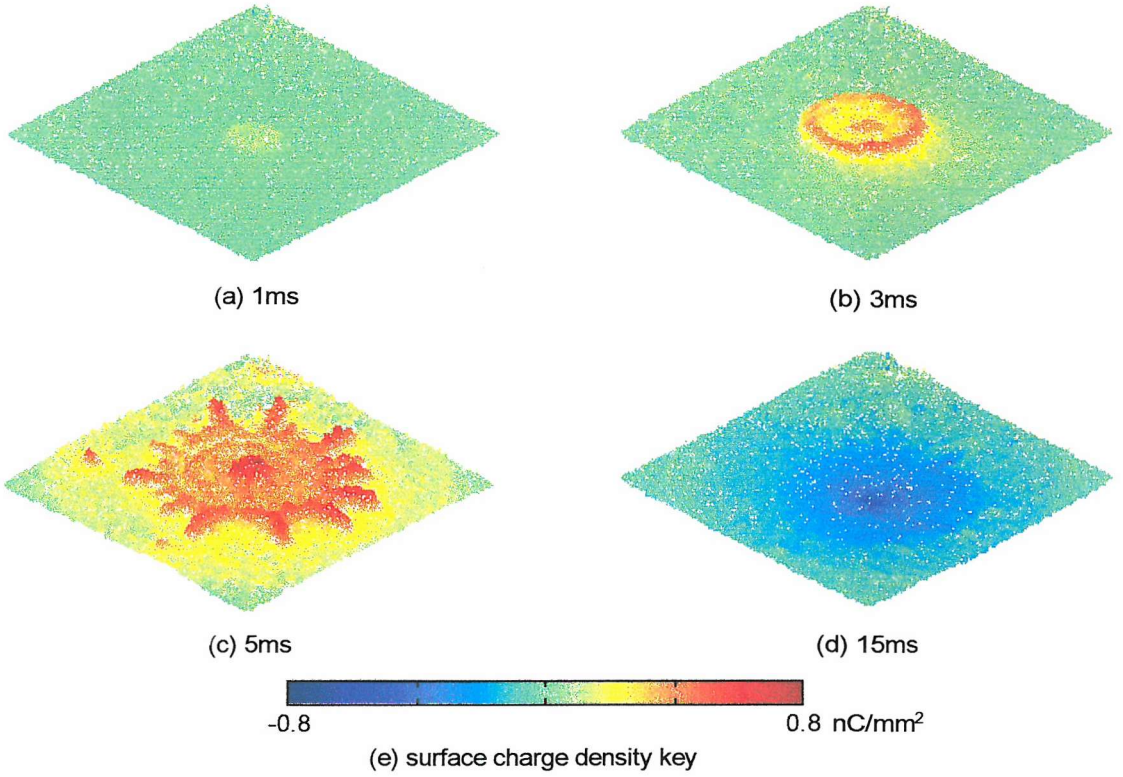

Figure 7.25 Surface charge distribution under AC response for 10% electro-negative gas SF_6 filled in the chamber at gas pressure 34.5kPa (5psi) (effective dimensions of these images are 8mm by 8mm)

7.6.3 Discussion

The experimental results show that surface discharge behaviour under an applied positive stress can be greatly limited by the use of an electro-negative gas (SF_6 with 10% concentration). The electro-negative gas strongly influences the propagation of positive charge, which does not form into streamers but remains concentrated near to the electrode. From the previous published research [99], it has been shown that even a concentration of 1% SF_6 effectively reduces ionisation by decreasing the free mean path of attachment. However, the performance of the electro-negative gas SF_6 can be degraded by the existence of impurities such as water vapour [100,101].

Chapter 8

Conclusions and Further Work

8.1 Conclusions

The dynamic measurement of surface charge has been achieved through the use of a Pockels cell. The measurement of a two-dimensional electric field is more complicated than single point measurements, it requires more optical components and additional control electronics. The resulting system allows accurate measurement of surface charge and the image processing removes non-uniform effects.

In the early stages of the development, a 1/8 wave-plate was used to bias the initial light intensity in order to distinguish charge polarity and obtain the maximum light intensity distribution across the crystal. This approach provides a simple measurement principle and image processing of the light intensity change due to Pockels effect is straightforward. However, this measurement approach does not account for the non-uniformity effects introduced by system components.

This was solved through the use of an Optical Phase Modulator, that allowed a laser with higher input power to be used improving the Signal to Noise Ratio (SNR). A thinner BSO crystal was also introduced in order to improve the spatial resolution A

Synchronisation Control Circuit (SCC) was designed to control the OPM and provide timing for the experiment. The modulating voltage generated by the SCC was amplified using a power amplifier in order to drive the OPM. This ensured that the light intensity of the image was modulated by the desired optical phase. The OPM is modulated at half the camera frame rate giving a temporal resolution of 1ms. This is a significant improvement when compared to previous published work. The difference between positive and negative modulated images is used to calculate the light intensity across the crystal and then the surface charge distribution. By using the methods of images, the constant off-set component due to dark current in the camera and leakage light intensity of PBS was eliminated. Furthermore, this approach also improves the signal magnitude. By using the OPM to measure light intensity before the application of a high voltage, it is possible to determine the natural birefringence of the crystal. The natural birefringence exists due to residual mechanical stress at the interface between optical components and their mountings. The subsequent removal of the effect due to natural birefringence from the light intensity processed image improves measurement accuracy. The use of image averaging technique also can remove time varying noise when observing static charge.

The surface discharge characteristics for two different polymers bonded to the BSO have been measured. Different thickness of PMMA and LDPE were tested under an applied AC stress. The results show that polymeric materials have different surface charge distributions compared to BSO. The streamer channels contain more branches and it is believed that polymeric materials enhance surface ionisation.

With the addition of a vacuum chamber the optical system has been used to investigate the relationship between surface discharge and atmospheric environment. The presence of electro-negative gas has a significant effect on positive streamer development.

8.2 Further Work

Further work can be carried out to improve system performance. A Pockels crystal having a higher optical gain than BSO (e.g. BGO) could be used as the sensing element. The electro-optic coefficient of BGO is double that of BSO and its dielectric constant is lower, hence, the electric field induced by surface charge within the BGO is higher. The light intensity in a thin BGO crystal would not become saturated by an AC applied voltage of ±7kV pk-pk. The measured light intensity could be enhanced by coating a dielectric mirror onto the backside of the crystal. Results from previous published work [32,33] show that a dielectric mirror will reflect more than 90% of the incident light. This would improve the measurement of surface charge characteristics of polymeric materials.

Measurements for insulating material such as HDPE, XLPE and Teflon should be undertaken. The relationship between material morphology and surface charge distribution needs to be investigated. Of particular interest are the surface charge effects due to ageing [88] and oxidation as well as the possible effect of gas discharge by-products [102,103,104,105,106] on insulator performance.

Appendix A

Developed Software for optical system including a waveplate

This program is written in the Matlab programming environment and calculates the surface charge density from the light intensity change data. The flow chart of the developed software is shown in Figure A.1

A.1 Flow chart

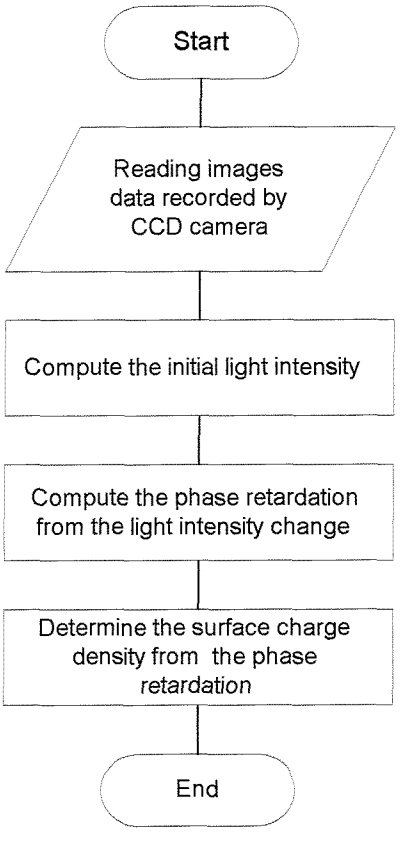

Figure A.1 Flow chart for the Matlab program of optical system including a waveplate

A.2 Matlab Program

"quarter.m"

```
% This program is written to determine the phase retardation change due to surface
% change by Pockels effect. The programe is used to determine the change of the
% phase retardation by an applied AC stress at BSO The images content of light
% intensity change is loaded from the computer and the measurement principle
% is based on the use of 1/8 waveplate derived from Chapter 4.


Ini=zeros(240,256);                 % Initial light intensity as Eqaution 4.2
tempload=zeros(240,256);            % temporary load file
Ia=zeros(240,256,1,40);             % array of images during discharge as Equation 4.3
theta=zeros(240,256,1,40);          % phase retardation due to surface charge

X=1:256; Y=1:240;                   % define image size

% definde images path
path1=('e:\quarter\positive\result4\');
file=('f_000196');
ext=('.bmp');

Ini=double(imread([path1,file,ext]));          % load the initial light intensity

% load the light intensity during discharge
file=('f_000');

m=1;
 for n=198: 237

    b=int2str(n);

    tempload=double(imread([path1,file,b,ext]));
    Ia(1:240,1:256,1,m)=tempload;
    m=m+1;

 end

% determine the phase retardtion using Eqaution 4.4
 for k=1:40
```

```
    theta(1:240,1:256,1,k)=-0.5*asin((Ia(1:240,1:256,1,k)-Ini)./Ini);

  end

% Using small image size up to 150X150 pixels
thetaz=zeros(150,150,1,40);

  for k=1:40
    thetaz(1:150,1:150,1,k)=theta(21:170,51:200,1,k);
  end

lamda=632.8e-9;                 % operating wavelength
no=2.54;                        % refractive index of BSO
r41=5e-12;                      % electro-optic coefficient of BSO
cd=.0005;                       % crystal thickness
epsilon=8.854e-12;              % permittivity of space
repsilon=56;                    % dielectric constant
Q=zeros(150,150,1,40);          % surface charge distrbution array

% convert phase retardation to surface charge density using Equation 3.7
Q(:,:)=thetaz(:,:)*lamda.*epsilon.*repsilon./(2*pi.*(no).^3.*r41.*cd)/10000;
```

Appendix B

Developed Software for optical system including an Optical Phase Modulator

This Matlab program is written for the optical system including an OPM based on the flow chart shown in Figure B.2. However, the OPM system has been used to obtain surface charge data either by AC or impulse voltages. Therefore, section B.2 shows the Matlab program written for impulse voltage measurements, whereas the section B.3 shows the Matlab program written for AC voltage measurements. Both have a common flow chart, the difference between these two programs is that the difference images are obtained after the discharge for an impulse voltage measurement, whereas for AC voltage measurement the difference images are obtained during the discharge.

B.1 Flow chart

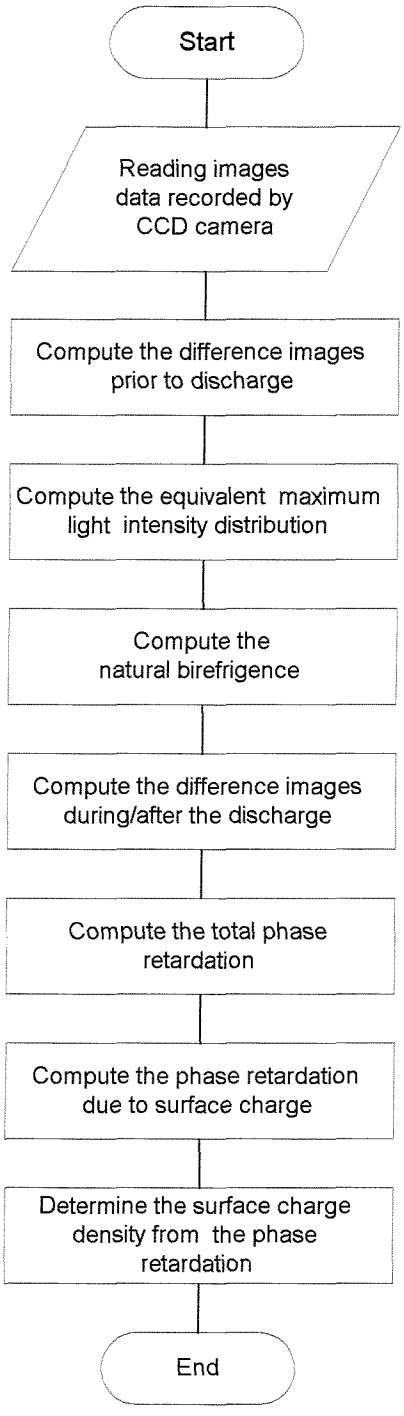

Figure B.1 Flow chart for the Matlab program of optical system including an OPM for impulse discharge

B.2 Matlab Program

"opmimpulse.m"

```
% This program is written to determine the phase retardation change due to surface
% change by Pockels effect. The programe is used to determine the change of the
% phase retardation by an applied positive or negative impulse stress.
% The images content of light intensity change is loaded from the computer and
% the measurement principle is based on the use of OPM derived from Chapter 5.

clear all
tempload=zeros(240,256);          % temporary load file
Po=zeros(240,256);                % positive modulated image prior to discharge
Ne=zeros(240,256);                % negative modulated image prior to discharge
Ini=zeros(240,256);               % Initial image prior to discharge
detI=zeros(240,256);              % diffrence modulated image prior to discharge
Ipo=zeros(240,256);               % positive modulated images prior to discharge
Ine=zeros(240,256);               % negative modulated images prior to discharge
temp1=zeros(240,256);             % temporary load file
temp2=zeros(240,256);             % temporary load file

X=1:256; Y=1:240;                 % define image size

% definde images path
path=('e:\modulat\impulse\positive\result1\');
file=('f_000');
ext=('.bmp');

% load the modulated images prior to discharge
k1=226;
k2=38;

for n=k1: 2: k1+k2

  c=int2str(n);
  d=int2str(n+1);
   temp1=double(imread([path,file,c,ext]));
   Po=Po+temp1;                   % load positive modulated images prior to discharge
   temp2=double(imread([path,file,d,ext]));
   Ne=Ne+temp2;                   % load negative modulate images prior to discharge
end

Po=Po./20;                        % averaging positive modulated image
Ne=Ne./20;                        % averaging negative modulated image


% load the initial light intensity
path=('e:\modulat\impulse\positive\result1\bias\');
file=('f_00');

k5=5400;
k6=29;
m=1;

for n=k5: k5+k6;

   b=int2str(n);
   tempload=double(imread([path,file,b,ext]));

   Ini=Ini+tempload;
```

```
end

% averaging technique
Ini=Ini./30;

detI=Po-Ne;                          % diffrence modulated images prior to discharge as Equation 5.8

TempI=Po+Ne-2.*Ini;                  % Equation 5.10

thetam=0.41646;                      % modulated phase

Tempsin=zeros(240,256);              % temporary sinusoidal term
Tempsin=(sin(2.*thetam)).^2./(1-(cos(2.*thetam))).^2;

Im=((detI).^2+(TempI).^2.*Tempsin).^0.5;
                                     % equivalent maximum light intensity distrbution as Equation 5.11

Diag=zeros(240,256);                 % diagnosis array

for k7=1:240
  for k8=1:256
    if Im(k7,k8)< 0                  % Im must be greater than 0
      Diag(k7,k8)=1;                 % return 1 in the invalid position
    end
  end
end

% Diagnosis base on Equation 5.20
AbsofI=zeros(240,256);               % absolute light intensity
AbsofI=abs(detI);
thenat=zeros(240,256);               % natural birefringence

for k9=1:240
  for k10=1:256
    if AbsofI(k9,k10)> Im(k9,k10) %as Equation 5.19
      Diag(k9,k10)=1;                % ignore process the invalid position
      thenat(k9,k10)=0;
    else
      thenat(k9,k10)=0.5*asin(detI(k9,k10)/Im(k9,k10));      % as Equation 5.9
    end
  end
end

% load images after impulse discharge
path=('e:\modulat\impulse\positive\result1\');
file=('f_000');

k1=286;
k2=28;

for n=k1: 2: k1+k2

  c=int2str(n);
  d=int2str(n+1);
   temp1=double(imread([path,file,c,ext]));
   Ipo=Ipo+temp1;                    % load positive modulated images prior to discharge
   temp2=double(imread([path,file,d,ext]));
   Ine=Ine+temp2;                    % load negative modulated images prior to discharge
end
```

```
Ipo=Ipo./15;                    % averaging positive modulated image
Ine=Ine./15;                    % averaging negative modulated image

Ia=zeros(240,256);              % difference modulated images

Ia=Ipo-Ine;                     % as Equation 5.4

thetall=zeros(240,256);         % total phase retardation
theta=zeros(240,256,1,22);      % phase retardation due to surface charge
AbsofI=zeros(240,256);          % absolute light intensity

% diagnosis based on Equation 5.19
AbsofI=abs(Ia);
  for y3=1:240
    for y4=1:256
      if AbsofI(y3,y4)>Im(y3,y4)      % as Equation 5.19
        Ia(y3,y4)=0;                % return 0 in the image if not valid
        Diag(y3,y4)=1;              % return 1 in the diagnosis array
      end
    end
  end
  thetall=0.5*asin(Ia./Im);

  theta=thetall-thenat;

lamda=632.8e-9;                 % operating wavelength
no=2.54;                        % refractive index of BSO
r41=5e-12;                      % electro-optic coefficient of BSO
cd=.00016;                      % crystal thickness
epsilon=8.854e-12;              % permittivity of space
repsilon=56;                    % dielectric constant
Q=zeros(240,256,1,40);          % surface charge distrbution array

% convert phase retardation to surface charge density using Equation 3.7
Q=theta*lamda.*epsilon.*repsilon./(2*pi.*(no).^3.*r41.*cd)/1000000;
```

B.3 Matlab Program

"opmac.m"

```
% This program is written to determine the phase retardation change due to surface
% change by Pockels effect. The programe is used to determine the change of the
% phase retardation by an applied AC stress at BSO, polymer material bonded on BSO and
% compressed gas environment. The images content of light intensity change is loaded
% from the computer and the measurement principle is based on the use of OPM
% derived from Chapter 5.

clear all
A=zeros(240,256,1,42);              % array of images during discharge
tempload=zeros(240,256);            % temporary load file
Po=zeros(240,256);                  % positive modulated image prior to discharge
Ne=zeros(240,256);                  % negative modulated image prior to discharge
Ini=zeros(240,256);                 % initial image prior to discharge
detI=zeros(240,256);                % diffrence modulated image prior to discharge
temp1=zeros(240,256);               % temporary load file
temp2=zeros(240,256);               % temporary load file

X=1:256; Y=1:240;                   % define image size

% definde images path
patha=('d:\normal2\s000wm.8\');
pathb=('d:\normal2\s000wm.7\');
file=('f_00000');
ext=('.bmp');

% load the modulated images prior to discharge
k1=2;
k2=6;

for n=k1: 2: k1+k2

  c=int2str(n);
  d=int2str(n+1);
   temp1=double(imread([patha,file,c,ext]));
   Po=Po+temp1;
   temp2=double(imread([patha,file,d,ext]));
   Ne=Ne+temp2;
end

file=('f_0000');

k3=10;
k4=18;

for n=k3: 2: k3+k4

  c=int2str(n);
  d=int2str(n+1);
   temp1=double(imread([patha,file,c,ext]));
   Po=Po+temp1;                     % load positive modulated images prior to discharge
   temp2=double(imread([patha,file,d,ext]));
   Ne=Ne+temp2;                     % load negative modulated images prior to discharge
end

Po=Po./14;                          % averaging positive modulated image
```

```
Ne=Ne./14;                          % averaging negative modulated image


% load the initial light intensity
file=('f_00');

k5=5400;
k6=29;
m=1;

for n=k5: k5+k6;

   b=int2str(n);
   tempload=double(imread([pathb,file,b,ext]));

   Ini=Ini+tempload;
end

% averaging technique
Ini=Ini./30;


detI=Po-Ne;                         % diffrence modulated images prior to
                                      % discharge as Equation 5.8

TempI=Po+Ne-2.*Ini;                 % Equation 5.10

thetam=0.41646;                     % modulated phase

Tempsin=zeros(240,256);             % temporary sinusoidal term
Tempsin=(sin(2.*thetam)).^2./(1-(cos(2.*thetam))).^2;

Im=((detI).^2+(TempI).^2.*Tempsin).^0.5;
                                    % equivalent maximum light intensity distrbution as Equation 5.11

Diag=zeros(240,256);                % diagnosis array

for k7=1:240
  for k8=1:256
    if Im(k7,k8)< 0                 % Im must be greater than 0
      Diag(k7,k8)=1;                % return 1 in the invalid position
    end
  end
end

% Diagnosis base on Equation 5.20
AbsofI=zeros(240,256);              % absolute light intensity
AbsofI=abs(detI);
thenat=zeros(240,256);              % natural birefringence

for k9=1:240
  for k10=1:256
    if AbsofI(k9,k10)> Im(k9,k10) % as Equation 5.20
      Diag(k9,k10)=1;               % ignore process the invalid position
      thenat(k9,k10)=0;
    else
      thenat(k9,k10)=0.5*asin(detI(k9,k10)/Im(k9,k10));
                                    % as Equation 5.9
    end
  end
```

```
end

% load images during discharge
file=('f_0000');
l1=30;
l2=39;                                  % load 40 images during discharge

m=1;
for n=l1: l1+l2;

   b=int2str(n);
   tempload=double(imread([patha,file,b,ext]));

   A(1:240,1:256,1,m)=tempload;
   m=m+1;
end

Ia=zeros(240,256,1,40);                 % difference modulated images array

for y=1: 2: 39

  Ia(1:240,1:256,1,y)=A(1:240,1:256,1,y)-A(1:240,1:256,1,y+1);          % as Equation 6.1a
  Ia(1:240,1:256,1,y+1)=A(1:240,1:256,1,y+2)-A(1:240,1:256,1,y+1);      % as Equation 6.1b
end

thetall=zeros(240,256);                 % total phase retardation
theta=zeros(240,256,1,40);              % phase retardation due to surface charge
AbsofI=zeros(240,256);                  % absolute light intensity


% diagnosis based on Equation 5.19
for y2=1: 40
  AbsofI=abs(Ia(1:240,1:256,1,y2));
  for y3=1:240
    for y4=1:256
      if AbsofI(y3,y4)>Im(y3,y4)        % as Equation 5.19
        AbsofI(y3,y4)=0;                % return 0 in the image if not valid
        Diag(y3,y4)=1;                  % return 1 in the diagnosis array
      end
    end
  end

  thetall=0.5*asin(Ia(1:240,1:256,1,y2)./Im);       % as Equation 5.5

  theta(1:240,1:256,1,y2)=thetall-thenat;           % as Equation 5.12
end

lamda=632.8e-9;                         % operating wavelength
no=2.54;                                % refractive index of BSO
r41=5e-12;                              % electro-optic coefficient of BSO
cd=.00016;                              % crystal thickness
epsilon=8.854e-12;                      % permittivity of space
repsilon=56;                            % dielectric constant
Q=zeros(240,256,1,40);                  % surface charge distrbution array

% convert phase retardation to surface charge density using Equation 3.7
Q(1:240,1:256,:,:)=theta(1:240,1:256,:,:)*lamda.*epsilon.*repsilon./(2*pi.*(no).^3.*r41.*cd)/1000000;
```

Appendix C

Synchronisation Control Circuit

The Synchronisation Control Circuit was designed and built in order to control the timing of the measurement system. This circuit utilises the PIC16F84 microcontroller to receive input signals and generate desired signals for the measurement system. Figure C.1 shows the schematic diagram of the circuit and Figure C.2 shows the flow chart of the microcontroller firmware..

C.1 Schematic diagram

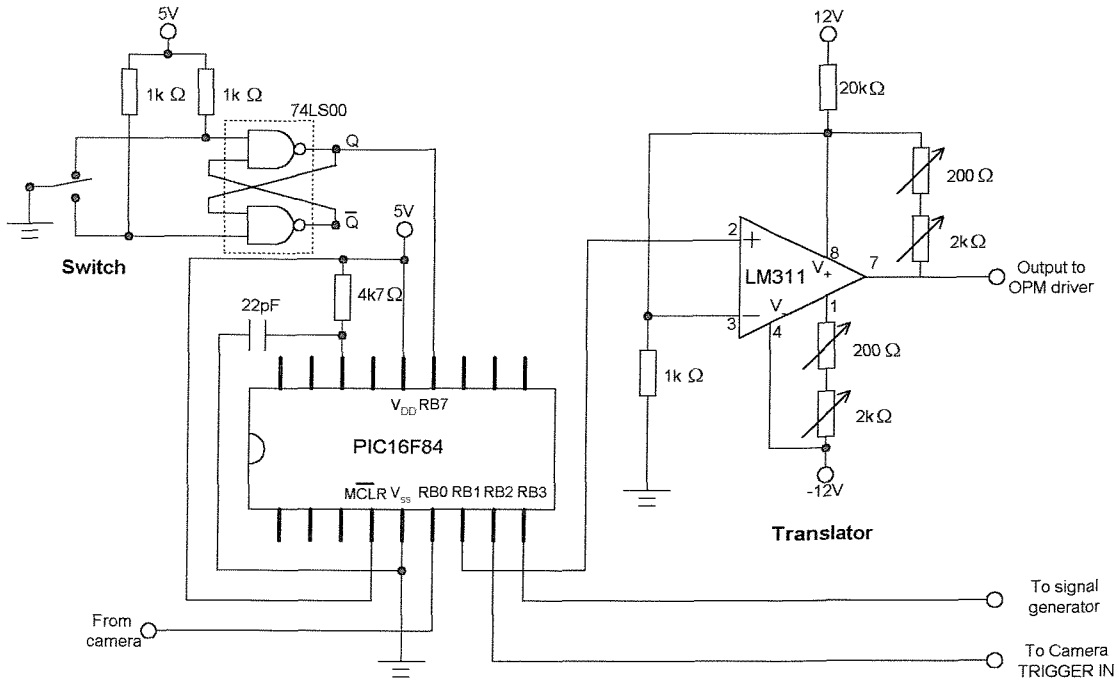

Figure C.1 Schematic diagram of the Synchronisation Control Circuit

C.2 Flow chart

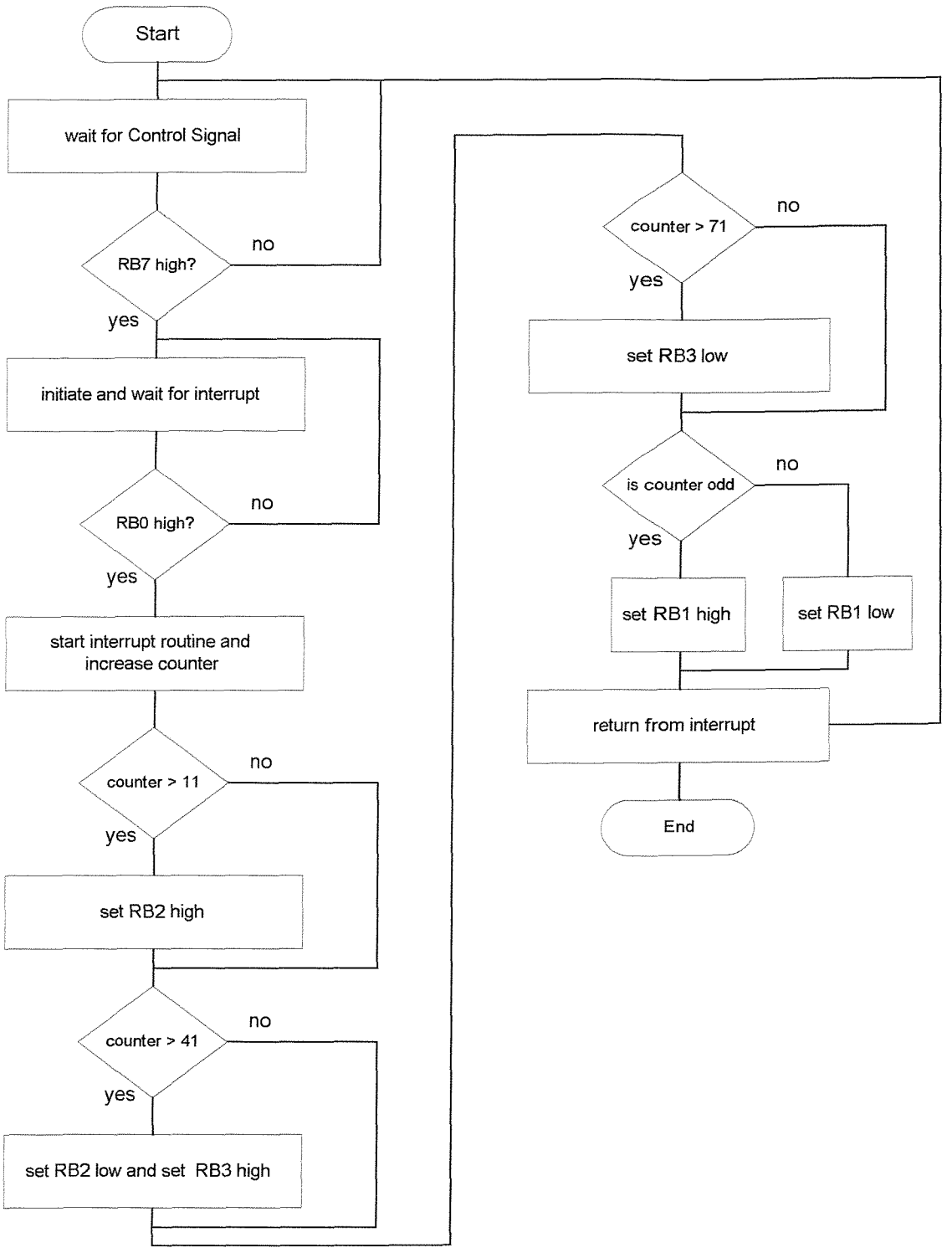

Figure C.2 Flow chart for the PIC16C84 program

C.3 PIC16C84 Program

"ssc.asm"

```
;This program is written in order to use the master source from the SYNC OUT of CCD camera
;to control the signals in the OPM system. Portb bit 1 received the pulse signal at 1000Hz
;from CCD camera and output 500Hz pulse signal with 50% duty cycle to the OPM. The output
;signal to the OPM driver is delay 0.5ms when the rising edge of the CCD camera is detect.
;Portb bit 2 is set to start the CCD camera recording frames and Portb bit 3 set to trigger
;the signal generator.

        list    p=16f84
        include <p16F84.inc>

; page 0 register:

timer   equ     0x01
statu   equ     0x03
portb   equ     0x06
intco   equ     0x0b

; page 1 register:

optio   equ     0x01
trisb   equ     0x06

; program register:

count   equ     0x0c

; Reset vector

        org     0x00
        nop
        goto    setup

; Main program

        org     0x100

setup   clrwdt
        bsf     statu,5         ; select memory page 1
        movlw   b'11000100'
        movwf   optio           ; set the rb0 rising edge trigger and timer div 32
        movlw   b'10000001'
        movwf   trisb           ; set rb0 and rb7 as input others as output
        bcf     statu,5         ; select memory page 0
        bsf     statu,0         ; clear carry bit
        clrf    portb
        movlw   b'10000000'
        movwf   intco           ; enable global interrupt

; test rb0

trig    movlw   b'00000000'
        movwf   count           ; clear the counter
        btfss   portb,7         ; wating for rb7 to be set
        goto    trig
        bsf     intco,4         ; enable INT interrup
```

```
loop    movf    count,0     ; move content of count to W register
        sublw   0x64         ; subtract W regiter from 100
        btfss   statu,2     ; if count is equal to 100 go to stand
        goto    loop        ; waiting for INT interrupt from portb bit 0

stand   bcf     intco,4     ; disable INT interrupt
        bcf     portb,1     ; clear portb bit 1
        btfss   portb,7     ; test the control signal from portb bit 7
        goto    stand       ; if no signal go to stand
        goto    trig        ; go to trig if portb bit 7 is high


        org     0x04        ; interupt vector

start   clrf    timer        ; clear timer
        incf    count,1     ; increase counter

check1  movf    count,0     ; move count into W register
        sublw   0x0b         ; subtract W regiter from 11
        btfsc   statu,0
        bsf     portb,2     ; set portb bit 2 high output to camera if count more than 11
        movf    count,0     ; move count into W register
        sublw   0x29         ; subtract W register from 41
        btfsc   statu,0
        bcf     portb,2     ; set portb bit 2 low output to camera if count more than 41

check2  movf    count,0     ; move count into W register
        sublw   0x29         ; subtract W register from 41
        btfsc   statu,0
        bsf     portb,3     ; set portb bit 3 high output to signal generator
                            ; if count more than 41
        movf    count,0     ; move count into W register
        sublw   0x47         ; subtract W register from 71
        btfsc   statu,0
        bcf     portb,3     ; set portb bit 3 low output to signal generator
                            ; if count more than 71

loop2   btfss   timer,4      ; delay of the output to the OPM
        goto    loop2


; check OPM high or low
hol     btfsc   count,0     ; check count is even or odd
        goto    high1       ; if odd go to high1
        goto    low1        ; if even go to low1

high1   bsf     portb,1     ; set portb bit 1 high output to OPM
        btfsc   portb,0     ; check portb bit 0
        goto    high1        ; if high go to high 1
        bcf     intco,1      ; clear intco flag bit
        retfie          ; return from interrupt

low1    bcf     portb,1     ; set portb bit 1 low output to OPM
        btfsc   portb,0     ; check portb bit 0
        goto    low1        ; if high go to low1
        bcf     intco,1     ; clear intco flag bit
        retfie                ; return from interrup

        end
```

Appendix D

List of Publications

(1) Y. L. Sam, P. L. Lewin, A. E. Davies, J. S. Wilkinson, S. J. Sutton, "Dynamic Measurement of Surface Charge" Proceedings of Eighth International Conference of Dielectric Material, Measurement and Application, pp.369-373, September 2000

(2) Y. L. Sam, P. L. Lewin, A. E. Davies, J. S. Wilkinson, S. J. Sutton, "Dynamic AC Surface Discharge Characteristics of PMMA and LDPE" Proceedings of Seventh. International Conference on Solid Dielectrics, pp.159-162, June 2001

(3) Y. L. Sam, P. L. Lewin, A. E. Davies, J. S. Wilkinson, S. J. Sutton, "The Influnce of Local Environmental Conditions on Surface Discharge Behaviour" Submitted to IEEE International Symposium on Electrical Insulation, Boston, USA, April 2002

References:

[1] R. J. Van Brunt, "Stochastic Properties of Partial-Discharge Phenomena", IEEE Trans. Electr. Insul., Vol.26, No.5, pp.902-948, October 1991.

[2] R. J. Van Brunt and M. Misakian, "Influence of a Dielectric Barrier on the Stochastic Behaviour of Trichel-Pulse Corona", IEEE Trans. Electr. Insul., Vol.26, No.3, pp.405-415, June 1991.

[3] F.H. Merrill and A. Von Hippel "The Atomphysical Interpretation of Lichtenberg Figures and Their Application to the Study of Gas Discharge Phenomena", J. Appl. Phys., Vol.10, pp.873-887, December 1939.

[4] Y. Murooka and S. Koyama, "Nanosecond Surface Discharge Study by Using Dust Figure Techniques", J. Appl. Phys., Vol.44, No.4, pp.1576-1580, April 1973.

[5] Y. Murooka and S. Koyama, "A Nanosecond Surface Discharge Study in Low Pressures", J. Appl. Phys., Vol.50, No.10, pp.6200-6206, October 1979.

[6] K. Hidaka and Y. Murooka, "3.0-ns Surface Discharge Development", J. Appl. Phys., Vol.59, No.1, pp.87-92, January 1986.

[7] E. Nasser and L. B. Loeb, "Impulse Streamer Branching from Lichtenberg Figure Studies", J. Appl. Phys., Vol.63, No.11, pp.3340-3348, July 1963.

[8] A. Kawashima and S. Hoh, "Lichtenberg Figures on Various Electrical Insulating Materials", IEEE Trans. Electr. Insul., Vol.13, No.1, pp.51-56, February 1978.

[9] M. Hara, J. Suehiro and T. Wakiyama, "Deflection of Streamer Channels in High Magnetic Field", IEEE Trans. Electr. Insul., Vol.27, No.6, pp.1179-1185, December 1992.

[10] A. Kawashima and S. Fukuda, "A Method for Observing Lichtenberg Figures Using High-Speed Image-Converter Cameras", Rev. Sci. Instrum., Vol.44, No.8, pp.1142-1143, August 1973.

[11] T. Shimazaki and I. Tsuneyasu, "Flashover Processes on the Surface of Solid Insulators under Positive Impulse Voltage in the Atmosphere", IEEE Trans. Electr. Insul., Vol.25, No.6, pp.1161-1169, December 1990.

[12] T. Shimazaki, "Flashover Characteristics and Surface Processes under Negative Impulse Voltage in the Atmospheric Air", IEEE Trans. Electr. Insul., Vol.27, No.3, pp.488-495, June 1992.

[13] T. Asokan and T. S. Sudarshan, "Streak Photography of Dynamic-electrical Discharge Behavior on Insulator Surfaces in Vacuum", IEEE Trans. Electr. Insul., Vol.28, No.1, pp.101-110, February 1993.

[14] A. Kumada, M. Chiba and K. Hidaka, "Potential Distribution Measurement of Surface Discharge by Pockels Sensing Technique", J. Appl. Phys., Vol.84. No.6, pp.3059-3065, September 1998.

[15] G. L. Hudson and L. B. Loeb, "Streamer Mechanism and Main Stroke in the Filamentary Spark Breakdown in Air as Revealed by Photomultipliers and Fast Oscilloscopic Techniques", Physical Review, Vol.123, No.1, pp.29-43, July 1961.

[16] L. B. Loeb and R. G. Westberg and H. C. Huang, "Streamer Mechanism in Filamentary Spark Breakdown in Argon by Photomultipliers Techniques", Physical Review, Vol.123, No.1, pp.43-50, July 1961.

[17] S. Larigaldie, "Spark Progation Mechanisms in Ambient Air at the Surface of a Charged Dielectric. I. Experimental: The Main Stages of the Discharge", J. Appl. Phys., Vol.61, No.1, pp.90-101, January 1987.

[18] D. K. Davies, "The Examination of the Electrical Properties of Insulators by Surface Charge Measurement", J. Sci. Instrum., Vol. 44, pp.521-524, 1967.

[19] H. Ootera and K. Nakanishi, "Analytical Method for Evaluation Surface Distribution on a Dielectric from Capacitive Probe Measurement - Application to a Cone-Type Spacer in ±500kV DC-GIS –" IEEE Trans. Power Delivery, Vol.3, No.1, pp.165-172, January 1988.

[20] J. Liesegang, B. C. Senn and E. R. Smith, "Resistivity of Static and Antistatic Insulators from Surface Charge Measurement", J. Appl. Phys., Vol.77, No.11, pp.5782-5785, June 1995.

[21] D. C. Faircloth, "Surface Charge Density and its Influence on Insulator Flashover", Ph.D Thesis, UMIST, UK, 2000.

[22] B. F. Hampton and C. Alderson, "A Technique for Measurement the DC Stress Distribution Across An Insulator", Colloquium on Surface Phenomena Affecting Insulator Performance, pp.6/1-6/3, 1998.

[23] A. Peterson, "On the Electrostatics of Probe Measurement of Accumulated Charge Density" Gaseous Dielectrics V, Pergamon Press, pp.242-247, 1987.

[24] A. Pedeson, G. C. Crinhton and I.W. McAllister, "The Function Relation Between Partial Discharge and Induced Charge", IEEE Trans. Diel. and Elect. Insul., Vol.2, No.4, pp.535-543, August 1995.

[25] T. O. Rerup, G. C. Crichton and I. W. McAllister, "Using the λ Function to Evaluate Probe Measurement of Charge Dielectric Surfaces", IEEE Trans. Diel. and Elect. Insul., Vol.3, No.6, pp.770-777, December 1996.

[26] K. Hidaka, "A New Method of Electric Field Measurement in Corana Discharge Using Pockels Device", J. Appl. Phys., Vol.53. No.9, pp.5999-6003, September 1982.

[27] K. Hidaka and Y. Murooka, "Electric Field Measurement in Long Gap Discharge Using Pockels Device", IEE Proceedings, Vol.132, Pt.A, No.3, pp.139-146, May 1985.

[28] K. Hidaka and T. Kouna, "Simultaneous Measurement of Two Orthogonal Components of Electric Field Using a Pockels Device", Rev. Sci. Instrum, Vol.60, No.7, pp.1252-1257, July 1989.

[29] S. R. M. Robertson, and A. J. Rogers, "Measurement of DC Electric Field Using the Electro-Optic Effect", IEE Proceedings, Vol.132, No.3, pp.195-198, June 1985.

[30] S. J. Huang and D. C. Erickson, "The Potential Use of Optical Sensors for the Measurement of Electric Field Distribution", IEEE Trans. Power Delivery, Vol.4, No.3, pp.1579-1585, July 1989.

[31] Y. Murooka and T. Nakano, "Optical High-Sensitive Field Sensor Using a Pockels Crystal", Rev. Sci. Instrum., Vol.63, No.12, pp.5582-5585, December 1992.

[32] Y. Murooka and T. Nakano, "High-Sensitive Pockels Field Sensor with a Dielectric Mirror", Rev. Sci. Instrum., Vol.65, No.7, pp.2351-2355, July 1994.

[33] Y. Murooka, T, Nakano, Y. Takahashi and T. Kawakami, "Modified Pockels Sensor for Electric-Field Measurements", IEE Proc. Sci. Meas. Technol., Vol.141, No.6, pp.481-485, November 1994.

[34] K. Hidaka, "Progress in Japan of Space Charge Field Measurement in Gaseous Dielectrics Using a Pockels Sensor", IEEE Electrical Insulation Magazine, Vol.12, No.1, pp.17-28, February 1996.

[35] M. Zahn, T. Takada and S. Voldman, "Kerr Electro-Optic Field Mapping Measurement in Water Using parallel Cylindrical Electrodes", J. Appl. Phys., Vol.54, No.9, pp.4749-4761, September 1983.

[36] M. Zahn and T. Takada, "High Voltage Electric Field and Space-Charge Distributions in Highly Purified Water", J. Appl. Phys., Vol.54, No.9, pp.4762-474775, September 1983.

[37] M. Zahn, M. Hikita, K.A. Wright, C.M. Cooke and J. Brennan, "Kerr Electro-Optic Field Mapping Measurement in Electron Beam Irradiated Polymethylmethacrylate", IEEE Trans. Electr. Insul., Vol.22, No.2, pp.181-185, April 1987.

[38] T. Maeno and T Takada, "Electric Field Measurement in Liquid Dielectrics Using A Combination of AC Voltage Modulation and a Small Retardation Angle", IEEE Trans. Electr. Insul., Vol.22, No.4, pp.503-508, August 1987.

[39] T. Maeno, Y. Nonaka and T. Takada, "Determination of Electric Field Distribution in Oil Using the Kerr-Effect Technique After Application of DC Voltage", IEEE Trans. Electr. Insul., Vol.25, No.3, pp.475-480, June 1990.

[40] S. M. Mahajan and T. S. Sudarshan, "Measurement of the Space Charge Field in Transformer Oil Using its Kerr Effect", IEEE Trans. Diel. and Elect. Insul., Vol.1, No.1, pp.63-70, February 1994.

[41] H. Okubo, R Shimizu, A. Sawada, K. Kato, N. Hayakawa and M. Hikita, "Kerr Electro-Optic Field Measurement and Charge Dynamics in Transformer-Oil/Solid Composite Insulation Systems", IEEE Trans. Diel. and Elect. Insul., Vol.4, No.1, pp.64-70, February 1997.

[42] R. Liu, A. Satoh, T. Kawasaki, K. Tanaka and T. Takada, "High-Sensitivity Kerr-Effect technique for Determination of 2-Dimensional Electric Field", IEEE Trans. Electr. Insul., Vol. 27, No.2, pp.245-254, April 1992.

[43] T. Kawasaki, Y. Arai and T. Takada, "two-Dimensional Measurement of Electrical Surface Charge Distribution on Insulating Material by Electrooptic Pockels Effect", Japanese J. Appl. Phys., Vol.30, No.6, pp.1262-1265, June 1991.

[44] T. Kawasaki, T. Terashima, S. Suzuki and T. Takada, "AC Surface Discharge on Dielectric Materials Observed by Advanced Pockels Effect Technique", J. Appl. Phys., Vol.76, No. 15, pp.3724-3729, September 1994.

[45] T. Kawasaki, T. Terashima, Y. Zhu, T. Takada and T. Maeno "Highly Sensitive Measurement of Surface Distribution Using the Pockels Effect and an Image Lock-in Amplifier", J. Phys. D: Appl. Phys., Vol.27, pp.1646-1652, 1994.

[46] Y. Zhu, T. Takada and D. Tu, "An Optical Measurement Technique for Studying Residual Surface Charge Distribution", J. Phys. D: Appl. Phys., Vol.28, pp.1468-1477, 1995.

[47] Y. Zhu, T. Takada, Y. Inoue and D. Tu, "Dynamic Observation of Needle-Plane Surface Discharge Using the Electro-Optical Pockels Effect", IEEE Trans. Diel. and Elect. Insul., Vol.3, No.3, pp.460-468, June 1996.

[48] Y. Zhu, T. Takada, K. Sakai and D. Tu, "The Dynamic Measurement of Surface Charge Distribution Deposited from Partial Discharge in Air by Pockels Effect Technique", J. Phys. D: Appl. Phys., Vol.29, pp.2892-2900, 1996.

[49] M. C. Simon, "Ray Tracing Formulas for Monoaxial Optical Component", Applied Optics, Vol.22, No.2, pp.354-360, January 1983.

[50] M. C. Simon and R. M. Echarri, "Ray Tracing Formulas for Monoaxial Optical Component; Vectorial Formulation", Applied Optics, Vol.25, No.12, pp.1935-1939, June 1986.

[51] M. C. Simon, "Refraction in Biaxial Crystals: a Formula for the Indices", J. Opt. Soc. Am. A, Vol.4, No.12, pp.2201-2204, December 1987.

[52] H. M. J. Boots, "Light Scattering in an Optically Anisotropic Medium", J. Opt. Soc. Am. A, Vol.11, No.9, pp.2539-2544, September 1994.

[53] T. S. Moss, G. J. Burrell and B. Ellis, "Semiconductor Opto-Electronics", London Butterworths, pp.23-25, 1973.

[54] S. A. Akhmanov and S. Y. Nikitin, "Physical Optics", Clarendon Press, Oxford, 1997.

[55] T. S. Moss, G. J. Burrell and B. Ellis, "Semiconductor Opto-Electronics", London Butterworths, pp.247-258, 1973.

[56] C. C. Davis "Lasers and Electro-optics Fundamentals and Engineering", Cambridge University Press, pp.508-517, 1996

[57] G. D. Boyd, A. Ashkin, J. M. Dziedzic and D. A. Kleiman, "Second Harmonic Generation of Light with Double Refraction", Physical Review, Vol.137, No.4A, pp.A1305-A1320, February 1965.

[58] A. Yariv, "Introduction to Optical Electronics", Holt, Rinehart and Winston, 1971.

[59] C. C. Davis "Lasers and Electro-optics Fundamentals and Engineering", Cambridge University Press, pp.472-486, 1996

[60] F. Pedrotti and L. Pedrotti, "Introduction to Optics", Prentice Hall, Inc, 1996.

[61] A. R. Mickelson, "Physical Optics", Van Nostrand Reinhold, New York, 1992.

[62] E. Hecht, "Optics", Addison-Wesley Publishing Company, 1987.

[63] P. Yeh, "Electromagnetic propagation in Birefringent Layered Media", J. Opt. Soc. Am., Vol.69, No.5, pp.742-755, May 1979.

[64] P. Yeh, "Extended Jones Matrix Method", J. Opt. Soc. Am., Vol.72, No.4, pp.507-513, April 1982.

[65] C. Gu and P. Yeh, "Extended Jones Matrix Method. II", J. Opt. Soc. Am. A, Vol.10, No.10, pp.966-973, April 1982.

[66] D. Penninckx and V. Morenas, "Jones Matrix of Polarization Mode Dispersion", Optics Letters, Vol.24, No.13, pp.875-877, July 1999.

[67] H. Kogelnik, L. E. Nelson, J. P. Gordon and R. M. Jopson, "Jones Matrix for Second-Order Polarization Mode Dispersion", Optics Letters, Vol.25, No.1, pp.19-21, January 2000.

[68] P. Yeh, "Optical Waves in Layered Media", John Wiley & Sons, 1988.

[69] C. Li and X. Cui, "Measuring Two-Dimension Electrostatic Field by Using Electrooptic Crystal", Proc. SPIE, Vol.2897, pp.243-249, 1996.

[70] F. T. Sheehy, W. B. Bridges and J. H. Schaffner, "60 GHz and 94 GHz Antenna-Coupled $LiNbO_3$ Electrooptic Modulators", IEEE Photonics Tech. Lett., Vol.5, No.3, pp.307-310, March 1993.

[71] S. Hopfer, "A Novel, Wideband, Lithium Niobate Electrooptic Modulater", J. Lightwave Tech., Vol.16, No.1, pp.73-77, January 1998.

[72] T. Yoneyama and D. Dawn, "Optical Intensity Modulator Using Inverted Slot line at 60 GHz", Optical and Quantum Electronics, Vol.30, No.11, pp.985-993, December 1998.

[73] O. Mitomi, K. Noguchi and H. Miyazawa, "Broadband and Low Driving-Voltage $LiNbO_3$ Optical Modulators", IEE Proc.-Optoeletronics, Vol.145, No.6, pp.360-364. December 1998.

[74] K. Nakanishi, A. Yoshioka, A. Arahata and Y. Shibuya, "Surface Charging on Epoxy Spacer at DC Stress in Compressed SF_6 Gas", IEEE Trans. PAS, Vol. PAS-102, No. 12, December 1983.

[75] T. Nitta and K. Nakanishi, "Charge Accumulation on Insulating Spacers for HVDC GIS", IEEE Trans. Electr. Insul., Vol.26, No.3, pp.418-427, June 1991.

[76] M. Sone, K. Toriyama and Y. Toriyama, "Liquid Crystal Lichtenberg Figure", Appl. Phys. Lett., Vol.24, No.3, pp.115-117, February 1974.

[77] J. R. Meyer-Arendt, "Introduction to Classical and Modern Optics", Prentice Hall, Inc, 1989.

[78] J. Wilson and J. Hawkes, "Optoelectronics an Introduction", Prentice Hall, Inc, 1998.

[79] K. Takizawa, H. Kikuchi and H. Fujikake, "Spatial Light Modulator Using Polymer-Disperrsed Liquid Crystal: Dependence of Resolution on Reading Light Intensity", J. Appl. Phys, Vol.75, No.6, pp.3158-3168, March 1994.

[80] Y. L. Sam, P. L. Lewin, A. E. Davies, J. S. Wilkinson, S. J. Sutton, "Dynamic Measurement of Surface Charge" Proceedings of Eighth International Conference of Dielectric Material, Measurement and Application, pp.369-373, September 2000

[81] Y. Zhu, "Development of Two-Dimensional Optical Measurement Techniques Using Dielectric Anisotropy", Ph.D Thesis, Electronic Measurement Laboratory, Mushashi Institute of Technology, Japan, March 1997

[82] T. J. Gallagher and A. J. Pearmain, "High Voltage Measurement, Testing and Design", John Wiley & Sons, pp.103-105, 1983.

[83] T. S. Sudarshan and R. A. Dougal, "Mechanisms of Surface Flashover Along Solid Dielectrics in Compress Gases: A Review", IEEE Trans. Electr. Insul., Vol.21, No.5, pp.727-746, October 1986.

[84] T. J. Gallagher and A. J. Pearmain, "High Voltage Measurement, Testing and Design", John Wiley & Sons, pp.46-47, 1983.

[85] I. Gallimberti, "A Computer Model for Streamer Propagation", J. Phys. D: Appl. Phys., Vol.5, pp.2179-2189, 1972.

[86] A. H. Cookson, "Review of High –Voltage Gas Breakdown and Insulators in Compressed Gas", IEE Proc., Vol.128, Pt.A, No.4, pp.303-312, May 1981.

[87] M. Tanaka, Y. Murooka and K. Hidaka, "Nanosecond Surface Discharge Development Using the Computer Simulation Method", J. Appl. Phys., Vol.61, No.1, pp.4471-4478, May 1987

[88] R. A. Anderson, "Anode-Initiated Surface Flashover", IEEE CEIDP, pp.173-179, 1979

[89] Y. L. Sam, P. L. Lewin, A. E. Davies, J. S. Wilkinson, S. J. Sutton, "Dynamic AC Surface Discharge Characteristics of PMMA and LDPE" Proceedings of Seventh. International Conference on Solid Dielectrics, pp.159-162, June 2001

[90] M. A. Plonus, "Applied Electromagnetics", McGraw-Hill Book Company.

[91] H. G. Miller, "Surface Flashover of Insulator", IEEE Trans. Electr. Insul., Vol.24, No.5, pp.765-786, October 1989.

[92] N. L. Allen and P. N. Mikropoulos, "Streamer Propagation along Insulating Surface", IEEE Trans. Diel. and Elect. Insul., Vol.6, No.3, pp.357-362, June 1999.

[93] N. L. Allen, "The Propagation of Positive Streamer in Air and at Air/Insulator Surfaces", Phenomena in Ionised Gases XXII, American Institute of Physics Conference Proceedings 363, pp.247-256, 1995.

[94] E. Husain and R. S. Nema, "Electric Stress at Breakdown in Uniform Field for Air, Nitrogen and Sulphur Hexafluoride", Gaseous Dielectric IV, Pergamon Press, pp.168-173, 1984.

[95] K. D. Srivastara and J. Zhou, "Surface Charge and Flashover of Spacer in SF_6 under Impulse Voltage", IEEE Trans. Electr. Insul., Vol26, No.3, pp.428-441, June 1991.

[96] A. Knecht, "Development of Surface Charges on Epoxy Resin Spacers Stressed with Direct Applied Voltage", Gaseous Dielectric III, Pergamon Press, pp.356-363, 1982.

[97] K. Nakanishi, A. Yoshioka, Y. Shibuya and T. Nitta, "Charge Accumulation on Spacer Surface at DC Stress in Compressed SF_6 Gas", Gaseous Dielectric III, Pergamon Press, pp.365-373, 1982.

[98] L. Niemeyer and F. Pinnekamp, "Surface Discharge in SF_6", Gaseous Dielectric III, Pergamon Press, pp.379-385, 1982

[99] I. Gallimberti, "Break Mechanism in Electro-negative Gases", Gaseous Dielectric V, Pergamon Press, pp.61-80, 1987

[100] G. Berger, B. Senouci, O. Belaber, B. Hutzler and G. Riquel, "Degradation of the Dielectric Properties of SF_6 due to the Presence of Gaseous Impurities", Gaseous Dielectric V, Pergamon Press, pp.182-190, 1987

[101] G. Berger, B. Senouci, B. Hutzler and G. Riquel, "The Influence of Impurities on the Dielectric Strenghth of SF_6 for Positive Polarity", Gaseous Dielectric V, Pergamon Press, pp.191-198, 1987

[102] F. J. J. G. Janssen, "Decomposition of SF_6 by Arc Discharge and the Determination of the Reaction Product S_2F_{10}", Gaseous Dielectric V, Pergamon Press, pp.153-162, 1987

[103] R. J. Van Brunt, J. T. Herron and C. Fenimore, "Corona-Induced Decomposition of Dielectric Gases", Gaseous Dielectric V, Pergamon Press, pp.163-173, 1987

[104] I. Sauers, "SOF_4 Production in Spark Breakdown of SF_6/O_2 Mixture", Gaseous Dielectric V, Pergamon Press, pp.205-211, 1987

[105] J. Lampe, H. Latour-Slowikowska and J. Slowikowska, "Study on Metal Fluoride Products Formation Caused by the Electric Arc in SF_6", Gaseous Dielectric III, Pergamon Press, pp.433-438, 1982.

[106] F. Y. Chu, "SF_6 Decomposition in Gas-Insulated Equipment", IEEE Trans. Electr. Insul. Vol21, No.5, pp.693-725, October 1986.